LOUGHBOROUGH UNIVERSITY

Electrified thin film flow over inclined topography

by

Morgan James Tudball

A DOCTORAL THESIS
Submitted in partial fulfillment of the requirements
for the award of
Doctor of Philosophy of Loughborough University

in the

School of Science
Department of Mathematical Sciences

November 2018

Declaration of Authorship

I, Morgan James Tudball, declare that this thesis titled, **"Electrified thin film flow over inclined topography"** and the work presented in it are my own. I confirm that:

- This work was done wholly or mainly while in candidature for a research degree at this University.
- Where any part of this thesis has previously been submitted for a degree or any other qualification at this University or any other institution, this has been clearly stated.
- Where I have consulted the published work of others, this is always clearly attributed.
- Where I have quoted from the work of others, the source is always given. With the exception of such quotations, this thesis is entirely my own work.
- I have acknowledged all main sources of help.
- Where the thesis is based on work done by myself jointly with others, I have made clear exactly what was done by others and what I have contributed myself.

Signed: _____

Date: **November 2018**

LOUGHBOROUGH UNIVERSITY

Abstract

School of Science
Department of Mathematical Sciences

Doctor of Philosophy

by Morgan James Tudball

We consider both a long-wave model and a first-order weighted-residual integral boundary layer (WIBL) model in the investigation of thin film flow down a topographical incline whilst under the effects of a normal electric field. The liquid is assumed to be a perfect dielectric, although is trivially extended to the case of a perfect conductor. The perfect dielectric case with no topography includes a simple modified electric Weber number which incorporates the relative electrical permittivity constant into itself. Linear stability analysis is carried out for both models, and critical Reynolds numbers which depend on the electric Weber number and the capillary number are produced. Regions of stability, convective instability and absolute instability are then determined for both models in terms of our electric Weber number and Reynolds number parameters in the case of no topography. Time-dependent simulations are produced to corroborate the aforementioned regions and investigate the effect of normal electric field strength in addition to sinusoidal and rectangular topographical amplitude on our system for various domain sizes. For the time-dependent simulations we find strong agreement with the linear stability analysis, and the results suggest that the inclusion of a normal electric field may have some stabilising properties in the long-wave model which are absent in the case of a flat wall, for which the electric field is always linearly destabilising. This stabilising effect is not observed for the same parameters in the WIBL model with a sinusoidal wall, although a similar effect is noticed in the WIBL model with a rectangular wall. We also investigate the simultaneous effect of domain size, wall amplitude and electric field strength on the critical Reynolds numbers for both models, and find that increasing the electric field strength can make large-amplitude sinusoidal topography stabilising rather than destabilising for the long-wave model. Continuation curves of steady solutions and bifurcation diagrams are also produced, and comparisons between the two models are made for various parameter values, which show excellent agreement with the literature. Subharmonic branches and time-periodic solutions are additionally included, similarly showing very good agreement with the literature.

In this thesis:

Chapters 3 and 4 of this thesis are based on a manuscript intended to be submitted in late 2018.

Acknowledgements

I would first like to sincerely thank my parents, not only for their unwavering support and encouragement over the past 7 years, but also for the invaluable opportunities afforded to me – I am truly grateful, and could not ask for more selfless and loving parents. I also wish to express my deepest thanks to my supervisors Dr Dmitri Tseluiko and Dr David Sibley, whose guidance, advice and expertise have been greatly appreciated throughout my studies, and without whom this thesis would not be possible. I would also like to thank my good friends Mike, James and Dan for their enlightening discussions and moral support, as well as my family for their kindness and patience during this time. I am also grateful to Te-Sheng Lin for his help with the development of the Auto-07p code.

This research has been financially supported by an award from Engineering and Physical Sciences Research Council (EPSRC), to whom I would also like to show my appreciation and sincere thanks.

Morgan James Tudball

Contents

List of Figures

Chapter 1

Introduction

As is befitting a field which so often focuses upon complex dynamics and the interesting behaviour of waves and fluids, the study of falling liquid films and thin film flow is characterised by a rich and colourful history, and a wealth of literature surrounding it. In 1822, George Stokes and Claude-Louis Navier (whose contributions are recognised by the engraving of his name on the Eiffel Tower) proposed a system of equations which could fully describe the flow of viscous fluids, and these equations continue to prove invaluable to this day. Not only do solutions to the equations appear to accurately reflect the true behaviour of fluids in the laminar regime, but in the turbulent regime as well. Osborne Reynolds [71] was the first to uncover the power of lubrication theory, which he used to explain the experimental observations by Tower [93] formally inconsistent with contemporary understandings of viscosity. As discussed by Craster and Matar [17] in their overview on thin liquid films, this interplay between experimental observations and theoretical study is especially pronounced in thin film flow; see, for example, the innovative work of P. Kapitza [42] measuring the viscosity of liquid helium in 1938, and the pioneering work with his son S. Kapitza [43] in 1949 which involved experimental research into the wave flow of thin layers of viscous liquids. The leaps in theoretical understanding of fluid dynamics provided by these authors and researchers (and the immeasurable number of contributors not included here) have eventually resulted in the long-wave approximations, and subsequently both the single and coupled nonlinear evolutions equations which we still use currently to describe the local film thickness of thin liquid films, in addition to a myriad of other fluid properties.

Due to the inherent length rescaling in thin film flows, we may observe thin film dynamics in a multitude of seemingly incomparable contexts; the motion of continental

ice sheets [17]; pulmonary flow in human lungs [30]; a thin layer of rain flowing down a window – the dynamics of all of these phenomena may be accurately described by thin film models. Needless to say, for such a robust and far-reaching mathematical framework, the industrial applications are similarly wildly varied; mass and heat transfer devices [82]; microfluidic electronics [84, 87], and electrostatic spraying and painting [13] are merely a select few.

This work focuses upon thin film flow in the context of electrohydrodynamics and the effects of topography, both of which have been studied considerably by previous authors. The action of an electric field on thin films has been shown to have some very desirable properties. For example, in the case of a heat exchanger acting in conjunction with an electric field, it has been demonstrated that the transfer efficiency of heat can be significantly electrohydrodynamically enhanced [22]. The use of electric fields also introduces novel ways of controlling the flow dynamics, as discussed by Tseluiko et al. [96, 99, 100, 103] in addition to Veremieiev et al. [110]. Earlier applications were investigated by Kim, Bankoff and Miksis [45, 46] for electrostatic flow down an inclined plane in 1992, and they outlined designs for a cylindrical electrostatic radiator in 1994.

When discussing the effects of electric fields on fluid dynamics, a potential starting point is the 1964 work by Taylor [88] on the disintegration of water droplets in an electric field, and the association between the the field and the internal pressure of the droplets. The following year Taylor and McEwan [89] investigated the interfacial dynamics between a conducting and a non-conducting layer of fluid when a normal electric field is applied, and examined the stability of the system. Melcher and Schwarz Jr. [56], in 1968, examined the effect of a tangential electric field acting on a fluid, and analysed the physical mechanisms through which the field affects the film interface, specifically focusing upon charge relaxation. In 1969 Taylor and Melcher [57] then summarised contemporary work in electrohydrodynamics, and proposed the so-called 'leaky dielectric' model, which, as opposed to the typical assumption of perfect dielectric or perfect conductor, allows for free charges to redistribute themselves on the fluid surface.

The Taylor-Melcher leaky dielectric model has been somewhat recently discussed by Saville [79], and its applications and validity are discussed in detail in his 1997 overview. The effects of tangential electric fields have also been discussed by Castellanos and Gonzalez [13] in their 1998 review of nonlinear hydrodynamics which primarily focuses upon balance equations. The monograph 'Electrohydrodynamics' [12] by Castellanos gives a detailed overview on electrical phenomena in hydrodynamics, as well as a

more current summary and review on stability and conduction properties in addition to a multitude of related topics.

In 2006 Tseluiko and Papageorgiou [104] investigated the effect of a normal electric field on a thin film down a flat inclined wall. The electric field was found to be linearly destabilising and to not contribute to the tangential stress balance for perfect conductor or perfect dielectric fluids, although this is not true for the leaky dielectric model. The main result was that the inclusion of a normal electric field widened the band of unstable wavenumbers to include those shorter than which would otherwise be observed in the case without the electric field, and they also observed that despite the linear stability of the film, it is possible to promote instability for sufficiently strong electric fields. This occurs even in the case of zero Reynolds number, due to the amount of energy provided into the system by the electric field.

Tseluiko et al. [99] in 2008 investigated the effect of a normal electric field on a fluid which is either a perfect conductor or a perfect dielectric and is flowing down an inclined and small-amplitude corrugated wall at zero Reynolds number. They used boundary-element methods in addition to boundary-integral formulation and a long-wave model, and demonstrated how the normal electric field could be used to eliminate the phase shift between the fluid and the topography. The work also focused upon the removal of the capillary ridge which is observed above downward rectangular steps and after upward rectangular steps. An extension to this work was carried out the following year by Tseluiko and Blyth [96] and the effect of inertia was investigated, with the Reynolds number now being taken as nonzero, and both the fluid and gas phases being taken as perfect dielectrics. The inertial effects were found to be dependent upon the relative electrical permittivity of the fluid, in addition to the strength of the electric field, although the normal electric field itself was found to be generally destabilising.

Tseluiko et al. [100] also considered gravity-driven flow of a perfect conductor film down sinusoidal or rectangular troughs whose narrowness is allowed to vary, with the film also having a normal electric field applied. Strong agreement was found between the results of the lubrication model and the experimental work of Decré and Baret [19], who considered gravity-driven viscous liquid flow over inclined topography in the absence of a normal electric field. The zero Reynolds number case was also discussed by Tseluiko et al. [103] in the case of rectangular step topography when a normal electric field is applied. It was found that for a given long-wave limit, the surface profile results of the lubrication approximation can be obtained from the asymptotic results in

the case of no electric field, and they found good agreement with the 1988 and 1990 experimental work of Stillwagon and Larson [85, 86] when examining the capillary ridges associated with the topography.

Tseluiko et al. [101] also developed a nonlinear long-wave model in the case of viscous gravity-driven flow over step topography. Small-amplitude asymptotics for the topography are used, and they similarly found the capillary ridges and oscillations which are characteristic of flow over rectangular steps and trenches. They also observed heavily-damped oscillations which occur after a downward step. The case where periodic arrays of electrodes produce the normal electric field has also been investigated by Tseluiko et al. [102] in 2010 for perfect conductor flow down an inclined wall. The effects are qualitatively different to the case of a single electrode held infinitely far away, and using this novel array it is possible to remove capillary ridges and depressions locally without causing their formation elsewhere on the surface of the film.

Pease and Russel [63] considered a leaky dielectric model for thin film flow subject to an electric field in lithographically induced self-assembly, and found large differences between the perfect dielectric and leaky dielectric models for the linear stability of a polymer film. Mukhopadhyay and Dandapat [59] later considered the nonlinear stability of a viscous film flow down an inclined plane whilst subject to a normal electric field and used a momentum integral method to derive a nonlinear equation for the free surface. They found that the electric field was destabilising, and that the normal electric field introduced additional stresses at the interface. Work on three-dimensional falling electrified films was carried out by Tomlin, Papageorgiou and Pavliotis [91] in the case of an inclined plane and gravity-driven flow for both overlying and hanging films. It was found that electric fields of sufficient strength were able to induce chaotic dynamics for certain domains, and two-dimensional waves were found to evolve on the interface.

The nonlinear dynamics have also been considered by Tseluiko and Papageorgiou [105] for an electrified thin film which wets either the top or the bottom of a flat horizontal wall. The electric field is modelled as a nonlocal Hilbert transform term, and they used energy functional arguments and numerical data to prove that the film thickness remains finite in finite time. They also investigated the electrostatic effects on a gravity-driven flow down a vertical wall using a nonlinear long-wave model for the free-surface deflections [106]. It was found that the electric field promotes the growth of short waves especially, and methods for increasing interfacial turbulence are discussed.

Recently, Blyth et al. [7] examined electrified film flow down a flat inclined plane and the effect of the electric field on solitary pulses and travelling waves for the full system of equations in the case of no inertia, and using a quasi-linear long-wave model in cases where inertia is included. It was shown that for certain parameter values, the presence of the normal electric field was sufficient for the system to transition from absolutely unstable to convectively unstable, such that the electric field can be partially stabilising in a sense, and this result has been corroborated by time-dependent simulations.

The effect of potentially inclined topography on film dynamics in the absence of an electric field is also a well-discussed avenue of research. Of course, for such a generic class of hydrodynamical problems as those relating to topography and inclination angle, it would be impossible to list all the relevant breakthroughs and notable papers, and as such only those which are closely related to the current work in the considered physical scenario, or the mathematical modelling framework employed shall be discussed. The 2011 monograph 'Falling Liquid Films' [41] by Kalliadasis et al. gives a detailed analysis and overview of more general falling thin film problems, including nonisothermal cases and various methodologies depending on Reynolds number.

Some of the earlier analytical work on fluid flow over inclined topography was performed by Tougou [92] in 1978, and focused upon weakly nonlinear long waves travelling on a viscous film which flows down an inclined and uneven wall for small-amplitude corrugations. Similar assumptions on the size of the amplitude of the uneven wall were made by Wang [111] in 1981, who also discussed thin film flow over a wavy incline for low Reynolds numbers. In 1984, Wang [112] considered the case where the wall amplitudes are no longer prescribed to be small relative to the thickness of the film, and instead focused upon flows where the bottom topography is highly curved, and imposed that the film thickness should be much smaller than the minimum radius of curvature of the topography.

Malamataris and Bontozoglou [53] used finite element methods to determine steady-state surface profiles of a thin viscous film flowing down a vertical wavy wall. They found that the capillary number is the driving force in the determination of free surface profile, and that the Reynolds number is primarily responsible for the relative phase shift between the thin film and the topography. In 2003, Decré and Baret [19] used phase-stepped interferometry to produce two-dimensonal maps of the surface profile for thin film flow over inclined rectangular and square topography, and found that their results were consistent with somewhat simple models, such as a two-dimensional Green's function as in the case discussed by Hayes, O'Brien and Lammers [32], suggesting the scope

of these models was greater than previously thought. In 2000, Kalliadasis, Bielarz and Homsy [39] used the lubrication approximation to investigate thin viscous film over either a rectangular trench or non-uniform mound, and were able to derive a single nonlinear equation which describes the spatiotemporal evolution of the free surface. The mechanism responsible for the formation of the capillary ridge is discussed for flow over topography, and practical methods for removing the ridge are discussed. Kalliadasis and Homsy [40] also examined the linear stability of the aforementioned capillary ridge and found it to be stable.

Tseluiko, Blyth and Papageorgio [98] also considered the stability of thin film flow over inclined topography using a nonlinear long-wave evolution equation for the film thickness. They produced dependencies of the critical Reynolds number on the rescaled wall amplitude for several domains and topographies, including sinusoidal and rectangular troughs of various steepness. The stabilising or destabilising properties of the topography were found to be highly sensitive to both domain length and wall amplitude.

Wierschem et al. [113] investigated gravity-driven viscous film flow over inclined small-amplitude topography. Notably the analysis is not restricted to thin films, and distinctions are made between the qualitative behaviour of the films when they are thick, thin, and intermediate; namely that in cases of weak resonance the free surface amplitude increases with increasing film thickness for thin films, whereas in thick films the surface amplitude decreases with increasing film thickness. Previously in 2005, Wierschem, Scholle and Aksel [114] performed an experimental study of gravity-driven film flow over large-amplitude sinusoidal topography. They were able to determine a critical film thickness above which vortices were formed inside the film within the nadirs of the topography, and found that this value is independent of the Reynolds number.

In 2009, D'Alessio, Pascal and Jasmine [18] considered the case of gravity-driven thin film flow over inclined sinusoidal topography using the full second-order weighted-residual integral boundary layer (WIBL) model. They found that the bottom topography may be stabilising or destabilising depending on whether the the surface tension is sufficiently weak or strong, respectively, although instability is also dependent on the wavelength of the topography being sufficiently short in addition to this. One of the mathematical models employed in this thesis is the WIBL model, albeit using a first-order form which contains neither the terms relating to viscous dispersion nor the corrections to these terms which are present in the full four-equation system and are typically required for accurate modelling in the regime of Reynolds numbers between $100 - 200$ [76]. We shall discuss these WIBL models in more detail later.

Trifonov [95] analysed the case of gravity-driven viscous thin film flow over corrugated topography, where the free surface is taken to be either one-dimensional, two-dimensional or three-dimensional. In the one-dimensional case, the flow is found to be primarily determined by surface tension. In 2006, Argyriadi et al. [3] discussed gravity-driven film flow over inclined rectangular topography, and analysed the effects of wall steepness on the film. Perhaps surprisingly, it was found that steep walls are strongly stabilising relative to smoother topographies, and increase the critical Reynolds number for the system. Two-dimensional flow over a semi-circular obstruction in a channel was considered by Vanden-Broeck [107] in 1987, who was able to determine critical Froude numbers which corresponded to the existence of supercritical solutions.

In 2014, Tseluiko, Blyth and Papageorgiou [97] analysed both electrified and non-electrified thin film flow down an inclined sinusoidal wall where the Reynolds number was taken as critical and a long-wave Benney-type equation was used. In the case of absence of the nonlocal Hilbert transform term relating to the electric field, the authors are able to analytically examine the instability of the film, although in the electrified case this must be done numerically, and close agreement is found between the experimental work by Cao, Vlachogiannis and Bontozoglou [11] and Tseluiko et al. in the non-electrified case.

For flow over topography in the range of moderate to large Reynolds numbers, we have the experimental work of Charogiannis et al. [16] on harmonically excited fluid flow. The authors used planar laser-induced flourescence and particle tracking velocimetry approaches in addition to direct numerical simulations (DNS), and found excellent agreement between the numerical and experimental methods. We also have the novel work of Heining and Aksel [33] in 2009, who, as opposed to determining the surface profiles of thin film flows for a prescribed topography, provide a methodology for determining the bottom topography required to produce a given surface profile. Their approach makes use of the WIBL equations produced by Oron and Heining [62] in the case of a vertical wavy wall with a thin film flowing down it. This paper by Oron and Heining also outlines the approach for dealing with a temporally-varying flat wall rather than a typical sinusoidal wall which remains fixed in time.

In 2015, Rohlfs and Scheid [73] investigated the conditions necessary for the onset of circulating waves and flow reversal using a second-order WIBL model and DNS for thin films falling down an inclined wall. The viscous dissipation of the film was found to heavily influence the onset of flow reversal, although the appearance of circulating waves was found to be independent of the viscous dissipation. Later in 2017, Rohlfs,

Pischke and Scheid [72] used the WIBL model and DNS to examine thin film flow in the case of stabilising gravity, destabilising gravity, and a flat vertical wall. Strong agreement was found between the WIBL model and DNS for the wave speed and the wave amplitude prior to dripping, although it was found that the WIBL approach does not accurately model the internal velocity field within the fluid for large-amplitude solitary-like waves.

The WIBL model has previously been utilised by Vellingiri, Tseluiko and Kalliadasis [109] for modelling thin film flow down an inclined plate which is also sheared by a turbulent gas flowing above the liquid upstream, where it was found that the WIBL model typically followed the results of the full equations more closely than the long-wave model considered.

The full second-order WIBL model has also been used by Pradas, Kalliadasis and Tseluiko [66] in 2012 for their investigation into the solitary pulse interactions for falling liquid films. It was found that the weak interaction theory is not applicable for all separation lengths, but only for those which are sufficiently large. Pradas, Tseluiko and Kalliadasis [67] developed the framework required for this analysis in 2011, also using the two-field second-order model proposed by Ruyer-Quil and Manneville [76]. The accurate modelling of the viscous dispersion effects which the full WIBL model allows led the authors to their rigorous coherent-structure theory for falling liquid films, which permits the determination of the required pulse-separation distances necessary for bound states to occur. We wish to make clear that the original models proposed by Ruyer-Quil and Manneville [75] were the first-order and simplified second-order models, and that the full four-equation second-order model was proposed later in 2002 [76], where it was shown that the Galerkin methodology of weighted-residuals is generally the most optimal, although we leave a more detailed analysis and discussion of the hierarchy of models for Chapter 2.

Recently in 2018, Denner et al. [21] performed a comparison between the WIBL model, DNS and experimental observations for solitary waves travelling along a falling liquid film which flows over an acutely angled inclined flat plate in the regime where inertia dominates. Below a specific reduced Reynolds number (which we emphasise is also dependent on the capillary number) the WIBL model shows very strong agreement with both the DNS and experimental results in terms of predicting the pressure field within the fluid, although if we are merely interested in the maxima and minima of the film thickness, we find that the model accurately predicts these even for reduced Reynolds numbers much greater than this specific value.

We would also be remiss to exclude Craster and Matar [17], who, in 2009, gave an in-depth review of thin film phenomena, flow over topography and discussed fluids driven by a wide range of forces. They also summarised current work and literature, and gave an overview of the advancements in dealing with nonlinear equations. Prior to this, we have the unifying review of Oron, Davis and Bankoff [61] on thin liquid films and their long-scale evolution, which focuses heavily on the interactions between body forces and the physical mechanisms through which thin film dynamics evolve. Later monographs include the work of Vanden-Broeck [108], which focuses upon gravity-capillary free-surface flows such as bubbles in a cylinder and flow over nonporous obstacles.

The aim of this work is to investigate the differences between a long-wave equation and the WIBL equations for the modelling of electrified thin film flow over both sinusoidal and rectangular topography, as well as the effects of these phenomena considered simultaneously for various finite domains. Long-wave equations are quite common in the literature when investigating electrified flow, as discussed previously, and the WIBL model may be thought of as an improvement to the long-wave equation - it is thus of interest to see the differences between the two modelling approaches with regards to an electric field and topography. Special attention will be given to the linear stability of the two models, and the effect of the electric field and the topography on the critical Reynolds number. The derivation of these two models is predicated upon knowledge of the Navier-Stokes equations, the continuity equation for the fluid flow, and the Laplace equation for the electric potential, in addition to the corresponding boundary conditions. These precursor equations, following standard manipulation, eventually yield a nonlinear equation for the time evolution of the film thickness, or a nonlinear equation system in the WIBL case. We seek to analyse these models analytically and solve both these models numerically for a wide range of parameters, and investigate the effect of electric field strength and topography on the film thickness, surface profiles, and linear stability.

The structure of this thesis takes the following form. We begin with an overview of the mathematical model in Chapter 2, where we define our terms, conventions and governing equations. We then proceed to systematically derive and list the corresponding boundary conditions as well as other assumptions and consequent mathematical implications. The hierarchy of models is then discussed, and the long-wave assumption is made. Following this, we nondimensionalise our equations, and produce both long-wave and first-order WIBL model equations.

In Chapter 3, we focus our attention on the linear stability analysis of both the long-wave and WIBL model equations. We derive critical Reynolds numbers in both of these cases which take into account the normal electric field in the case of no topography, and then determine which Reynolds number and electric Weber number parameter values correspond to stable flows, as well as absolutely unstable and convective unstable flows, and the criteria required for a transition between the absolute and convective instabilities. The dispersion relations are also produced for both models, expressions for the most unstable wavenumbers are derived, and the spectra of the linear operators are examined. We also investigate the real and imaginary branches of the wavenumber of a perturbation which is acting upon our systems near the transition from convective to absolute instability. Furthermore, we produce time-dependent simulations which corroborate the parameter-space which describes transitions from stable to convectively unstable to absolutely unstable in the case of a flat wall. These time-dependent simulations are also performed for the sinusoidal and rectangular walls. Finally, we produce plots of the critical Reynolds number for the long-wave and WIBL models as a function of the topographical amplitude for various electric Weber numbers, and discuss the effect of both the electric field and both types of topography on our systems.

In Chapter 4, we examine steady-state results produced for both models, discuss the implications of these results and compare the two models. We further examine surface profiles, film thicknesses, and continuation curves of film thickness norms against wall amplitudes, and proceed to analyse the bifurcation diagrams produced for both models for a variety of parameter values. Time-periodic solutions and subharmonic branches are detected and analysed in addition to the main branches.

Finally, a conclusion and brief summary is given is Chapter 5, and we outline several avenues for future research.

Chapter 2

Models and derivations

2.1 Governing equations

We consider a gravity-driven two-dimensional flow of an incompressible Newtonian liquid down an inclined wavy wall. For now we assume that the liquid is a perfect dielectric, and we will later show how the perfect conductor case can be recovered in the appropriate limit. We introduce a Cartesian coordinate system (x, y) so that the x-axis is pointing in the direction of the flow, and the y-axis is perpendicular to the x-axis and pointing into the liquid. Time is denoted by t, g denotes the acceleration due to gravity, and β denotes the angle between the inclined wall and the horizontal. The free

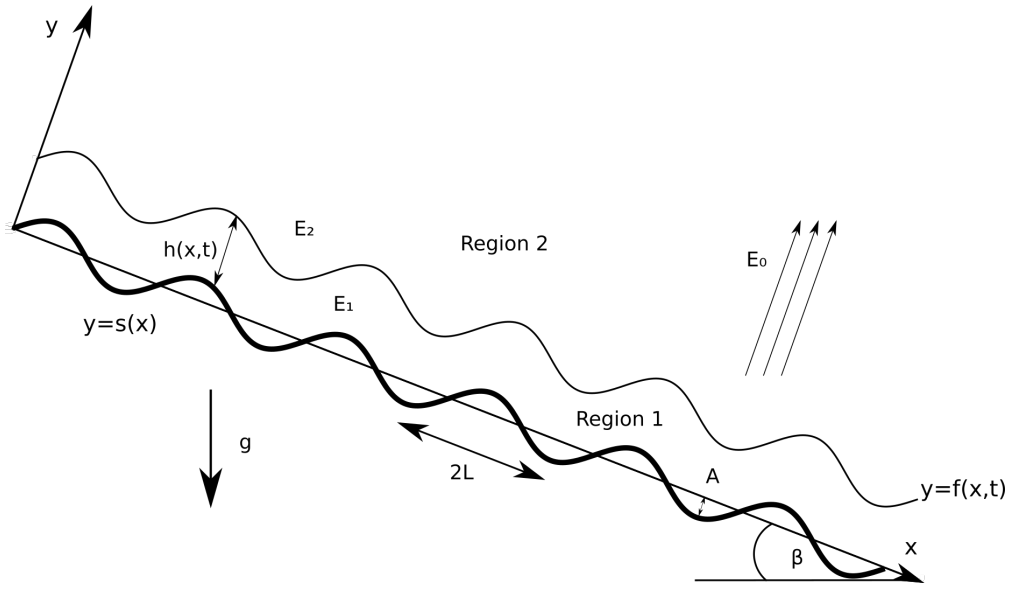

Figure 2.1: *Liquid film flow down an inclined wavy wall.*

surface is located at $y = f(x,t)$, the film thickness is given by $h(x,t)$, and the wall topography is given by $y = s(x)$, so that $f(x,t) = s(x) + h(x,t)$. The density and viscosity of the liquid are defined as ρ and μ respectively. A graphical representation of this model is given in Figure 2.1.

The wall topography itself is modelled as either a sinusoidal or rectangular trough-shaped topography, and is given by

$$s(x) = A\cos\left(\frac{\pi x}{L}\right), \tag{2.1}$$

or

$$s(x) = A\tanh\left(\frac{\cos(\frac{\pi x}{L})}{d}\right), \tag{2.2}$$

respectively. Here A is the wall amplitude, L is half of the period of the wall, and d controls the steepness of the walls in the rectangular case. In the limit of $d \to 0$ we recover completely straight edges such that we have right-angles between the corners of our troughs, although in practice we shall always take $d = 0.1$. In the literature, it is also not uncommon for the gas above the liquid to be modelled as a laminar or turbulent one, shearing the liquid flow (see, for example, the 2015 work by Vellingiri, Tseluiko and Kalliadasis [109]) although this is not considered for the current model, and the gas is taken to be hydrodynamically inert.

We define Region 1 to be the region consisting of the liquid and Region 2 to be the region consisting of the surrounding air. The electric field is assumed to be uniformly acting on the liquid from infinity in the y-direction, and is assumed to be acting normal to the flow direction. In our model the wall is an electrode and the other electrode is sufficiently far away from the wall. The potential difference between the two electrodes is chosen such that as $y \to \infty$ we have $\boldsymbol{E} \to -E_0\hat{\boldsymbol{j}}$, where $\hat{\boldsymbol{j}}$ is defined as the unit vector pointing in the y-direction. It is well-documented [45, 79, 99, 104] that the inclusion of a normal electric field causes additional Maxwell normal stresses which have the possibility to affect the flow stability and dynamics. In addition, the liquid and air are both assumed to be perfect dielectrics, with permittivity ϵ_1 and ϵ_2, respectively, although as $\epsilon_p = \epsilon_2/\epsilon_1 \to \infty$ we approach the limit of the film as a perfect conductor instead.

We begin our mathematical description of the model by recalling the Navier-Stokes equations, which ensure momentum conservation in the liquid [4, 12, 25, 38, 41, 65];

$$\rho\left(\frac{\partial u}{\partial t}+u\frac{\partial u}{\partial x}+v\frac{\partial u}{\partial y}\right)=-\frac{\partial p}{\partial x}+\mu\left(\frac{\partial^2 u}{\partial x^2}+\frac{\partial^2 u}{\partial y^2}\right)+\rho g\sin\beta, \tag{2.3}$$

$$\rho\left(\frac{\partial v}{\partial t}+u\frac{\partial v}{\partial x}+v\frac{\partial v}{\partial y}\right)=-\frac{\partial p}{\partial y}+\mu\left(\frac{\partial^2 v}{\partial x^2}+\frac{\partial^2 v}{\partial y^2}\right)-\rho g\cos\beta. \tag{2.4}$$

Here $\boldsymbol{u}=(u,v)$ is the velocity in the liquid with u and v denoting the streamwise and cross-stream velocity components, and p denotes the pressure. We also have the continuity equation for the liquid

$$\frac{\partial u}{\partial x}+\frac{\partial v}{\partial y}=0, \tag{2.5}$$

which ensures mass conservation in the liquid [4, 12, 25, 38, 41, 65]. Having described the equations governing the dynamics of the liquid itself, we now turn our attention to the effect of the electric field, and the corresponding governing electric equations. We begin with the Maxwell equations [12, 69, 70], starting with Gauss's law

$$\nabla\cdot\boldsymbol{D}=q, \tag{2.6}$$

which relates electric volume charge density q and the electric displacement field $\boldsymbol{D}$. The time derivative of the electrical displacement is analogous to current, although instead of corresponding to the movement in time of charged particles, it corresponds to time-variations in the electric field itself, not solely due to the movement of particles. In this work we shall focus upon uniform electric fields which slightly vary due to the time evolution of the free surface. We also make use of the relation between the electric displacement field and the electric field

$$\boldsymbol{D_{1,2}}=(1+\chi_{e_{1,2}})\epsilon_0\boldsymbol{E}, \tag{2.7}$$

where $\boldsymbol{D_{1,2}}$ are the electric displacement fields in the liquid and the gas respectively, and $\chi_{e_{1,2}}$ are the electric susceptibilities for the liquid and the gas respectively, which we assume to be constant. We also have ϵ_0 as the electrical permittivity of free space, and the quantities $(1+\chi_{e_{1,2}})=\kappa_{e_{1,2}}$ are called the dielectric constants. The electrical permittivities of the liquid and gas mentioned earlier, ϵ_1 and ϵ_2 are given by

$$\epsilon_{1,2}=\kappa_{e_{1,2}}\epsilon_0. \tag{2.8}$$

By substitution of (2.7) into (2.6) we are hence able to obtain a relation for the electric field in the film and the surrounding air respectively;

$$\nabla \cdot \boldsymbol{E} = \frac{q}{\epsilon_1} \quad \text{and} \quad \nabla \cdot \boldsymbol{E} = \frac{q}{\epsilon_2}. \tag{2.9}$$

We also have

$$\nabla \times \boldsymbol{E} = -\frac{\partial \boldsymbol{B}}{\partial t}, \tag{2.10}$$

which is the Maxwell-Faraday equation, where $\boldsymbol{B}$ is the magnetic field. This equation describes the fact that for a given non-irrotational electric field there is a corresponding magnetic field the magnitude of which is found to vary in time. We also have Ampere's law

$$\nabla \times \boldsymbol{H} = \boldsymbol{J} + \frac{\partial \boldsymbol{D}}{\partial t}, \tag{2.11}$$

which relates current density $\boldsymbol{J}$ to the curl of the magnetic field intensity $\boldsymbol{H}$. The fields $\boldsymbol{H}$ and $\boldsymbol{B}$ are related through the expression

$$\boldsymbol{B} = \Lambda \boldsymbol{H}, \tag{2.12}$$

where Λ is the permeability of the medium, in this case air. We finally have Gauss' law for magnetism

$$\nabla \cdot \boldsymbol{B} = 0, \tag{2.13}$$

which states that magnetic fields are solenoidal and equivalently that unlike for electric fields, the source of magnetic fields are restricted to dipoles instead of monopoles.

We seek to use the so-called electroquasistatic approximation to neglect the effect of the magnetic field on our system since it is dominated by the electric field in the sense that the electrical contributions are orders of magnitude greater than the magnetic contributions. This is mathematically equivalent to setting the right-hand side of (2.10) equal to zero, and hence if the electroquasistatic approximation is satisfied, we have

$$\nabla \times \boldsymbol{E} = 0, \tag{2.14}$$

and subsequently we may define ϕ_1 and ϕ_2 as the electric potentials such that we may have the following two equations for the electric field;

$$\boldsymbol{E}_1 = -\nabla \phi_1, \tag{2.15}$$

$$\boldsymbol{E}_2 = -\nabla \phi_2. \tag{2.16}$$

In both the perfect dielectric and perfect conductor cases, we are able to set the electric volume charge density $q = 0$ in both the film and the air. Under the electroquasistatic assumption, the charge density decays to zero in finite time, and the electroquasistatic assumption is satisfied so long as we have

$$lk \ll 1, \tag{2.17}$$

where k is the wavenumber associated with the electric field and l is the characteristic length of the system, see, for example, [12, 34, 56, 79]. Exclusive to the strong dielectric case, we note in practice that the inherent low conductivity of the film means that the electroquasistatic assumption is verified automatically, as evident from an examination of the energy ratio of the magnetic field to the electric field as discussed by Zhakin [12].

Physically, the electroquasistatic assumption corresponds to the case where a coupled electromagnetic wave is heavily electrically dominated, and the magnetic contributions can be wholly neglected. Equivalently this may be thought of as the electrical energy being significantly larger than the magnetic energy, and under this assumption then, substitution of (2.15) and (2.16) into the two equations corresponding to Gauss's law (2.9) simply yields Laplace's equation in the liquid

$$\nabla^2 \phi_1 = 0, \tag{2.18}$$

and Laplace's equation in the air,

$$\nabla^2 \phi_2 = 0. \tag{2.19}$$

We note that when treating the film as a perfect conductor, by definition we would expect there to be no electric field inside the bulk, and hence (2.15) reduces to zero. In the case of a perfect dielectric, an electric field is to be expected inside the film instead. Both of these cases are to be represented by a single equation which holds true for perfect dielectrics when we have finite ϵ_p, and for perfect conductors in the limit of $\epsilon_p \to \infty$. The boundary conditions for ϕ_2 are identical for both cases, although the boundary conditions for ϕ_1 are such that $\phi_1 \to 0$ within the film as $\epsilon_p \to \infty$. In situations where we have sharp topographical features (i.e. steep rectangular troughs and steps for example), the necessity of finding the electric field within the film for perfect dielectrics can adversely affect the smoothness of solutions, as demonstrated by Tseluiko et al. [99, 101].

As the liquid is assumed to be a perfect dielectric, we model the liquid as containing no

free charges, and being comprised solely of bound charges [69], such that the external electric field induces polarisation, causing an internal electric field within the liquid. This internal electric field acts in opposition to the external electric field, and this effect may be seen in the $(1 - \frac{1}{\epsilon_p})$ coefficient which multiplies the term corresponding to the electric field, as we shall see later. A perfect dielectric corresponds to any finite value of ϵ_p, whereas the perfect conductor case is obtained in the limit of $\epsilon_p \to \infty$, and as such it is clear to see that qualitatively the perfect dielectric case is somewhat similar to the perfect conductor case albeit with a weaker electric field (for cases where $\epsilon_p > 1$), although this is not strictly true since, as we shall see, the topography introduces an additional $(1 - \frac{1}{\epsilon_p})$ term which cannot be factored into the electric Weber number term. We also note the qualitative difference for cases where $\epsilon_p < 1$ in the literature (see, for example, Tseluiko et al. [101]), although this is not considered here.

2.2 Boundary conditions

We now discuss the boundary conditions corresponding to the physical scenario under consideration. As is typical for liquids, we impose no-slip and no-penetration conditions that apply at a solid impermeable boundary;

$$u = v = 0 \quad \text{on} \quad y = s(x). \tag{2.20}$$

At the free surface, we have the kinematic condition – a formulation of the imposition that a particle on the free surface of the film $y = f(x, t)$, shall remain on the free surface independent of time. This condition is given by the following equation

$$\frac{\partial f}{\partial t} + u\frac{\partial f}{\partial x} + v\frac{\partial f}{\partial y} = 0. \tag{2.21}$$

Another important condition to consider is the dynamic balance of stress on the free surface, and it is this dynamic balance of stress through which the electric field affects the liquid under consideration, specifically through the normal component. The equation for the dynamic balance of stress is given as

$$\hat{\boldsymbol{n}} \cdot \boldsymbol{\sigma} = \gamma\kappa\hat{\boldsymbol{n}} - p_a\hat{\boldsymbol{n}} + \hat{\boldsymbol{n}} \cdot (\boldsymbol{M_2} - \boldsymbol{M_1}), \tag{2.22}$$

where we define the following variables: firstly we have p_a as the atmospheric pressure, or equivalently the pressure in Region 2, and define $\hat{\boldsymbol{n}}$ to be the normal vector to the

free surface, which is pointing into the liquid. We also note that γ is the surface tension coefficient, and κ is the curvature of the free surface and is defined as

$$\kappa = \nabla \cdot \hat{\boldsymbol{n}}, \tag{2.23}$$

and hence the curvature is negative when the free surface is concave up. In addition, for an incompressible fluid we can define the Newtonian stress tensor $\boldsymbol{\sigma}$ as

$$\boldsymbol{\sigma} = -p\boldsymbol{\delta} + 2\mu\boldsymbol{S}, \tag{2.24}$$

where $\boldsymbol{\delta}$ is the identity tensor, and the strain-rate tensor $\boldsymbol{S}$ is defined as

$$\boldsymbol{S} = \frac{1}{2}((\nabla \boldsymbol{u})^T + \nabla \boldsymbol{u}). \tag{2.25}$$

The only terms left to define are the Maxwell stress tensors for the liquid and air, $\boldsymbol{M_1}$ and $\boldsymbol{M_2}$, respectively, which correspond to the electric force exerted on the liquid and air phases [79] and are given by

$$\boldsymbol{M_1} = \epsilon_1 \boldsymbol{E}_1 \boldsymbol{E}_1 - \frac{\epsilon_1}{2}|\boldsymbol{E}_1|^2 \boldsymbol{\delta}, \tag{2.26}$$

$$\boldsymbol{M_2} = \epsilon_2 \boldsymbol{E}_2 \boldsymbol{E}_2 - \frac{\epsilon_2}{2}|\boldsymbol{E}_2|^2 \boldsymbol{\delta}. \tag{2.27}$$

Due to continuity of the electric potential and the normal component of the electric displacement across the free surface $y = f(x,t)$, we also have the conditions

$$\phi_1 = \phi_2 \qquad \text{on} \qquad y = f(x,t), \tag{2.28}$$

$$\epsilon_1 \left(\hat{\boldsymbol{n}} \cdot \nabla \phi_1\right) = \epsilon_2 \left(\hat{\boldsymbol{n}} \cdot \nabla \phi_2\right) \qquad \text{on} \qquad y = f(x,t) \tag{2.29}$$

We now note the final conditions for the electric potentials corresponding to the physics of the situation, i.e. constant (or zero, without loss of generality) electric potential at the wall, and the uniform electric field conditions as $y \to \infty$;

$$\phi_1 = 0 \qquad \text{on} \qquad y = s(x), \tag{2.30}$$

$$\frac{\partial \phi_2}{\partial x} \to 0 \qquad \text{as} \qquad y \to \infty, \tag{2.31}$$

$$\frac{\partial \phi_2}{\partial y} \to -E_0 \qquad \text{as} \qquad y \to \infty. \tag{2.32}$$

2.2.1 Tangential stress balance

We now examine the tangential component of the dynamic balance of stress given in (2.22). By considering the tangential components on each side, we obtain

$$\hat{\boldsymbol{n}} \cdot \boldsymbol{\sigma} \cdot \hat{\boldsymbol{t}} = \gamma\kappa\hat{\boldsymbol{n}} \cdot \hat{\boldsymbol{t}} - p_a\hat{\boldsymbol{n}} \cdot \hat{\boldsymbol{t}} + \hat{\boldsymbol{n}} \cdot (\boldsymbol{M_2} - \boldsymbol{M_1}) \cdot \hat{\boldsymbol{t}}, \tag{2.33}$$

where $\hat{\boldsymbol{t}}$ is the tangent vector to the free surface. As $\hat{\boldsymbol{n}} \cdot \hat{\boldsymbol{t}} = 0$ is trivially known, we subsequently see that

$$\gamma\kappa\hat{\boldsymbol{n}} \cdot \hat{\boldsymbol{t}} = 0 \qquad \text{and} \qquad p_a\hat{\boldsymbol{n}} \cdot \hat{\boldsymbol{t}} = 0. \tag{2.34}$$

It can also be shown that

$$\hat{\boldsymbol{n}} \cdot (\boldsymbol{M_2} - \boldsymbol{M_1}) \cdot \hat{\boldsymbol{t}} = 0, \tag{2.35}$$

and hence we see that

$$\hat{\boldsymbol{n}} \cdot \boldsymbol{\sigma} \cdot \hat{\boldsymbol{t}} = 0. \tag{2.36}$$

From (2.24) we see that

$$\hat{\boldsymbol{n}} \cdot \boldsymbol{\sigma} \cdot \hat{\boldsymbol{t}} = -p\hat{\boldsymbol{n}} \cdot \boldsymbol{\delta} \cdot \hat{\boldsymbol{t}} + 2\mu\hat{\boldsymbol{n}} \cdot \boldsymbol{S} \cdot \hat{\boldsymbol{t}}. \tag{2.37}$$

If we then recall the definition of the Newtonian stress tensor given in (2.24) and write $2\mu\boldsymbol{S}$ in matrix form as

$$2\mu\boldsymbol{S} = \begin{bmatrix} 2u_x & v_x + u_y \\ v_x + u_y & 2v_y \end{bmatrix} \mu, \tag{2.38}$$

then since $p\hat{\boldsymbol{n}} \cdot \boldsymbol{\delta} \cdot \hat{\boldsymbol{t}} = 0$, the tangential stress balance condition becomes

$$\hat{\boldsymbol{n}} \cdot \boldsymbol{S} \cdot \hat{\boldsymbol{t}} = 0. \tag{2.39}$$

We then write the normal and tangential unit vectors explicitly as

$$\hat{\boldsymbol{t}} = \frac{1}{\sqrt{1 + f_x^2}} \begin{pmatrix} 1 \\ f_x \end{pmatrix}, \tag{2.40}$$

$$\hat{\boldsymbol{n}} = \frac{1}{\sqrt{1 + f_x^2}} \begin{pmatrix} f_x \\ -1 \end{pmatrix}. \tag{2.41}$$

Hence through substitution of $\hat{\boldsymbol{n}}$, $\hat{\boldsymbol{t}}$ and $\boldsymbol{S}$ into equation (2.39) we obtain the result

$$2\hat{\boldsymbol{n}}\cdot\boldsymbol{S}\cdot\hat{\boldsymbol{t}} = \frac{1}{1+f_x^2}\begin{pmatrix} f_x & -1 \end{pmatrix}\begin{pmatrix} 2u_x & v_x+u_y \\ v_x+u_y & 2v_y \end{pmatrix}\begin{pmatrix} 1 \\ f_x \end{pmatrix} = 0. \tag{2.42}$$

By rearranging equation (2.42), the equation for the tangential stress balance reduces to

$$2f_x(u_x - v_y) + (v_x + u_y)(f_x^2 - 1) = 0 \qquad \text{on} \qquad y = f(x,t). \tag{2.43}$$

It can be seen that the contributions from the normal electric field do not appear in the tangential stress balance equation (2.43), which is consistent with the literature [13, 99, 104], and the entirety of the electric field acts solely through the normal component of the stress balance on the free surface.

2.2.2 Normal stress balance

Similarly to the previous section, we reexamine the dynamic balance of stress given in (2.22), although now we consider the normal components on both sides of the equation. Such consideration gives us

$$\hat{\boldsymbol{n}}\cdot\boldsymbol{\sigma}\cdot\hat{\boldsymbol{n}} = \gamma\kappa\hat{\boldsymbol{n}}\cdot\hat{\boldsymbol{n}} - p_a\hat{\boldsymbol{n}}\cdot\hat{\boldsymbol{n}} + \hat{\boldsymbol{n}}\cdot(\boldsymbol{M_2}-\boldsymbol{M_1})\cdot\hat{\boldsymbol{n}}. \tag{2.44}$$

Using that $\hat{\boldsymbol{n}}\cdot\hat{\boldsymbol{n}} = 1$ allows for simplification to the form

$$\hat{\boldsymbol{n}}\cdot\boldsymbol{\sigma}\cdot\hat{\boldsymbol{n}} = \gamma\kappa - p_a + \hat{\boldsymbol{n}}\cdot(\boldsymbol{M_2}-\boldsymbol{M_1})\cdot\hat{\boldsymbol{n}}. \tag{2.45}$$

As we expressed $\boldsymbol{\sigma}$ explicitly previously, we know that the normal component of the definition of the Newtonian stress tensor is given by

$$\hat{\boldsymbol{n}}\cdot\boldsymbol{\sigma}\cdot\hat{\boldsymbol{n}} = -p\hat{\boldsymbol{n}}\cdot\boldsymbol{\delta}\cdot\hat{\boldsymbol{n}} + 2\mu\hat{\boldsymbol{n}}\cdot\boldsymbol{S}\cdot\hat{\boldsymbol{n}}. \tag{2.46}$$

We once again make use of the fact that $\hat{\boldsymbol{n}}\cdot\hat{\boldsymbol{n}} = 1$, such that we may write $-p\hat{\boldsymbol{n}}\cdot\boldsymbol{\delta}\cdot\hat{\boldsymbol{n}}$ simply as $-p$. Thus upon substitution of the normal component of the definition of the Newtonian stress tensor into (2.45), we obtain

$$-p + 2\mu\hat{\boldsymbol{n}}\cdot\boldsymbol{S}\cdot\hat{\boldsymbol{n}} = \gamma\kappa - p_a + \hat{\boldsymbol{n}}\cdot(\boldsymbol{M_2}-\boldsymbol{M_1})\cdot\hat{\boldsymbol{n}}, \tag{2.47}$$

where $\hat{\boldsymbol{n}} \cdot \boldsymbol{S} \cdot \hat{\boldsymbol{n}}$ is expressed as

$$\hat{\boldsymbol{n}} \cdot \boldsymbol{S} \cdot \hat{\boldsymbol{n}} = \frac{1}{(1+f_x^2)} \begin{pmatrix} f_x & -1 \end{pmatrix} \begin{pmatrix} u_x & \frac{1}{2}(v_x+u_y) \\ \frac{1}{2}(v_x+u_y) & v_y \end{pmatrix} \begin{pmatrix} f_x \\ -1 \end{pmatrix}. \quad (2.48)$$

Using the definitions of the Maxwell stress tensors, $\boldsymbol{M_1}$ and $\boldsymbol{M_2}$, and upon dotting from either side with the normal unit vector, we obtain

$$\hat{\boldsymbol{n}} \cdot \boldsymbol{M_1} \cdot \hat{\boldsymbol{n}} = \epsilon_1 \cdot \hat{\boldsymbol{n}} \cdot \boldsymbol{E}_1 \boldsymbol{E}_1 \cdot \hat{\boldsymbol{n}} - \frac{\epsilon_1}{2} \hat{\boldsymbol{n}} \cdot |\boldsymbol{E}_1|^2 \cdot \hat{\boldsymbol{n}}, \quad (2.49)$$

$$\hat{\boldsymbol{n}} \cdot \boldsymbol{M_2} \cdot \hat{\boldsymbol{n}} = \epsilon_2 \cdot \hat{\boldsymbol{n}} \cdot \boldsymbol{E}_2 \boldsymbol{E}_2 \cdot \hat{\boldsymbol{n}} - \frac{\epsilon_2}{2} \hat{\boldsymbol{n}} \cdot |\boldsymbol{E}_2|^2 \cdot \hat{\boldsymbol{n}}. \quad (2.50)$$

Using additionally that

$$\boldsymbol{E}_1 \boldsymbol{E}_1 = \begin{pmatrix} \phi_{1x}^2 & \phi_{1x}\phi_{1y} \\ \phi_{1x}\phi_{1y} & \phi_{1y}^2 \end{pmatrix}, \quad (2.51)$$

$$\boldsymbol{E}_2 \boldsymbol{E}_2 = \begin{pmatrix} \phi_{2x}^2 & \phi_{2x}\phi_{2y} \\ \phi_{2x}\phi_{2y} & \phi_{2y}^2 \end{pmatrix}, \quad (2.52)$$

and upon substitution into (2.47), we obtain the normal stress balance equation

$$\begin{aligned} &-p + \frac{2\mu}{1+{f_x}^2}\left[{f_x}^2 u_x - f_x(v_x+u_y) + v_y\right] \\ &\quad = \frac{\gamma f_{xx}}{(1+{f_x}^2)^{3/2}} - p_a + \frac{\epsilon_2}{1+{f_x}^2}\left[f_x\phi_{2x} - \phi_{2y}\right]^2 - \frac{\epsilon_2}{2}\left[\phi_{2x}^2 + \phi_{2y}^2\right] \\ &\qquad -\frac{\epsilon_1}{1+{f_x}^2}\left[f_x\phi_{1x} - \phi_{1y}\right]^2 + \frac{\epsilon_1}{2}\left[\phi_{1x}^2 + \phi_{1y}^2\right] \qquad \text{on} \qquad y = f(x,t). \end{aligned} \quad (2.53)$$

2.3 Nondimensionalisation

As we nondimensionalise our equations, we introduce the $*$ notation to indicate that a quantinity is dimensionless. We begin to nondimensionalise our equations through the following substitutions

$$x^* = \frac{x}{h_0}, \quad y^* = \frac{y}{h_0}, \quad f^* = \frac{f}{h_0}, \quad s^* = \frac{s}{h_0}, \quad t^* = \frac{tu_0}{h_0}, \quad u^* = \frac{u}{u_0}, \quad v^* = \frac{v}{u_0},$$

$$p^* = \frac{h_0}{\mu u_0} p,$$

$$\phi^*_{1,2} = \frac{\phi_{1,2}}{E_0 h_0},$$

where u_0 is the Nusselt surface speed for the case of a flat wall in the absence of the electric field given by

$$u_0 = \frac{\rho g h_0^2 \sin\beta}{2\mu}.$$

We also note that use has been made of h_0, which is defined to be the Nusselt flat film thickness. We may then nondimensionalise the Navier-Stokes equations as follows;

$$R(u^*_{t^*} + u^* u^*_{x^*} + v^* u^*_{y^*}) = -p^*_{x^*} + u^*_{x^*x^*} + u^*_{y^*y^*} + 2, \tag{2.54}$$

$$R(v^*_{t^*} + u^* v^*_{x^*} + v^* v^*_{y^*}) = -p^*_{y^*} + v^*_{x^*x^*} + v^*_{y^*y^*} - 2\cot\beta. \tag{2.55}$$

We may now begin collecting dimensionless quantities, and using dimensionless numbers. In the above equations, use has already been made of the Reynolds number, defined qualitatively as the ratio of inertia to viscosity, and mathematically by the relation

$$R = \frac{\rho h_0 u_0}{\mu}. \tag{2.56}$$

We also introduce the capillary number, a measure of the relative importance of viscosity to surface tension, and defined as

$$C = \frac{\mu u_0}{\gamma}, \tag{2.57}$$

which may be equivalently written in the form

$$C = \frac{R^{2/3}\sin^{1/3}\beta}{2^{1/3}K}, \tag{2.58}$$

where use has been made of K, the Kapitza number, a dimensionless ratio of surface tension to inertial forces, which is constant for a given material at a given temperature, and is defined explicitly through the equation

$$K = \frac{\gamma\rho^{1/3}}{g^{1/3}\mu^{4/3}}, \tag{2.59}$$

such that for water at room temperature the Kapitza number is a constant which takes a value of approximately 3364.5. Finally, we define the electric Weber number, a measure of the strength of the electric field under consideration relative to viscous forces, which

is defined as

$$W_e = \frac{\epsilon_2 E_0^2 h_0}{2\mu u_0}. \tag{2.60}$$

Using the aforementioned substitutions, upon non-dimensionalisation the continuity equation takes the form

$$u^*_{x^*} + v^*_{y^*} = 0, \tag{2.61}$$

i.e. it remains unchanged, due to u_x and v_y having the same scaling and dimensions, at least before we make our long-wave assumption. We also consider the dimensionless boundary conditions. The no-slip condition and the no-penetration condition reduce respectively to

$$u^* = 0 \qquad \text{on} \qquad y^* = s^*(x^*), \tag{2.62}$$

$$v^* = 0 \qquad \text{on} \qquad y^* = s^*(x^*). \tag{2.63}$$

The kinematic condition takes the form

$$f^*_{t^*} + u^* f^*_{x^*} + v^* f^*_{y^*} = 0 \qquad \text{on} \qquad y^* = f^*(x^*, t^*). \tag{2.64}$$

The dimensionless tangential stress balance and normal stress balance equations at the free surface, $y^* = f^*(x^*, t^*)$, are respectively reduced to

$$2f^*_{x^*}(u^*_{x^*} - v^*_{y^*}) + (v^*_{x^*} + u^*_{y^*})({f^*_{x^*}}^2 - 1) = 0, \tag{2.65}$$

$$\begin{aligned} -p^* + \frac{2}{1+{f^*_{x^*}}^2}\left[{f^*_{x^*}}^2 u^*_{x^*} - f^*_{x^*}(v^*_{x^*} + u^*_{y^*}) + v^*_{y^*}\right] &= \frac{f^*_{x^*x^*}}{C(1+{f^*_{x^*}}^2)^{\frac{3}{2}}} \\ -p^*_a + 2W_e\left(\frac{[f^*_{x^*}\phi^*{}_{2x^*} - \phi^*{}_{2y^*}]^2}{1+{f^*_{x^*}}^2} - \frac{1}{2}\left[{\phi^*{}_{2x^*}}^2 + {\phi^*{}_{2y^*}}^2\right]\right) & \\ -2W_e\epsilon_p\left(\frac{[f^*_{x^*}\phi^*{}_{1x^*} - \phi^*{}_{1y^*}]^2}{1+{f^*_{x^*}}^2} - \frac{1}{2}\left[{\phi^*{}_{1x^*}}^2 + {\phi^*{}_{1y^*}}^2\right]\right). & \end{aligned} \tag{2.66}$$

The dimensionless equations for the electric field are as follows;

$$\phi^*_{1x^*x^*} + \phi^*_{1y^*y^*} = 0 \qquad \text{for} \qquad f^*(x^*, t^*) > y^* > s^*(x^*), \tag{2.67}$$

$$\phi^*_{2x^*x^*} + \phi^*_{2y^*y^*} = 0 \qquad \text{for} \qquad y^* > f^*(x^*, t^*). \tag{2.68}$$

We additionally have the following dimensionless boundary conditions for the electric potentials;

$$\phi^*_1 = \phi^*_2 \qquad \text{on} \qquad y^* = f^*(x^*, t^*), \tag{2.69}$$

$$\epsilon_p \left(f^*_{x^*} \phi^*_{1x^*} - \phi^*_{1y^*} \right) = \left(f^*_{x^*} \phi^*_{2x^*} - \phi^*_{2y^*} \right) \qquad \text{on} \qquad y^* = f^*(x^*, t^*), \tag{2.70}$$

$$\phi^*_{2x^*} \to 0 \qquad \text{as} \qquad y^* \to \infty, \tag{2.71}$$

$$\phi^*_{2y^*} \to -1 \qquad \text{as} \qquad y^* \to \infty, \tag{2.72}$$

$$\phi^*_1 = 0 \qquad \text{on} \qquad y^* = s^*(x^*). \tag{2.73}$$

For brevity the $*$ notation shall now be neglected, and it is to be implicity assumed from this section onwards that the variables are nondimensional.

2.4 Modelling assumptions

2.4.1 Hierarchy of models

Here we discuss the benefits and drawbacks of models based on the long-wave assumption and the integral boundary layer approximation as well as the ranges of validity of such models.

One of the most well-known evolution equations for the local film thickness is the so-called Benney equation, first derived by Benney [6] in 1966. Although this model has some success close to criticality, we observe blowup in finite-time in the region of moderate Reynolds numbers [37, 68] and this nonphysical blowup phenomenon is still observed even if we increase the order of our gradient expansion [75]. There are methods for dealing with this finite-time blowup behaviour, however. Ooshida [60] has shown that it can be removed via the use of Padé approximants close to criticality. Despite this improvement over the original Benney equation, undesirable behaviour is still observed further away from criticality. Another alternative to the Benney equation is the Kuramoto-Sivashinsky equation, which is derived by taking the limit of small amplitude modulations [14, 75]. We note that the Benney equation, the Kuramoto-Sivashinsky equation and the Korteweg-de Vries (KdV) equation are all closely related, such that we can create solutions to the generalised Benney equation by taking linear combinations of solutions to the generalised Kuramoto-Sivashinsky equation and solutions to the generalised KdV equation [115]. Joo, Davis and Bankoff [37] found that the Kuramoto-Sivashinsky equation inaccurately modelled wave profiles for long-wave instabilities of viscous thin films flowing down inclines through comparison with numerical results for the full long-wave equation.

The integral boundary layer (IBL) model was produced by Shkadov [83] in 1967, and although it does not suffer the finite-time blow-up observed in Benney's equation, and it accurately models nonlinear waves when we are far from criticality, it is known to underestimate the onset of instability and inaccurately predict the critical Reynolds number, and does not include terms relating to viscous dispersion. When comparing long-wave-type equations to IBL equations and solving the full Navier-Stokes equations via a finite element method, Salamon, Armstrong and Brown [77] found that the long-wave results qualitatively diverged from the other calculations for large-amplitude travelling waves down an inclined flat wall. In 2000, Ruyer-Quil and Manneville [75] proposed an improvement to the IBL equations which allowed for the correct determination of the onset of instability, and produced the weighted-residual integral boundary layer equations, also known as the WIBL equations. These equations are generally characterised by two coupled, nonlinear equations for local flow rate and film thickness, in addition to weighted-residuals techniques and gradient expansions [80]. The modelling approach also makes use of Prandtl's elimination of cross-stream momentum equation typical in aerodynamics, such that we are no longer constrained by our cross-stream dependence [81].

Since the inception of the WIBL model, it has shown good agreements with experiments and direct numerical simulations in a wide variety of contexts; see, for example, Pradas, Kalliadasis and Tseluiko [66], Vellingiri, Tseluiko and Kalliadasis [109] and Rohlfs and Scheid [73]. The most widespread forms of the WIBL model are the first-order model, the simplified second-order model, and the full second-order model. The form used in this work is the first-order model, and whilst generally speaking it is an improvement over the long-wave model, it still has its drawbacks, however. For example, without the second-order terms pertaining to viscous dispersion which are found in the simplified second-order and full second-order models, the first-order model overestimates the amplitudes of capillary ripples ahead of solitary pulses, as discussed by Ruyer-Quil and Manneville [75] in addition to Pradas, Tseluiko and Kalliadasis [66, 67] and corroborated by their numerical computations. The terms themselves are a result of the tangential stress balance condition in addition to the streamwise momentum equation, and the corrections to these terms are absent in the simplified second-order model but present in the full four-equation second-order model.

The viscous dispersion terms are also responsible for the accurate modelling of the fluid at moderately-high Reynolds numbers; comparisons to the experiments of Liu,

Paul and Gollub [52] by Ruyer-Quil and Manneville yielded the result that the simplified second-order model closely followed the experimental results up to approximately $R = 100$, whereas in the full second-order model we instead see close agreement up until Reynolds numbers of approximately $R = 200$. In the original work by Ruyer-Quil and Manneville [75], the agreement between the first-order and second-order models appears excellent in the range $R \lesssim 5$ for the amplitude of one-hump solitary waves down a vertical plate. The Reynolds numbers focused upon in this work range between $R = 1$ and $R = 30$, with $R = 1.25$ corresponding to criticality in many cases, and as such the reduced complexity of the equations corresponding to the first-order model is highly desirable. The first-order model can be obtained either by deriving the simplified second-order (or full second-order) WIBL model and then neglecting the viscous dispersion terms (and their corrections for the full second-order model), or by deriving boundary layer equations and then integrating via, say, the Galerkin method [73], as is the case here. Ruyer-Quil and Manneville [76] gave an overview of the various weighted-residual approaches, and found that the Galerkin technique was generally the most optimal in the sense that it converges in the fewest number of weight functions. In the Galerkin methodology for both the first-order and simplified second-order models, the weight functions are chosen to be identical to the basis functions, and convergence to the typical equations is achieved even if we truncate the number of weight functions such that we only have a single term [74, 76].

2.4.2 Long-wave assumption

As the dimensionless Navier-Stokes equations, along with the various boundary conditions, are highly non-trivial to solve numerically, a number of assumptions regarding the model are required to reduce the equations to a more amenable form for numerical and analytical treatment. This step is a prerequisite for both the leading-order and first-order modelling approaches, as well as the WIBL modelling approach.

We begin by assuming slow variations in the streamwise direction, which is longer than the mean film thickness h_0. A rigorous justification may be found in many papers, but naively, this is justified by assuming (consistent with theory and experimental observations) that the time evolution of the surface dynamics of our falling film is governed primarily by long-wave modes (waves for which the variations in x and t are slow compared to the variations in y) [41].

The mathematical representation of this assumption is given by

$$\left(\frac{\partial}{\partial t}, \frac{\partial}{\partial x}, \frac{\partial^2}{\partial x^2}\right) \mapsto \left(\delta\frac{\partial}{\partial t}, \delta\frac{\partial}{\partial x}, \delta^2\frac{\partial^2}{\partial x^2}\right), \tag{2.74}$$

where δ is a small ordering parameter which is often called the thin-film parameter, and is defined as the ratio of the film thickness h_0 to the typical wave length λ. This is then simply a consequence of our long-wave assumption, as the scaling is a formulation of the imposition of slow variations in time and in the streamwise direction. We therefore correspondingly rescale the problem by changing the variables in the liquid film. The rescaling is as follows;

$$\xi = \delta x,$$

$$\tau = \delta t.$$

The capillary number, C, and the electric Weber number, W_e, are rescaled in order to keep surface tension and electric field effects in the resulting models (as will be seen later);

$$C = \delta^2 C',$$

$$W_e = \frac{W_e{}'}{\delta},$$

It is imperative to note that our continuity equation under this assumption then becomes

$$\delta u_\xi + v_y = 0, \tag{2.75}$$

which implies that the cross-stream velocity v must be of $O(\delta)$ in order for the conservation of mass to be satisfied. Hence our scaling convention implicitly includes the additional transformation

$$v = \delta w, \tag{2.76}$$

where $w = O(1)$. Implementation of this long-wave scaling, in addition to the aforementioned implicit scaling, then causes the dimensionless Navier-Stokes equations (2.54) and (2.55) to take the form

$$\delta R(u_\tau + uu_\xi + wu_y) = -\delta p_\xi + \delta^2 u_{\xi\xi} + u_{yy} + 2, \tag{2.77}$$

$$\delta^2 R(w_\tau + uw_\xi + ww_y) = -p_y + \delta^3 w_{\xi\xi} + \delta w_{yy} - 2\cot\beta. \tag{2.78}$$

The dimensionless continuity equation (2.64), upon making these substitutions, thus becomes

$$u_\xi + w_y = 0. \tag{2.79}$$

Similarly, the normal stress balance and tangential stress balance equations, under this rescaling, are reduced to the following forms, respectively,

$$\begin{aligned} -p + \frac{2}{1+\delta^2 {f_\xi}^2}[\delta^3 {f_\xi}^2 u_\xi - \delta^3 f_\xi w_\xi + \delta f_\xi u_y + \delta w_y] = \frac{f_{\xi\xi}}{C'(1+\delta^2 {f_\xi}^2)^{\frac{3}{2}}} \\ -p_a + 2\frac{{W_e}'}{\delta}\left[\frac{(\delta^2 f_\xi \phi_{2\xi} - \phi_{2y})^2}{1+\delta^2 {f_\xi}^2} - \frac{1}{2}(\delta^2 f_\xi \phi_{2\xi}^2 - \phi_{2y}^2)\right] \\ -2\frac{{W_e}'\epsilon_p}{\delta}\left[\frac{(\delta^2 f_\xi \phi_{1\xi} - \phi_{1y})^2}{1+\delta^2 {f_\xi}^2} - \frac{1}{2}(\delta^2 f_\xi \phi_{1\xi}^2 - \phi_{1y}^2)\right], \end{aligned} \tag{2.80}$$

$$2\delta^2 f_\xi (u_\xi - w_y) + (\delta^2 w_\xi + u_y)(\delta^2 f_\xi^2 - 1) = 0. \tag{2.81}$$

Whilst it is clear that the normal stress balance equation will reduce considerably when terms of $O(\delta)$ (or only $O(\delta^2)$ in higher-order models) are neglected, it is useful to rewrite the electric potential terms in an alternate form. We begin as follows, first recalling the dimensionless equations for the electric field, (2.67) in Region 1 and (2.68) in Region 2, whilst simultaneously making use of (2.70) and the dimensionless equations for the the boundary conditions at the wall and at the free surface. As Region 1 and Region 2 have distinct x and y scales associated with them, it is beneficial to define the following new variables for x and y. In both Region 1 and Region 2 we introduce

$$x = \frac{1}{\delta}\xi, \tag{2.82}$$

and in Region 2 exclusively we introduce

$$y = \frac{1}{\delta}\eta. \tag{2.83}$$

Re-examination of (2.67) and (2.68) with this rescaling in mind, leads us to the following equations for the electric potentials;

$$\delta^2 \phi_{1\xi\xi} + \phi_{1yy} = 0 \qquad \text{for} \qquad \text{Region 1}, \tag{2.84}$$

$$\phi_{2\xi\xi} + \phi_{2\eta\eta} = 0 \qquad \text{for} \qquad \text{Region 2}. \tag{2.85}$$

We additionally recall that

$$\phi_1 = 0 \qquad \text{on} \qquad y = s(\xi), \tag{2.86}$$

$$\phi_1 = \phi_2 \qquad \text{on} \qquad y = f(\xi, \tau), \tag{2.87}$$

$$\epsilon_p(\delta^2 f_\xi \phi_{1\xi} - \phi_{1y}) = \delta^2 f_\xi \phi_{2\xi} - \delta\phi_{2\eta} \qquad \text{on} \qquad y = f(\xi, \tau). \tag{2.88}$$

It is also known that as $\eta \to \infty$ we have

$$\phi_{2\xi} \to 0, \tag{2.89}$$

$$\phi_{2\eta} \to -1. \tag{2.90}$$

For simplicity, we now introduce the notation

$$\phi_2 = \tilde{\phi}_2 - y. \tag{2.91}$$

The implication of which is that

$$\tilde{\phi}_{2\xi\xi} + \tilde{\phi}_{2\eta\eta} = 0 \qquad \text{for} \qquad \text{Region 2}, \tag{2.92}$$

and, as is clear from inspection of (2.87),

$$\phi_1 = \tilde{\phi}_2 - f \qquad \text{on} \qquad y = f(\xi, \tau). \tag{2.93}$$

Hence we obtain

$$\epsilon_p(\delta^2 f_\xi \phi_{1\xi} - \phi_{1y}) = \delta^2 f_\xi \tilde{\phi}_{2\xi} - \delta\tilde{\phi}_{2\eta} + 1 \qquad \text{on} \qquad y = f(\xi, \tau). \tag{2.94}$$

Furthermore, as $y \to \infty$ we have

$$\tilde{\phi}_{2\xi} \to 0, \tag{2.95}$$

$$\tilde{\phi}_{2\eta} \to 0. \tag{2.96}$$

We now expand ϕ_1 and $\tilde{\phi}_2$ as follows

$$\phi_1 = \phi_{10} + \delta\phi_{11} + \cdots, \tag{2.97}$$

$$\tilde{\phi}_2 = \tilde{\phi}_{20} + \delta\tilde{\phi}_{21} + \cdots. \tag{2.98}$$

Then the leading-order problem for ϕ_1 is formulated as

$$\left.\begin{aligned} \phi_{10yy} &= 0 & & \\ \phi_{10} &= 0 \quad \text{on} \quad & y &= s(\xi) \\ -\epsilon_p \phi_{10y} &= 1 \quad \text{on} \quad & y &= f(\xi,\tau) \end{aligned}\right\} \implies \phi_{10} = -\frac{1}{\epsilon_p}(y - s(\xi)). \tag{2.99}$$

The first-order problem for ϕ_1 is also required, and can be expressed as

$$\left.\begin{aligned} \phi_{11yy} &= 0 & & \\ \phi_{11} &= 0 \quad \text{on} \quad & y &= s(\xi) \\ -\epsilon_p \phi_{11y} &= -\tilde{\phi}_{20\eta} \quad \text{on} \quad & y &= f(\xi,\tau) \end{aligned}\right\} \implies \phi_{11} = \frac{\phi_{20\eta}}{\epsilon_p}(y - s). \tag{2.100}$$

For $\tilde{\phi}_2$, the leading-order problem is given by

$$\tilde{\phi}_{20\xi\xi} + \tilde{\phi}_{20\eta\eta} = 0, \tag{2.101}$$

$$\tilde{\phi}_{20} = \phi_{10} + f = -\frac{1}{\epsilon_p}(f - s) + f = \left(1 - \frac{1}{\epsilon_p}\right) f + \frac{1}{\epsilon_p} s \qquad \text{on} \qquad \eta = \delta f. \tag{2.102}$$

We also have, for $\eta \to \infty$,

$$\tilde{\phi}_{2\xi} \to 0, \tag{2.103}$$

$$\tilde{\phi}_{2\eta} \to 0. \tag{2.104}$$

Now, as we know that

$$\tilde{\phi}_{20}|_{\eta=\delta f} = \tilde{\phi}_{20}|_{\eta=0} + \delta f(\tilde{\phi}_{20\xi}|_{\eta=0} + \tilde{\phi}_{20\eta}|_{\eta=0}) + \cdots, \tag{2.105}$$

we may rewrite (2.102) in the following form

$$\tilde{\phi}_{20} = \left(1 - \frac{1}{\epsilon_p}\right) f + \frac{1}{\epsilon_p} s \qquad \text{on} \qquad \eta = 0. \tag{2.106}$$

At this point it is convenient to introduce the Hilbert transform, defined as

$$\mathcal{H}[g](\xi) = \frac{1}{\pi} PV \int_{-\infty}^{\infty} \frac{g(\xi')}{\xi - \xi'} d\xi', \tag{2.107}$$

where PV denotes the principal value of the integral. The Hilbert transform is linear and nonlocal, and later we shall make use of the property that

$$\mathcal{F}\big[\mathcal{H}[g]\big](k) = -i \ \mathrm{sgn}(k) \mathcal{F}[g](k), \tag{2.108}$$

where $\mathcal{F}$ denotes the Fourier transform operator which is defined as

$$\mathcal{F}[f(x)](k) = \int_{-\infty}^{\infty} f(x)e^{-ikx}dx. \tag{2.109}$$

Following the same methodology as Gonzalez and Castellanos [29] in addition to Tilley, Petropoulos and Papageorgiou [90], and through use of the Cauchy integral formula, we are able to express $\tilde{\phi}_{20\eta}$ and $\tilde{\phi}_{20y}$ using the Hilbert transform as

$$\tilde{\phi}_{20\eta} = -\mathcal{H}\left[\left(1-\frac{1}{\epsilon_p}\right)f_\xi + \frac{1}{\epsilon_p}s_\xi\right], \tag{2.110}$$

$$\tilde{\phi}_{20y} = -\delta\mathcal{H}\left[\left(1-\frac{1}{\epsilon_p}\right)f_\xi + \frac{1}{\epsilon_p}s_\xi\right], \tag{2.111}$$

or equivalently

$$\tilde{\phi}_{20\eta} = -\mathcal{H}\left[\left(1-\frac{1}{\epsilon_p}\right)h_\xi + s_\xi\right], \tag{2.112}$$

$$\tilde{\phi}_{20y} = -\delta\mathcal{H}\left[\left(1-\frac{1}{\epsilon_p}\right)h_\xi + s_\xi\right]. \tag{2.113}$$

The electric potential terms corresponding to $\tilde{\phi}_2$ in the normal stress boundary condition may now be written as

$$\begin{aligned} 2\frac{W_e{}'}{\delta}\left[\frac{(\delta^2 f_\xi\phi_{2\xi}-\phi_{2y})^2}{(1+\delta^2 {f_\xi}^2)} - \frac{1}{2}(\delta^2 f_\xi\phi_{2\xi}^2 - \phi_{2y}^2)\right] \\ = 2\frac{W_e{}'}{\delta}\left\{\left[1+\delta\mathcal{H}\left[\left(1-\frac{1}{\epsilon_p}\right)h_\xi + s_\xi\right]\right]^2 \right. \\ \left. - \frac{1}{2}\left[1+\delta\mathcal{H}\left[\left(1-\frac{1}{\epsilon_p}\right)h_\xi + s_\xi\right]\right]^2\right\}, \end{aligned} \tag{2.114}$$

which reduces to

$$\frac{W_e{}'}{\delta} + 2W_e{}'\mathcal{H}\left[\left(1-\frac{1}{\epsilon_p}\right)h_\xi + s_\xi\right] + O(\delta) = 0. \tag{2.115}$$

Similarly, the electric potential terms corresponding to ϕ_1 may be expressed as

$$-\delta\left[\frac{(\delta^2 f_\xi\phi_{1\xi}-\phi_{1y})^2}{1+\delta^2 {f_\xi}^2} - \frac{1}{2}(\delta^2 f_\xi\phi_{1\xi}^2 - \phi_{1y}^2)\right] = {\phi_{1y}}^2 - \frac{1}{2}{\phi_{1y}}^2, \tag{2.116}$$

which, through use of (2.100) and the expansion of ϕ_1, reduces to

$$-\frac{W_e{}'}{\delta\epsilon_p}+2\frac{W_e{}'}{\epsilon_p}\mathcal{H}\left[\left(1-\frac{1}{\epsilon_p}\right)h_\xi+s_\xi\right]+O(\delta)=0. \tag{2.117}$$

Thus finally, upon substitution of (2.115) and (2.117) into (2.80), the normal stress boundary condition takes the form

$$\begin{aligned}-p+O(\delta)=-p_a+\frac{1}{C'}f_{\xi\xi}+\frac{W_e{}'}{\delta}\left(1-\frac{1}{\epsilon_p}\right)\\ +2W_e{}'\left(1-\frac{1}{\epsilon_p}\right)\mathcal{H}\left[\left(1-\frac{1}{\epsilon_p}\right)h_\xi+s_\xi\right]+O(\delta).\end{aligned} \tag{2.118}$$

For brevity, terms of $O(\delta)$ are not expressed fully, due to the knowledge that even for first-order models, during later work all terms in the equation are multiplied by δ.

2.5 Leading-order and first-order equations

The leading-order and first-order equations are derived though expanding the flow variables, using the following asymptotic expansions

$$u=u_0+\delta u_1+\cdots, \tag{2.119}$$

$$w=w_0+\delta w_1+\cdots, \tag{2.120}$$

$$p=p_0+\delta p_1+\cdots, \tag{2.121}$$

$$\phi_1=\phi_{10}+\delta\phi_{11}+\cdots, \tag{2.122}$$

$$\phi_2=\phi_{20}+\delta\phi_{21}+\cdots. \tag{2.123}$$

2.5.1 Leading-order

The leading-order equations are derived through direct substitution of the expanded flow variables into the dimensionless equations of the model, neglecting terms of $O(\delta)$ and higher. The Navier-Stokes equations, (2.77) and (2.78), at leading-order, hence take the form

$$u_{0yy}+2=0, \tag{2.124}$$

$$-p_{0y}-2\cot\beta=0. \tag{2.125}$$

For the continuity equation at leading-order, we have

$$u_{0\xi} + w_{0y} = 0, \tag{2.126}$$

and at leading-order we have the following boundary conditions:

No-slip and no-penetration boundary conditions;

$$u_0 = w_0 = 0 \qquad \text{on} \qquad y = s(\xi), \tag{2.127}$$

the tangential stress boundary condition;

$$u_{0y} = 0 \qquad \text{on} \qquad y = f(\xi, \tau), \tag{2.128}$$

and the normal stress boundary condition;

$$\begin{aligned} p_0 = p_a - \frac{{W_e}'}{\delta}\left(1 - \frac{1}{\epsilon_p}\right) - \frac{f_{\xi\xi}}{C'} \\ - 2{W_e}'\left(1 - \frac{1}{\epsilon_p}\right)\mathcal{H}\left[\left(1 - \frac{1}{\epsilon_p}\right) f_\xi + \frac{1}{\epsilon_p} s_\xi\right] \qquad \text{on} \qquad y = f(\xi, \tau). \end{aligned} \tag{2.129}$$

Note that the kinematic boundary condition will be considered later.

2.5.2 First-order

Analogously to the derivation of the leading-order equations, the first-order equations are obtained through substitution of the asymptotic expansions, albeit with additional terms corresponding to the higher order. The first-order Navier-Stokes equations are hence given by

$$R(u_{0\tau} + u_0 u_{0\xi} + w_0 u_{0y}) = -p_{0\xi} + u_{1yy}, \tag{2.130}$$

$$0 = -p_{1y} + w_{0yy}. \tag{2.131}$$

The first-order continuity equation, follows from (2.79) and may be written as

$$u_{1y} + w_{1y} = 0. \tag{2.132}$$

We similarly obtain the first-order boundary conditions at the wall

$$u_1 = w_1 = 0 \qquad \text{on} \qquad y = s(\xi), \tag{2.133}$$

and the tangential stress balance at the free surface

$$u_{1y} = 0 \qquad \text{on} \qquad y = f(\xi, \tau). \tag{2.134}$$

The first-order normal stress boundary condition will not be used and hence is not given here.

2.5.3 Long-wave equation

As we wish to find the long-wave equation for film thickness, we note that the leading-order equations can be solved through integration with respect to y. Integrating (2.124) with respect to y yields

$$u_{0y} = -2y + c_1, \tag{2.135}$$

where $c_1 = c_1(\xi, \tau)$. In order to determine c_1, we seek to make use of the tangential stress balance equation $u_{0y} = 0$ on $y = f(\xi, \tau)$, and thereby obtain

$$-2f + c_1 = 0, \tag{2.136}$$

and hence

$$u_{0y} = -2y + 2f = 2(f - y). \tag{2.137}$$

Once again, we integrate with respect to y, and get

$$u_0 = -y^2 + 2fy + c_2, \tag{2.138}$$

where $c_2 = c_2(\xi, \tau)$. We now use the no-slip boundary condition at the wall, $u_0 = 0$ on $y = s(\xi)$, to find c_2

$$-s^2 + 2fs + c_2 = 0, \qquad \Longrightarrow \qquad c_2 = s^2 - 2fs, \tag{2.139}$$

and hence we obtain the equation

$$u_0 = -y^2 + 2fy + s^2 - 2fs. \tag{2.140}$$

At leading-order, the continuity equation relates $u_{0\xi}$ and w_{0y} directly, and hence it can be deduced that

$$w_{0y} = -u_{0\xi} = 2f_\xi y + 2ss_\xi - 2f_\xi s - 2fs_\xi, \tag{2.141}$$

Once again, integration leads us to

$$w_0 = f_\xi y^2 + (2ss_\xi - 2f_\xi s - 2fs_\xi)y + c_3, \tag{2.142}$$

where $c_3 = c_3(\xi, \tau)$. Again, as we wish to determine c_3, we are required to use one of our boundary conditions. In this case we use the no-penetration boundary condition at the wall, $w_0 = 0$ on $y = s(\xi)$. Determination of c_3 leads us to the equation for w_0, which takes the form

$$w_0 = f_\xi y^2 + (2ss_\xi - 2f_\xi s - 2fs_\xi)y - f_\xi s^2 - (2ss_\xi - 2f_\xi s - 2fs_\xi)s. \tag{2.143}$$

We then integrate our leading-order pressure expression (2.125) with respect to y, and apply our leading-order normal stress boundary condition (2.129), such that we obtain

$$\begin{aligned} p_0 = p_a + 2\cot\beta(f - y) - \frac{1}{C'} f_{\xi\xi} \\ - 2W_e{}' \left(1 - \frac{1}{\epsilon_p}\right) \mathcal{H} \left[\left(1 - \frac{1}{\epsilon_p}\right) f_\xi + \frac{1}{\epsilon_p} s_\xi\right] - \frac{1}{\delta} W_e{}' \left(1 - \frac{1}{\epsilon_p}\right). \end{aligned} \tag{2.144}$$

In order to determine u_1, it is required to integrate u_{1yy} twice with respect to y, where we recall that u_{1yy} was previously used in (2.130). Hence, upon making use of the condition that $u_{1y} = 0$ on $y = f(\xi, t)$, in addition to the previously defined terms u_0, w_0 and p_0, we obtain

$$\begin{aligned} u_{1y} = (s+h)_{\xi\xi\xi} \left(\frac{(s+h)}{C'} - C'y\right) + 2\cot\beta\,(s+h)_\xi\,(y - s - h) + h_\tau R\,(s-y)^2 \\ + 2W_e{}'(1 - \frac{1}{\epsilon_p})\mathcal{H} \left[\left(1 - \frac{1}{\epsilon_p}\right) f_{\xi\xi} + \frac{1}{\epsilon_p} s_{\xi\xi}\right] \\ + (s + y - h) + 2hh_\xi ys\,(s - y)\,. \end{aligned} \tag{2.145}$$

Upon another integration, and upon making use of the no-slip boundary condition on the wall, we obtain the equation for u_1 as

$$\begin{aligned} u_1 = \frac{1}{C'} \left[(s+h)_{\xi\xi\xi} \left(-\frac{1}{2}\left(s^2 - y^2\right)\right) + h\,(y - s)\right] \\ + W_e{}' \left(1 - \frac{1}{\epsilon_p}\right) \mathcal{H} \left[\left(1 - \frac{1}{\epsilon_p}\right) f_{\xi\xi} + \frac{1}{\epsilon_p} s_{\xi\xi}\right] + \left(-(y-s)^2 + 2hy - hs\right) \end{aligned}$$

$$+hh_\xi R\left[\frac{2}{3}h^3(s-y)+\frac{1}{6}y^3(1-4s)+\frac{1}{6}\left(s^2+6y^2-4sy\right)\right]$$
$$+\cot\beta\,(h+s)_\xi\left[(y-s)^2-2y(s+h)\right]$$
$$+h_\tau R\left[\frac{1}{3}\left(y^3-s^3\right)+h^2(s-y)+ys(y-s)\right]. \tag{2.146}$$

We now seek to use the newly-derived streamwise velocity at first-order to determine the streamwise flow rate $q(\xi,\tau)$, which is defined through the relation

$$q(\xi,\tau)=\int_{s(\xi)}^{f(\xi,\tau)}u(\xi,y,\tau)dy. \tag{2.147}$$

Substitution of our previously defined asymptotic expansion and integration then yields the following result

$$q=\frac{2}{3}h^3+\frac{8\delta R}{15}h^6h_\xi-\frac{2\delta\cot\beta}{3}h^3(s+h)_\xi+\frac{\delta}{3C'}h^3(s+h)_{\xi\xi\xi}$$
$$+\frac{2\delta W_e{}'}{3}h^3\left(1-\frac{1}{\epsilon_p}\right)\mathcal{H}\left[\left(1-\frac{1}{\epsilon_p}\right)h_{\xi\xi}+s_{\xi\xi}\right]+O(\delta^2). \tag{2.148}$$

Now, by making use of the alternative form of the kinematic condition,

$$h_\tau+q_\xi=0, \tag{2.149}$$

we can formulate a non-linear equation for the film thickness, which we may express as

$$h_\tau+\left[\frac{2}{3}h^3+\frac{8\delta R}{15}h^6h_\xi-\frac{2\delta\cot\beta}{3}h^3(s+h)_\xi\right.$$
$$\left.+\frac{2\delta W_e{}'}{3}\left(1-\frac{1}{\epsilon_p}\right)h^3\mathcal{H}\left[\left(1-\frac{1}{\epsilon_p}\right)h_{\xi\xi}+s_{\xi\xi}\right]+\frac{\delta}{3C'}h^3(s+h)_{\xi\xi\xi}\right]_\xi=0. \tag{2.150}$$

Upon scaling back to t and x, we finally obtain the equation

$$h_t+\left[\frac{2}{3}h^3+\frac{8R}{15}h^6h_x-\frac{2\cot\beta}{3}h^3(s+h)_x\right.$$
$$\left.+\frac{2W_e}{3}\left(1-\frac{1}{\epsilon_p}\right)h^3\mathcal{H}\left[\left(1-\frac{1}{\epsilon_p}\right)h_{xx}+s_{xx}\right]+\frac{1}{3C}h^3(s+h)_{xxx}\right]_x=0. \tag{2.151}$$

Base states are obtained as steady-state solutions of the latter evolution equation. In the case of a local equation, i.e. when $W_e=0$, such solutions can be obtained in a rather straight-forward way using the continuation and bifurcation software Auto-07p [24]. To do this, we need to rewrite the ODE for steady states as an autonomous system

of first-order ODEs. We thus introduce a new set of variables:

$$y_1 = h, \tag{2.152}$$

$$y_2 = h_x, \tag{2.153}$$

$$y_3 = h_{xx}, \tag{2.154}$$

$$y_4 = x/(2L_c), \tag{2.155}$$

where $L_c = 2L$ is the half-period of the computational domain (it must be an integer multiple of the half-period of the wall, L). Hence, $2L_c$ is the period of the computational domain and the steady-state solution is $2L$-periodic. A comparative analysis and in-depth explanation of the choice of the half-period of the computational domain is given by Tseluiko, Blyth and Papageorgiou [98]. We begin by rearranging (2.151) for h_{xxx}, using that $h_t = 0$ for steady solutions, and upon integrating we obtain

$$h_{xxx} = \frac{3C}{h^3}\left(q - \frac{2}{3}h^3 - \frac{8R}{15}h^6 h_x + \frac{2\cot\beta}{3}h^3(s+h)_x\right) - s_{xxx} \tag{2.156}$$

We now take the derivatives of equations (2.152) through (2.155) with respect to y_4, and obtain the following autonomous differential equation system

$$y_1' = 2L_c y_2, \tag{2.157}$$

$$y_2' = 2L_c y_3, \tag{2.158}$$

$$y_3' = \frac{6L_c C}{y_1^3}\left(q - \frac{2}{3}y_1^3 - \frac{8R}{15}y_1^6 y_2 + \frac{2\cot\beta}{3}y_1^3\left(\frac{s'}{2L_c} + y_2\right)\right) - \frac{s'''}{(2L_c)^2}. \tag{2.159}$$

$$y_4' = 1, \tag{2.160}$$

where we have rewritten s_x and s_{xxx} in terms of y_4, using the notation where a dash corresponds to derivatives taken with respect to y_4. We remind the reader that sinusoidal and rectangular wall topographies are given by

$$s(x) = A\cos\left(\frac{\pi x}{L}\right), \tag{2.161}$$

and

$$s(x) = A\tanh\left(\frac{\cos(\frac{\pi x}{L})}{d}\right), \tag{2.162}$$

respectively. We thus have

$$s' = -2\pi A\sin(2\pi y_4), \tag{2.163}$$

$$s''' = (2\pi)^3 A\sin(2\pi y_4), \tag{2.164}$$

in the sinusoidal wall case and

$$s' = -\frac{2A\pi \sin(2\pi y_4)\,\mathrm{sech}^2\left(\frac{\cos(2\pi y_4)}{d}\right)}{Ld}, \tag{2.165}$$

in the rectangular wall case, with the third derivative being excluded for brevity. Our equation system (2.157)-(2.160) can hence be solved using continuation software provided we choose an appropriate constraint, such as the integral volume constraint or the fixed flux constraint. The integral volume constraint imposes that the volume of the liquid in one period of the computational domain is fixed so that the mean film thickness is unity. Mathematically, this is represented by $\int_0^1 y_1 dy_4 = 1$. In this regime, since we have a steady solution (i.e. the fluid is not moving), we have $q(x,t) = q_0$ where q_0 is a constant which is found as part of the solution. This is the regime which we use in practice throughout this thesis. An alternative to the fixed volume constraint is the fixed flux constraint. In this case, we assume that the flow rate is given by $q(x,t) = q_0 = 2/3$, and then proceed as before. In either case, we then have our periodic boundary conditions

$$y_1(0) = y_1(2L_c), \tag{2.166}$$

$$y_2(0) = y_2(2L_c), \tag{2.167}$$

$$y_3(0) = y_3(2L_c), \tag{2.168}$$

$$y_4(0) = y_4(2L_c), \tag{2.169}$$

which we may use to solve for steady-state solutions.

2.6 First-order boundary layer equations

In order to obtain the first-order boundary layer equations, we start from the non-dimensionalised equations after the long-wave assumption, (2.77) and (2.78):

$$\delta R(u_\tau + uu_\xi + wu_y) = -\delta p_\xi + u_{yy} + 2, \tag{2.170}$$

$$0 = -p_y + \delta w_{yy} - 2\cot\beta, \tag{2.171}$$

where terms of $O(\delta^2)$ have been neglected for our first-order model. We additionally have the corresponding boundary conditions. The tangential stress boundary condition

is simply given by

$$u_y = 0. \tag{2.172}$$

The normal stress boundary condition on the free surface does not reduce to such a simple form, and instead becomes

$$\begin{aligned} -p = -p_a + \frac{1}{C'} f_{\xi\xi} + \frac{W_e{}'}{\delta}\Big(1 - \frac{1}{\epsilon_p}\Big) \\ +2W_e{}'\Big(1 - \frac{1}{\epsilon_p}\Big)\mathcal{H}\Big[\Big(1 - \frac{1}{\epsilon_p}\Big)h_\xi + s_\xi\Big] + O(\delta). \end{aligned} \tag{2.173}$$

It is clear that (2.171) can be integrated with respect to y in order to obtain an equation for the pressure, which gives

$$p = \delta w_y - 2y\cot(\beta) + g(\xi, \tau), \tag{2.174}$$

where $g(\xi, \tau)$ is some function of ξ and τ to be determined from the normal stress boundary condition. Indeed, substituting (2.174) into the normal stress boundary condition (2.173) and setting $y = f(\xi, t)$ gives, upon resubstitution, our expression for the pressure p as

$$\begin{aligned} p = p_a + 2\cot\beta(f - y) - \frac{1}{C'} f_{\xi\xi} - 2W_e{}'\Big(1 - \frac{1}{\epsilon_p}\Big)\mathcal{H}\left[\left(1 - \frac{1}{\epsilon_p}\right) f_\xi + \frac{1}{\epsilon_p} s_\xi\right] \\ - \frac{1}{\delta} W_e{}' \left(1 - \frac{1}{\epsilon_p}\right). \end{aligned} \tag{2.175}$$

It is apparent that when we take the partial derivative of (2.175) with respect to ξ, many constant terms will vanish. Furthermore due to the additional δ in (2.170) prefacing the p_ξ term, any $O(\delta)$ terms will become $O(\delta^2)$, and hence neglectable for our first-order boundary layer model, retrospectively justifying our choice not to fully specify the $O(\delta)$ terms in the pressure equation. We then obtain

$$p_\xi = 2f_\xi \cot\beta - \frac{1}{C'} f_{\xi\xi\xi} - 2W_e{}'\Big(1 - \frac{1}{\epsilon_p}\Big)\mathcal{H}\left[\left(1 - \frac{1}{\epsilon_p}\right) f_{\xi\xi} + \frac{1}{\epsilon_p} s_{\xi\xi}\right], \tag{2.176}$$

where use has been made of the property of the Hilbert transform that $\frac{d}{d\xi}\mathcal{H}[f(\xi)] = \mathcal{H}[\frac{d}{d\xi} f(\xi)]$. Finally, upon substitution into the ξ-component of the Navier-Stokes equation, we obtain

$$\delta R(u_\tau + uu_\xi + wu_y) = -2\delta f_\xi \cot\beta + \frac{\delta}{C'} f_{\xi\xi\xi} + 2\delta {W_e}' \left(1 - \frac{1}{\epsilon_p}\right) \mathcal{H} \left[\left(1 - \frac{1}{\epsilon_p}\right) f_{\xi\xi} + \frac{1}{\epsilon_p} s_{\xi\xi} \right] + u_{yy} + 2, \tag{2.177}$$

which, in addition to the continuity equation

$$u_\xi + w_y = 0, \tag{2.178}$$

and the boundary conditions

$$u = w = 0 \qquad \text{on} \qquad y = s(\xi), \tag{2.179}$$

$$f_\tau + uf_\xi + wf_y = 0 \qquad \text{on} \qquad y = f(\xi, \tau), \tag{2.180}$$

forms the first-order boundary layer equations.

2.6.1 Integral boundary layer approximation

Next, we introduce the integral boundary layer approximation. First, we assume that the streamwise velocity profile u may be written as a linear combination of polynomial functions of y. For simplicity, we seek a form of the streamwise velocity for which the no-slip boundary condition is identically satisfied, and for which $y = f(\xi, \tau)$ causes the polynomial term to reduce to 1. The form of the polynomial can thus be deduced as taking the form

$$u(\xi, y, \tau) = \sum_{i=1}^{N} a_i \left(\frac{y - s(\xi)}{f(\xi, \tau) - s(\xi)} \right)^i. \tag{2.181}$$

We then use the definition of streamwise flow rate

$$q = \int_{s(\xi)}^{f(\xi,\tau)} u(\xi, y, \tau) dy, \tag{2.182}$$

as well as our tangential stress boundary condition (2.172)

$$u_y(\xi, f(\xi, \tau), \tau) = 0, \tag{2.183}$$

to solve for a_1 and a_2 through simple substitution of our polynomial approximation to the velocity given in (2.181);

$$u_y(\xi, f(\xi,\tau),\tau) = 0 \quad \Longrightarrow \quad a_1 = -2a_2 - \sum_{i=3}^{N} i a_i, \tag{2.184}$$

$$\int_{s(\xi)}^{f(\xi,\tau)} u(\xi, y, \tau) dy = q \quad \Longrightarrow \quad a_1 = \frac{2q}{f(\xi,\tau) - s(\xi)} - \frac{2a_2}{3} - 2\sum_{i=3}^{N} \frac{a_i}{i+1}. \tag{2.185}$$

These equations can then be solved to give

$$a_1 = \frac{3q}{f(\xi,\tau) - s(\xi)} + \sum_{i=3}^{N} a_i \Big(\frac{i}{2} - \frac{3}{i+1}\Big), \tag{2.186}$$

$$a_2 = \frac{-3q}{2(f(\xi,\tau) - s(\xi))} + \sum_{i=3}^{N} a_i \Big(\frac{3}{2(i+1)} - \frac{3i}{4}\Big). \tag{2.187}$$

From this point it is convenient to introduce the variable

$$\eta = \frac{y - s(\xi)}{f(\xi,\tau) - s(\xi)}, \tag{2.188}$$

and thus we are able to rewrite the streamwise velocity $u(\xi, y, \tau)$ in the following form

$$u = a_1\eta + a_2\eta^2 + \sum_{i=3}^{N} a_i \eta^i. \tag{2.189}$$

Upon substitution of (2.186) and (2.187) into (2.189), we obtain

$$\begin{aligned} u = &\frac{3q}{f(\xi,\tau) - s(\xi)} \left(\eta - \frac{\eta^2}{2}\right) + \sum_{i=2}^{N-1} a_{i+1} \left[\eta \left(\frac{i+1}{2} - \frac{3}{i+2}\right)\right. \\ &\left. + \eta^2 \left(\frac{3}{2(i+2)} - \frac{3(i+1)}{4}\right) + \eta^{i+1}\right], \end{aligned} \tag{2.190}$$

which, after labelling the first term on the right-hand side as $u^{(0)}$, becomes

$$\begin{aligned} u(\xi, y, \tau) = &u^{(0)} + \sum_{i=2}^{N-1} a_{i+1} \left[\eta \left(\frac{i+1}{2} - \frac{3}{i+2}\right)\right. \\ &\left. + \eta^2 \left(\frac{3}{2(i+2)} - \frac{3(i+1)}{4}\right) + \eta^{i+1}\right]. \end{aligned} \tag{2.191}$$

A more compact form of this equation can be formulated as

$$u = \sum_{i=1}^{N-1} b_i \phi_i(\eta), \tag{2.192}$$

where $\phi_1(\eta) = u^{(0)}$ given previously, and $b_1 = 1$. For the Galerkin method, it is sufficient to take $N = 2$, such that our streamwise velocity u is solely approximated by the $u^{(0)}$ term. This may seem a great simplification, however, it is known that close to criticality, this assumption is valid for the free-falling film model focused upon in this paper. Following the methodology of Galerkin, we then substitute this expression for the velocity into the residual of (2.177), which then takes the following form

$$\begin{aligned}\mathcal{R} = \delta R({u_\tau}^{(0)} + u^{(0)}u_\xi^{(0)} + w^{(0)}u_y^{(0)}) + 2\delta f_\xi \cot\beta - \frac{\delta}{C'} f_{\xi\xi\xi} \\ + 2\delta {W_e}'(1 - \frac{1}{\epsilon_p})\mathcal{H}\left[\left(1 - \frac{1}{\epsilon_p}\right) f_{\xi\xi} + \frac{1}{\epsilon_p} s_{\xi\xi}\right] - u_{yy}^{(0)} - 2,\end{aligned} \tag{2.193}$$

To obtain $w^{(0)}$, we use the continuity equation:

$$w^{(0)} = -\int_s^y u_x^{(0)} dy. \tag{2.194}$$

We then impose orthogonality between this residual (2.193) and a weight function w_1, which for our system is given by $\phi_1 = 3q(\eta - \frac{\eta^2}{2})/(f - s)$, such that

$$\begin{aligned}\int_0^1 \Bigg\{ \Bigg(\delta R({u_\tau}^{(0)} + u^{(0)}u_\xi^{(0)} + w^{(0)}u_y^{(0)}) + 2\delta f_\xi \cot\beta - \frac{\delta}{C'} f_{\xi\xi\xi} \\ + 2\delta {W_e}'(1 - \frac{1}{\epsilon_p})\mathcal{H}\left[\left(1 - \frac{1}{\epsilon_p}\right) f_{\xi\xi} + \frac{1}{\epsilon_p} s_{\xi\xi}\right] - u_{yy}^{(0)} - 2 \Bigg) \\ \times \left(\frac{3q}{f - s}\right)\left(\eta - \frac{\eta^2}{2}\right) \Bigg\} d\eta = 0,\end{aligned} \tag{2.195}$$

where we use that $d\eta = d((y - s)/(f - s)) = dy/(f - s)$ in order to simplify the integration. Upon solving for q_t, we obtain the following differential equation

$$\begin{aligned}q_\tau = -\frac{5\cot\beta}{3R} h(h_\xi + s_\xi) + \frac{5{W_e}'}{3R}\left(1 - \frac{1}{\epsilon_p}\right) h\,\mathcal{H}\left[\left(1 - \frac{1}{\epsilon_p}\right) h_{\xi\xi} + s_{\xi\xi}\right] \\ + \frac{9h_\xi q^2}{7h^2} - \frac{17qq_\xi}{7h} + \frac{5}{6C'R} h(h_{\xi\xi\xi} + s_{\xi\xi\xi}) + \frac{5h}{3\delta R} - \frac{5q}{2\delta R h^2}.\end{aligned} \tag{2.196}$$

As we wish to obtain an equation which does not contain any $f(\xi, \tau)$ terms, and is

expressed solely in terms of the streamwise flow rate and the film thickness, we have simply used the definition of the film thickness $h(\xi,\tau)$ and the known function describing the topography, $s(\xi)$, to eliminate $f(\xi,\tau)$ from the equation. Scaling our variables back to x and t, our equation becomes

$$q_t = -\frac{5\cot\beta}{3R}h(h_x+s_x)+\frac{5W_e}{3R}\left(1-\frac{1}{\epsilon_p}\right)h\mathcal{H}\left[\left(1-\frac{1}{\epsilon_p}\right)h_{xx}+s_{xx}\right] + \frac{9h_xq^2}{7h^2}-\frac{17qq_x}{7h}+\frac{5}{6CR}h(h_{xxx}+s_{xxx})+\frac{5h}{3R}-\frac{5q}{2Rh^2}. \quad (2.197)$$

Finally, this, in addition to the kinematic condition

$$h_t+q_x=0, \quad (2.198)$$

forms the two-equation first-order boundary layer model.

If we set $W_e=0$, corresponding to the absence of the electric field, we recover a WIBL evolution equation in direct agreement with the literature for cases with no electric field (see, for example, D'Alessio, Pascal and Jasmine [18]). Also note that through setting the wall topography to be flat by the imposition $s(x)=0$, we also recover with direct agreement with the literature the long-wave evolution equation which includes an electric field but is only valid for flat inclined surfaces (see, for example, Tseluiko and Papageorgiou [104]).

As with the long-wave equation, base states are obtained as steady-state solutions of the coupled system of evolution equations. When $W_e=0$, such solutions can be obtained in a rather straight-forward way using the continuation and bifurcation software Auto-07p [24]. Otherwise, the model can be represented as a system of ODEs, e.g. for the Fourier coefficients of the unknown functions, and the fixed points of this system would correspond to steady states of the WIBL model.

Let us consider the scenario where $W_e=0$. There are then two cases that we can consider, as before. The first case we shall discuss is the fixed flow rate case, for which $q(x,t)=q_0=2/3$, as known from the Nusselt flat film solution of thickness $h_0=1$ when the wall is flat. The second case is the fixed volume case, where we assume that the volume of the liquid in one period of the computational domain is fixed so that the mean film thickness is unity. Therefore we impose the integral constraint $(1/2L_c)\int_{-L_c}^{L_c}h_0dx=1$, equivalent to the representation using y_4 which was used in the

long-wave case previously. Note that for this regime, q_0 is not prescribed before the numerical analysis, and is instead one of solutions obtained. As we seek steady solutions we have $h_t = q_t = q_x = 0$, and proceed by rearranging (2.196) for h_{xxx}, such that we have

$$h_{xxx} = \frac{6CR}{5}\left(\frac{5\cot\beta}{3R}(h_x + s_x) - \frac{9h_x q_0^2}{7h^3} - \frac{5}{3R} + \frac{5q_0}{2Rh^3}\right) - s_{xxx}. \tag{2.199}$$

We proceed as in the long-wave case, introducing the same new variables from equations (2.152)-(2.155). The topographical terms s_x and s_{xxx} are then rewritten in terms of y_4, using the notation where a dash corresponds to derivatives taken with respect to y_4. These terms are identical in both models, and are given by equations (2.163)-(2.165).

$$y_1' = 2L_c y_2, \tag{2.200}$$

$$y_2' = 2L_c y_3, \tag{2.201}$$

$$y_3' = \frac{12L_cCR}{5}\left(\frac{5\cot\beta}{3R}\left(y_2 + \frac{s'}{2L_c}\right) - \frac{9y_2 q_0^2}{7{y_1}^3} - \frac{5}{3R} + \frac{5q_0}{2R{y_1}^3}\right) - \frac{s'''}{(2L_c)^2}, \tag{2.202}$$

$$y_4' = 1. \tag{2.203}$$

This system of equations, along with the integral condition in the volume constraint case or the imposed flow rate in the fixed flux case, in addition to the boundary conditions (2.166)-(2.169) can also be solved using standard continuation software, i.e. Auto-07p [24].

Finally, we mention that for the case of non-zero electric field, the approaches mentioned above are not applicable, since then the governing equations become nonlocal and cannot be represented as a low-dimensional dynamical system. In such a case, we shall instead use the aforementioned Fourier spectral method by representing the model as a system of ODEs for the Fourier coefficients of the unknown functions, and a detailed explanation of this approach may be found in Chapter 4. For both the long-wave and WIBL models we use 450 Fourier modes for the unknown function. We note that in using such an approach we shall make use of the fact that in the Fourier space, the nonlocal Hilbert transform term reduces to a simple sgn function.

Chapter 3

Linear stability analysis

3.1 Introduction

In Chapter 4 we will compute steady-state solutions to our long-wave model (2.151) and two-equation WIBL model (2.196) and (2.198). However, the stability of such solutions to small perturbations is also very important, and will be analysed in this chapter. In addition to the trivially distinct stable and unstable steady-state solutions, we also make a distinction between absolutely unstable and convectively unstable solutions. Due to the large amount of literature carefully examining in great detail these instabilities and their properties, and due to the fact that the majority of this research falls outside the scope of this thesis, we shall merely give a brief overview of the salient features which are relevant to the work under consideration, and refer readers to the relevant papers for more general information. A natural starting point in the literature is the work of Benjamin [5] and Yih [116] in determining the critical Reynolds number for a liquid flowing down an inclined plane, and the subsequent experimental corroborations by Liu, Paul and Gollub [52] in addition to Floryan, Davis and Kelly [26].

The most obvious discrepancy between absolute and convective instabilities is that for convective instabilities, despite being linearly unstable and the norm of the perturbation growing in time, the perturbation decays at any fixed point in space, or rather naively, we may say that the perturbation is eponymously 'convected' downstream or upstream, away from the source of instability [78]. Contrariwise, it is known that for absolute instabilities the perturbation grows at every point in the domain as time increases. A

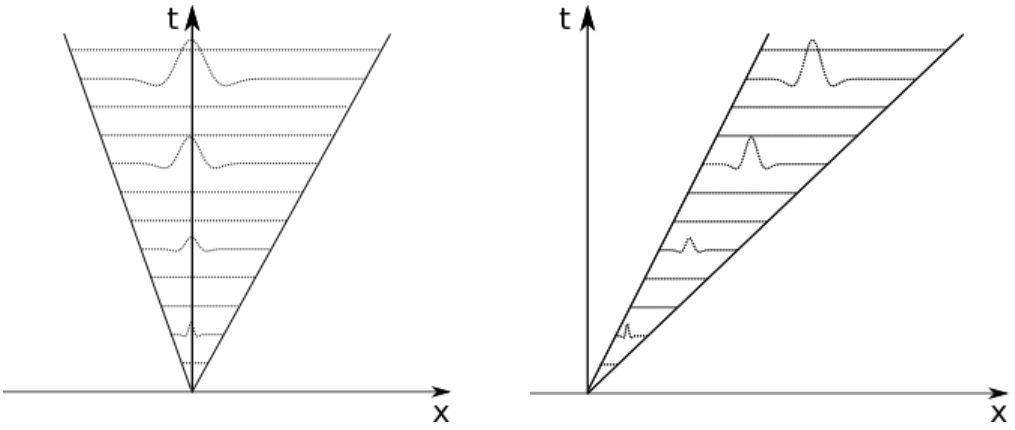

Figure 3.1: *Sketch of the behaviour of a perturbation in the absolutely (left) and convectively (right) unstable cases.*

sketch of these two behaviours is given in Figure 3.1. A subset of convective instabilities that warrant discussion are known as transient instabilities. Despite convective instabilities allowing for a perturbation to travel either upstream, downstream, or in both directions simultaneously, transient instabilities are characterised by the perturbation only travelling in a single direction [78, 98]. As each of these types of instabilities represents a physically distinct scenario, consequently, we seek to employ a mathematical framework whereby these may be distinguished.

Exponentially weighted spaces are typically used in such matters, however, due to the nonlocal Hilbert transform term corresponding to the electric field, this approach is not suitable, and we instead follow a methodology similar to that by Papageorgiou and Fokas [27], as opposed to alternative methodologies, i.e. those of Delbende, Chomaz and Huerre [20] or Monkewitz [58].

3.2 Critical Reynolds numbers for flat walls

In this section, we derive the critical Reynolds numbers for both the long-wave and WIBL models. We also determine the critical electric Weber number corresponding to instability for a given Reynolds number, and provide the critical wavenumber corresponding to the most unstable mode. In this section, we neglect the topography and instead consider the flat inclined slope case.

3.2.1 Long-wave model

We begin by linearising the long-wave equation around a general steady-state solution $h_0(x)$. To achieve this, we make the substitution $h(x,t) = h_0(x) + h_1(x,t)$ into (2.151), where $|h_1| \ll 1$. It is important to note that despite the topography of the wall and the steady-state solutions taking periodic forms, the perturbation $h_1(x,t)$ is not necessarily periodic. By neglecting the higher-order terms following the substitution, we obtain the following linear nonlocal evolution equation with non-constant coefficients for the perturbation h_1:

$$h_{1t} = -\big(b_0 h_1 + b_1 h_{1x} + b_2 h_{1xxx} + b_3 \mathcal{H}[h_{1xx}]\big)_x, \tag{3.1}$$

where the coefficients are

$$\begin{aligned} b_0 &= 2h_0^2 + \frac{16R}{5} h_0^5 h_{0x} - 2\cot\beta h_0^2 (h_0+s)_x \\ &\quad + \frac{1}{C} h_0^2 (h_0+s)_{xxx} + 2W_e \left(1 - \frac{1}{\epsilon_p}\right) h_0^2 \mathcal{H}\left[\left(1 - \frac{1}{\epsilon_p}\right) h_{0xx} + s_{xx}\right], \end{aligned} \tag{3.2}$$

$$b_1 = \frac{8R}{15} h_0^6 - \frac{2\cot\beta}{3} h_0^3, \tag{3.3}$$

$$b_2 = \frac{1}{3C} h_0^3, \tag{3.4}$$

$$b_3 = \frac{2W_e}{3} \left(1 - \frac{1}{\epsilon_p}\right)^2 h_0^3. \tag{3.5}$$

For the case of a flat wall, $s(x) = 0$, we then obtain

$$\begin{aligned} h_{1t} = -\Bigg[& 2h_0^2 h_1 + \frac{8R}{15} h_0^6 h_{1x} - \frac{2\cot\beta}{3} h_0^3 h_{1x} \\ & + \frac{2W_e}{3} \left(1 - \frac{1}{\epsilon_p}\right) h_0^3 \mathcal{H}\left[\left(1 - \frac{1}{\epsilon_p}\right) h_{1xx}\right] + \frac{1}{3C} h_0^3 h_{1xxx} \Bigg]_x. \end{aligned} \tag{3.6}$$

Following the substitution of the uniform film thickness $h_0 = 1$, and perturbation $h_1(x,t) = \tilde{h}_1 e^{\omega t + ikx}$, we then obtain the dispersion relation

$$\omega = -2ik + \frac{8R}{15} k^2 - \frac{2\cot\beta}{3} k^2 - \frac{k^4}{3C} + \frac{2W_e}{3} \left(1 - \frac{1}{\epsilon_p}\right)^2 |k|^3. \tag{3.7}$$

It is here that we may choose to investigate either the temporal or spatial linear stability theory, depending on whether we allow either ω or k to take complex values, whilst

only permitting real values of the remaining variable [35]. As we initially focus upon temporal instabilities, rather than spatial instabilities, we begin with the assumption that our wavenumber k is real and our frequency ω is complex, as opposed to spatial instabilities, in which case we assume that our wavenumber k is complex and our frequency ω is real [35]. We also know that, due to the nonlocal Hilbert transform term, we have a $|k|^3$ term in the dispersion relation, which is not analytic at $k = 0$. We will demonstrate, however, that in the analysis it will possible to replace $|k|^3$ with k^3 and avoid non-analyticity.

For the real part of ω we have

$$Re[\omega] = \left(\frac{8R}{15} - \frac{2\cot\beta}{3}\right)k^2 + \frac{2W_e}{3}\left(1 - \frac{1}{\epsilon_p}\right)^2 |k|^3 - \frac{k^4}{3C}. \tag{3.8}$$

We then have two cases to discuss – the case in which we have an electric field, and the case without. Although the case without the electric field can be trivially obtained by taking the limit of $W_e \to 0$ in the equation corresponding to the inclusion of the electric field, a more rigorous and strict derivation is required. The difference between the two approaches may be summarised as follows – in the case of no electric field, we have simply one parameter through which our flow may be destabilised, the Reynolds number. Contrariwise, in the case including the electric field, we have two such parameters, both the Reynolds number and the electric Weber number.

In case of no electric field, if there is a local maximum in $Re[w]$ at $k = 0$, then $Re[w]$ will remain negative for all $k \neq 0$. If there is a local minimum in $Re[w]$ at $k = 0$, then there will be a band of unstable wavenumbers extending from $k = 0$ to a certain cut-off value $k = k_c$. For $W_e = 0$, we thus have the criteria

$$Re[\omega] = 0 \quad \text{at} \quad k = 0, \tag{3.9}$$

$$\frac{d^2 Re[\omega]}{dk^2} = 0 \quad \text{at} \quad k = 0. \tag{3.10}$$

This system can be easily solved to give the following critical Reynolds number:

$$R_{c1} = \frac{5\cot\beta}{4}. \tag{3.11}$$

In the case with an electric field, the base solution may be destabilised even when $R < R_{c1}$, since the corresponding term in the dispersion relation is always positive

and therefore destabilising, and there may appear a band of unstable wavenumbers that is separated from zero. The transition from the linearly stable to the linearly unstable regime then happens when the value of $Re[\omega]$ at the local maximum at a nonzero value of k is zero. We thus proceed as follows. We begin with the imposition of the following two conditions on (3.8), corresponding to the location of a local maximum at some critical wavenumber k^* which we assume to be positive:

$$Re[\omega] = 0 \quad \text{at} \quad k = k^*, \tag{3.12}$$

$$\frac{dRe[\omega]}{dk} = 0 \quad \text{at} \quad k = k^*, \tag{3.13}$$

which leads us to two equations for k^*. Thus we have

$$\left(\frac{8R}{15} - \frac{2\cot\beta}{3}\right) + \frac{2W_e k^*}{3}\left(1 - \frac{1}{\epsilon_p}\right)^2 - \frac{k^{*2}}{3C} = 0, \tag{3.14}$$

$$2\left(\frac{8R}{15} - \frac{2\cot\beta}{3}\right) + 2W_e k^*\left(1 - \frac{1}{\epsilon_p}\right)^2 - \frac{4k^{*2}}{3C} = 0. \tag{3.15}$$

By solving this set of equations, we find that the positive solution is

$$k^* = \frac{3}{W_e}\left(\frac{2\cot\beta}{3} - \frac{8R}{15}\right)\left(1 - \frac{1}{\epsilon_p}\right)^{-2}. \tag{3.16}$$

Substituting this k^* back into (3.14) and taking the limit of $\epsilon_p \to \infty$ for a perfect conductor, we thus obtain the following expression for the critical Reynolds number:

$$R_{c2} = \frac{5\cot\beta}{4} - \frac{5W_e^2}{8C}. \tag{3.17}$$

We thus confirm that the normal electric field is always linearly destabilising in the absence of topography.

3.2.2 WIBL model

We begin by following the same methodology as in the long-wave case – assuming that $h_0(x)$ and $q_0(x)$ are steady-state solutions, $h_1(x,t)$ is a small perturbation to the film thickness, and $q_1(x,t)$ is a small perturbation to the flow rate. We remind the reader that despite the topography of the wall and the steady-state solutions taking periodic forms, the perturbations $h_1(x,t)$ and $q_1(x,t)$ are not necessarily periodic themselves. Upon

substituting $h(x,t) = h_0(x) + h_1(x,t)$ and $q(x,t) = q_0(x) + q_1(x,t)$ into our kinematic condition (2.198), we obtain the following at first order:

$$h_{1t} = -q_{1x}. \tag{3.18}$$

Upon substituting the steady-state solutions for flow rate and film thickness, along with the corresponding small perturbations, into our remaining equation (2.197) and upon linearising, we obtain the following result at first order:

$$\begin{aligned} q_{1t} = {} & \frac{5W_e}{3R}\left(1-\frac{1}{\epsilon_p}\right)\left(\left(1-\frac{1}{\epsilon_p}\right)h_0\mathcal{H}[h_{1xx}] + \mathcal{H}\left[\left(1-\frac{1}{\epsilon_p}\right)h_{0xx} + s_{xx}\right]h_1\right) \\ & - \frac{5\cot\beta}{3R}(h_0h_{1x} + (h_{0x}+s_x)h_1) + \frac{5}{6CR}(h_0h_{1xxx} + (h_{0xxx}+s_{xxx})h_1) + \frac{5}{3R}h_1 \\ & - \frac{17q_0q_{1x}}{7h_0} - \frac{18q_0^2h_{0x}h_1}{7h_0^3} + \frac{9q_0}{7h_0^2}(q_0h_{1x} + 2h_{0x}q_1) + \frac{5q_0h_1}{Rh_0^3} - \frac{5q_1}{2Rh_0^2}. \end{aligned} \tag{3.19}$$

Thus it is clear that through the substitution of the perturbations into our kinematic condition, we have a linear relation between h_{1t} and q_{1x}, and through the above equation, we have a linear relation between q_{1t}, q_1 and h_1. Thus, in matrix representation, we have the following

$$\begin{bmatrix} h_{1t} \\ q_{1t} \end{bmatrix} = \begin{bmatrix} 0 & \mathrm{L}_{12} \\ \mathrm{L}_{21} & \mathrm{L}_{22} \end{bmatrix} \begin{bmatrix} h_1 \\ q_1 \end{bmatrix}, \tag{3.20}$$

where L_{12}, L_{21}, and L_{22} are linear operators given by

$$\mathrm{L}_{12}q_1 = -q_{1x}, \tag{3.21}$$

$$\mathrm{L}_{21}h_1 = b_0h_1 + b_1h_{1x} + b_2h_{1xxx} + b_3\mathcal{H}[h_{1xx}], \tag{3.22}$$

$$\mathrm{L}_{22}q_1 = c_0q_1 + c_1q_{1x}, \tag{3.23}$$

and where the b and c coefficients are given by

$$\begin{aligned} b_0 = {} & \frac{5W_e}{3R}\left(1-\frac{1}{\epsilon_p}\right)\mathcal{H}\left[\left(1-\frac{1}{\epsilon_p}\right)h_{0xx} + s_{xx}\right] - \frac{5}{3R}(h_{0x}+s_x)\cot\beta \\ & + \frac{5}{6CR}(h_{0xxx}+s_{xxx}) + \frac{5}{3R} - \frac{18q_0^2h_{0x}}{7h_0^3} + \frac{5q_0}{Rh_0^3}, \end{aligned} \tag{3.24}$$

$$b_1 = -\frac{5h_0}{3R}\cot\beta + \frac{9q_0^2}{7h_0^2}, \tag{3.25}$$

$$b_2 = \frac{5h_0}{6CR}, \tag{3.26}$$

$$b_3 = \frac{5W_e h_0}{3R}, \tag{3.27}$$

$$c_0 = \frac{18q_0 h_{0x}}{7h_0^2} - \frac{5}{2Rh_0^2}, \tag{3.28}$$

$$c_1 = -\frac{17q_0}{7h_0}. \tag{3.29}$$

As we wish to determine the effect on the stability of the steady-state solutions caused by the perturbations, we seek to examine the spectrum of the matrix operator given in (3.20). To proceed, we set $s(x) = 0$, $q_0 = \frac{2}{3}$, $h_0 = 1$, $q_1 = \tilde{q}_1 e^{\omega t + ikx}$ and $h_1 = \tilde{h}_1 e^{\omega t + ikx}$, and hence obtain the following

$$\omega \begin{bmatrix} \tilde{h}_1 \\ \tilde{q}_1 \end{bmatrix} = \begin{bmatrix} 0 & -ik \\ -\frac{5\cot\beta}{3R}ik + \frac{5}{R} + \frac{5W_e}{3R}ik^2\,\mathrm{sgn}(k) - \frac{5}{6CR}ik^3 + \frac{4}{7}ik & -\frac{34}{21}ik - \frac{5}{2R} \end{bmatrix} \begin{bmatrix} \tilde{h}_1 \\ \tilde{q}_1 \end{bmatrix}. \tag{3.30}$$

Hence we simply obtain a quadratic equation in ω, with two distinct solutions, ω_1 and ω_2, given by

$$\omega_1 = \hat{A} + i\hat{B} - \sqrt{\hat{C} + i\hat{D}}, \tag{3.31}$$

$$\omega_2 = \hat{A} + i\hat{B} + \sqrt{\hat{C} + i\hat{D}}, \tag{3.32}$$

where $\hat{A}, \hat{B}, \hat{C}$ and $\hat{D}$ are defined by the following

$$\hat{A} = -\frac{5}{4R}, \tag{3.33}$$

$$\hat{B} = -\frac{17k}{21}, \tag{3.34}$$

$$\hat{C} = (-592\,C^2R^2k^2 + 11760\,C^2R\,W_e|k|^3 - 5880\,CR\,k^4 \\ -11760\,C^2R\,k^2\cot\beta + 11025\,C^2)/7056\,C^2R^2, \tag{3.35}$$

$$\hat{D} = -\frac{125k}{42R}. \tag{3.36}$$

Using the fact that in polar form of the complex number under the square root, $\rho = \sqrt{\hat{C}^2 + \hat{D}^2}$ and $\theta = \arctan(\hat{D}/\hat{C})$, we are able to write the real part of ω_1 and ω_2 in a more manipulatable form. We begin with

$$\omega_{1,2} = \hat{A} + i\hat{B} \pm \sqrt{\rho e^{i\theta}}, \tag{3.37}$$

following which we express $e^{i\theta}$ in terms of trigonometric functions:

$$\omega_{1,2} = \hat{A} + i\hat{B} \pm \sqrt{\rho}(\cos(\theta/2) + i\sin(\theta/2)). \tag{3.38}$$

For the real part of $\omega_{1,2}$ then, we have

$$Re[\omega_{1,2}] = \hat{A} \pm \sqrt{\rho}\cos(\theta/2), \tag{3.39}$$

and following use of the half-angle formula

$$\cos(\theta/2) = \sqrt{\frac{1+\cos(\theta)}{2}}, \tag{3.40}$$

and substitution of θ into (3.39), we obtain

$$Re[\omega_1] = \hat{A} - \sqrt{\frac{\hat{C}+\rho}{2}}, \tag{3.41}$$

$$Re[\omega_2] = \hat{A} + \sqrt{\frac{\hat{C}+\rho}{2}}. \tag{3.42}$$

We similarly note that the imaginary parts of ω_1 and ω_2 may be written as

$$Im[\omega_1] = \hat{B} - \sqrt{\frac{-\hat{C}+\rho}{2}}, \tag{3.43}$$

$$Im[\omega_2] = \hat{B} + \sqrt{\frac{-\hat{C}+\rho}{2}}. \tag{3.44}$$

As we know that $\hat{A}$ is negative by definition, it is clear that $Re[\omega_2] > Re[\omega_1]$ for all physical parameter values. As we are interested in the point at which $Re[\omega]$ becomes positive, corresponding to the onset of instability, we may thus neglect $Re[\omega_1]$ in subsequent analysis, and focus solely upon $Re[\omega_2]$. These two solutions are shown visually in Figure 3.2 for the case of $R = 1$, corresponding to the linearly stable case. Also included is the solution for the long-wave model for the same parameter values. For $k \lesssim 0.07$ we see close agreement between the long-wave and WIBL models, although for larger k we note that the two models diverge significantly. The long-wave model predicts lower growth rates until $k \approx 0.18$, at which point we observe the long-wave

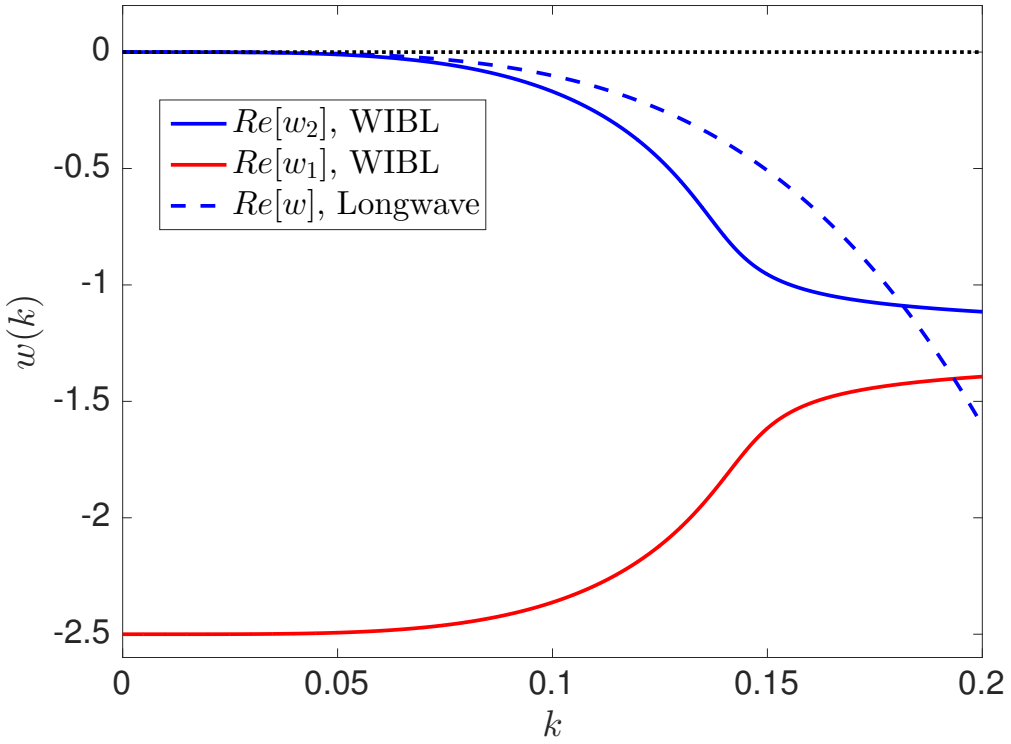

Figure 3.2: *Real parts of the solutions to the WIBL dispersion relation (3.30) for $R = 1$, $\beta = \pi/4$ and $K = 3364.5$ with equation (3.41) shown in red and equation (3.42) shown in blue. The long-wave equivalent given in (3.8 is shown by a dashed blue line.*

model predicting a monotonically increasing growth rate and the WIBL model predicting a much slower growth rate, following its decrease at $k \approx 0.14$.

We then continue with the same methodology as in the long-wave case, where we consider the case with the electric field and the case without the electric field separately. In the case without the electric field, we have the criteria

$$Re[\omega_2] = 0 \quad \text{at} \quad k = 0, \tag{3.45}$$

$$\frac{d^2 Re[\omega_2]}{dk^2} = 0 \quad \text{at} \quad k = 0. \tag{3.46}$$

This system can once again be solved to give the following critical Reynolds number:

$$R_{c1} = \frac{5 \cot \beta}{4}, \tag{3.47}$$

which is the same as for the long-wave model.

In the case including the electric field, we impose the following conditions at a nonzero value of k^* (to be found):

$$Re[\omega_2] = 0 \quad \text{at} \quad k = k^*, \tag{3.48}$$

$$\frac{dRe[\omega_2]}{dk} = 0 \quad \text{at} \quad k = k^*. \tag{3.49}$$

Solving for k^*, we obtain

$$k^* = W_e C + \sqrt{C^2 W_e^2 + \frac{8}{5} CR - 2C \cot \beta}, \tag{3.50}$$

which upon resubstitution into (3.48), leads us once again to the critical Reynolds number

$$R_{c2} = \frac{5 \cot \beta}{4} - \frac{5 W_e^2}{8C}, \tag{3.51}$$

such that we find complete agreement between the long-wave and WIBL models for the onset of instability with a flat wall. In Figure 3.3 we see the dispersion relation (3.32) in the case of no electric field for both models. For the relatively small values of k examined here, we find near-perfect agreement between the two models, although we remind the reader that for larger k the two models begin to diverge. We have a single point of inflection at the origin, and at Reynolds numbers above the critical value (as seen for the red curve), we have a range of wavenumbers extending from zero with positive growth rates, thus corresponding to unstable flow. In Figure 3.4 we see the dispersion relation in the case where we have the electric field. For Reynolds numbers above the secondary critical value R_{c2} (red), we see that there exists a range of wavenumbers not originating from the origin where the growth rate is positive, and therefore the flow is unstable. Again we find near-perfect agreement between the long-wave and WIBL models for the low values of k under investigation.

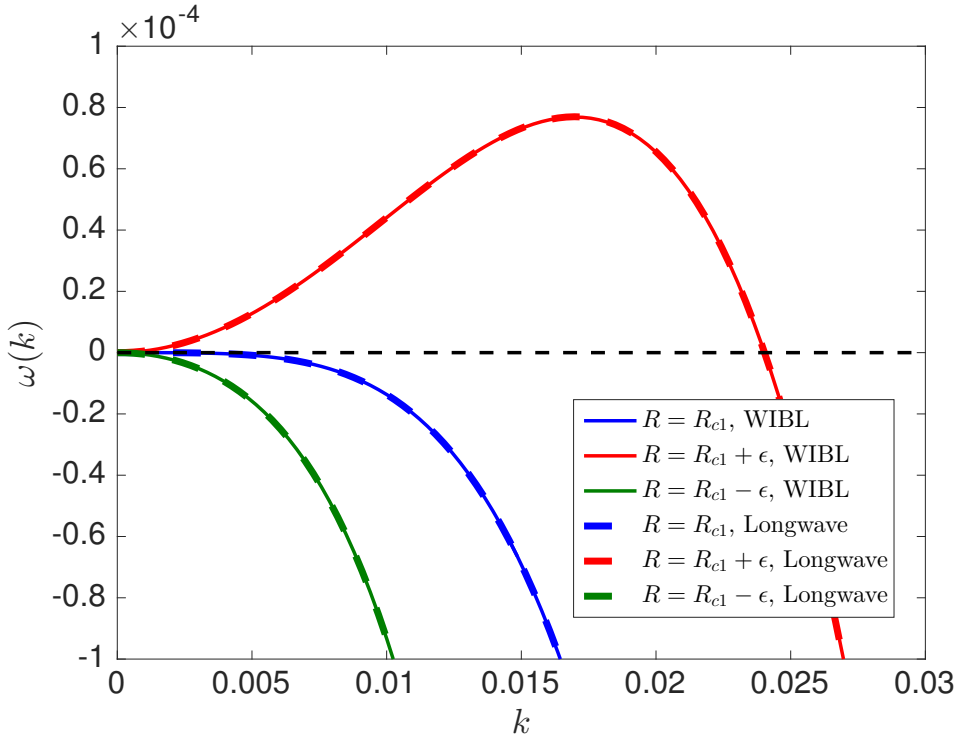

Figure 3.3: *Dispersion relations in the case of no electric field for the long-wave and WIBL models, with Reynolds numbers slightly above (red), below (green) and at the critical value (blue). Here we have R_{c1}=1.25, $K = 3364.5$ and $\epsilon = 1$.*

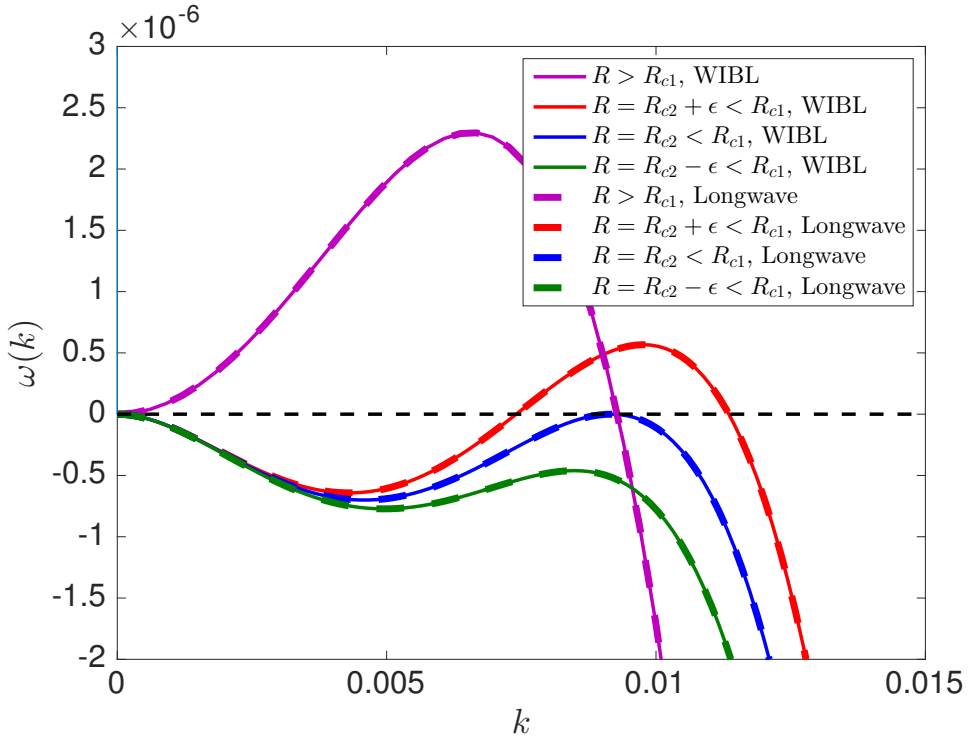

Figure 3.4: *Dispersion relations in the case of electric field for the long-wave and WIBL models, with Reynolds numbers slightly above (red), below (green) and at the critical value (blue). The purple curve corresponds to a Reynolds number above R_{c1}, the critical Reynolds number in the case of no electric field. Here we have R_{c1}=1.25, $K = 3364.5$, $\epsilon = 0.2$ and $W_e = 0.01$.*

3.3 Absolute and convective instabilities

Here we discuss the conditions required for absolute instability in both models, and examine the transition between the convectively unstable and absolutely unstable cases. We begin with the long-wave case, by reexamining (3.14), where it can be seen that linear instability is only obtained in the case where

$$CW_e^2 > \frac{8}{5}R - 2\cot\beta. \tag{3.52}$$

We similarly see that there exists a range of unstable wavenumbers $|k| \in (k_+, k_-)$, where k_+ and k_- are given by

$$k_+ = C^2W_e^2 + \frac{8}{5}CR - 2C\cot\beta, \tag{3.53}$$

$$k_- = \max\left\{0,\ C^2W_e^2 - \frac{8}{5}CR - 2C\cot\beta\right\}, \tag{3.54}$$

such that any $|k|$ within this range corresponds to a spectrally unstable flow. Following this, we now permit complex wavenumbers, rather than the imposition of only real and positive wavenumbers, as discussed earlier. Also recall that we have a linear operator (2.151) which acts on our small perturbation h_1. In general, the solution to the linearised equation can be written in terms of a summation involving the discrete eigenvalues, and an integral involving the essential spectrum, as per Chang, Demekhin and Kopelevich [15] and Lin et al. [49]:

$$h_1(x,t) = \sum_n e^{\lambda_n t}B_n\phi_n(x) + \int_{-\infty}^{\infty} e^{\omega(k)t}B(k)\Phi(x,k)dk, \tag{3.55}$$

where λ_n are the discrete eigenvalues with the corresponding eigenfunctions $\phi_n(x)$, B_n are constants, $\Phi(x,k)$ are the 'eigenfunctions' from the essential spectrum which we may pick such that $\Phi(x,-k) = \overline{\Phi(x,k)}$. We also remark that $\omega(-k) = \overline{\omega(k)}$, and in the case of real h_1, $B(-k) = \overline{B(k)}$ [49]. In our case, the discrete spectrum is empty so that there is no the first summation term on the right-hand side, and $\Phi(x,k)$ can be chosen to be $\Phi(x,k) = \exp(ikx)$.

Typically, an argument would need to be made to the effect of showing that the summation term involving the discrete eigenvalues decays in time, however, due to the system under consideration having no discrete eigenvalues, we may focus solely upon the integral term, as the properties of this term are what shall determine whether our flow is

either convectively or absolutely unstable. As we are interested in the range of unstable wavenumbers in this analysis, it is sufficient to consider our integral between the previously derived k_- and k_+. Due to the presence of the $|k|^3$ term, we are required to replace it with a k^3 term if we wish for I_c to be analytic in the complex k-plane, and this is possible after appropriate rewriting of the integral as integration from 0 to ∞, see, for example, Vellingiri, Tseluiko and Kalliadasis [109] and Lin et al. [49]. As the integrand is now known to be analytic for this range of k, we are thus able to deform the contour of integration into any such path connecting k_- and k_+, and the stability properties of the flow shall be determined by whether or not the contour of integration Γ passes through regions of exclusively $Re(\omega) < 0$, corresponding to convective instability, or whether the contour of integration Γ always has to pass through a region where $Re(\omega) > 0$, corresponding to absolute instability. See, for example, the work by Vellingiri, Tseluiko and Kalliadasis [109].

However, we note that the only way for our contour of integration Γ to transition from the path described in the convectively unstable case, to the path described in the absolutely unstable case, via a continuous parameter change (either the Reynolds number or the electric Weber number), is through a saddle point where our two branches of $Re(\omega) = 0$ meet, as discussed by Monkewitz [58].

In Figure 3.5 we observe the convectively unstable case approaching the transition to absolute instability. The two branches do not touch, but begin to pinch together at $Re(k) \approx 0.14$. The transitory case is shown in Figure 3.6, where the two branches intersect and form a saddle point. At this point, if we slightly increase R, we transition to the absolutely unstable case, which may be seen in Figure 3.7, where the saddle point now vanishes and the branches of $Re[\omega(k)]$ are now qualitatively different than observed in the convectively unstable case. We see that the lower branch on the left and the lower branch on the right have now joined, and similarly for the two intermediary branch segments on the right. In all cases we fix $\beta = \pi/4$, $K = 3364.5$ and $W_e = 1$, and we cause the transition by increasing the Reynolds number from $R = 14.7$ in the convectively unstable case, to 14.9 at the transition, to $R = 15.2$ in the absolutely unstable case.

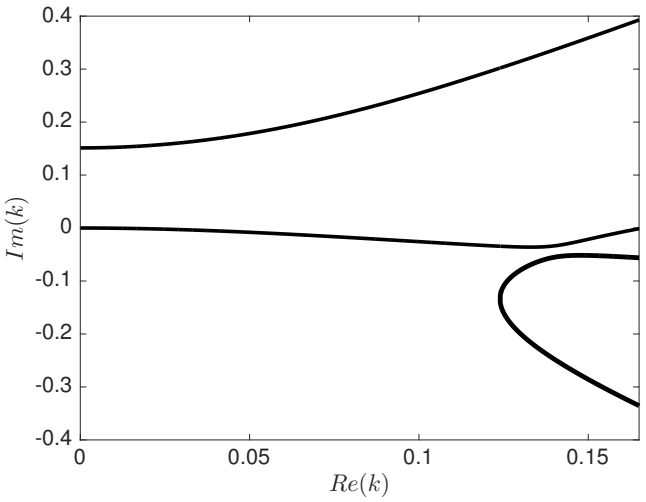

Figure 3.5: *The curves $Re[\omega(k)] = 0$ in the complex plane for the WIBL model in the case of no topography, with $R = 14.7$, $W_e = 1$, $K = 3364.5$ and $\beta = \pi/4$, corresponding to the convectively unstable case.*

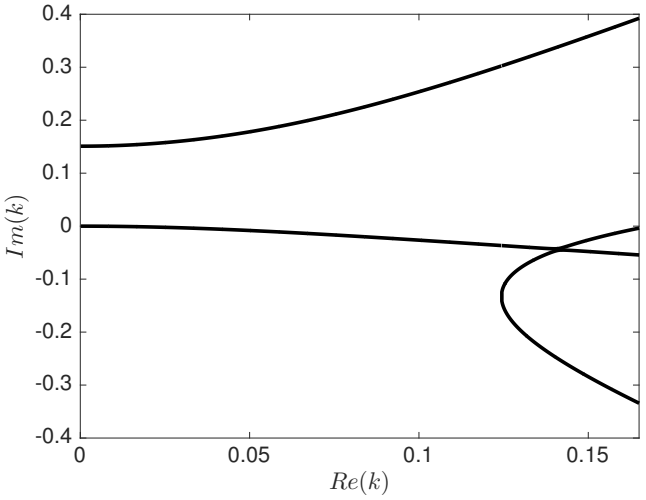

Figure 3.6: *The curves $Re[\omega(k)] = 0$ in the complex plane for the WIBL model in the case of no topography, with $R = 14.9$, $W_e = 1$, $K = 3364.5$ and $\beta = \pi/4$, corresponding to slightly below the transition between the convectively unstable and absolutely unstable cases.*

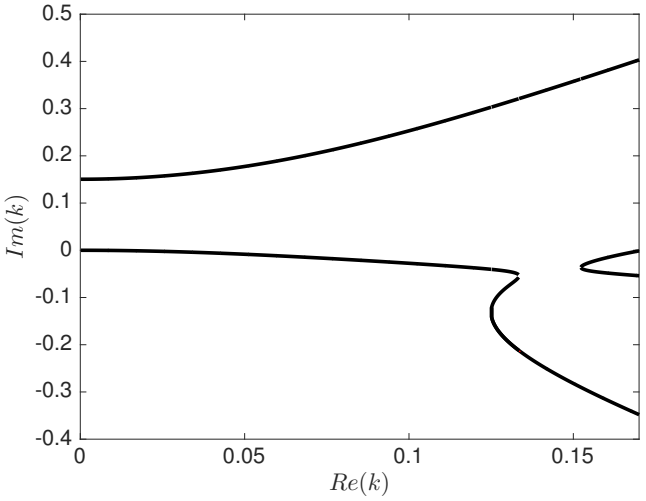

Figure 3.7: *The curves $Re[\omega(k)] = 0$ in the complex plane for the WIBL model in the case of no topography, with $R = 15.2$, $W_e = 1$, $K = 3364.5$ and $\beta = \pi/4$, corresponding to the absolutely unstable case.*

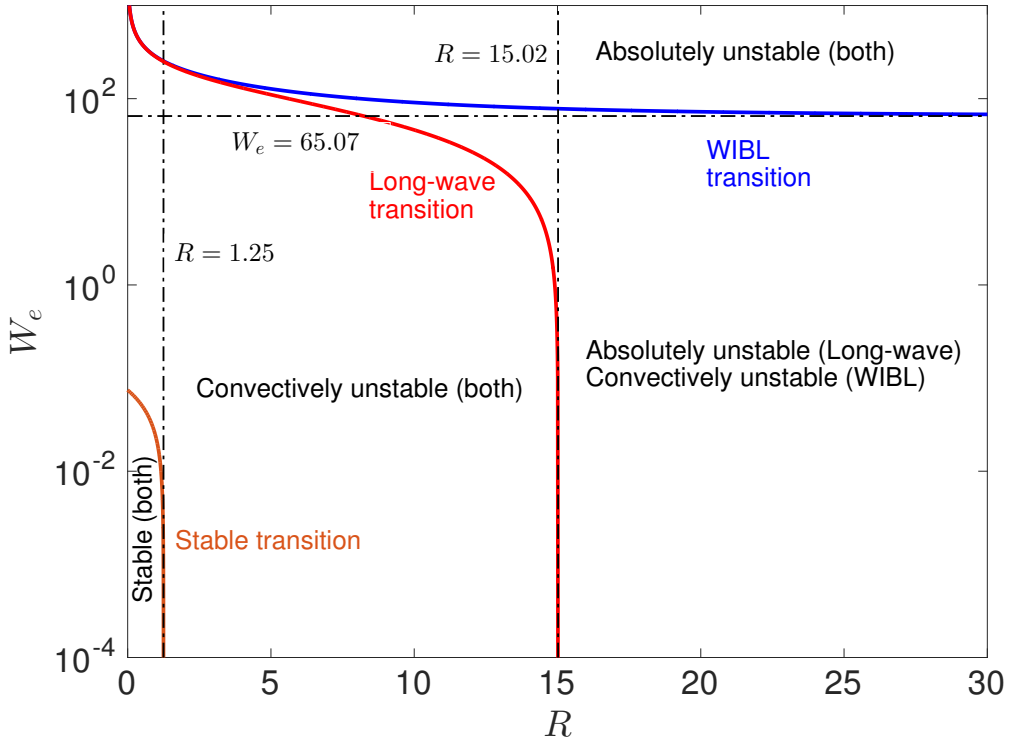

Figure 3.8: *Regions of stability, convective instability, and absolute instability for given values of W_e and R in the case of no topography for the long-wave and WIBL models. The plate inclination angle is $\pi/4$ and the corresponding critical Reynolds number for non-electrified flow is $R = 1.25$. The Kapitza number is given by $K = 3364.5$ corresponding to water at room temperature.*

If we wish to determine this transition phenomena analytically, we then have the following system of equations:

$$Re[\omega] = 0, \tag{3.56}$$

$$Re\left[\frac{d\omega}{dk}\right] = 0, \tag{3.57}$$

$$Im\left[\frac{d\omega}{dk}\right] = 0, \tag{3.58}$$

and three unknowns to solve for; k_R, k_I, where k_R is the real part of k and k_I is the imaginary part of k, such that both k_R and k_I are real, and in addition W_e or R or C (or, equivalently, the Kapitza number) or β (assuming that the remaining three out of these parameters are fixed).

In the WIBL case, we proceed very similarly to the long-wave case, albeit with a different form of the dispersion relation. Here, we use the form given in (3.32), such that we have

$$\omega = \hat{A} + i\hat{B} + \sqrt{\hat{C} + i\hat{D}}, \tag{3.59}$$

where $\hat{A}$, $\hat{B}$, $\hat{C}$ and $\hat{D}$ were defined previously. Figure 3.8 shows the regions of stability, convective instability and absolute instability for both the long-wave and WIBL models.

The curve corresponding to the stable transition is defined simply by the equation for the critical Reynolds number (3.51). The long-wave and WIBL curves for the transitions between absolute and convective instabilities are determined by numerically solving (3.56)-(3.58), where in the long-wave model we use (3.7) as a form for ω, and in the WIBL model we use (3.59) instead. We first solve the system of equations for $R = 0.0075$, and then increase R in increments of 0.0075 and solve at each R-step until we reach $R = 30$. For the long-wave model, it can be seen that absolute instability can be reached solely by increasing R in the case of $W_e = 0$, unlike for the WIBL model, for which we find that the flow is always either stable or convectively unstable for $W_e = 0$, depending on R. Further, we see that for $R > 15.02$, the long-wave model predicts absolute instability for all values of the electric Weber number. In contrast, we see for the WIBL model that absolute instability can only be reached in cases where $W_e \geq 65.07$, and below this value instabilities can only be convective regardless of the Reynolds number. We emphasise that previous work by Brevdo et al. [9] tells us that the absolute instability predicted by the long-wave model for $W_e = 0$ is not observed for the full equations and is nonphysical behaviour. This is then something of an assurance that the WIBL equations are providing a more accurate model, with absolute instabilities not occurring for non-electrified flow.

At this point it is convenient to make explicit the most unstable wavenumber for the long-wave and WIBL models, i.e. the wavenumber which satisfies

$$\frac{dRe[\omega]}{dk} = 0. \tag{3.60}$$

In the long-wave case this is the wavenumber obtained by solving (3.15), and we thus we are able to write this most unstable wavenumber as

$$k_u = \frac{3CW_e}{4} + \sqrt{\frac{9C^2{W_e}^2}{16} + \frac{4CR}{5}} - C\cot\beta. \tag{3.61}$$

This expression is reminiscent of the one derived by Tseluiko and Papageorgiou [105] albeit with minor rescaling and without the term relating to the inclination angle of the wall. In the WIBL case, we once again use our dispersion relation (3.59), and we write

$$\frac{dRe[\omega]}{dk} = \frac{1}{2}(\hat{C} + i\hat{D})^{-1/2}(\hat{E} + i\hat{F}), \tag{3.62}$$

where we have

$$\begin{aligned}\hat{C} = &(-592\,C^2R^2k^2 + 11760\,C^2R\,W_ek^3 \\ &- 5880\,CR\,k^4 - 11760\,C^2R\,k^2\cot\beta + 11025\,C^2)/7056\,C^2R^2,\end{aligned} \tag{3.63}$$

$$\hat{D} = -\frac{125k}{42R}, \tag{3.64}$$

$$\hat{E} = \frac{-1184\,CRk + 35280\,C\,W_ek^2 - 23520\;k^3 - 23520\,Ck\cot\beta}{7056\,CR}, \tag{3.65}$$

$$\hat{F} = -\frac{125}{42R}. \tag{3.66}$$

Solving this equation numerically gives k_u for the WIBL model. We use the long-wave model as an initial guess for when $R = 0.04$, and then use the solution of the WIBL model at the previous value of R to compute the next solution as we increase R in 0.04 increments. This wavenumber is used for the perturbations which are added onto steady-state solutions such that their time evolution may be noted, and the classification of stable, convectively unstable or absolutely unstable flow may be determined. Figure 3.9 shows $Re(k_u)$ as a function of R for both models at low Reynolds numbers for $W_e = 0$ (solid lines), $W_e = 100$ (dashed lines) and $W_e = 200$ (dotted lines). The red lines correspond to the long-wave model and the blue lines correspond to the WIBL model. It can be seen that there is excellent agreement between the two models within this range of Reynolds numbers, which corresponds to the stable and convectively unstable regimes. The most unstable wavenumbers for the stable regimes are not shown in the figure, since when we are in the stable regime the most unstable wavenumber is complex with nonzero real and imaginary parts, however, we may infer the Reynolds numbers corresponding to the stable regime for a given electric Weber number from the solid circles which denote the end-points of the convectively unstable case. In this way, we may again see the destabilising effect of the normal electric field – lowering the critical Reynolds number corresponding to the onset of instability.

Figure 3.10 shows $Re(k_u)$ as a function of R for a larger range of Reynolds numbers, where it can be seen that generally speaking the two models diverge increasingly with increasing Reynolds number. The models appear to diverge at lower Reynolds numbers when the electric Weber number is increased, although we also note that for $W_e = 200$ the two models appear to diverge to a lesser degree than is observed for $W_e = 100$. We

note that there is no obvious transition between the convectively unstable and absolutely unstable regimes, which we would expect to occur at or prior to $R = 15.02$ in the long-wave model for $W_e = 0$.

As we only wish to permit real values of the wavenumber for time-dependent simulations when adding a perturbation to steady-states, we are only able to use the most unstable wavenumber in the convectively and absolutely unstable regions, and in regions of stability we instead use a more generic form of perturbation, the details of which are discussed in the next section.

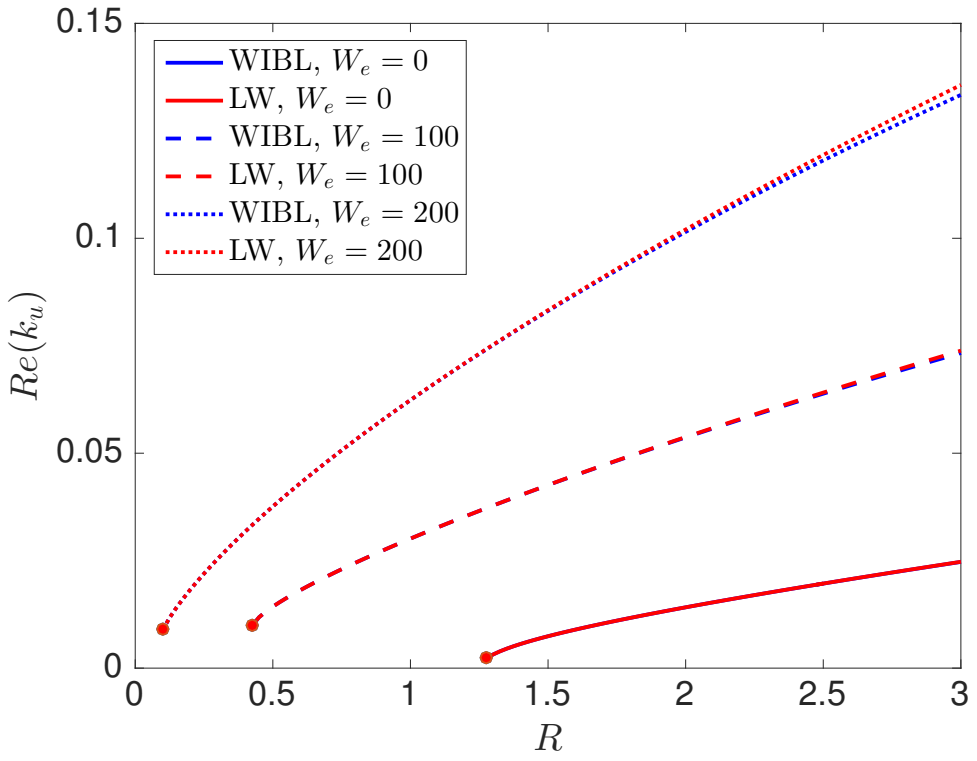

Figure 3.9: *$Re(k_u)$ as a function of R for both the long-wave (red) and WIBL (blue) models at various electric Weber numbers.*

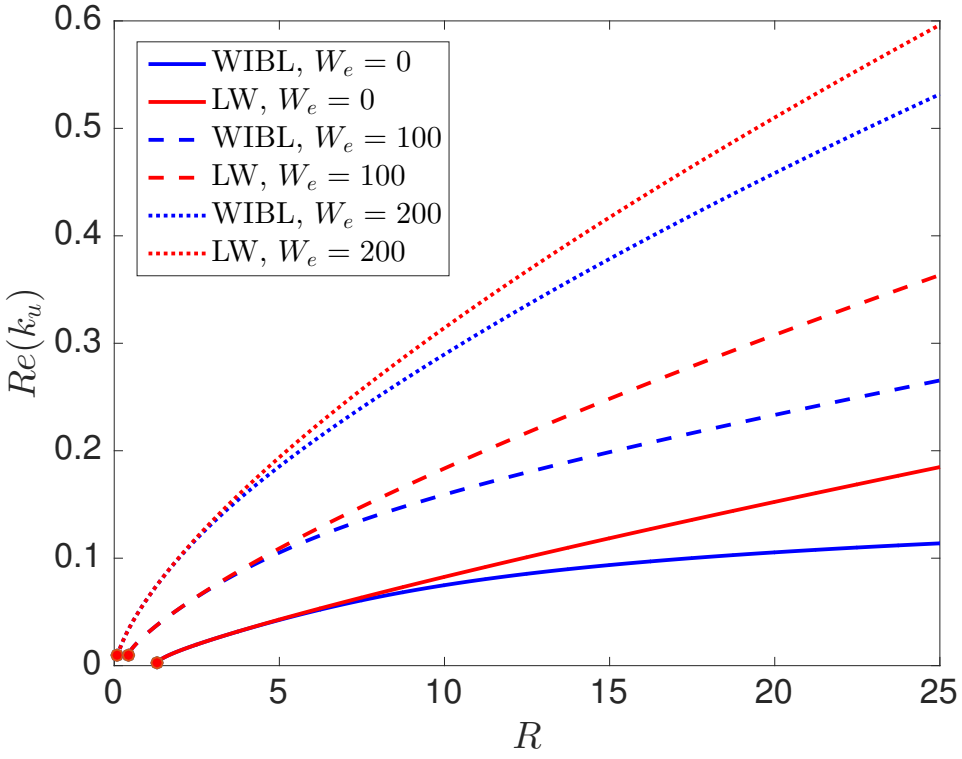

Figure 3.10: *Reproduction of Figure3.9 showing a larger range of Reynolds numbers. $Re(k_u)$ as a function of R for both the long-wave and WIBL models at various electric Weber numbers.*

3.4 Time-dependent simulations

Here we seek to show that the regions depicted in Figure 3.8 are consistent with time-dependent simulations, and we also wish to investigate the simultaneous effect of electric field strength and topography amplitude on steady solutions to both models. In these time-dependent simulations, we choose either to have a Nusselt flat film solution for a flat wall in the case of corroborating the aforementioned regions, or we may directly import our steady-state solutions from Auto-07p in cases where we have nonzero topography, the computation of which is discussed in Chapter 4. Steady-state solutions can also be produced in cases with topography by allowing flat film solutions to converge to a steady-state, although this clearly works only in regions of stability.

We begin by calculating the most unstable wavenumber for the set of parameters of a given run in the long-wave case using our analytic expression (3.61). If we are solving the long-wave equation, then we simply use this value, whereas if we are solving our WIBL system instead we then use this long-wave value as an initial guess for a solution to our equation (3.62) for the most unstable wavenumber in the WIBL case, which we solve for numerically. We then import previously-computed steady-states from Auto-07p and extract the arrays corresponding to the film thickness, the flow rate, and the topography profile. We subsequently take fast Fourier transforms (FFTs) of these quantities using FFTW [28] and fix the film thickness by setting the first element of our Fourier transform of $h(x,t)$ to be equal to the length of the array, such that on average the film thickness within the fluid is set to 1.

The inverse fast Fourier transforms (IFFTs) are then taken of our flow parameters, and we record these quantities prior to adding any kind of perturbation to our steady-state. For the case without a perturbation, we allow the system to evolve using Fourier representation (for simplified dealing with the nonlocal Hilbert transform term) by using a variable-step, variable-order multistep numerical solver implemented as an 'ode15s' MATLAB [36] algorithm.

The system is permitted to evolve for 5 time units, at which point we record the film thickness profile and the flow rate. If the difference between the norm of the film thickness for the initial solution and the final solution is below some prescribed tolerance (10^{-6}) then we are satisfied that the imported solution is indeed a steady-state. In this case, we then add a perturbation centred about the midpoint of our domain to our final steady-state, where perturbation uses the most unstable wavenumber k_u and is of the

form

$$\eta = a\cos(k_u(x - L_c))e^{-b(x-L_c)^2}, \tag{3.67}$$

where a is the amplitude of the perturbation (typically chosen to be 0.0005) and b is chosen so that the perturbation is sufficiently localised. In cases where k_u has nonzero imaginary part, we use $k_u = \pi/L_c$ instead. We remind the reader that L is the half-period of the topography, and the computational domain is taken to be $2L_c = 4L$, where we solve for $2L$-periodic solutions and $4L$-periodic subharmonic solutions. We hence have L_c as the half-period of the computational domain, such that the perturbation originates in the centre of our steady-state. We then allow the perturbed system to evolve, and calculate the difference in film thickness between the time evolution of the perturbed system, and the final film thickness found after the time evolution of the unperturbed system. This allows us to more clearly see the behaviour of the perturbation in time, as we are subsequently able to ignore the well-known phenomena of the surface profile following the profile of the topography, albeit with a phase shift, and large-amplitude topographical features no longer overshadow the smaller-scale perturbation evolutions.

3.4.1 Flat wall

As mentioned previously, we wish use these time-dependent simulations to verify the regions of absolute and convective instability shown in Figure 3.8. To begin, we examine the case of $R = 25$ and $W_e = 0$, and these results are shown in Figures 3.11–3.15. Here the computational domain $2L_c$ is adapted such that it is always equal to 5 times the maximally unstable wavelength, this is done to ensure that the domain is always sufficiently large to allow for the full evolution of unstable behaviour.

In Figure 3.11 we see the time evolution of a perturbation to the Nusselt flat film solution in the long-wave (left) and WIBL (right) models. From Figure 3.8, we expect a small perturbation to the Nusselt flat film solution for $R = 25$ and $W_e = 0$ to result in a convective instability for the WIBL model, and an absolute instability for the long-wave model. In the long-wave case, we see that the perturbation appears to travel upstream as well as downstream and the amplitude of the perturbation increases monotonically in time, i.e. we observe the perturbation undergoing unbounded growth at all points of reference, indicative of an absolute instability.

In the WIBL case we see that the perturbation is convected downstream only, despite being allowed to evolve for a longer time, and we note the difference in magnitude of the perturbation at the final time unit between the long-wave and WIBL models (a range of 0.0252 to -0.0206 in the long-wave case in comparison to the $10.7431\text{x}10^{-4}$ to $-5.88\text{x}10^{-4}$ range in the WIBL case), indicative of a convective instability in the WIBL case. In Figure 3.12 we see the time evolution of the absolute value of the perturbation at the origin for the same parameter values. In the long-wave case, we note that the absolute value of the perturbation at the original location was found to increase in time, whereas in the WIBL case we see that the perturbation at the origin location was found to decay, as the perturbation is being convected solely downstream, providing further evidence that the long-wave model displays absolutely unstable behaviour and the WIBL model displays convectively unstable behaviour.

In Figure 3.13 we see the maximum value of η at each time unit for both models. In the long-wave model the maximum was found to increase monotonically, whereas in the WIBL case we first observed a decrease in the maximum for approximately 15 time units.

Figure 3.14 shows the initial, intermediate and final surface profiles for both models. In the long-wave case we are able to clearly see the small perturbation in the midpoint of the domain in the initial solution, and then see that in the final solution the perturbation has travelled to the left of this midpoint, i.e. upstream. In the WIBL case however, we note that despite the amplitude of the perturbation growing in time, it exclusively travels to the right. In Figure 3.15 we see the contour plots of the perturbation as time increases. With the aid of the white line indicating the exact midpoint of the domain and the origin of the perturbation, it is once again clear that in the long-wave case the perturbation travels in both directions simultaneously and also increases in magnitude from the point of reference of the origin, indicating absolute instability, whereas in the WIBL model the perturbation is clearly convected downstream.

We now examine cases where the transition between convective instability and absolute instability occurs solely due to variations in the electric Weber number. From Figure 3.8 we predict that for $R = 10$, in the long-wave model we expect $W_e = 40$ to correspond to a convectively unstable solution, and for $W_e = 80, 120$ to correspond to absolutely

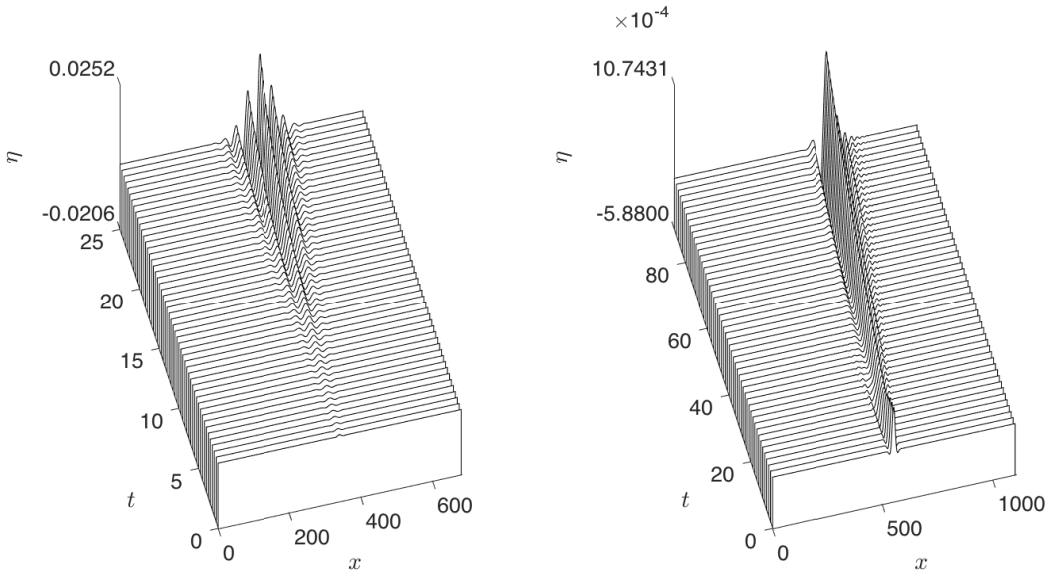

Figure 3.11: *Time evolution of the perturbation η originating at midpoint $x = 2L$ with $R = 25$, $K = 3364.5$ and $W_e = 0$ in the long-wave case (left) and the WIBL case (right).*

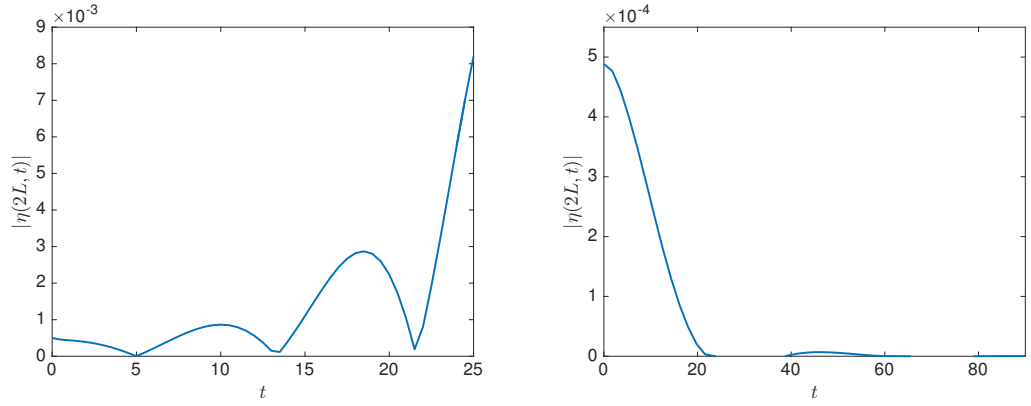

Figure 3.12: *Time evolution of the absolute value of the perturbation at the midpoint $x = 2L$ for $R = 25$, $K = 3364.5$ and $W_e = 0$ in the long-wave case (left) and the WIBL case (right).*

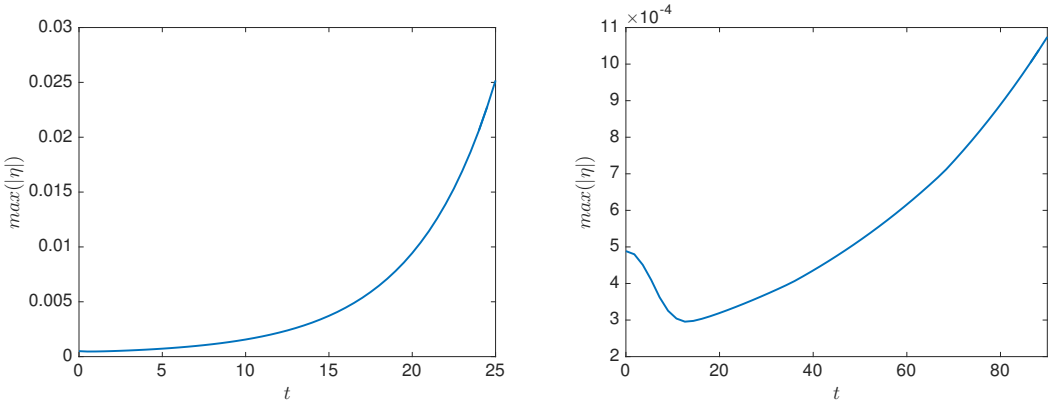

Figure 3.13: *Time evolution of the maximum of the absolute value of the perturbation for $R = 25$, $K = 3364.5$ and $W_e = 0$ in the long-wave case (left) and the WIBL case (right).*

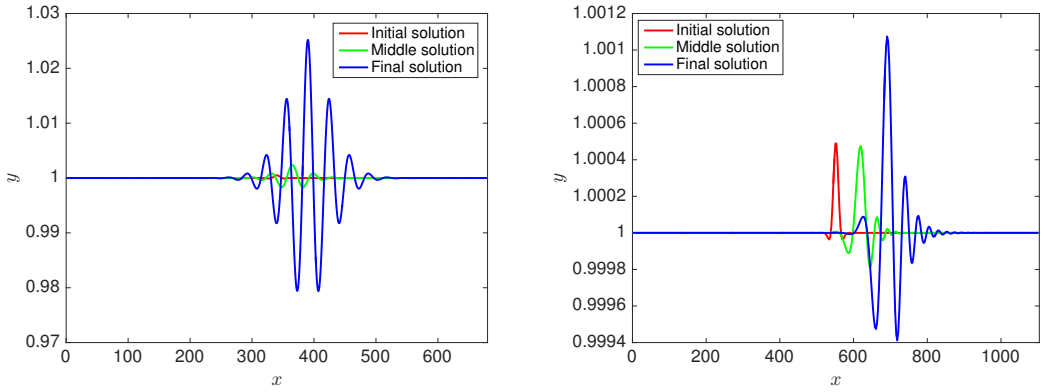

Figure 3.14: *The initial, intermediate and final surface profiles of the film for* $R = 25$, $K = 3364.5$ *and* $W_e = 0$ *in the long-wave case (left) and the WIBL case (right).*

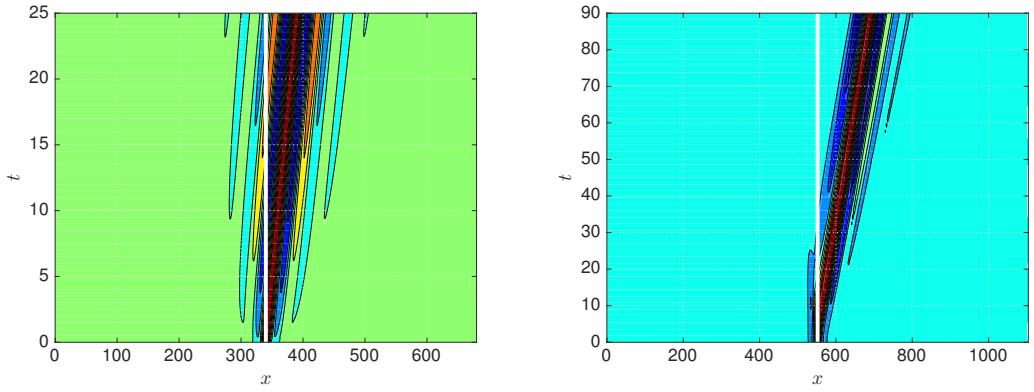

Figure 3.15: *Contour plot showing the propagation of the perturbation, with a solid white line showing the origin of the perturbation, for* $R = 25$, $K = 3364.5$ *and* $W_e = 0$ *in the long-wave case (left) and the WIBL case (right).*

unstable solutions. Contrariwise, for the WIBL model, we expect that for $R = 10$ and $W_e = 40, 80$, we should have a convectively unstable solution, and for $W_e = 120$ we should have an absolutely unstable solution. In Figure 3.16 we observe the time evolution of the perturbation for $R = 10$ and $W_e = 40$. In both the long-wave and WIBL models it can be seen that the perturbation travels downstream and grows in magnitude in time, indicative of a convective instability. Figure 3.17 corroborates this, in which we observe both norms of the perturbation at the origin decaying in time. In the long-wave case, the norm was found to decay in an oscillatory fashion, whereas in the WIBL case the norm was found to decay rapidly and then remain near-constant.

Figure 3.17 alone is not sufficient for the classification of a convective instability however, as this decay of the perturbation at the origin may also be indicative of a stable steady-state solution, and Figure 3.18 is necessary to rule out this possibility. Indeed, we observe growth in the maximum of the absolute value of the perturbation as time increases for both the long-wave and WIBL models. In Figure 3.19 we see the initial,

intermediate and final surface profiles, and for both models we see the same qualitative behaviour – a travelling wave is formed and is convected downstream to the right. It can also be observed that the perturbation in the WIBL model grows much slower; despite being allowed to evolve for a slightly greater time than was allowed for the long-wave case, the amplitude of the wave in the WIBL model is approximately an order of magnitude smaller than the wave in the long-wave case. Figure 3.20 and Figure 3.21 show the contour plot and normalised contour plot of the perturbation respectively as time increases, and we are again reassured of the convective nature of both solutions, as it is observed that both perturbations grow in magnitude but remain to the right of the white line which indicates the x position of the original perturbation.

In Figure 3.22 we observe the time evolution of the perturbation for $R = 10$ and $W_e = 80$. In the WIBL model, we observe the same qualitative behaviour as seen for the $W_e = 40$ case in Figure 3.16, indicative of a convective instability. In the long-wave case however, we observe qualitatively different behaviour in comparison to the $W_e = 40$ case – it appears that the perturbation begins to travel upstream as well as downstream, which is an indication of absolute instability. In Figure 3.23 we find further evidence that the long-wave model predicts absolutely unstable behaviour for our parameter values – the absolute value of the perturbation at the origin increases in time in an oscillatory way, corresponding to the crests and troughs of the perturbation passing through the midpoint as the perturbation spreads over the domain in time. In the WIBL case, we instead find that the norm decays in a rapid but oscillatory fashion. Despite the aforementioned phenomena that the absolute nature of the instability predicted by the long-wave model is nonphysical for non-electrified flow (see Brevdo et al. [9]), the absolute behaviour observed for electrified flow has not been shown to be nonphysical by comparisons with solving the full equations or DNS methods, at least to this author's knowledge. Indeed, the nonlocal nature of the normal electric field seems a reasonable justification for assuming that the absolute instabilities predicted by increasing the electric Weber number are physical, and not simply failings of the models.

In Figure 3.24 we see that both the long-wave and WIBL models show the maximum of the absolute value of the perturbation monotonically increasing in time, consistent with unstable behaviour. In the $R = 25, W_e = 0$ case as well as the $R = 10, W_e = 40$ case for the WIBL model, we previously observed a decrease in the maximum of the absolute value of the perturbation for the initial time units, prior to the subsequent growth in time, although this behaviour is not noted here. This behaviour could perhaps be explained

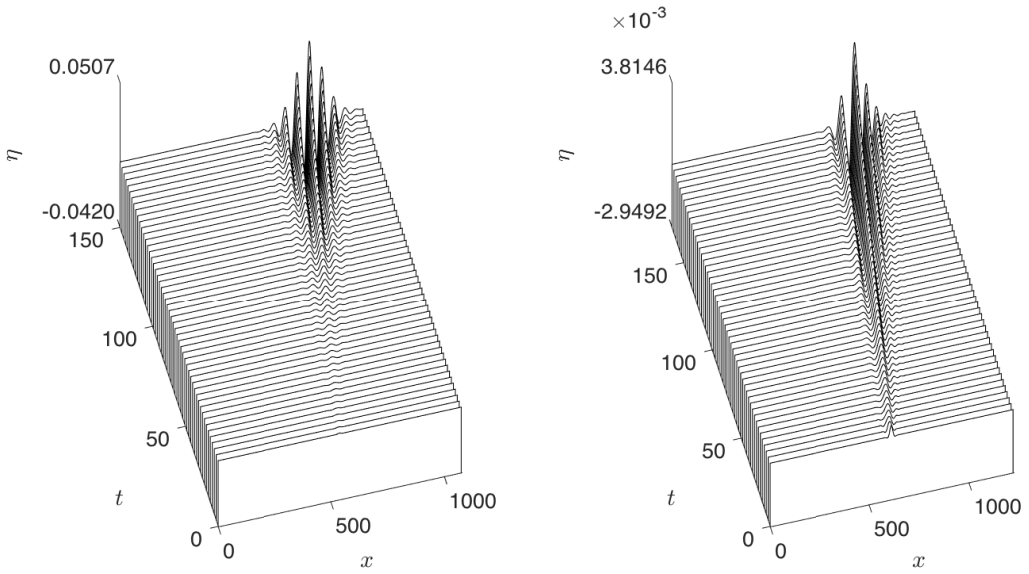

Figure 3.16: *Time evolution of the perturbation η originating at midpoint $x = 2L$ with $R = 10$, $K = 3364.5$ and $W_e = 40$ in the long-wave case (left) and the WIBL case (right).*

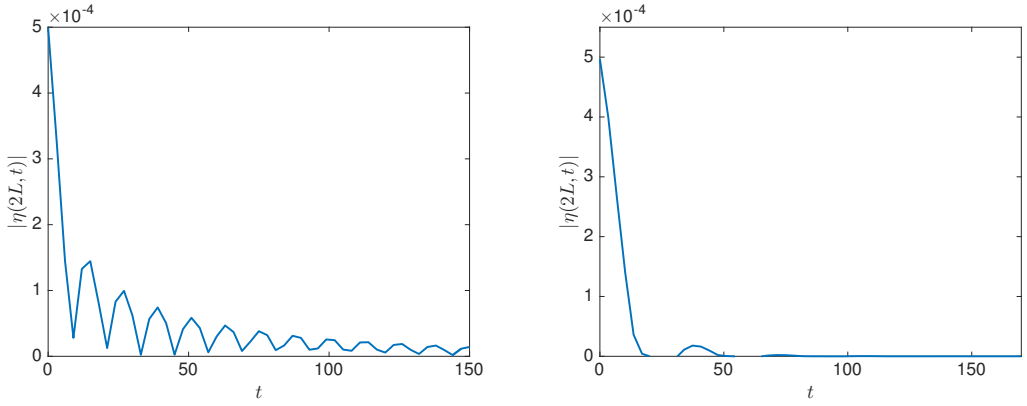

Figure 3.17: *Time evolution of the absolute value of the perturbation at the midpoint $x = 2L$ for $R = 10$, $K = 3364.5$ and $W_e = 40$ in the long-wave case (left) and the WIBL case (right).*

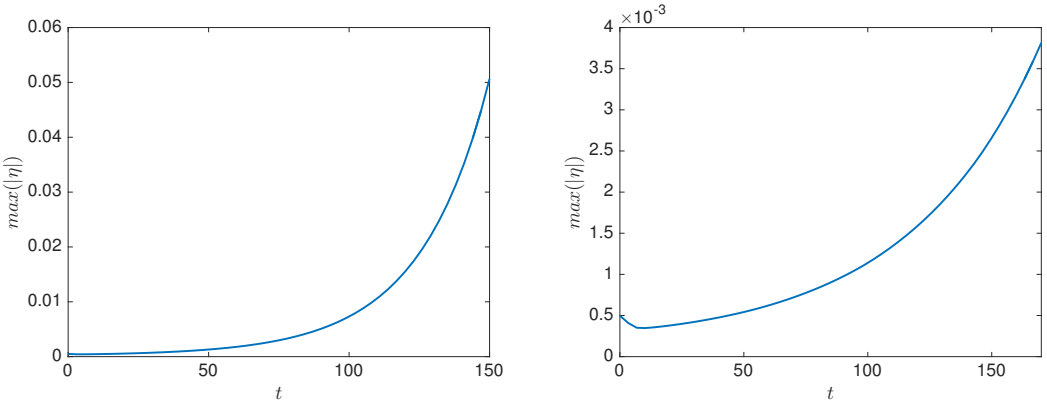

Figure 3.18: *Time evolution of the maximum of the absolute value of the perturbation for $R = 10$, $K = 3364.5$ and $W_e = 40$ in the long-wave case (left) and the WIBL case (right).*

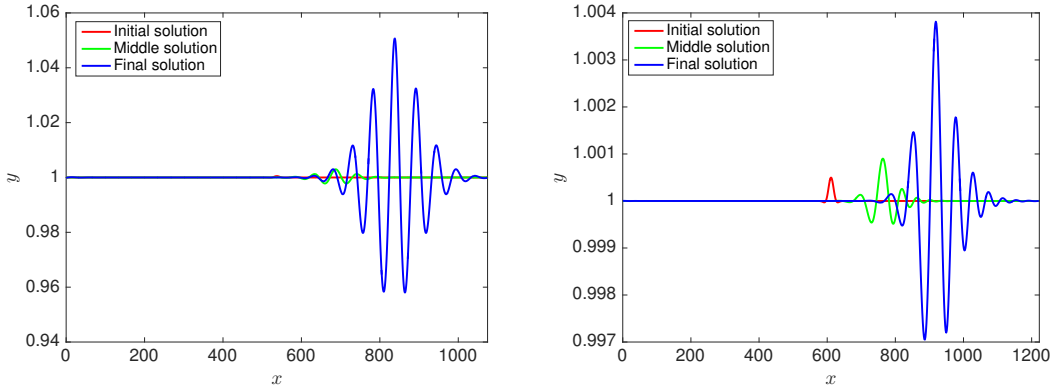

Figure 3.19: *The initial, intermediate and final surface profiles of the film for* $R = 10$, $K = 3364.5$ *and* $W_e = 40$ *in the long-wave case (left) and the WIBL case (right).*

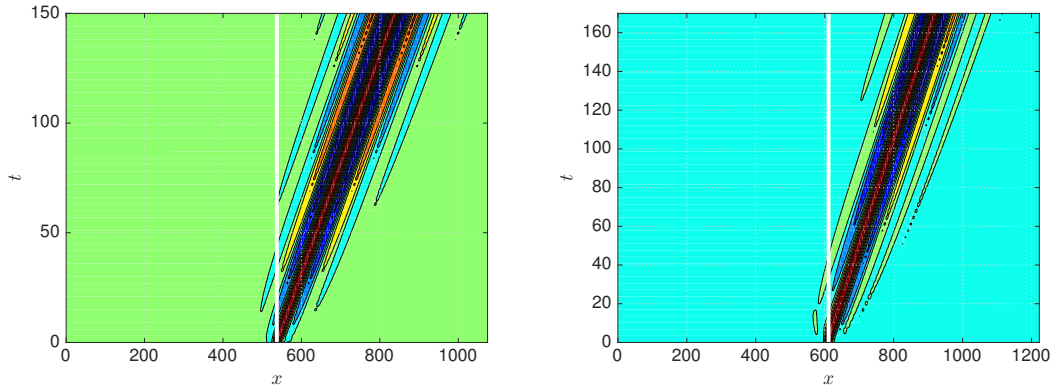

Figure 3.20: *Contour plot showing the propagation of the perturbation, with a solid white line showing the origin of the perturbation, for* $R = 10$, $K = 3364.5$ *and* $W_e = 40$ *in the long-wave case (left) and the WIBL case (right).*

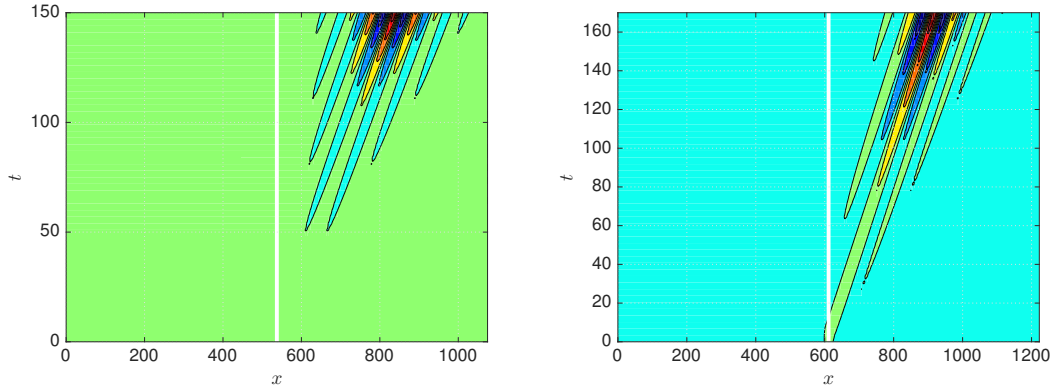

Figure 3.21: *Normalised contour plot showing the propagation of the perturbation, with a solid white line showing the origin of the perturbation, for* $R = 10$, $K = 3364.5$ *and* $W_e = 40$ *in the long-wave case (left) and the WIBL case (right).*

by the knowledge that the WIBL model is predicted to be approaching the transition to absolute instability due to the increasing electric Weber number, and as such displays greater growth in time.

Figure 3.25 shows the initial, intermediate and final surface profiles for both models. For the WIBL model we observe a travelling wave being convected downstream. The initial perturbation in red is found at the exact middle of the domain, and as time increases the perturbation increases in amplitude but moves exclusively to the right. Contrariwise in the long-wave model we instead see that our final solution has partially travelled to the left of the original location of the perturbation, which is indicative of an absolute instability. This determination is aided by Figures 3.26 and 3.27 which correspond to the contour plot of the perturbation and the normalised version of such a contour plot, respectively. As the white line shows the starting location of the perturbation, it is clear that in the long-wave model we see the perturbation travelling to the left and right of the origin, whereas in the WIBL model we see the perturbation travelling to the right only. Figure 3.28 shows the time evolution of the perturbation for the long-wave and WIBL models in the case of $R = 10$ and $W_e = 120$. For both models behaviour indicative of an absolute instability is exhibited; in the long-wave case the perturbation clearly travels upstream in the final time units, whereas in the WIBL model the perturbation appears to travel upstream in the final time units, but further evidence is required to definitively state this. Figure 3.29 shows the absolute value of the perturbation at its origin - in both models the norm is initially somewhat constant, then rapidly increases, indicative of an absolute instability.

In Figure 3.30 we see the maximum of the absolute value of the perturbation at each time unit. For both long-wave and WIBL models we observe a monotonic increase in time, although in the WIBL model we notice a slight decrease in the growth rate of the maximum of the absolute value of the perturbation for sufficiently large times (i.e. time units greater than 100) which may appear to suggest that the solution is converging to a steady-state. However, allowing the system to evolve for longer times simply results in a saturation of the surface profile with travelling wave oscillations, and we eventually obtain a fully nonlinear solution which rapidly breaks down in finite time. Figure 3.31 shows the surface profiles for the long-wave and WIBL models for $R = 10$ and $W_e = 120$. In both cases we note that for the final solution, the perturbation has

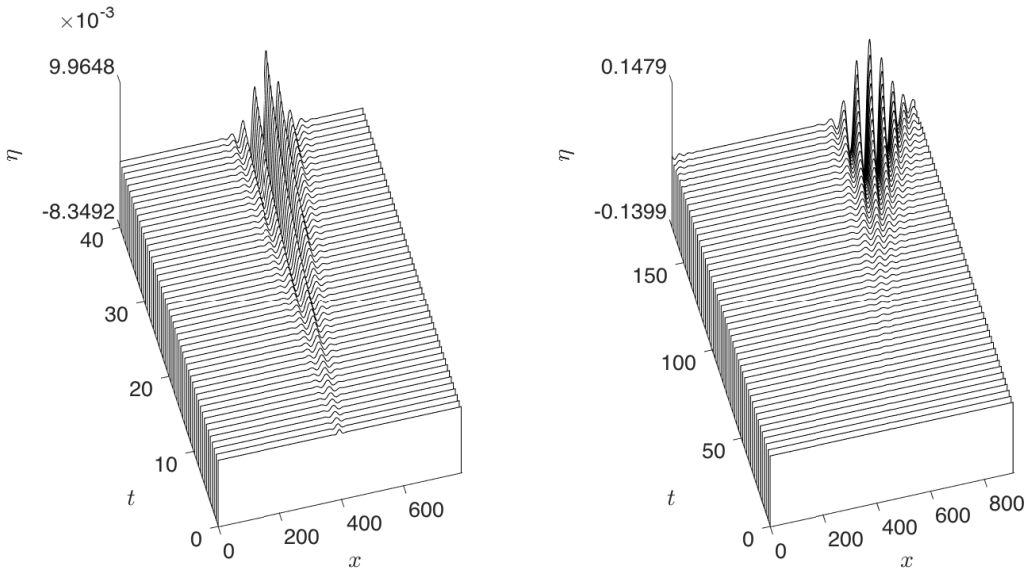

Figure 3.22: *Time evolution of the perturbation η originating at midpoint $x = 2L$ with $R = 10$, $K = 3364.5$ and $W_e = 80$ in the long-wave case (left) and the WIBL case (right).*

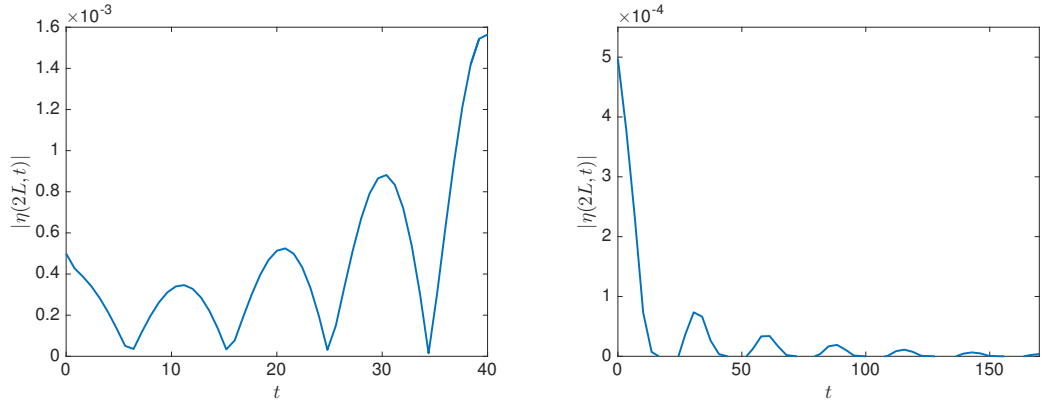

Figure 3.23: *Time evolution of the absolute value of the perturbation at the midpoint $x = 2L$ for $R = 10$, $K = 3364.5$ and $W_e = 80$ in the long-wave case (left) and the WIBL case (right).*

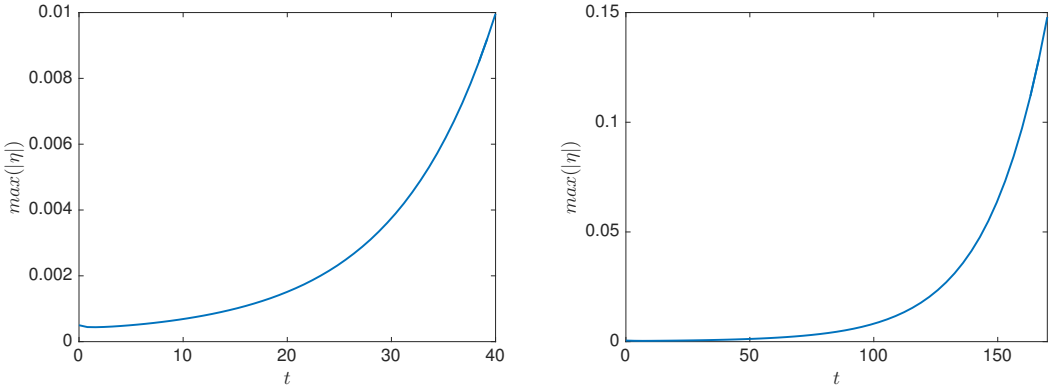

Figure 3.24: *Time evolution of the maximum of the absolute value of the perturbation for $R = 10$, $K = 3364.5$ and $W_e = 80$ in the long-wave case (left) and the WIBL case (right).*

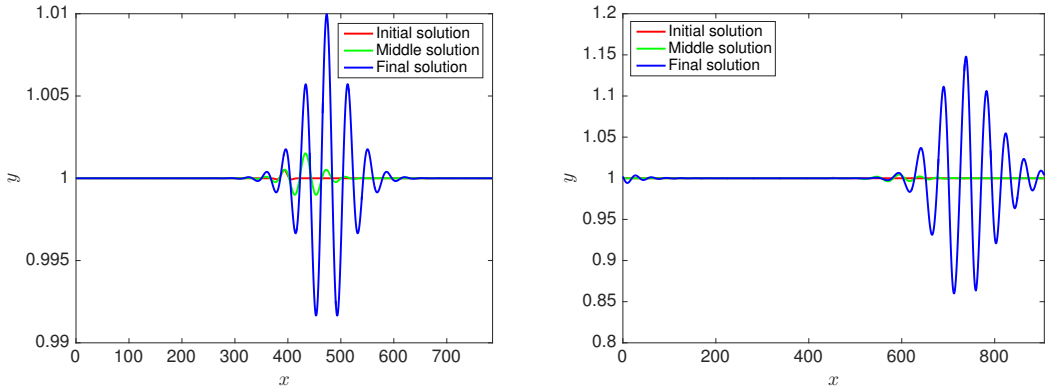

Figure 3.25: *The initial, intermediate and final surface profiles of the film for* $R = 10$, $K = 3364.5$ *and* $W_e = 80$ *in the long-wave case (left) and the WIBL case (right).*

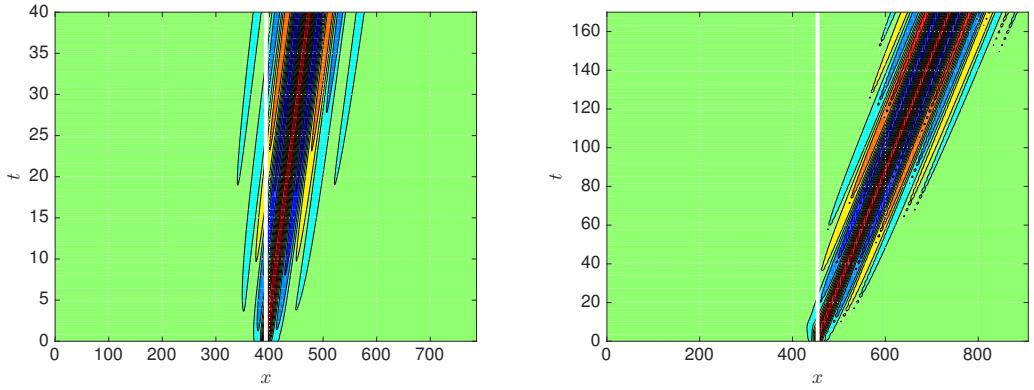

Figure 3.26: *Contour plot showing the propagation of the perturbation, with a solid white line showing the origin of the perturbation, for* $R = 10$, $K = 3364.5$ *and* $W_e = 80$ *in the long-wave case (left) and the WIBL case (right).*

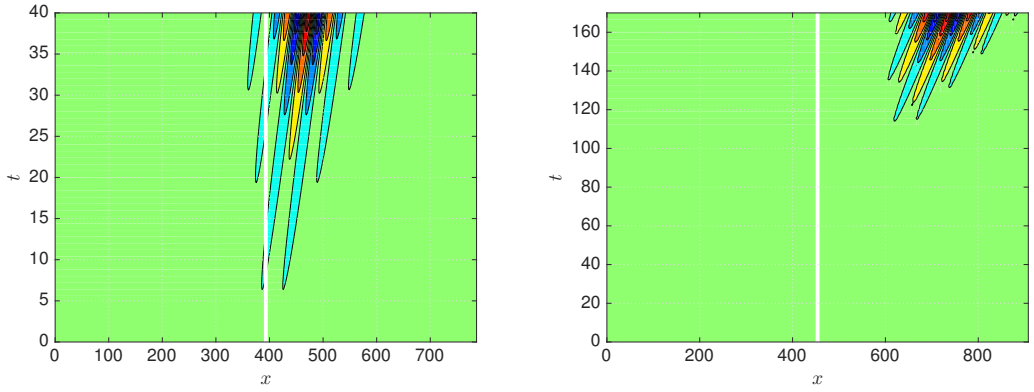

Figure 3.27: *Normalised contour plot showing the propagation of the perturbation, with a solid white line showing the origin of the perturbation, for* $R = 10$, $K = 3364.5$ *and* $W_e = 80$ *in the long-wave case (left) and the WIBL case (right).*

travelled to the left of the origin and has hence propagated upstream. Although the long-wave model more clearly shows the upstream propagation of the perturbation, with aid from Figures 3.32 and 3.33, we can see that both models distinctly show the perturbation travelling to the left of the white line, which corresponds to the location of the origin of the perturbation.

Overall then we find excellent agreement between the linear stability analysis predictions for a flat wall found in Figure 3.8 and the time-dependent simulations for a flat wall included here. The linear stability analysis predicted that for $R = 10$, the long-wave model would be convectively unstable for $W_e = 40$ and absolutely unstable for $W_e = 80$ and $W_e = 120$, which is consistent with our findings. It also predicted that for the WIBL model with $R = 10$, $W_e = 40$ and $W_e = 80$ would correspond to convectively unstable solutions, and $W_e = 120$ would correspond to an absolutely unstable solution, again consistent with our simulations. We further recover the result that the steady-state solutions to the long-wave model can transition from the convectively unstable regime to the absolutely unstable regime purely by increasing the Reynolds number – in the case of $R = 25$ and $W_e = 0$ we found the long-wave model to display absolutely unstable behaviour, in contrast with the convectively unstable behaviour observed for the WIBL model with the same parameters.

3.4.2 Sinusoidal wall

In this section we include the effects of sinusoidal topography in addition to the normal electric field. For the purposes of better comparison with the literature, here we prescribe numerical values for the computational domain instead of allowing it to adapt based upon the maximally unstable wavelength. As discussed by Tseluiko, Blyth and Papageorgiou [98] in addition to D'Alessio, Pascal and Jasmine [18], it is well known that sinusoidal topography can be stabilising or destabilising depending on the amplitude and period of the topography. Indeed, we know from the aforementioned work by Tseluiko et al. that for $L_0 = 150$ and $A_0 = 17$, the long-wave model predicts that the topography is stabilising, whereas for $A_0 = 24$, the topography is greatly destabilising.

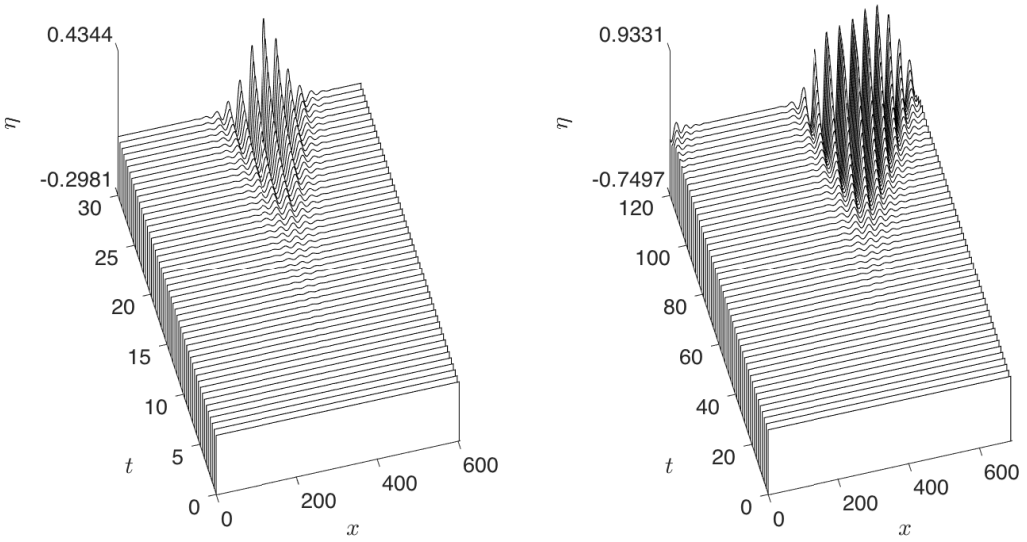

Figure 3.28: *Time evolution of the perturbation η originating at midpoint $x = 2L$ with $R = 10$, $K = 3364.5$ and $W_e = 120$ in the long-wave case (left) and the WIBL case (right).*

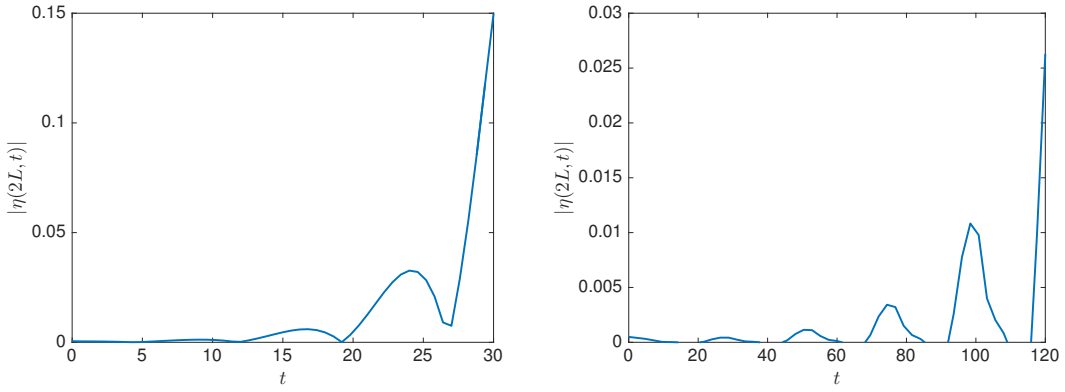

Figure 3.29: *Time evolution of the absolute value of the perturbation at the midpoint $x = 2L$ for $R = 10$, $K = 3364.5$ and $W_e = 120$ in the long-wave case (left) and the WIBL case (right).*

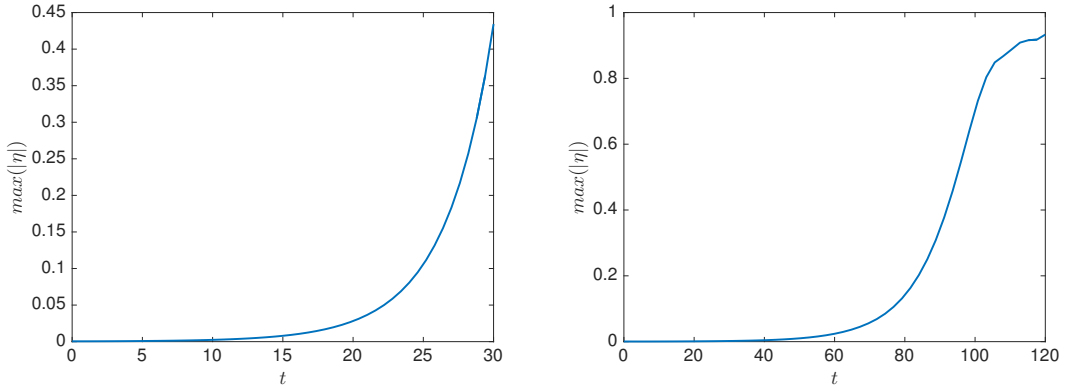

Figure 3.30: *Time evolution of the maximum of the absolute value of the perturbation for $R = 10$, $K = 3364.5$ and $W_e = 120$ in the long-wave case (left) and the WIBL case (right).*

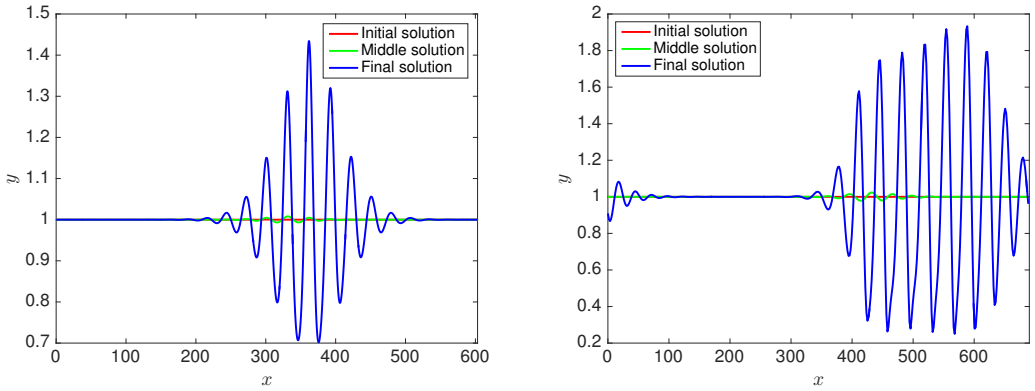

Figure 3.31: *The initial, intermediate and final surface profiles of the film for* $R = 10$, $K = 3364.5$ *and* $W_e = 120$ *in the long-wave case (left) and the WIBL case (right).*

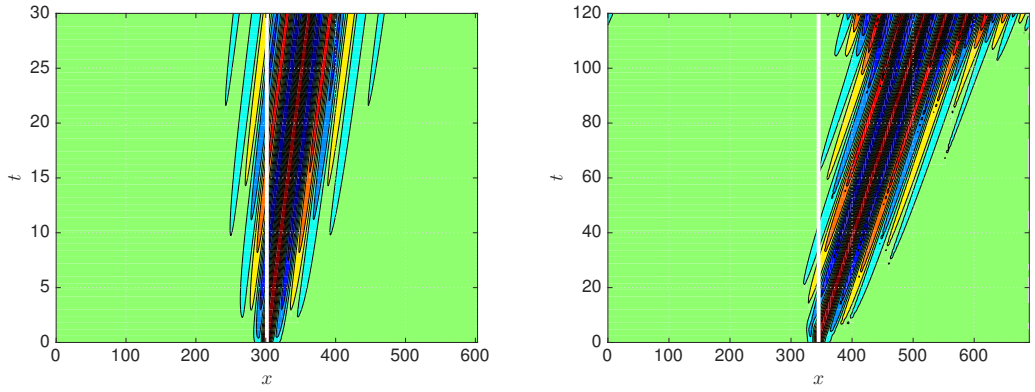

Figure 3.32: *Contour plot showing the propagation of the perturbation, with a solid white line showing the origin of the perturbation, for* $R = 10$, $K = 3364.5$ *and* $W_e = 120$ *in the long-wave case (left) and the WIBL case (right).*

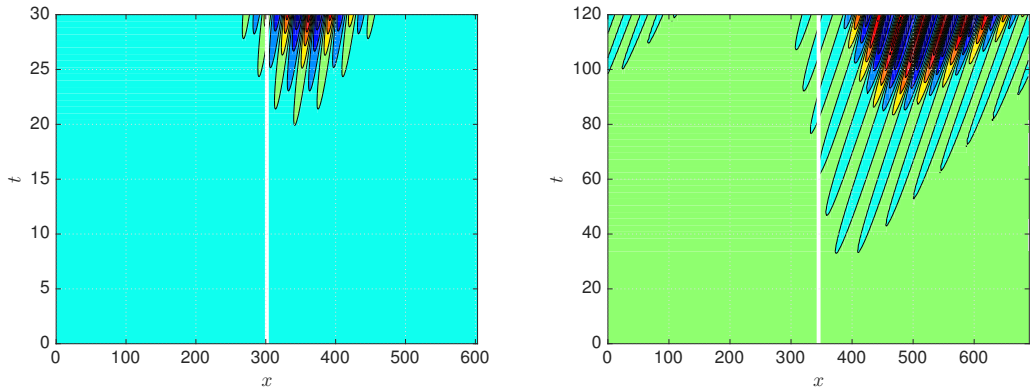

Figure 3.33: *Normalised contour plot showing the propagation of the perturbation, with a solid white line showing the origin of the perturbation, for* $R = 10$, $K = 3364.5$ *and* $W_e = 120$ *in the long-wave case (left) and the WIBL case (right).*

Here L_0 and A_0 are defined by the following rescaling

$$A_0 = A\left(\frac{\sin\beta}{R}\right)^{1/3} = \frac{\tilde{A}\rho^{2/3}g^{1/3}}{2^{1/3}\mu^{2/3}}, \tag{3.68}$$

$$L_0 = L\left(\frac{\sin\beta}{R}\right)^{1/3} = \frac{\tilde{L}\rho^{2/3}g^{1/3}}{2^{1/3}\mu^{2/3}}, \tag{3.69}$$

with $\tilde{A}$ and $\tilde{L}$ denoting the actual dimensional wall amplitude and half-wavelength, respectively, so that the dimensionless quantities A_0 and L_0 are then fully determined by the liquid properties and are independent of the wall inclination angle and the liquid flow rate.

We seek to investigate the behaviour of the WIBL model for these parameter values and compare the observed results to the long-wave equivalent. We also intend to investigate the effect of the normal electric field for both models in these scenarios. In this section we shall take the Reynolds number to be $R = 1.25$, corresponding to the critical Reynolds number for non-electrified flow over a flat wall inclined at angle $\theta = \pi/4$.

In Figure 3.34 we see the evolution of the perturbation for the two models in the case of $W_e = 0$ and $A_0 = 17$. In both cases it can be seen that the perturbation decays in time and is convected downstream, indicative of a stable solution. The stable classification of both models is corroborated by Figure 3.35 and Figure 3.36. In Figure 3.35 we observe that the absolute value of the perturbation at the origin of the perturbation clearly decays for both models, although we note that there is a small increase in the norm at approximately $t = 300$. However, this is simply due to the perturbation travelling to the right downstream, and then reappearing at the left-most side of the domain upstream, and the slight increase in the norm which is observed is simply the perturbation travelling past the origin point a second time. Figure 3.36 shows the maximum value of the absolute value of the perturbation at each time unit - for both models the maximum was found to decay in time, and this decay exhibits periodic behaviour, with similar periodicity being observed for both models. We are able to conclude that both models are stable for these parameter values, consistent with the literature [98].

In Figure 3.37 we see the time evolution of the perturbation in the case of $A_0 = 24$ and $W_e = 0$. In the long-wave case we see that the perturbation grows rapidly upstream, and the film thickness quickly becomes zero if the system is allowed to evolve for longer times. In the WIBL case however, we instead see that the perturbation decays and is

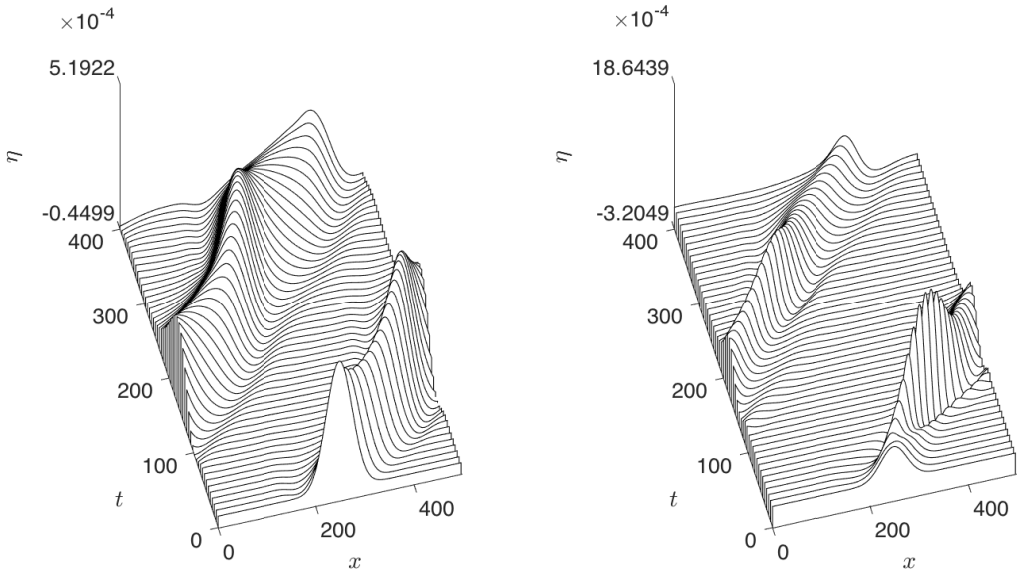

Figure 3.34: *Time evolution of the perturbation η originating at midpoint $x = 2L$ with $R = 1.25$, $K = 3364.5$, $W_e = 0$, $A_0 = 17$ and $L_0 = 150$ for a sinusoidal wall in the long-wave case (left) and the WIBL case (right).*

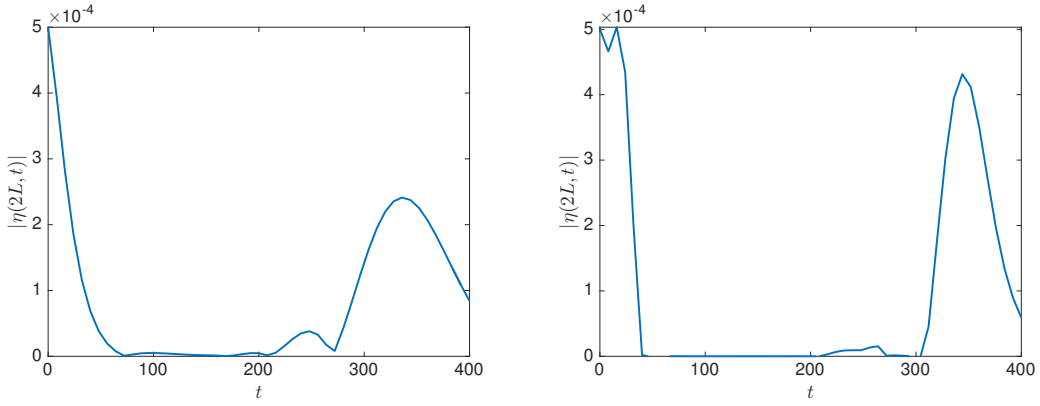

Figure 3.35: *Time evolution of the absolute value of the perturbation at the midpoint $x = 2L$ for $R = 1.25$, $K = 3364.5$, $W_e = 0$, $A_0 = 17$ and $L_0 = 150$ for a sinusoidal wall in the long-wave case (left) and the WIBL case (right).*

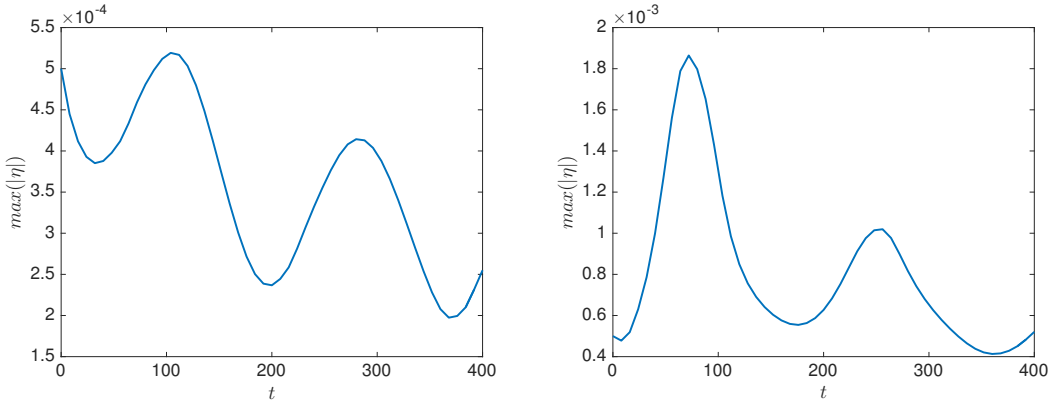

Figure 3.36: *Time evolution of the maximum of the absolute value of the perturbation for $R = 1.25$, $K = 3364.5$, $W_e = 0$, $A_0 = 17$ and $L_0 = 150$ for a sinusoidal wall in the long-wave case (left) and the WIBL case (right).*

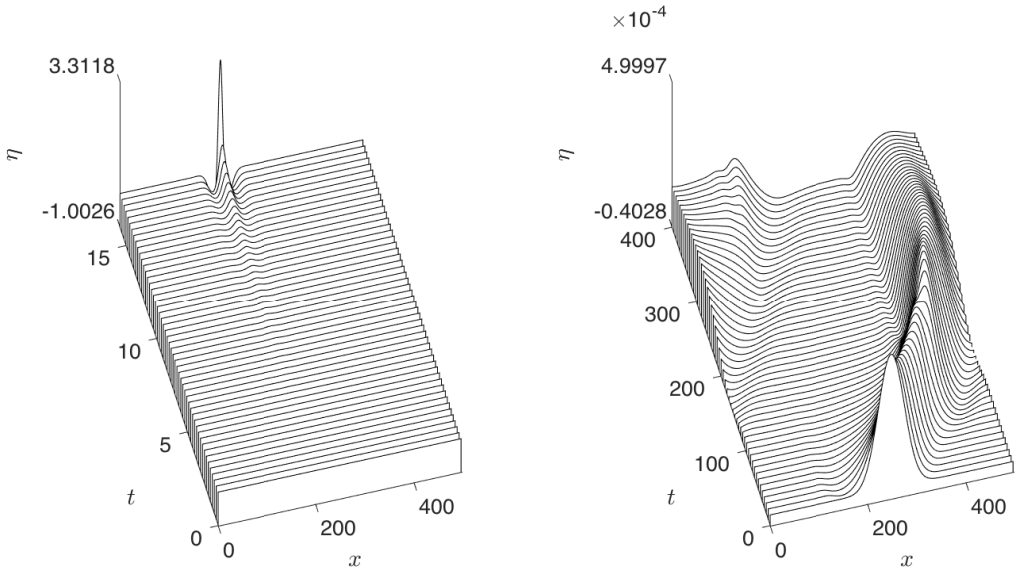

Figure 3.37: *Time evolution of the perturbation η originating at midpoint $x = 2L$ with $R = 1.25$, $K = 3364.5$, $W_e = 0$, $A_0 = 24$ and $L_0 = 150$ for a sinusoidal wall in the long-wave case (left) and the WIBL case (right).*

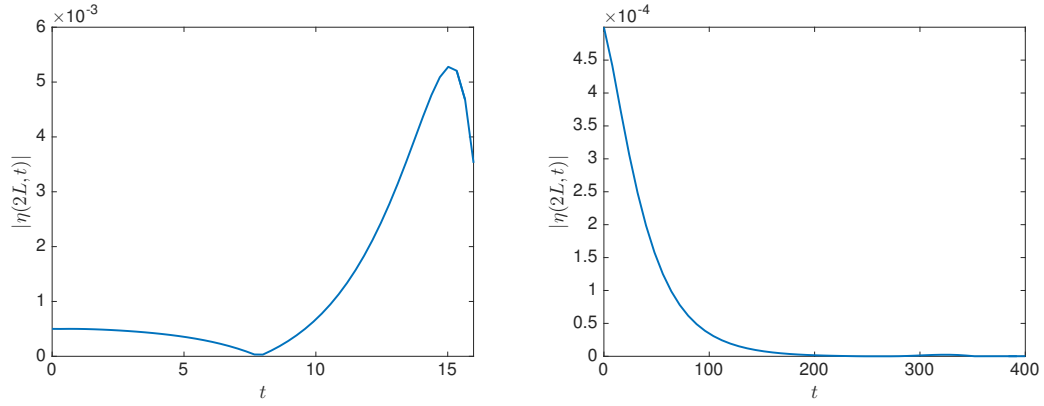

Figure 3.38: *Time evolution of the absolute value of the perturbation at the midpoint $x = 2L$ for $R = 1.25$, $K = 3364.5$, $W_e = 0$, $A_0 = 24$ and $L_0 = 150$ for a sinusoidal wall in the long-wave case (left) and the WIBL case (right).*

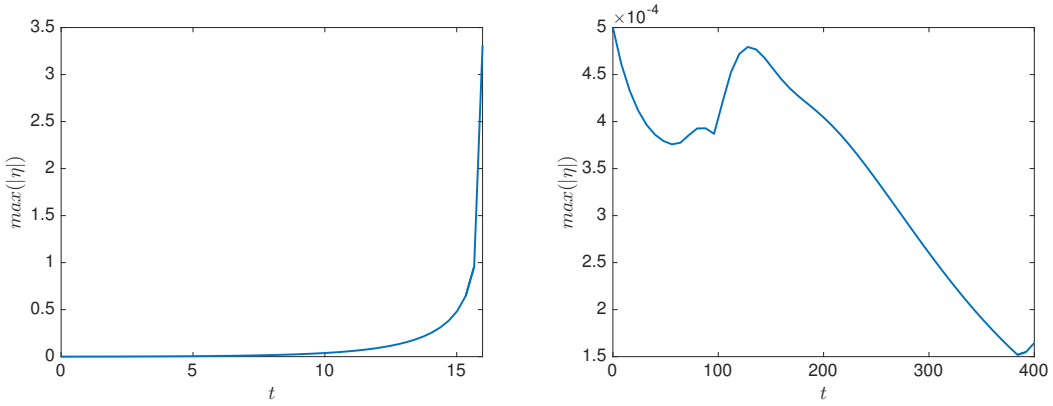

Figure 3.39: *Time evolution of the maximum of the absolute value of the perturbation for $R = 1.25$, $K = 3364.5$, $W_e = 0$, $A_0 = 24$ and $L_0 = 150$ for a sinusoidal wall in the long-wave case (left) and the WIBL case (right).*

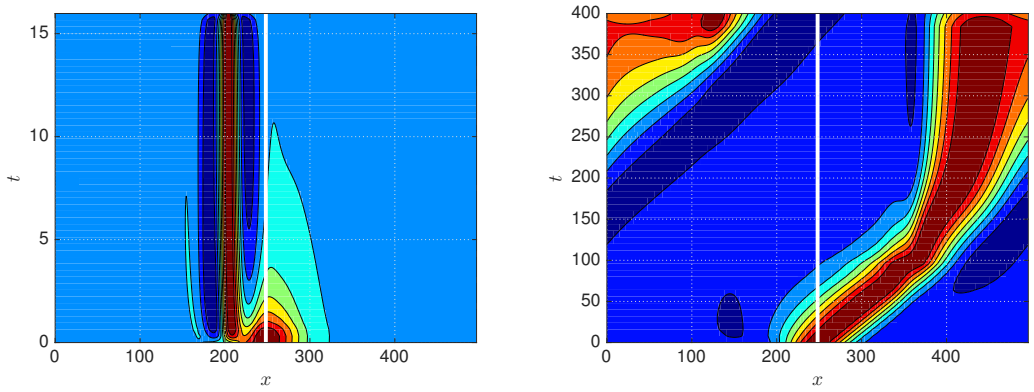

Figure 3.40: *Contour plot showing the propagation of the perturbation, with a solid white line showing the origin of the perturbation, for* $R = 1.25$, $K = 3364.5$, $W_e = 0$, $A_0 = 24$ *and* $L_0 = 150$ *for a sinusoidal wall in the long-wave case (left) and the WIBL case (right).*

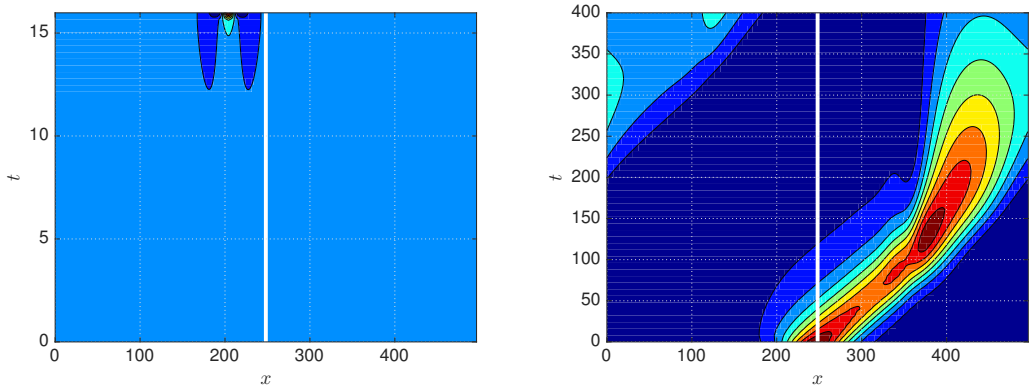

Figure 3.41: *Normalised contour plot showing the propagation of the perturbation, with a solid white line showing the origin of the perturbation, for* $R = 1.25$, $K = 3364.5$, $W_e = 0$, $A_0 = 24$ *and* $L_0 = 150$ *for a sinusoidal wall in the long-wave case (left) and the WIBL case (right).*

convected downstream, and consequently the system can be allowed to evolve for much longer times than possible in the long-wave model without film perforation becoming a concern. Figure 3.38 for the WIBL model shows rapid decay to near-zero from the frame of reference of the origin of the perturbation, whereas in the long-wave model we observe overall growth, although near the end of the simulation we observe a small decrease in the absolute value at the midpoint.

For the long-wave case, Figure 3.39 shows the maximum of the absolute value of the perturbation monotonically increasing until approximately $t = 15$, at which point the rate of growth increases significantly and the film thickness approaches zero at the location of the perturbation. For the WIBL model, the maximum was generally found to decrease in time, although we note that the maximum begins to grow at the end of

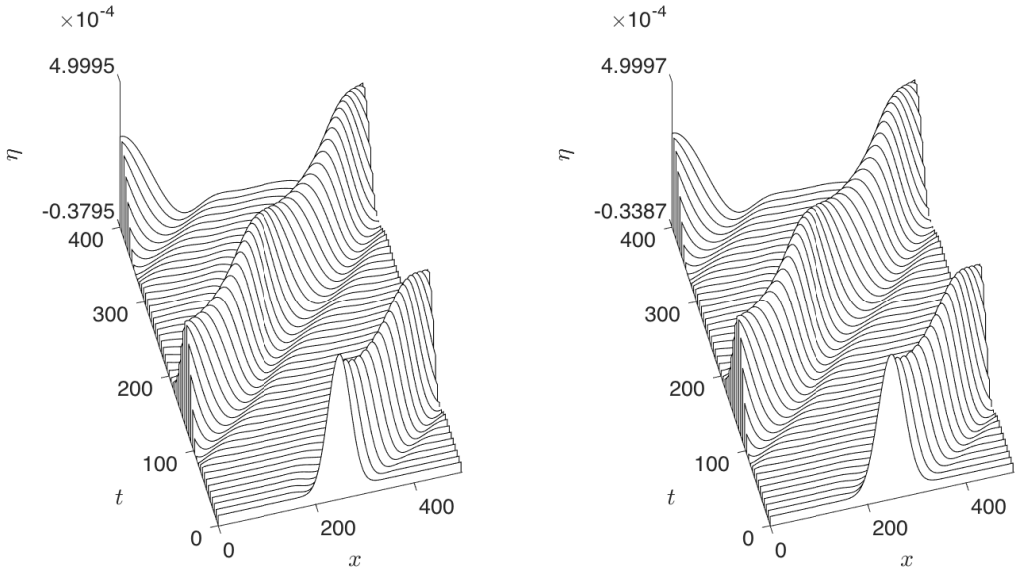

Figure 3.42: *Time evolution of the perturbation η originating at midpoint $x = 2L$ with $R = 1.25$, $K = 3364.5$, $W_e = 45$, $A_0 = 17$ and $L_0 = 150$ for a sinusoidal wall in the long-wave case (left) and the WIBL case (right).*

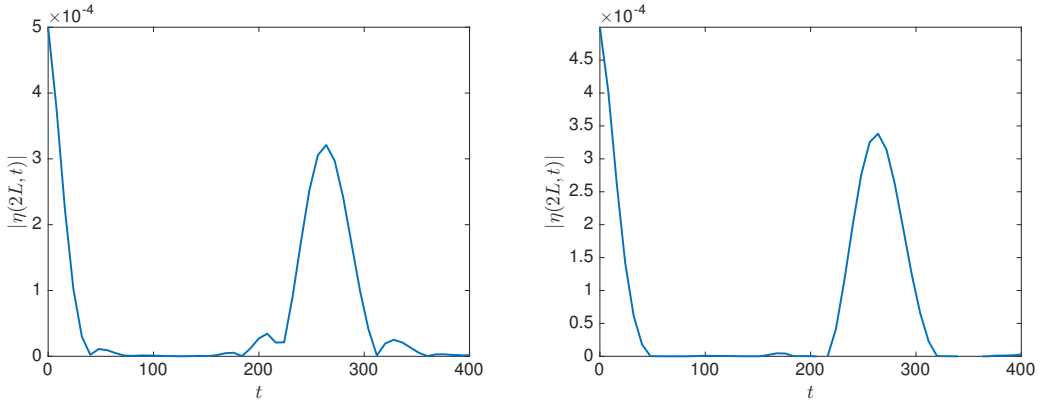

Figure 3.43: *Time evolution of the absolute value of the perturbation at the midpoint $x = 2L$ for $R = 1.25$, $K = 3364.5$, $W_e = 45$, $A_0 = 17$ and $L_0 = 150$ for a sinusoidal wall in the long-wave case (left) and the WIBL case (right).*

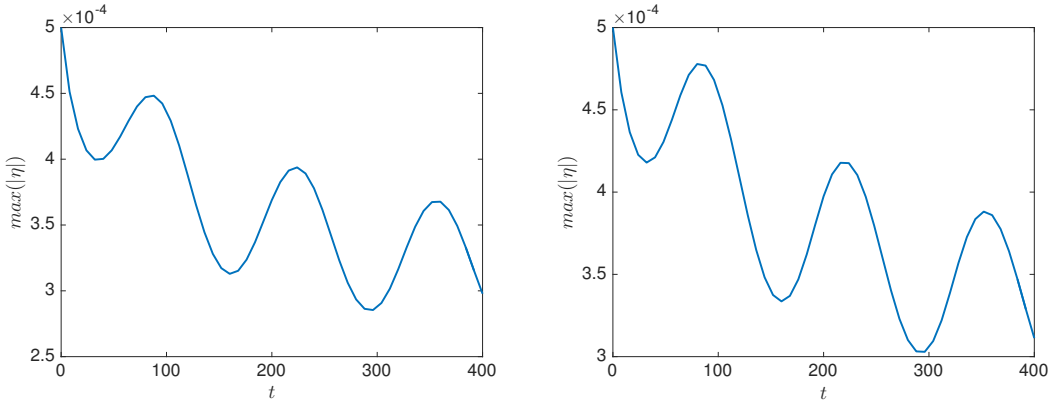

Figure 3.44: *Time evolution of the maximum of the absolute value of the perturbation for $R = 1.25$, $K = 3364.5$, $W_e = 45$, $A_0 = 17$ and $L_0 = 150$ for a sinusoidal wall in the long-wave case (left) and the WIBL case (right).*

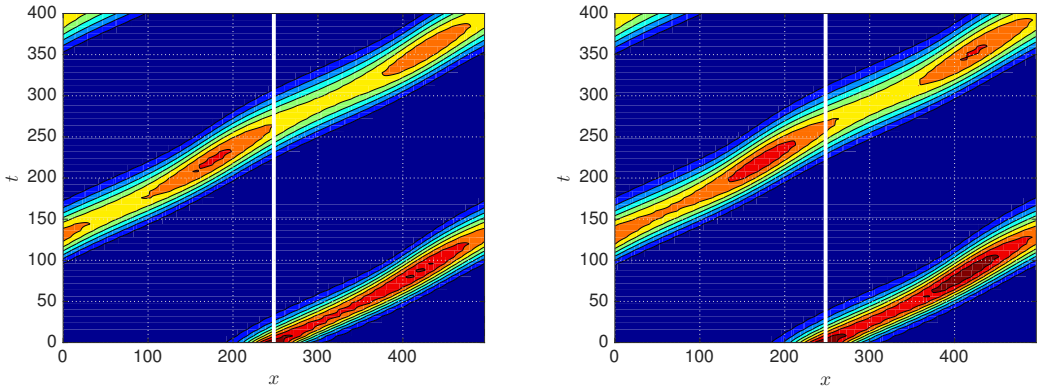

Figure 3.45: *Normalised contour plot showing the propagation of the perturbation, with a solid white line showing the origin of the perturbation, for* $R = 1.25$*,* $K = 3364.5$*,* $W_e = 45$*,* $A_0 = 17$ *and* $L_0 = 150$ *for a sinusoidal wall in the long-wave case (left) and the WIBL case (right).*

the simulation, and that at approximately $t = 130$ we observe the maximum increasing slightly before once again decaying.

Figures 3.40 and 3.41 show the contour plots and normalised contour plots of the perturbation respectively, and in the long-wave case we are able to clearly see the perturbation travelling upstream and growing in time. For the WIBL model, although we similarly observe the perturbation growing in time, it can be seen that the perturbation is exclusively convected downstream.

For the sinusoidal wall in the case of $W_e = 0$ then, we may say the following. For the long-wave model it was shown that for $L_0 = 150$, a wall amplitude of $A_0 = 17$ was found to be stabilising, whereas a wall amplitude of $A_0 = 24$ was found to be greatly destabilising to the point of film perforation, and thus our long-wave results are consistent with those found in the literature [98]. In the WIBL case, the steady-state solutions appears to be stable for both wall amplitudes, although we note some qualitative differences between the wall amplitudes; for $A_0 = 17$ we observe large initial increase followed by somewhat periodic decay and growth, whereas for $A_0 = 24$ we observe near-monotonic decay following the initial small increase at approximately $t = 130$.

In Figure 3.42 we see the time evolution of the perturbation now for $W_e = 45$ and $A_0 = 17$. For both models, the perturbation was found to decay and travel downstream, indicative of stability. This is corroborated by Figures 3.43 and 3.44 which both show decay in time, although we observe from Figure 3.44 that despite the fact that the two models are very similar for these parameter values, we note that the maximum of the absolute value of the perturbation decays slightly faster in the WIBL model as opposed

to the long-wave model. The normalised contour plots of the perturbation shown in Figure 3.45 demonstrate for both models the stability of our steady-state solutions – the perturbations remain to the right of the original location of the perturbation, and decay as time evolves.

Increasing the sinusoidal wall amplitude to $A_0 = 24$, we then obtain the following results. In Figure 3.46 we observe the time evolution of our perturbation for the long-wave and WIBL models. In both cases the perturbation was found to decay and was convected downstream, suggesting our steady-state solutions are stable. This is also consistent with the behaviour observed in Figures 3.47 and 3.49; the time evolution of the maximum of the absolute value of the perturbation and the normalised contour plot of the perturbation, respectively, for which we observe again the decay and convection of the perturbation for increasing time in both models. Figure 3.48 shows the initial, intermediate and final surface profiles for both models, and it can be observed that the perturbation has no noticeable effect on our steady solutions.

However, there is an interesting feature of this stable behaviour; in the case of $W_e = 0$, $L_0 = 150$ and $A_0 = 24$, for sinusoidal topography, our steady-state solution was found to be absolutely unstable for the long-wave model. Thus by increasing the electric Weber number, it is possible to obtain a stable steady-state solution rather than an unstable one, and we find that our electric field is not purely destabilising. Indeed, the stabilising or destabilising nature of the normal electric field depends strongly on both L_0 and A_0, as we shall see. Recent work by Blyth et al. [7] found that a normal electric field was able to cause a transition from absolute instability to convective instability for single-hump solitary pulses down a flat wall using the long-wave model, so this apparent stabilising potential of the normal electric field is not unprecedented.

We now increase the strength of the electric field, corresponding to $W_e = 200$. In Figure 3.50 we see the time evolution of the perturbation; in the long-wave case, we see that the amplitude of the perturbation greatly increases with time in a sharp and localised fashion, although we cannot immediately determine whether the perturbation travels upstream, and require more information. In the WIBL case, we similarly observe the perturbation growing in time, however, the overall growth of the perturbation is much slower compared to the behaviour observed for the long-wave model. The perturbation in the WIBL model also appears much less localised, and appears to curve as it propagates. We notice that by the final time unit we are nearing the nonlinear regime

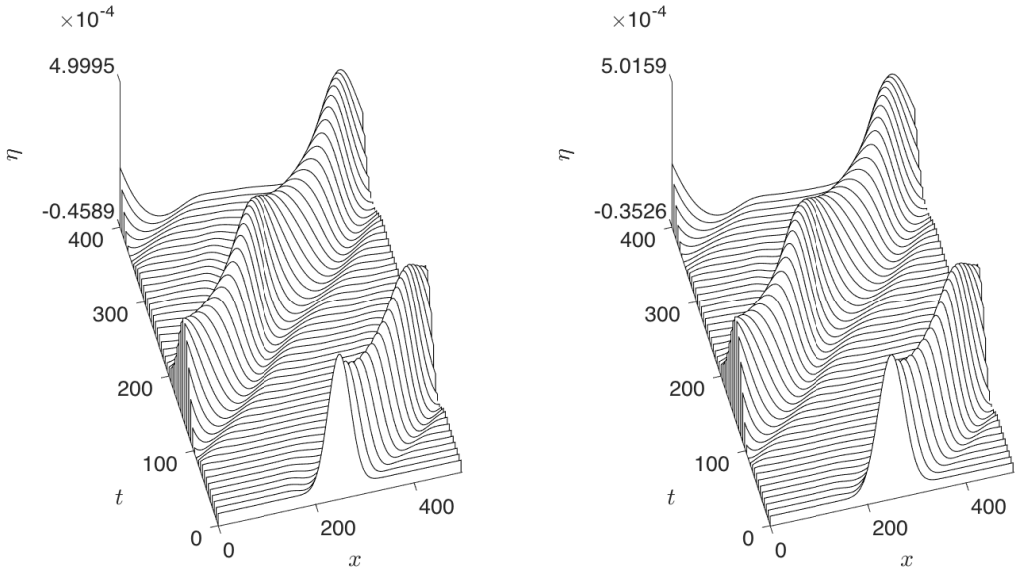

Figure 3.46: *Time evolution of the perturbation η originating at midpoint $x = 2L$ with $R = 1.25$, $K = 3364.5$, $W_e = 45$, $A_0 = 24$ and $L_0 = 150$ for a sinusoidal wall in the long-wave case (left) and the WIBL case (right).*

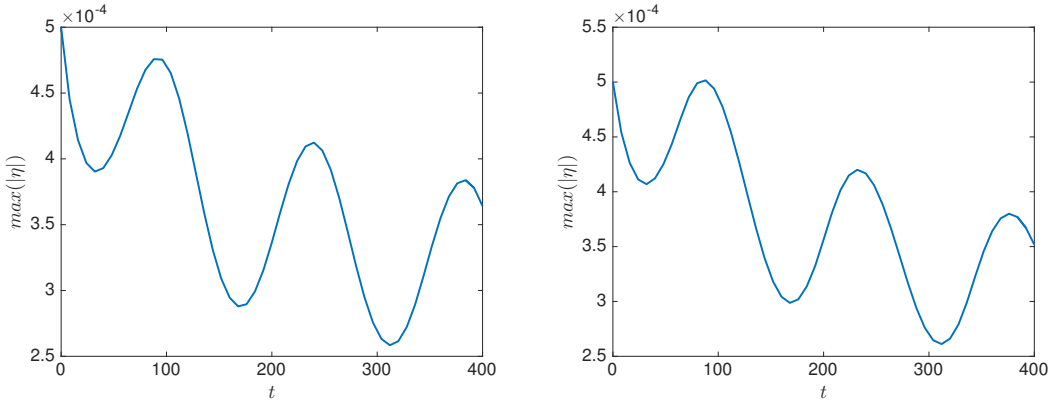

Figure 3.47: *Time evolution of the maximum of the absolute value of the perturbation for $R = 1.25$, $K = 3364.5$, $W_e = 45$, $A_0 = 24$ and $L_0 = 150$ for a sinusoidal wall in the long-wave case (left) and the WIBL case (right).*

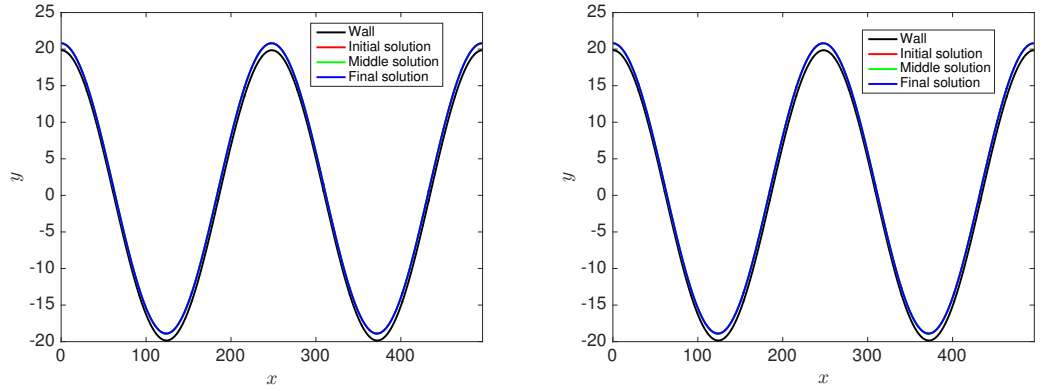

Figure 3.48: *The initial, intermediate and final surface profiles of the film for $R = 1.25$, $K = 3364.5$, $W_e = 45$, $A_0 = 24$ and $L_0 = 150$ for a sinusoidal wall in the long-wave case (left) and the WIBL case (right).*

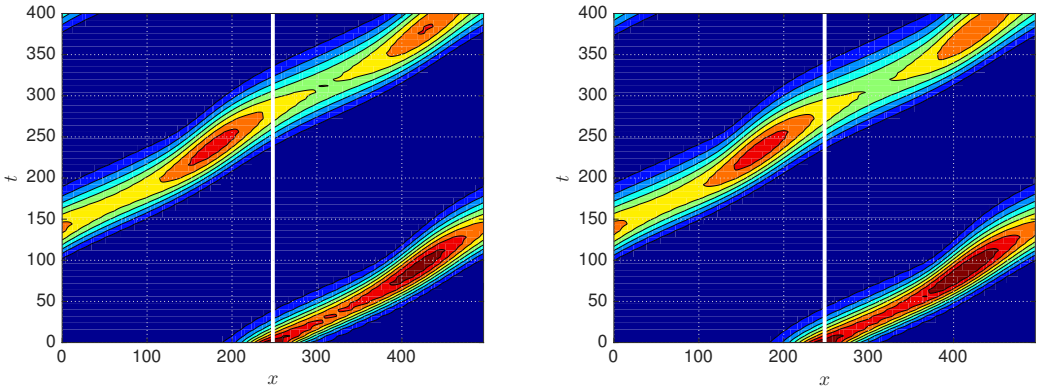

Figure 3.49: *Normalised contour plot showing the propagation of the perturbation, with a solid white line showing the origin of the perturbation, for* $R = 1.25$*,* $K = 3364.5$*,* $W_e = 45$*,* $A_0 = 24$ *and* $L_0 = 150$ *for a sinusoidal wall in the long-wave case (left) and the WIBL case (right).*

corresponding to the right-most part of the perturbation travelling across the domain and interacting with the left-most part of the perturbation. This can equivalently be thought of as the length of the perturbation becoming longer than the length of the domain, such that superposition rapidly results in the breakdown of the system, although careful analysis shows that the system is still within the linear regime.

Figure 3.51 shows the absolute value of the perturbation at the origin of the perturbation as time evolves; in the long-wave case we see that this grows greatly in time, and the sharp peak at approximately $t = 180$ corresponds to the crest of the wave travelling through the midpoint of the domain. In the WIBL case, we instead see an initial decay as the perturbation is convected away from the origin, and then what appears to be a resurgence as perturbation begins travelling back slightly upstream at approximately $t = 50$. Figure 3.52 shows the maximum of the absolute value of the perturbation at each time unit for both models, and we clearly observe unstable behaviour in both, with very sharp growth as $t \to 200$ for the long-wave model in particular. In the WIBL model we note the absolute value of the maximum of the absolute value of the perturbation monotonically increasing until $t = 125$, after which point we observe monotonic decay instead. We remark that allowing the model to evolve for slightly longer times shows the maximum once again growing, and in conjunction with Figure 3.50 we are able to classify the steady-state in the WIBL model as convectively unstable and in the long-wave model as absolutely unstable.

In Figure 3.53 we examine the surface profiles of both models, showing the initial, intermediary and final solutions. For the long-wave model for the final time unit, we observe the sharp and localised structure discussed from Figure 3.50, and it can be seen

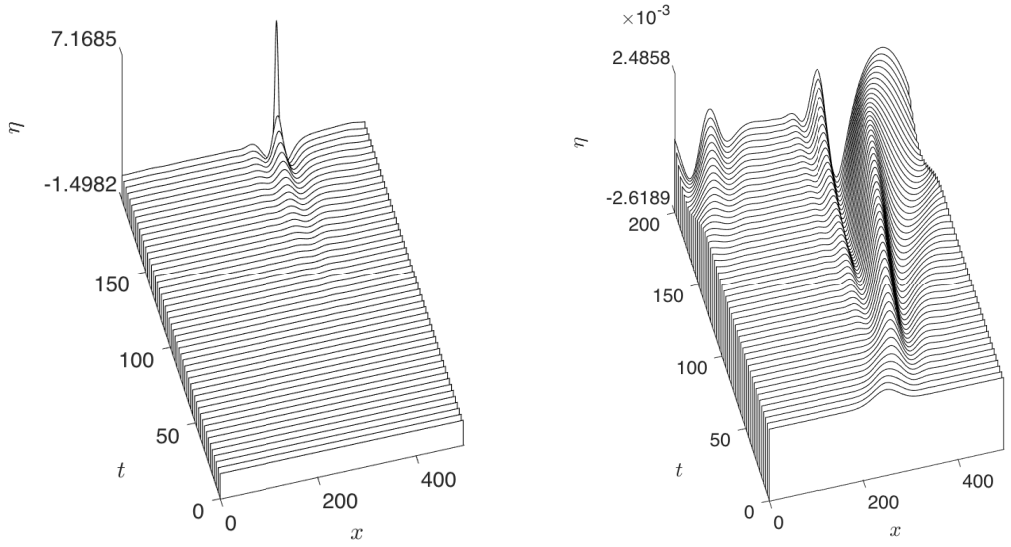

Figure 3.50: *Time evolution of the perturbation η originating at midpoint $x = 2L$ with $R = 1.25$, $K = 3364.5$, $W_e = 200$, $A_0 = 17$ and $L_0 = 150$ for a sinusoidal wall in the long-wave case (left) and the WIBL case (right).*

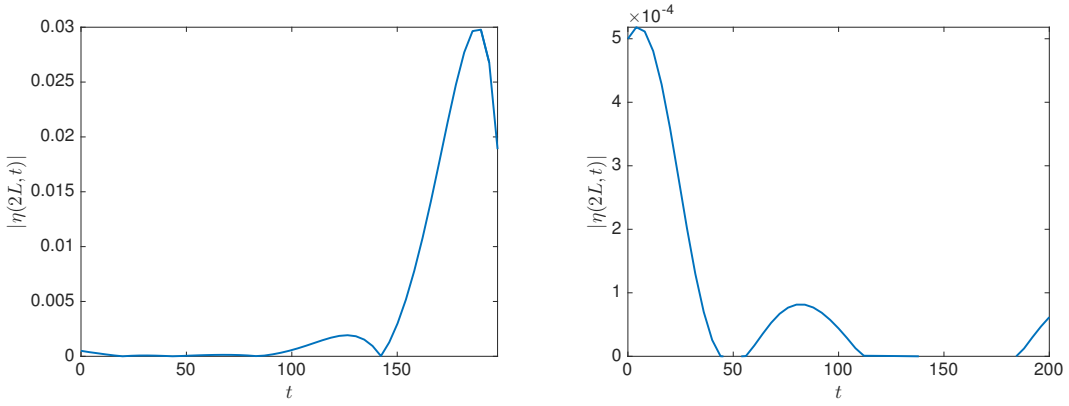

Figure 3.51: *Time evolution of the absolute value of the perturbation at the midpoint $x = 2L$ for $R = 1.25$, $K = 3364.5$, $W_e = 200$, $A_0 = 17$ and $L_0 = 150$ for a sinusoidal wall in the long-wave case (left) and the WIBL case (right).*

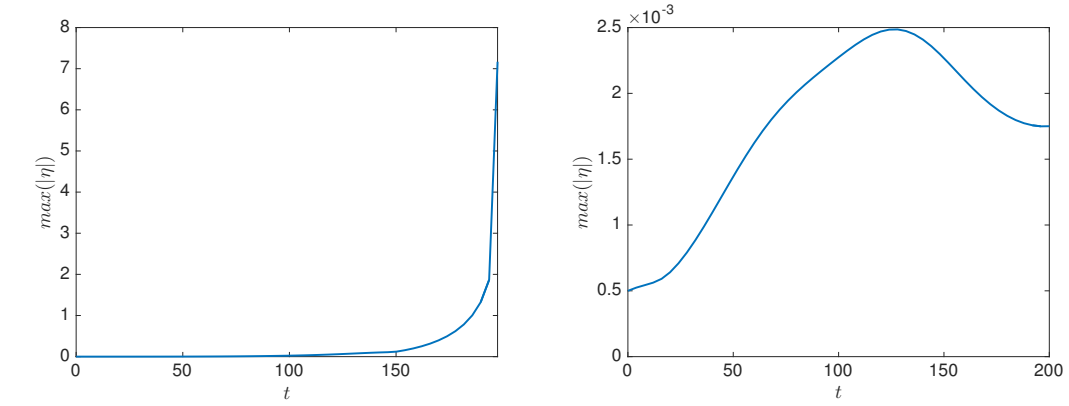

Figure 3.52: *Time evolution of the maximum of the absolute value of the perturbation for $R = 1.25$, $K = 3364.5$, $W_e = 200$, $A_0 = 17$ and $L_0 = 150$ for a sinusoidal wall in the long-wave case (left) and the WIBL case (right).*

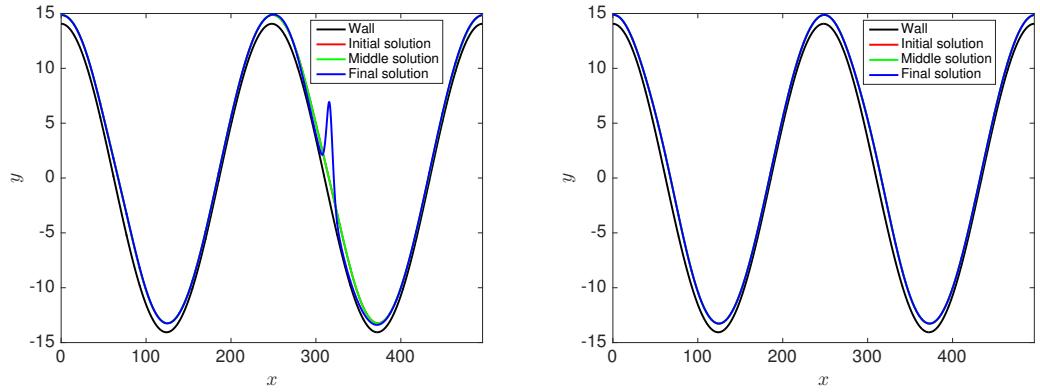

Figure 3.53: *The initial, intermediate and final surface profiles of the film for* $R = 1.25$, $K = 3364.5$, $W_e = 200$, $A_0 = 17$ *and* $L_0 = 150$ *for a sinusoidal wall in the long-wave case (left) and the WIBL case (right).*

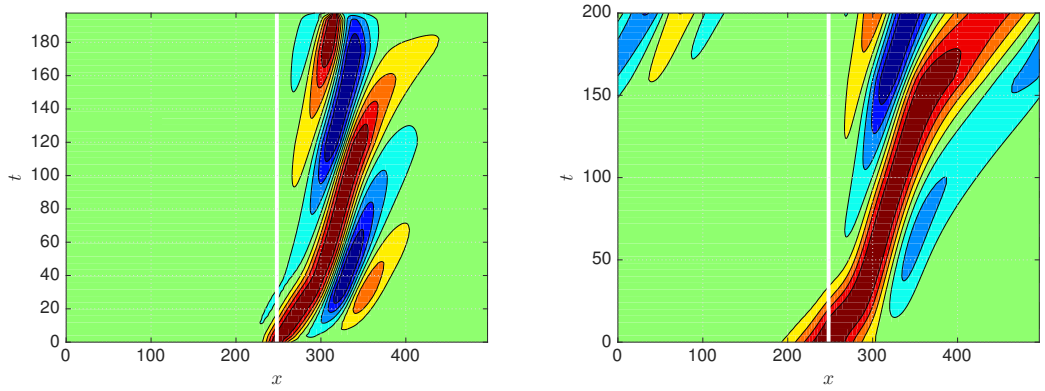

Figure 3.54: *Contour plot showing the propagation of the perturbation, with a solid white line showing the origin of the perturbation, for* $R = 1.25$, $K = 3364.5$, $W_e = 200$, $A_0 = 17$ *and* $L_0 = 150$ *for a sinusoidal wall in the long-wave case (left) and the WIBL case (right).*

that the volume of fluid required for this structure is drawn from the downward slope of the wall, although not from the crest or trough of the topography. If the perturbation is allowed to evolve for longer, film perforation occurs as the film thickness becomes minimal, and the model rapidly breaks down. In the WIBL model however, the perturbation remains small relative to the amplitude of the topography, such that we observe little macroscopic difference between the initial and final steady-state surface profiles.

Figure 3.54 shows the contour plot of the perturbation for both models. In the long-wave model, we see that the perturbation appears to 'curve' upstream after travelling downstream, whereas for the WIBL model the perturbation is more clearly convected downstream. The convective nature of the steady-state in the WIBL model is more obvious when examining the normalised contour plot in Figure 3.55; the main body of

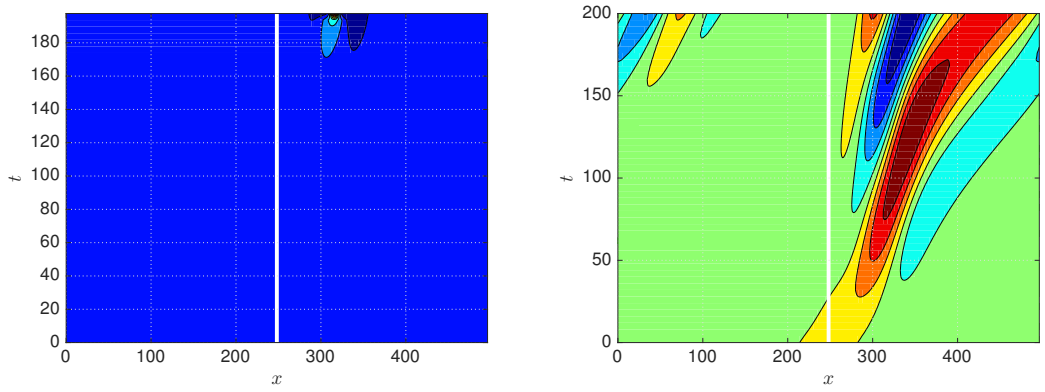

Figure 3.55: *Normalised contour plot showing the propagation of the perturbation, with a solid white line showing the origin of the perturbation, for* $R = 1.25$*,* $K = 3364.5$*,* $W_e = 200$*,* $A_0 = 17$ *and* $L_0 = 150$ *for a sinusoidal wall in the long-wave case (left) and the WIBL case (right).*

the perturbation remains travelling downstream, with the only upstream features being those which have travelled the entire length of the domain. For the long-wave model, we instead see the perturbation is highly-localised by the final time-step, so much so that it dwarfs all of the behaviour observed prior to approximately $t = 170$.

We again reexamine the wall amplitude $A_0 = 24$, albeit now with the electric field strength given by $W_e = 200$. Firstly, we note that in the WIBL case no steady-states were found for $A_0 = 24$ with this value of the electric field strength using the numerical continuation techniques that are discussed in Chapter 4 – the film thickness was found to become minimal at $A_0 = 20.55$ following a turning point, after which wall amplitude we find no physically-relevant steady-state solutions. Instead, we choose a steady-state solution corresponding to $A_0 = 20.55$ prior to this turning point in the WIBL case for the purposes of comparison with the long-wave results and behaviour, where the minimum of the film thickness takes the value $h_{min} = 0.0432$, which is above the typical threshold tolerance of $h_{min} = 0.005$ which dictates whether the solution is deemed physical or nonphysical. The film thickness at this amplitude after the turning point was instead found to be $h_{min} = 1.72\text{x}10^{-6}$.

In Figure 3.56 we observe the time evolution of the perturbation, and for both models we are able to see that the perturbation results in deformations to the steady-state being observed upstream as well as downstream, and an overall growth in the amplitude of the perturbation in both cases. In the long-wave case, we observe much larger overall growth of the perturbation despite evolving for a much shorter period in comparison to the WIBL model. Indeed, t.

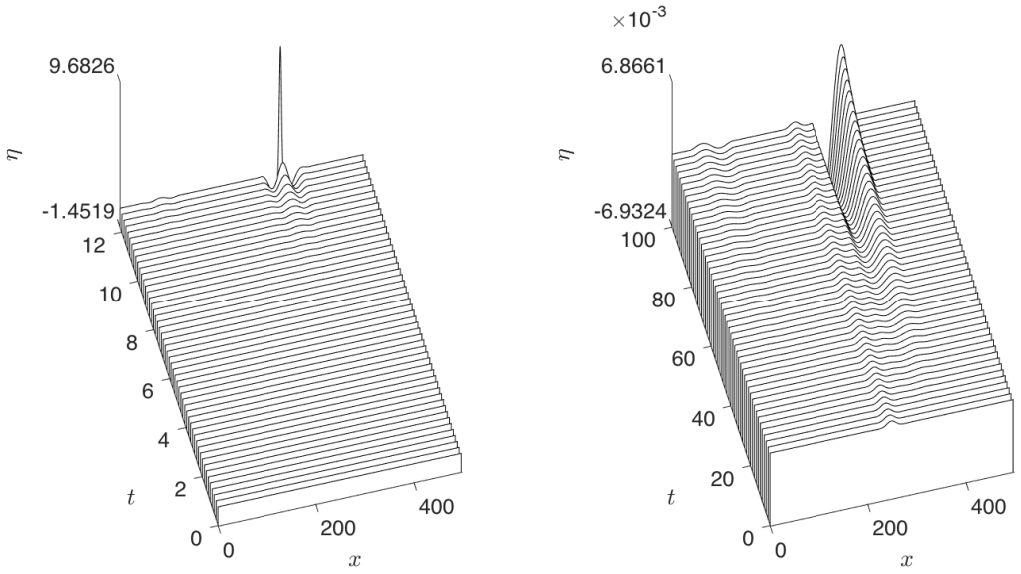

Figure 3.56: *Time evolution of the perturbation η originating at midpoint $x = 2L$ with $R = 1.25$, $K = 3364.5$, $W_e = 200$, $A_0 = 24$ (long-wave) or $A_0 = 20.55$ (WIBL) and $L_0 = 150$ for a sinusoidal wall in the long-wave case (left) and the WIBL case (right).*

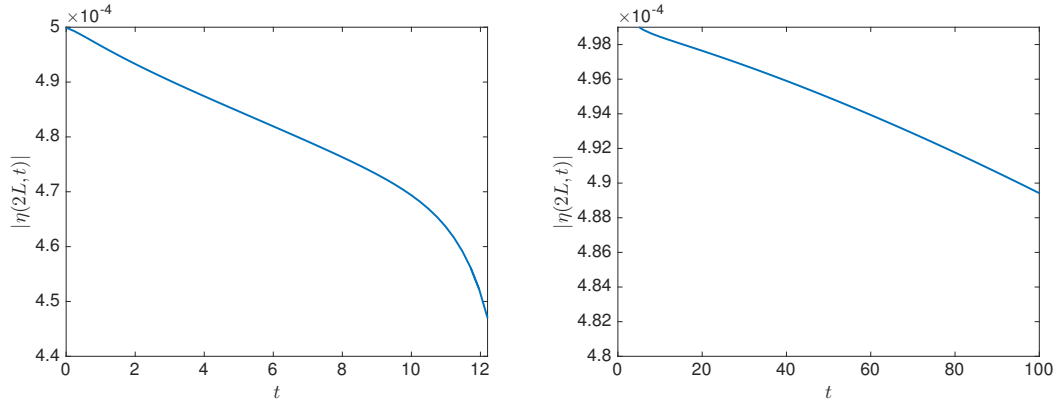

Figure 3.57: *Time evolution of the absolute value of the perturbation at the midpoint $x = 2L$ for $R = 1.25$, $K = 3364.5$, $W_e = 200$, $A_0 = 24$ (long-wave) or $A_0 = 20.55$ (WIBL) and $L_0 = 150$ for a sinusoidal wall in the long-wave case (left) and the WIBL case (right).*

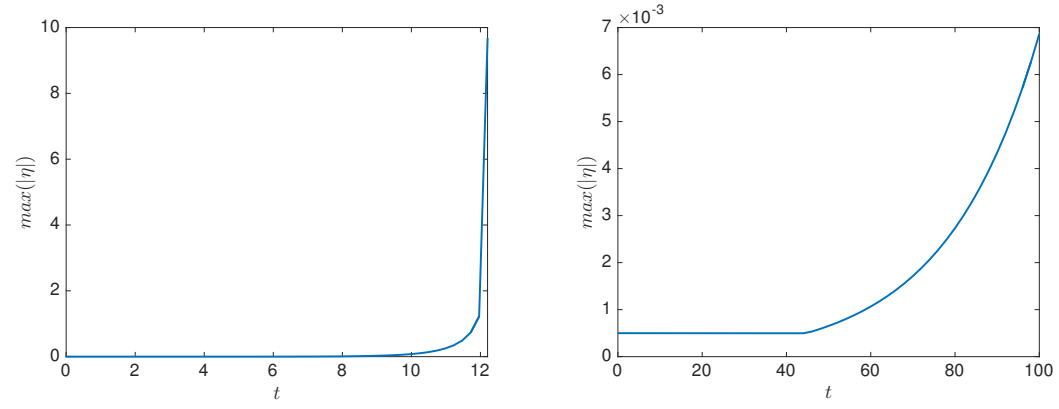

Figure 3.58: *Time evolution of the maximum of the absolute value of the perturbation for $R = 1.25$, $K = 3364.5$, $W_e = 200$, $A_0 = 24$ (long-wave) or $A_0 = 20.55$ (WIBL) and $L_0 = 150$ for a sinusoidal wall in the long-wave case (left) and the WIBL case (right).*

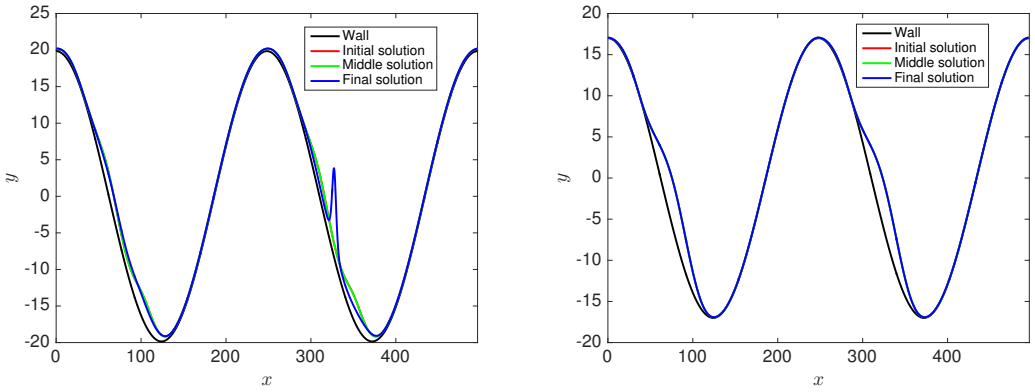

Figure 3.59: *The initial, intermediate and final surface profiles of the film for* $R = 1.25$, $K = 3364.5$, $W_e = 200$, $A_0 = 24$ *(long-wave) or* $A_0 = 20.55$ *(WIBL) and* $L_0 = 150$ *for a sinusoidal wall in the long-wave case (left) and the WIBL case (right).*

Figures 3.57 and 3.58 show the absolute value of the perturbation at its origin, as well as the maximum of the absolute value of the perturbation for both the long-wave and WIBL models respectively. In Figure 3.57 we observe decay for both models, the implication of which is that the steady-states are not absolutely unstable. However, we also note that in the long-wave case, the system was found to break down before it could evolve for 13 time units, such that more information is required to make a determination on the stability. In Figure 3.58, we observe growth for both models, indicative of instability. For the WIBL model,the maximum appears relatively constant until approximately $t = 45$, at which point we observe monotonic growth. In the long-wave case we instead see extremely rapid growth during the final time units, such that all previous growth is negligible by comparison.

Figure 3.59 shows the steady-state surface profiles for both the long-wave and WIBL models at the initial time unit, the middle time unit and the final time unit. In the long-wave case we again observe a very sharp and localised structure on the film surface, and the liquid required for this structure is provided from the downward slope of the topography. For the WIBL model we observe little qualitative difference between the surface profiles, due to the much slower comparative growth of the perturbation. Figures 3.60 and 3.61 correspond to the contour plot and normalised contour plot of the perturbation for both models respectively. For the long-wave model, the contour plot clearly shows the appearance of the perturbation to the left of the white line corresponding to the origin of the perturbation, the implication of which is either that the perturbation travelled downstream to the right and then reappeared to the left once it reached the boundary, or that the perturbation simply travelled upstream as well as downstream simultaneously. However, as shown in Figure 3.60, the perturbation does not travel over the domain in

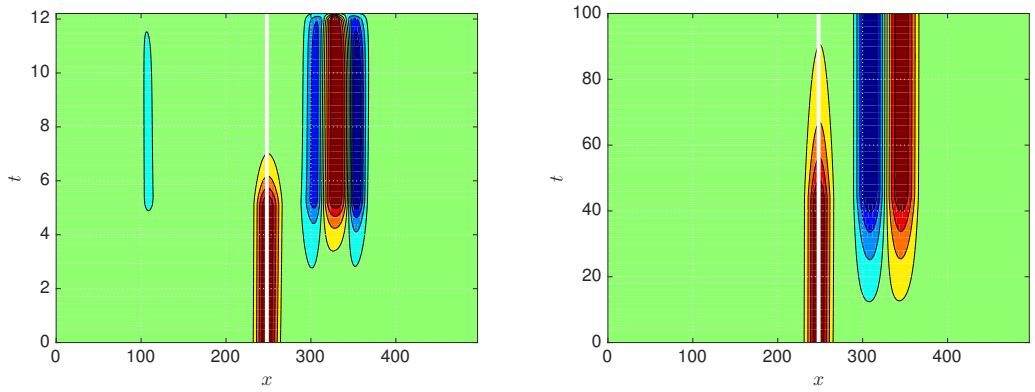

Figure 3.60: *Contour plot showing the propagation of the perturbation, with a solid white line showing the origin of the perturbation, for* $R = 1.25$*,* $K = 3364.5$*,* $W_e = 200$*,* $A_0 = 24$ *(long-wave) or* $A_0 = 20.55$ *(WIBL) and* $L_0 = 150$ *for a sinusoidal wall in the long-wave case (left) and the WIBL case (right).*

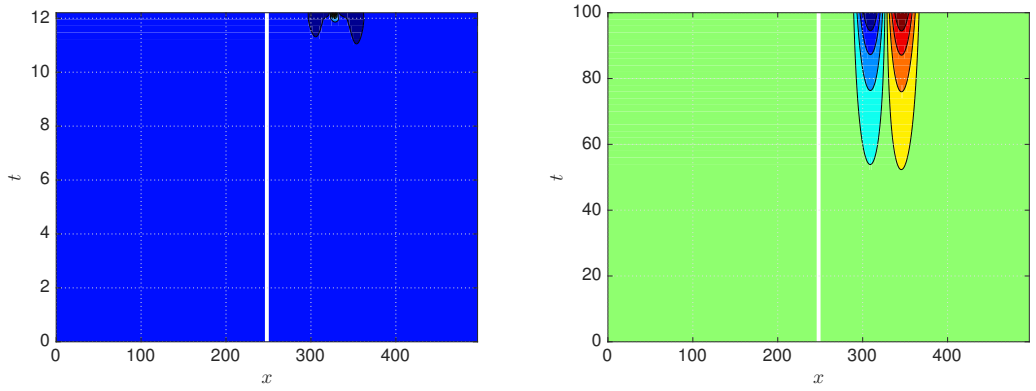

Figure 3.61: *Normalised contour plot showing the propagation of the perturbation, with a solid white line showing the origin of the perturbation, for* $R = 1.25$*,* $K = 3364.5$*,* $W_e = 200$*,* $A_0 = 24$ *(long-wave) or* $A_0 = 20.55$ *(WIBL) and* $L_0 = 150$ *for a sinusoidal wall in the long-wave case (left) and the WIBL case (right).*

the 10 time units over which the simulation took place, and we may thus deduce that the instability is absolute. Contrariwise for the WIBL model, we do not see the appearance of the perturbation to the left of its origin; instead we see that the perturbation remains relatively spatially fixed, despite allowing a somewhat large number of time units for the simulation. However, the normalised contour plot for the WIBL model shown in Figure 3.61 makes apparent that we are dealing with a convective instability, due to the exclusive appearance of features downstream and not upstream, and the overall growth of the absolute value of the perturbation.

For a sinusoidal wall with $L_0 = 150$ then, we may summarise our results as follows. For $W_e = 0$, we find that the long-wave model predicts stability for $A_0 = 17$, and absolute instability for $A_0 = 24$, which is consistent with the work by Blyth et al. [7]. For the WIBL model, both $A_0 = 17$ and $A_0 = 24$ are stable. In the case of electrified film flow with $W_e = 45$, the long-wave model now predicts stable solutions for both $A_0 = 17$ and

$A_0 = 24$, the implications of which for the stabilising properties of the normal electric field have been discussed earlier. The WIBL model for $W_e = 45$ similarly predicts stable solutions for both $A_0 = 17$ and $A_0 = 24$. As the $W_e = 0$ case for $A_0 = 24$ was also stable in the WIBL model, we do not find the same stabilising properties. For $W_e = 200$ the long-wave model appears to be absolutely unstable for $A_0 = 17$ although could conceivably be convectively unstable, and the numerical breakdown prevents a concrete classification. For $A_0 = 24$ however, the long-wave model exhibits more clearly absolutely unstable behaviour. In the WIBL model we find that the solutions are convectively unstable for both $A_0 = 17$ and $A_0 = 24$.

3.4.3 Rectangular wall

In this subsection we now focus upon the rectangular topography instead of the sinusoidal topography. As discussed by Tseluiko, Blyth and Papageorgiou [98], the stabilising and destabilising properties of rectangular topography for the long-wave model are highly dependent upon both the domain size and the amplitude of the topography. For smaller domain sizes, e.g. $L_0 = 31$, the topography is initially destabilising for small amplitudes, e.g. $A_0 = 0.2$, but for larger wall amplitudes, e.g. $A_0 = 0.4$, the topography becomes stabilising. For larger domain sizes, e.g. $L_0 = 57$, the topography is initially stabilising for small amplitudes, but rapidly becomes destabilising as we increase the amplitude of the wall. We now seek to understand the relationship between domain size, wall amplitude and electric field for both the long-wave and WIBL models.

We begin with Figure 3.62, which shows the time evolution of the perturbation for both models with $L_0 = 57$, $W_e = 0$ and $A_0 = 0.27$. We observe a decay in the amplitude of the perturbation in both cases, and the perturbation is clearly convected downstream to the right. Figures 3.63 and 3.64 show the absolute value of the perturbation at its origin, and the maximum of the absolute value of the perturbation respectively; in both figures we see that the norm decays in time, although in Figure 3.63 we observe a growth near $t = 65$ for both models. However, once again this is simply due to the perturbation passing from the right-side of the domain to the left-side of the domain after passing through the boundary, with the growth corresponding to the perturbation being convected downstream through the origin location once again. It is hence clear that the steady-states are stable for both models.

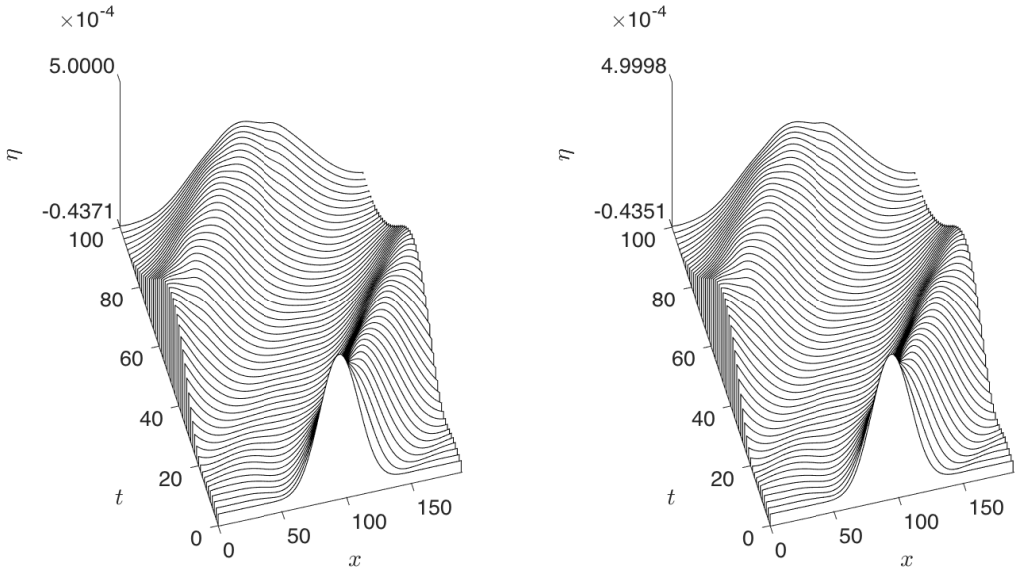

Figure 3.62: *Time evolution of the perturbation η originating at midpoint $x = 2L$ with $R = 1.25$, $K = 3364.5$, $W_e = 0$, $A_0 = 0.27$ and $L_0 = 57$ for a rectangular wall in the long-wave case (left) and the WIBL case (right).*

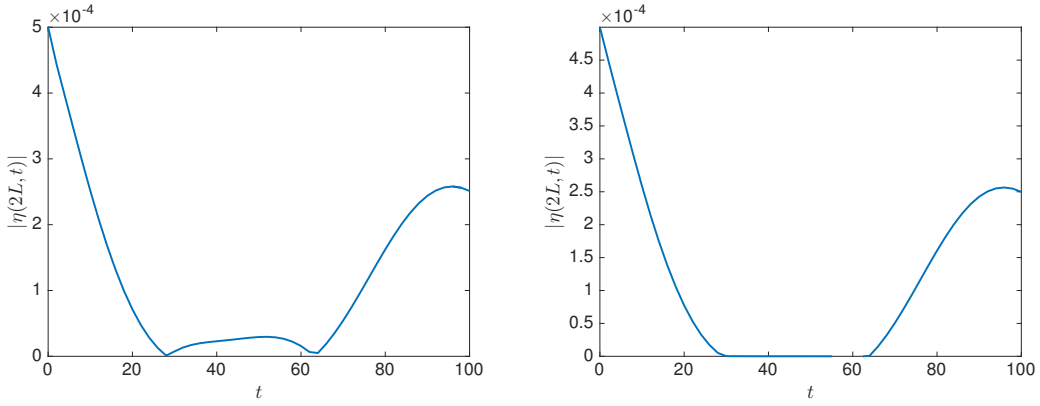

Figure 3.63: *Time evolution of the absolute value of the perturbation at the midpoint $x = 2L$ for $R = 1.25$, $K = 3364.5$, $W_e = 0$, $A_0 = 0.27$ and $L_0 = 57$ for a rectangular wall in the long-wave case (left) and the WIBL case (right).*

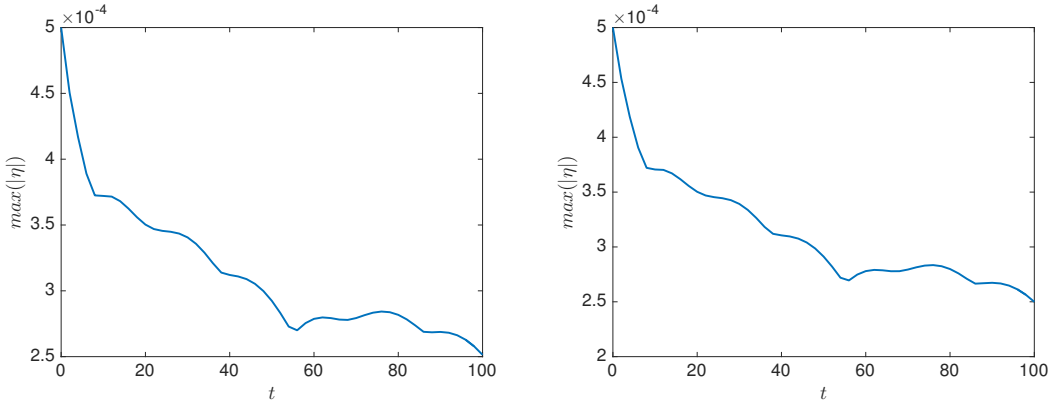

Figure 3.64: *Time evolution of the maximum of the absolute value of the perturbation for $R = 1.25$, $K = 3364.5$, $W_e = 0$, $A_0 = 0.27$ and $L_0 = 57$ for a rectangular wall in the long-wave case (left) and the WIBL case (right).*

We now increase the amplitude of the rectangular wall to $A_0 = 1.462$. As seen in Figure 3.65, we now observe the perturbation growing for both the long-wave and WIBL models as time evolves. In both models the solution appears to be absolutely unstable; whilst the main body of the perturbation is convected downstream and grows, there is a trough which travels to the left upstream. Figures 3.66 and 3.67 show the behaviour of the absolute value of the perturbation in time; in Figure 3.66 we initially observe the perturbation decaying in time for both models to near-zero, although the norm then begins to grow again at $t \approx 60$. In Figure 3.67 for both models we can see the maximum of the absolute value of the perturbation increases monotonically with time following an initial large decrease. Figures 3.68 and 3.69 show the contour plot and normalised contour plot of the perturbation respectively, and in both figures it is clear to see that although the crest of perturbation grows in time and is convected downstream, we also observe upstream features. In cases such as these, it is difficult to distinguish between a convective instability travelling in both directions simultaneously and an absolute instability, due to the lack of a mathematical framework applicable to nonlocal equations for determining this objectively. As we know from Brevdo et al. [9] that absolute instability in the non-electrified case is nonphysical, we must consider the possiblity that the perturbation consists of a pulse convecting both upstream and downstream simultaneously.

We now return to an amplitude of $A_0 = 0.27$ albeit whilst simultaneously increasing electric Weber number to $W_e = 45$. In Figure 3.70 we see the time evolution of the perturbation for both models. Similarly to the $W_e = 0$ case, here we observe the perturbation decaying in time and travelling downstream, indicative of a stable solution. This classification is corroborated by Figures 3.71 and 3.72, which show not only the norms of the perturbations decreasing at their origins, but also the maximums of the norms of the perturbations decreasing respectively.

Again the rectangular wall amplitude is increased to $A_0 = 1.462$ and we add our perturbation to the steady-state solution, the time evolution of which may be seen in Figure 3.73. In both models we again observe the indeterminate behaviour noted in the $A_0 = 1.462$ case for $W_e = 0$. Figure 3.74 shows the absolute value of the perturbation at its origin for both models and we can initially see decay for both models, although we then observe monotonic growth. Figure 3.75 instead shows the maximum of the absolute value of the perturbation for both models, which was found to similarly increase after an initial decrease. Figures 3.76 and 3.77 show the contour plot and normalised contour plot of the perturbation respectively for both models. Again, the steady-states

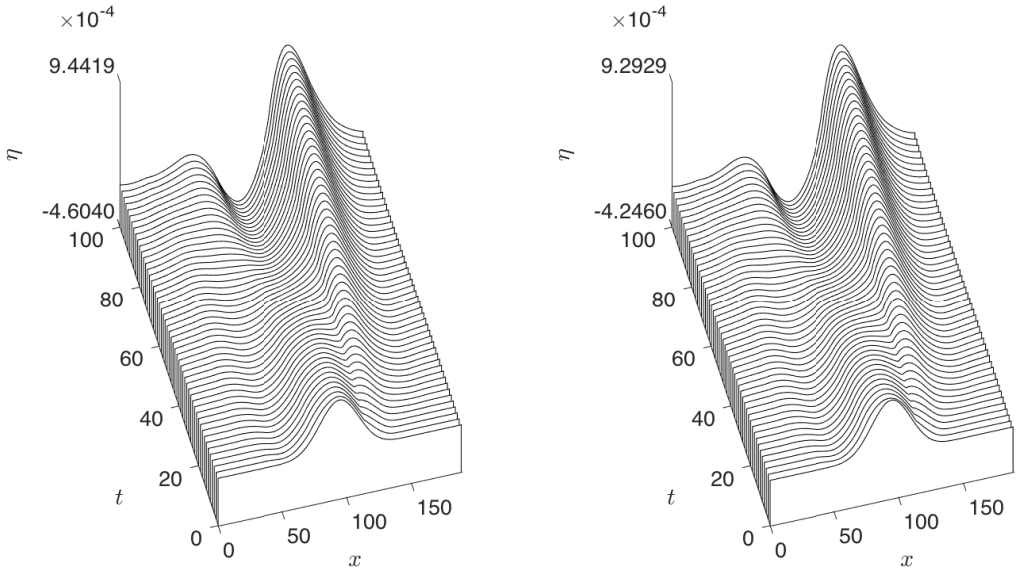

Figure 3.65: *Time evolution of the perturbation η originating at midpoint $x = 2L$ with $R = 1.25$, $K = 3364.5$, $W_e = 0$, $A_0 = 1.462$ and $L_0 = 57$ for a rectangular wall in the long-wave case (left) and the WIBL case (right).*

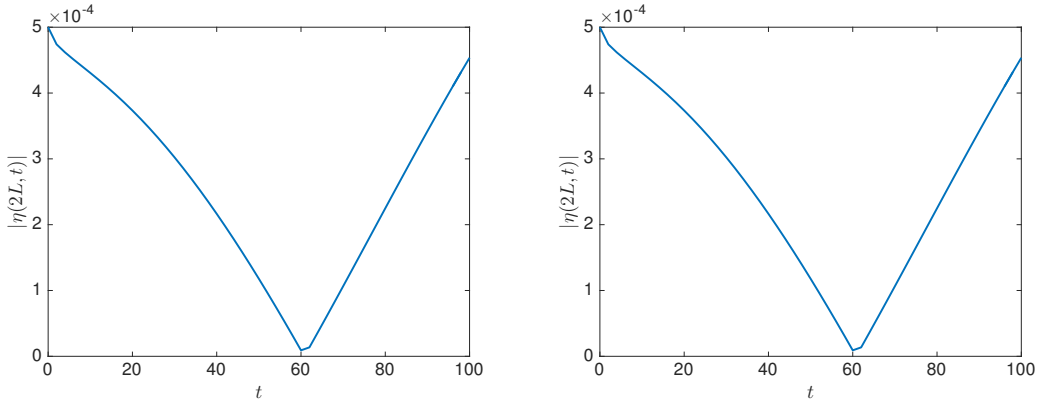

Figure 3.66: *Time evolution of the absolute value of the perturbation at the midpoint $x = 2L$ for $R = 1.25$, $K = 3364.5$, $W_e = 0$, $A_0 = 1.462$ and $L_0 = 57$ for a rectangular wall in the long-wave case (left) and the WIBL case (right).*

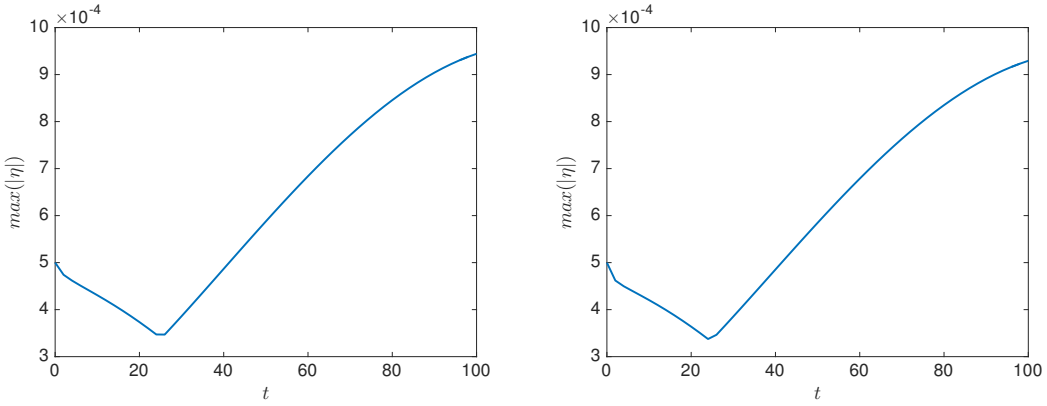

Figure 3.67: *Time evolution of the maximum of the absolute value of the perturbation for $R = 1.25$, $K = 3364.5$, $W_e = 0$, $A_0 = 1.462$ and $L_0 = 57$ for a rectangular wall in the long-wave case (left) and the WIBL case (right).*

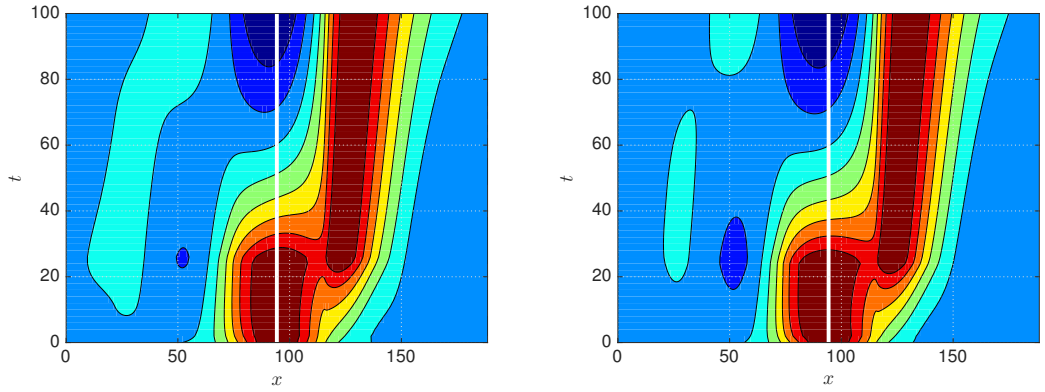

Figure 3.68: *Contour plot showing the propagation of the perturbation, with a solid white line showing the origin of the perturbation, for* $R = 1.25$, $K = 3364.5$, $W_e = 0$, $A_0 = 1.462$ *and* $L_0 = 57$ *for a rectangular wall in the long-wave case (left) and the WIBL case (right).*

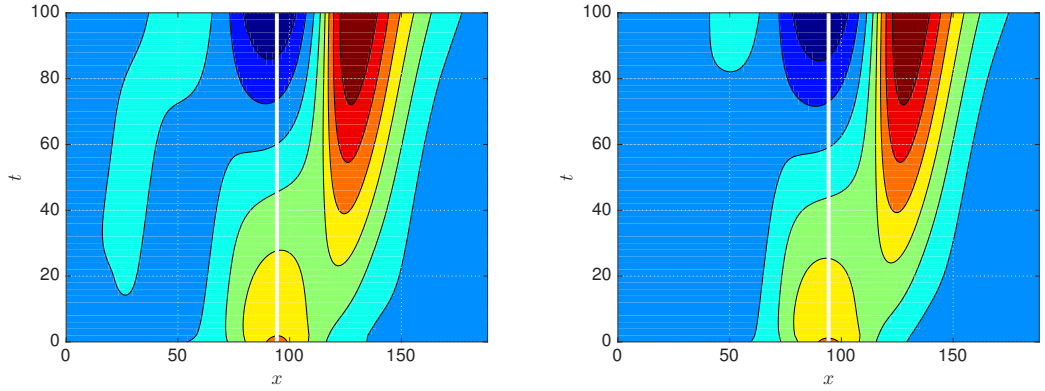

Figure 3.69: *Normalised contour plot showing the propagation of the perturbation, with a solid white line showing the origin of the perturbation, for* $R = 1.25$, $K = 3364.5$, $W_e = 0$, $A_0 = 1.462$ *and* $L_0 = 57$ *for a rectangular wall in the long-wave case (left) and the WIBL case (right).*

could be convectively unstable (but not transiently unstable) or absolutely unstable, and due to the similarities to the $W_e = 0$ case we may suspect the steady-states are convectively unstable.

The electric Weber number is now increased to $W_e = 200$ and the wall amplitude is set to $A_0 = 0.27$. Figure 3.78 shows the time evolution for the perturbation for both the long-wave and WIBL models. In both models we see that the perturbation grows in time and is convected to the right downstream. In Figure 3.79 we see the absolute value of the perturbation at its origin; in both models the norm initially decreases, but increases once the perturbation travels the length of the domain and returns to its original location. Figure 3.80 shows the maximum of the absolute value of the perturbation at each time unit for both models. In the long-wave case, we observe near-monotonic periodic growth. Figure 3.81 shows the normalised contour plot of the perturbation,

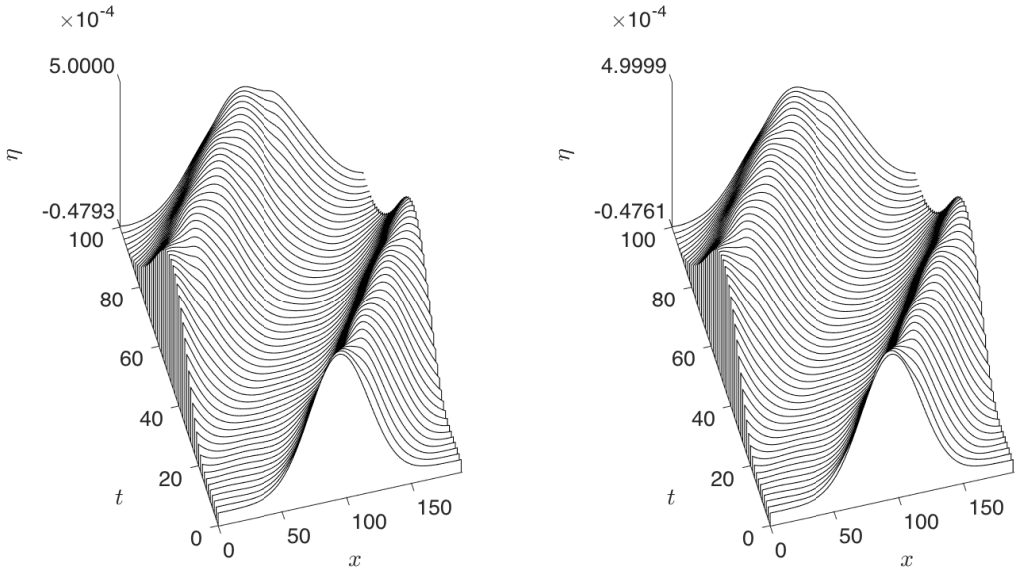

Figure 3.70: *Time evolution of the perturbation η originating at midpoint $x = 2L$ with $R = 1.25$, $K = 3364.5$, $W_e = 45$, $A_0 = 0.27$ and $L_0 = 57$ for a rectangular wall in the long-wave case (left) and the WIBL case (right).*

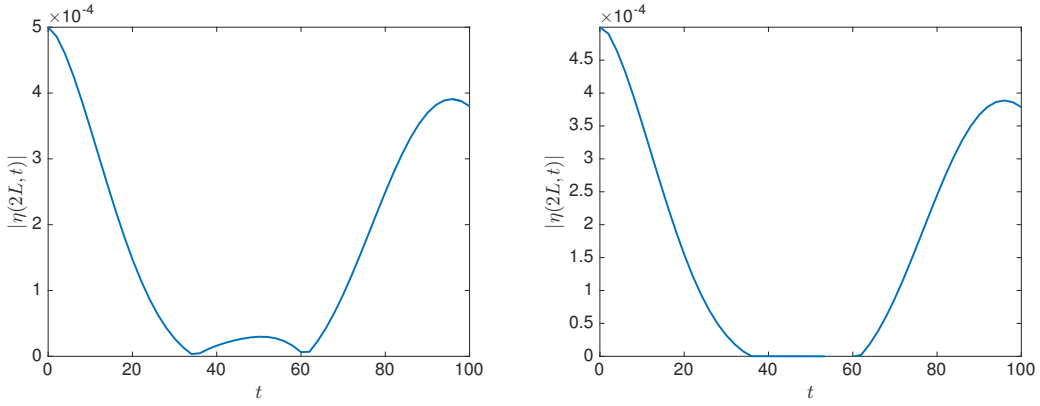

Figure 3.71: *Time evolution of the absolute value of the perturbation at the midpoint $x = 2L$ for $R = 1.25$, $K = 3364.5$, $W_e = 45$, $A_0 = 0.27$ and $L_0 = 57$ for a rectangular wall in the long-wave case (left) and the WIBL case (right).*

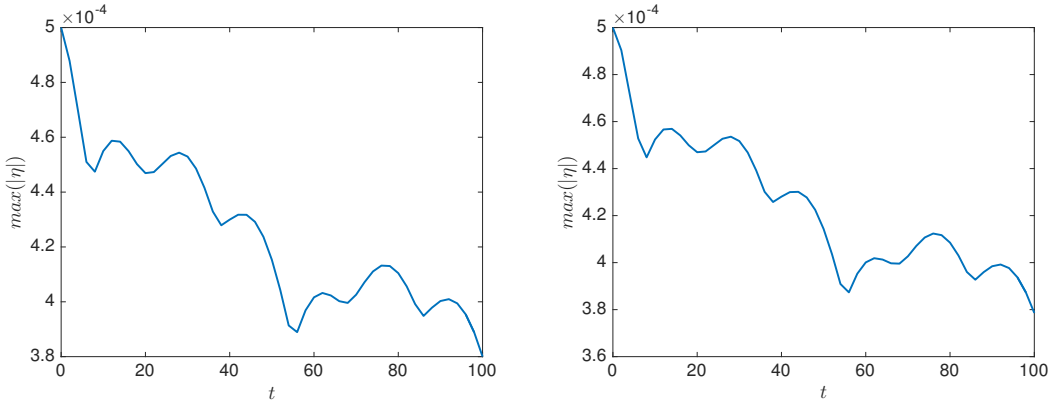

Figure 3.72: *Time evolution of the maximum of the absolute value of the perturbation for $R = 1.25$, $K = 3364.5$, $W_e = 45$, $A_0 = 0.27$ and $L_0 = 57$ for a rectangular wall in the long-wave case (left) and the WIBL case (right).*

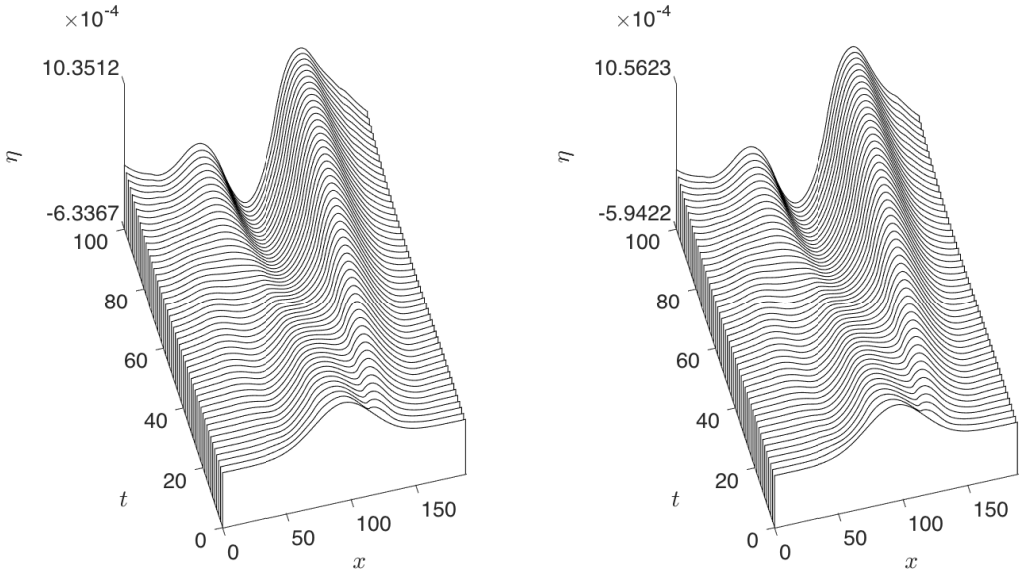

Figure 3.73: *Time evolution of the perturbation η originating at midpoint $x = 2L$ with $R = 1.25$, $K = 3364.5$, $W_e = 45$, $A_0 = 1.462$ and $L_0 = 57$ for a rectangular wall in the long-wave case (left) and the WIBL case (right).*

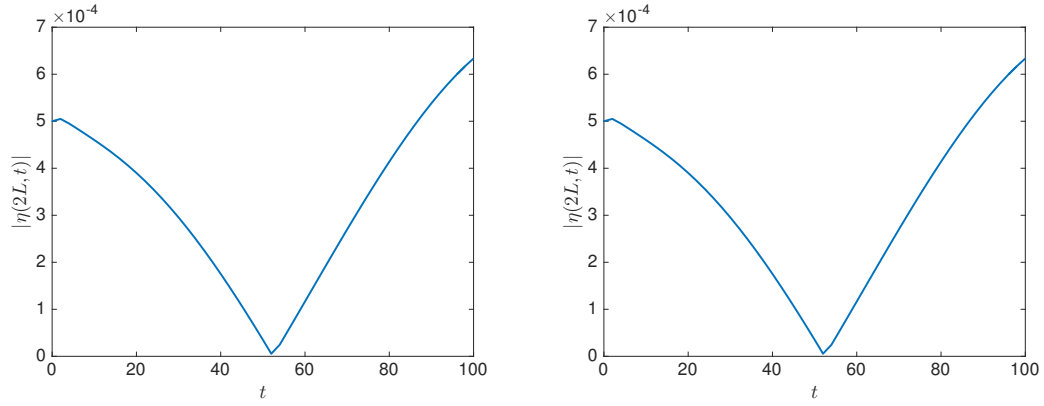

Figure 3.74: *Time evolution of the absolute value of the perturbation at the midpoint $x = 2L$ for $R = 1.25$, $K = 3364.5$, $W_e = 45$, $A_0 = 1.462$ and $L_0 = 57$ for a rectangular wall in the long-wave case (left) and the WIBL case (right).*

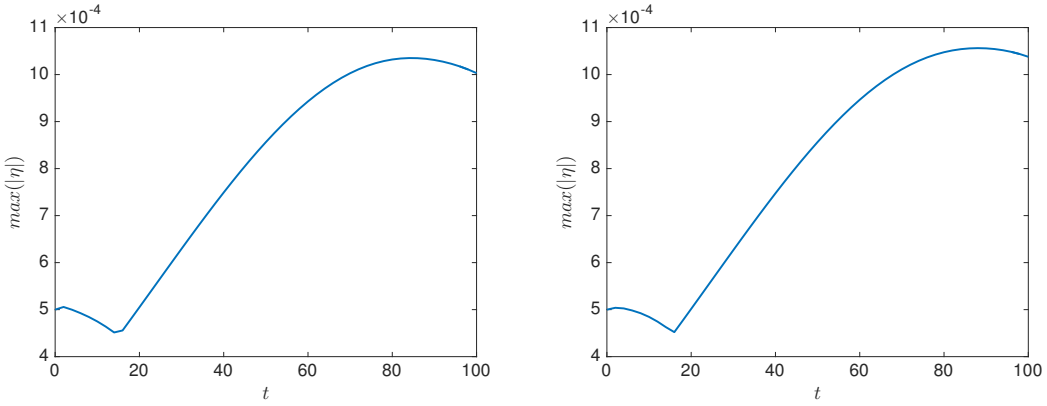

Figure 3.75: *Time evolution of the maximum of the absolute value of the perturbation for $R = 1.25$, $K = 3364.5$, $W_e = 45$, $A_0 = 1.462$ and $L_0 = 57$ for a rectangular wall in the long-wave case (left) and the WIBL case (right).*

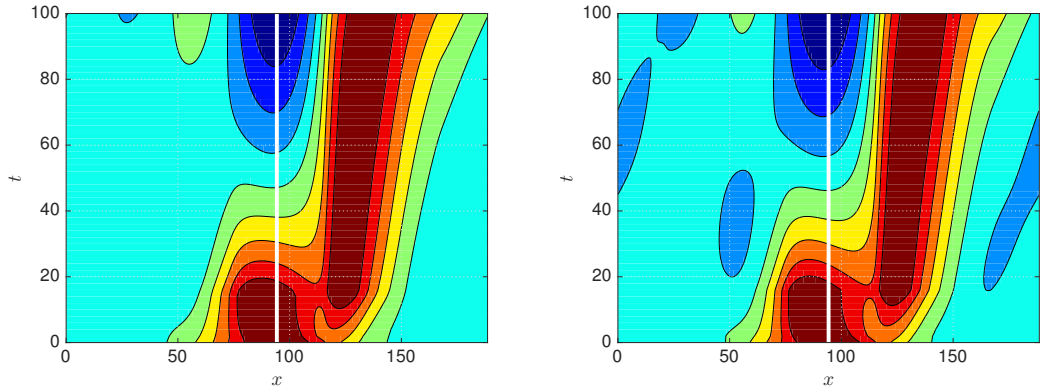

Figure 3.76: *Contour plot showing the propagation of the perturbation, with a solid white line showing the origin of the perturbation, for* $R = 1.25$, $K = 3364.5$, $W_e = 45$, $A_0 = 1.462$ *and* $L_0 = 57$ *for a rectangular wall in the long-wave case (left) and the WIBL case (right).*

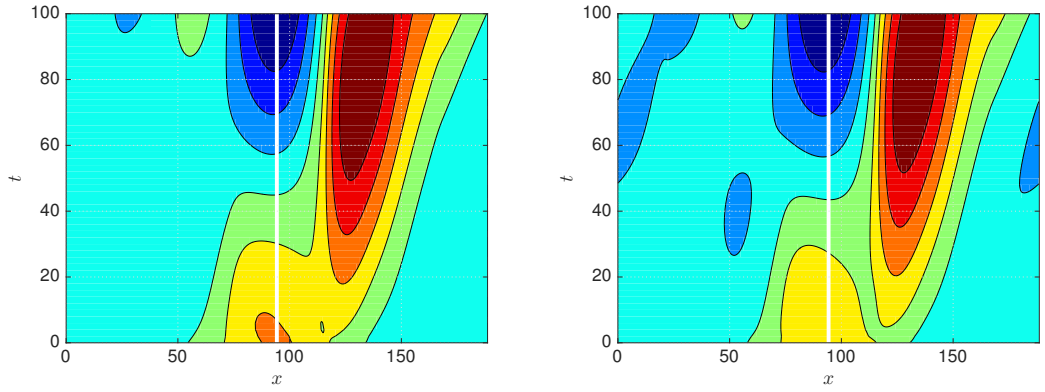

Figure 3.77: *Normalised contour plot showing the propagation of the perturbation, with a solid white line showing the origin of the perturbation, for* $R = 1.25$, $K = 3364.5$, $W_e = 45$, $A_0 = 1.462$ *and* $L_0 = 57$ *for a rectangular wall in the long-wave case (left) and the WIBL case (right).*

and in both models the perturbation can be seen growing in time and being convected away from its original position.

We now examine our final case, where we have $W_e = 200$ for $A_0 = 1.462$ and $L_0 = 57$. In Figure 3.82 we see the time evolution of the perturbation to our steady state for both models, for which we see near-identical qualitative behaviour of the perturbation growing in time and travelling downstream, consistent with a transient instability. Figures 3.83 and 3.85 share many features – the absolute value of the perturbation at its origin was found to initially decrease in time for both models in Figure 3.83, then increase slightly as the perturbation is convected downstream.

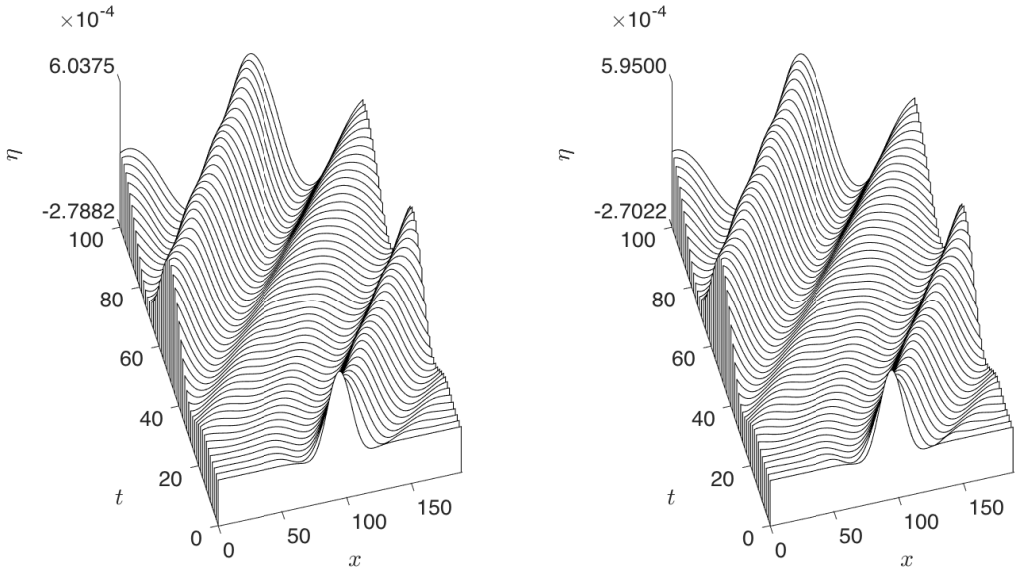

Figure 3.78: *Time evolution of the perturbation η originating at midpoint $x = 2L$ with $R = 1.25$, $K = 3364.5$, $W_e = 200$, $A_0 = 0.27$ and $L_0 = 57$ for a rectangular wall in the long-wave case (left) and the WIBL case (right).*

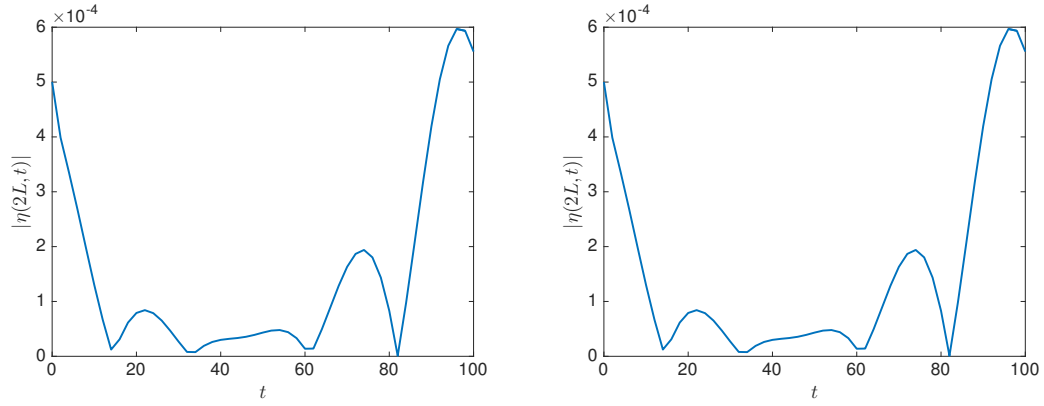

Figure 3.79: *Time evolution of the absolute value of the perturbation at the midpoint $x = 2L$ for $R = 1.25$, $K = 3364.5$, $W_e = 200$, $A_0 = 0.27$ and $L_0 = 57$ for a rectangular wall in the long-wave case (left) and the WIBL case (right).*

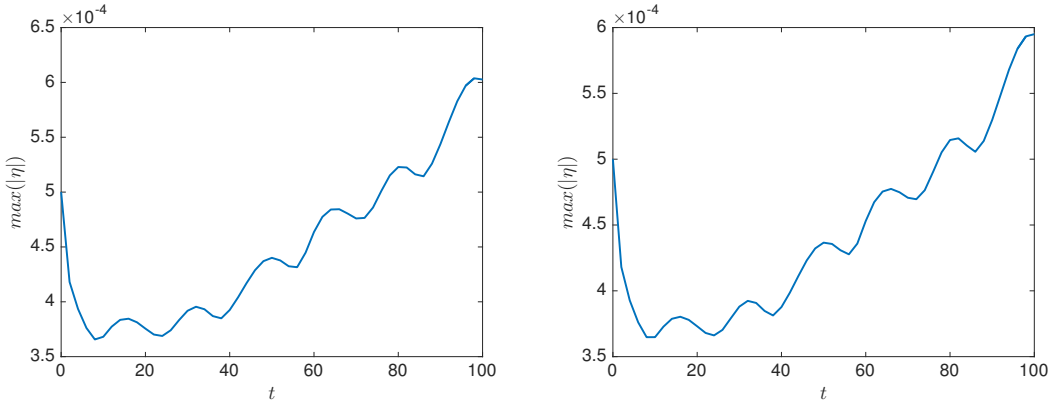

Figure 3.80: *Time evolution of the maximum of the absolute value of the perturbation for $R = 1.25$, $K = 3364.5$, $W_e = 200$, $A_0 = 0.27$ and $L_0 = 57$ for a rectangular wall in the long-wave case (left) and the WIBL case (right).*

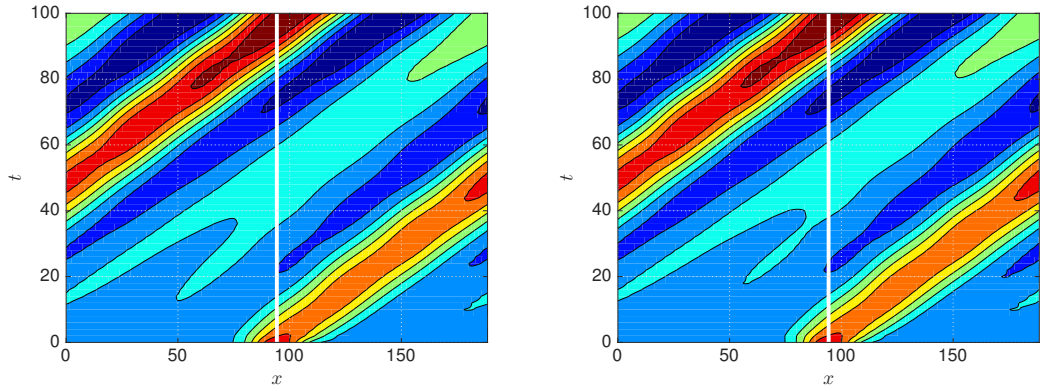

Figure 3.81: *Normalised contour plot showing the propagation of the perturbation, with a solid white line showing the origin of the perturbation, for* $R = 1.25$, $K = 3364.5$, $W_e = 200$, $A_0 = 0.27$ *and* $L_0 = 57$ *for a rectangular wall in the long-wave case (left) and the WIBL case (right).*

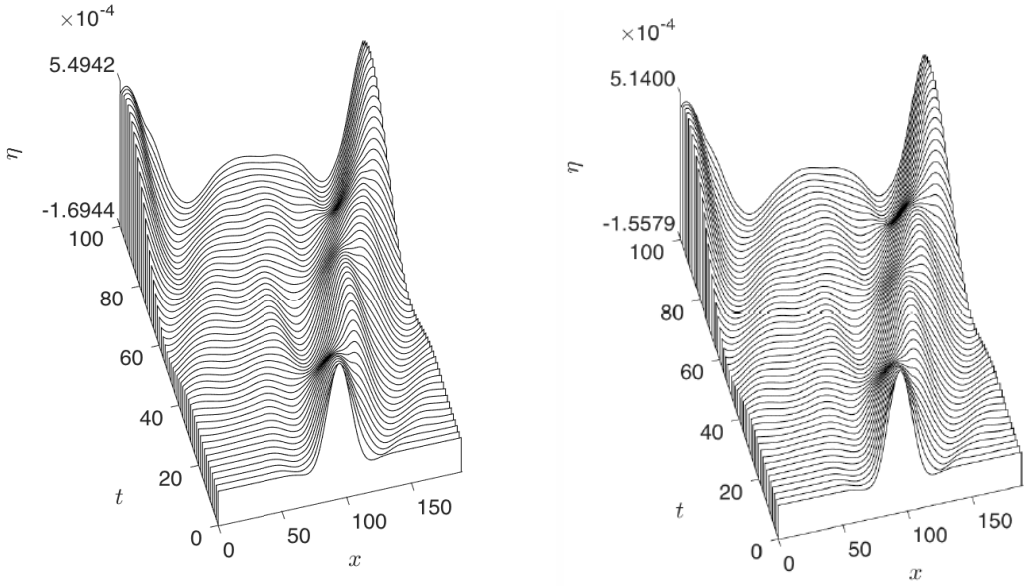

Figure 3.82: *Time evolution of the perturbation* η *originating at midpoint* $x = 2L$ *with* $R = 1.25$, $K = 3364.5$, $W_e = 200$, $A_0 = 1.462$ *and* $L_0 = 57$ *for a rectangular wall in the long-wave case (left) and the WIBL case (right).*

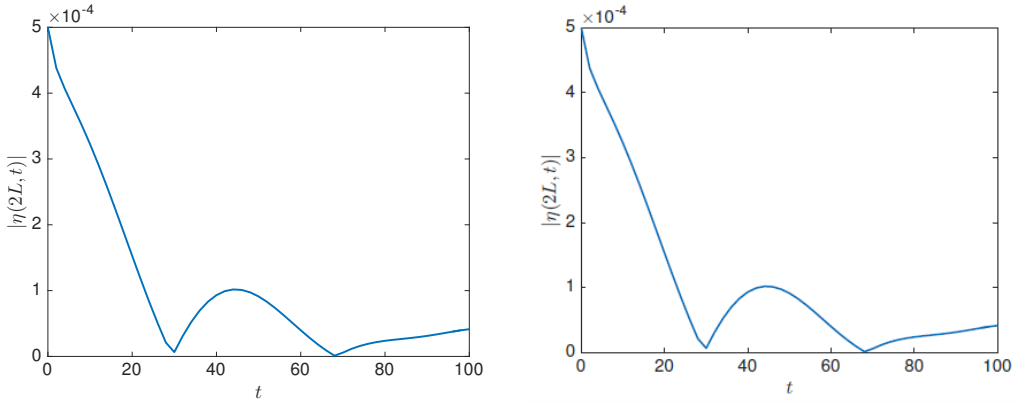

Figure 3.83: *Time evolution of the absolute value of the perturbation at the midpoint* $x = 2L$ *for* $R = 1.25$, $K = 3364.5$, $W_e = 200$, $A_0 = 1.462$ *and* $L_0 = 57$ *for a rectangular wall in the long-wave case (left) and the WIBL case (right).*

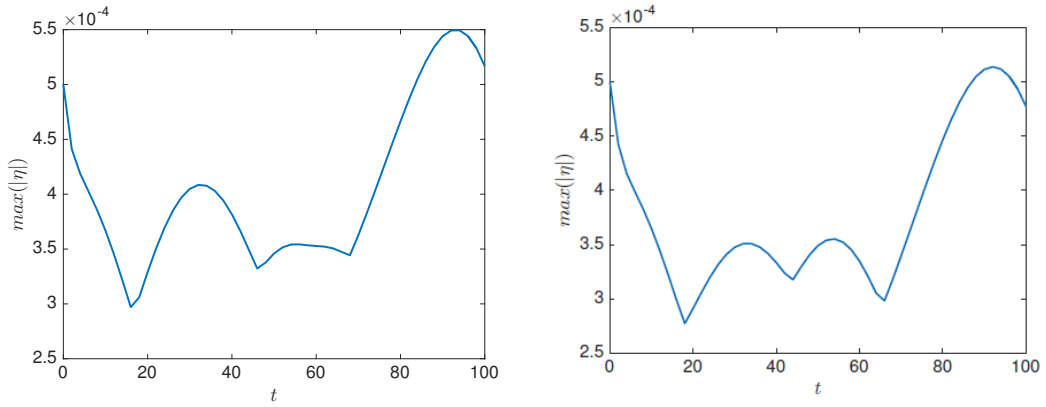

Figure 3.84: *Time evolution of the maximum of the absolute value of the perturbation for* $R = 1.25$, $K = 3364.5$, $W_e = 200$, $A_0 = 1.462$ *and* $L_0 = 57$ *for a rectangular wall in the long-wave case (left) and the WIBL case (right).*

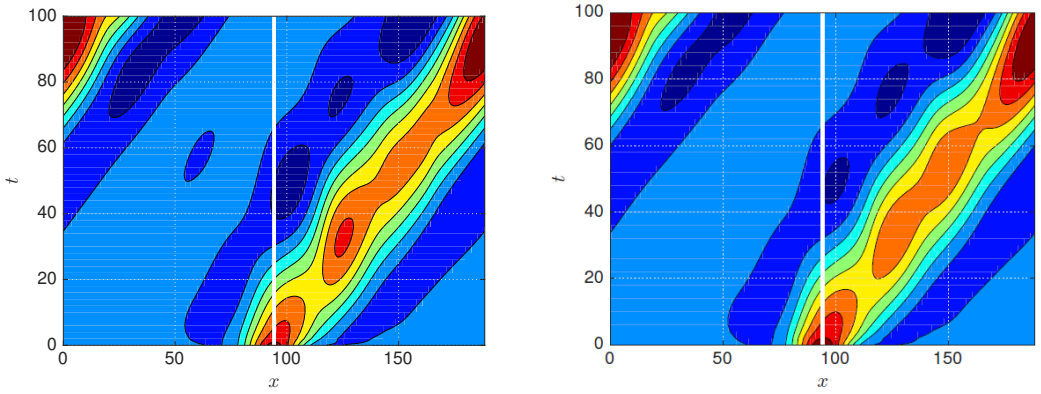

Figure 3.85: *Normalised contour plot showing the propagation of the perturbation, with a solid white line showing the origin of the perturbation, for* $R = 1.25$, $K = 3364.5$, $W_e = 200$, $A_0 = 1.462$ *and* $L_0 = 57$ *for a rectangular wall in the long-wave case (left) and the WIBL case (right).*

In Figure 3.85 we see overall growth for both models, indicative of instability, the implication of which is that both steady-states are transiently unstable. We may thus summarise the findings for the rectangular wall as follows. For $A_0 = 0.27$, the steady-state solutions to both the long-wave and WIBL models were found to be stable for $W_e = 0$ and $W_e = 45$, and convectively unstable for $W_e = 200$. For the case of $A_0 = 1.462$, it was found in both models that the steady-states were convectively unstable for $W_e = 0$ and $W_e = 45$, and transiently unstable for $W_e = 200$. We thus see that a convective instability may be 'reduced' to a transient instability solely by the inclusion of a normal electric field.

3.5 Critical Reynolds numbers for flows over topographical substrates

Here we numerically compute the critical Reynolds numbers for a given domain as a function of our rescaled wall amplitude A_0 for both the long-wave and WIBL models and for a variety of electric Weber numbers with both sinusoidal and rectangular topography, in a partial extension of the work done by Tseluiko, Blyth and Papageorgiou [98] for the long-wave model in the absence of a normal electric field. We begin with an initial guess for the critical Reynolds number which is based on the previously derived equation (3.17) which depends on our electric Weber number:

$$R_c = \frac{5\cot\beta}{4} - \frac{5W_e^2}{8C}. \tag{3.70}$$

3.5.1 Long-wave model

We start with the aforementioned formula for the critical Reynolds number (3.70) for a flat wall in the case of a normal electric field, and we calculate its value for a given set of parameters. We then assume that we have a Nusselt flat film solution, and try to find the corresponding critical Reynolds number using our initial guess, with the MATLAB [36] 'fzero' algorithm employed using a combination of quadratic interpolation, secant and bisection methods. Following this, we incrementally increase the amplitude of the wall, then recompute our steady-state now in the case of a non-flat wall using a trust-region dogleg method of MATLAB [36] implemented as an 'fsolve' algorithm. With this new film thickness array corresponding to the determined steady solution, we then examine the effect of our linearised operator on the perturbation to our film thickness (and corresponding flux in the case of the WIBL model). If we then introduce the standard Floquet-Bloch mapping for the perturbation, $h_1 \to e^{iKx}\tilde{h}_1(x)$, where $K \in [-\pi/L, \pi/L]$ is the Bloch wavenumber, then the eigenvalues of our linearised operator determine whether our steady-state is stable or unstable [47, 98]. Starting from $-\pi/L$ we increase K in increments of $\pi/(50L)$ up until π/L, and for each value we recompute our eigenvalues and check to see whether any are above some prescribed tolerance (here taken as 10^{-9}). If such a K exists, then the essential spectrum of our linearised operator is shifted into the right half-plane and we are dealing with a spectrally unstable

steady-state, whereas if this K does not exist, we know we are dealing with a spectrally stable solution. We also note that due to the nonlocal Hilbert transform term, we solve our linearised operator in Fourier space, and a full derivation of this representation in Fourier space may be found for the WIBL model in the following subsection, although is not included for the long-wave model for brevity.

In Figure 3.86 we see the relationship between the critical Reynolds number and the rescaled amplitude sinusoidal wall topography in the case of $L_0 = 150$ for $W_e = 0, 10, 50$ and 100 for the long-wave model. Due to variations in the critical Reynolds number being small in the case of $W_e = 50$ and $W_e = 100$, at least relative to the variations in the case of $W_e = 0$ and $W_e = 10$, we show a zoom-in of these two cases in Figure 3.87 on the left-hand side and right-hand side, respectively. The most obvious effect of the electric field is the overall lowering of the critical Reynolds number. In the case of no electric field, we know both analytically and from our numerical results that in the case of zero topographical amplitude the critical Reynolds number is 1.25, whereas in the case of $W_e = 50$ for example, we find that the critical Reynolds number in the case of no topography is instead $R_c = 0.936$.

However, there are also more complicated dynamics which can be observed. For example, in the case of no electric field, we find that the critical Reynolds number monotonically increases until the wall amplitude $A_0 \approx 18.25$ is reached, at which point the critical Reynolds number begins monotonically decreasing, and eventually rapidly decays once the wall amplitude is increased past $A_0 \approx 22.37$. In the case of $W_e = 10$ however, our results are already qualitatively different - we instead see that the critical Reynolds number instead decreases initially, until the wall amplitude reaches approximately $A_0 \approx 8.35$. Once again we see the characteristic growth, although now the region of increasing critical Reynolds number terminates for $A_0 \approx 19.35$, such that the aforementioned rapid decay now occurs for larger sinusoidal wall amplitudes than was observed in the case of no electric field. In the case of $W_e = 50$, we again see drastically qualitatively different behaviour. The critical Reynolds number now monotonically decreases for all sinusoidal wall amplitudes, as observed in Figure 3.87. We also observe that the variations in the critical Reynolds number are much smaller in comparison to the previously discussed cases of smaller electric Weber numbers. Finally, in the $W_e = 100$ case we see the opposite dynamics; the critical Reynolds number now increases monotonically with our rescaled wall amplitude, although again we observe much smaller

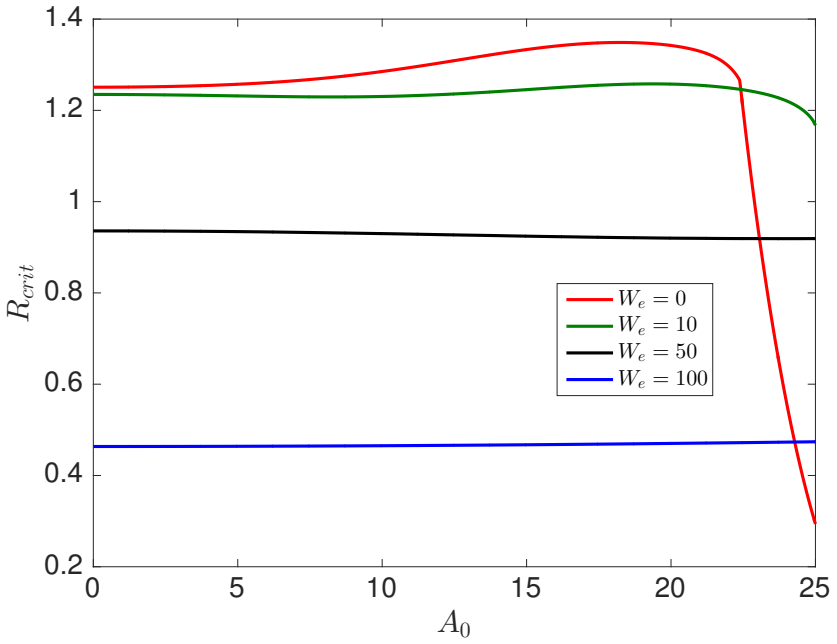

Figure 3.86: *Plot of the critical Reynolds number against the rescaled sinusoidal wall amplitude for* $W_e = 0$ *(red),* $W_e = 10$ *(green),* $W_e = 50$ *(black) and* $W_e = 100$ *(blue) for* $L_0 = 150$ *in the long-wave model.*

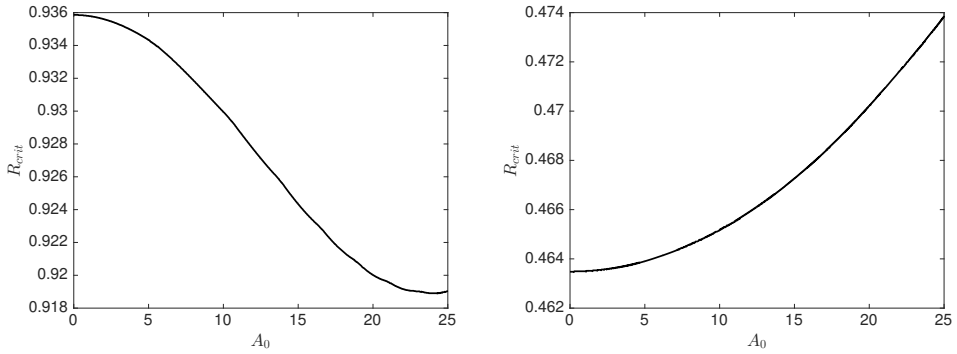

Figure 3.87: *Plot of the critical Reynolds number against the rescaled sinusoidal wall amplitude in the case of* $W_e = 50$ *(left) and* $W_e = 100$ *(right) for* $L_0 = 150$ *in the long-wave model.*

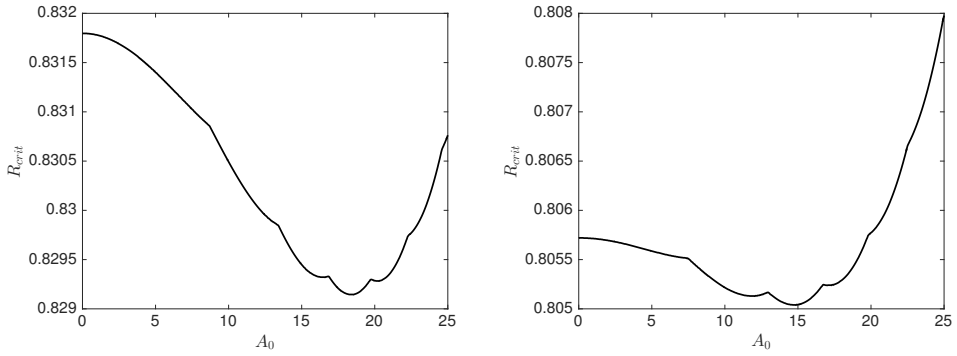

Figure 3.88: *Plot of the critical Reynolds number against the rescaled sinusoidal wall amplitude in the case of* $W_e = 60$ *(left) and* $W_e = 62.5$ *(right) for* $L_0 = 150$ *in the long-wave model.*

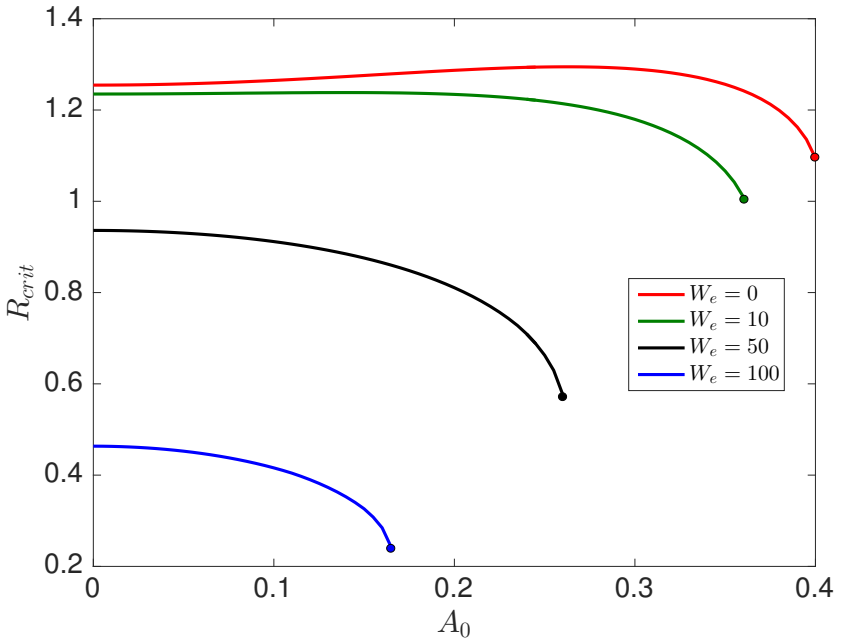

Figure 3.89: *Plot of the critical Reynolds number against the rescaled rectangular wall amplitude for* $W_e = 0$ *(red),* $W_e = 10$ *(green),* $W_e = 50$ *(black) and* $W_e = 100$ *(blue) for* $L_0 = 57$ *in the long-wave model.*

variations in the critical Reynolds number in comparison to the $W_e = 0$ and $W_e = 10$ cases.

Following these results, we choose to examine intermediary electric Weber numbers and the transition between the monotonically decreasing behaviour observed for $W_e = 50$ and the monotonically increasing behaviour observed for $W_e = 100$. Figure 3.88 shows the relation between R_c and A_0 for $W_e = 60$ and $W_e = 62.5$. For $W_e = 62.5$, we see that the relationship appears similar to the $W_e = 100$ case, although we also observe curious behaviour for intermediary amplitudes where the critical Reynolds number decreases and increases in a seemingly periodic way – after the start of this behaviour at approximately $A_0 \approx 7.5$, we find that every increase in A_0 by ~ 4 corresponds to a discontinuity in the slope. For $W_e = 60$ we observe the same 'lumpy' behaviour observed for $W_e = 62.5$, although now it is clear that we are closer to the transition from the $W_e = 50$ side than the $W_e = 100$ side, as evident from the overall decrease in critical Reynolds number as A_0 increases from $A_0 = 0$ to $A_0 = 25$, as opposed to the overall growth observed for $W_e = 62.5$. The aforementioned 'lumpy' behaviour could perhaps be explained by different pairs of complex eigenvalues crossing the imaginary axis for various scaled wall amplitudes, although a more thorough investigation is left for future work.

For the long-wave model then, we may hypothesise the following: it would appear that for small electric field strengths (i.e. $W_e \approx 0 \sim 10$), both small-amplitude and large amplitude sinusoidal topography are destabilising, whereas moderate wall amplitudes are stabilising. For sufficiently large electric field strengths ($W_e \gtrapprox 100$), the sinusoidal topography is stabilising for all wall amplitudes. For intermediary electric field strengths we find that there is a transition in the range $W_e \approx (60 - 62.5)$ whereby the sinusoidal wall changes from being destabilising at $A_0 = 25$ to stabilising at $A_0 = 25$.

For rectangular topography instead, we find the relationship between R_c and A_0 given in Figure 3.89. For $W_e = 0$ we observe that for scaled rectangular wall amplitudes up to $A_0 = 0.27$ the wall is stabilising compared to a flat wall, and the critical Reynolds number increases with scaled wall amplitude. Past this scaled amplitude, we find that the wall is still stabilising, but the stationary point signifies the change in the rectangular topography from stabilising to destabilising, and the critical Reynolds number now rapidly decreases with wall amplitude, until we reach $A_0 \approx 0.4$, at which point we no longer find solutions for R_c. We emphasise that this point corresponding to the lack of solutions is caused by neither the stopping condition for the film thickness $h_{min} = 0.005$ nor the discretisation parameters, and that this behaviour is also observed for the WIBL model with a rectangular wall. Due to the clear relationship between this lack of solutions and the electric Weber number, we also do not expect that this is a numerical issue related perhaps to the steepness of the rectangular walls and the well-known Gibbs phenomenon common when using Fourier mode representation. One possible explanation may be that we have turning points at the end-points of the curves, which correspond to the onset of a multiplicity of solutions and hence we would have a large change between the steady solutions at the end-points and the steady solutions for slightly larger scaled wall amplitudes.

For $W_e = 10$ the wall is stabilising for amplitudes up until $A_0 = 0.16$ at which point the wall becomes rapidly destabilising as we increase the amplitude, until we reach a similar point as in the $W_e = 0$ case, whereby we stop finding solutions for R_c, and we note that this point is at $A_0 = 0.36$ instead of $A_0 = 0.4$. For $W_e = 50$ and $W_e = 100$ we find the wall destabilising for all amplitudes, and similarly note the dependence of the break-point on the electric Weber number. We may also observe the overall decrease in the critical Reynolds number which is observed as we increase the electric Weber number.

3.5.2 WIBL model

We now proceed similarly for the WIBL model. We begin with an initial guess for the critical Reynolds number using the same equation (3.70) as in the long-wave case, which includes the effects of the electric field. We then solve a reduced equation for the film thickness, where we make use of the fact that as we are purely interested in the transition between stability and instability, and no longer concerned with distinguishing between types of instability, we are aware that for a steady-state, there is no temporal dependence for the film thickness, and as such our kinematic condition implies that we have constant flux. We can then substitute this constant flux $q(x,t) = q_0$ and the steady-state film thickness $h_0(x,t) = h_0(x)$ into our linearised equations (3.18) and (3.19) and analyse the behaviour of the perturbations to the steady-state solution.

We use the Floquet-Bloch representation for the perturbations, $h_1 \to e^{iKx}\tilde{h}_1(x)$, $q_1 \to e^{iKx}\tilde{q}_1(x)$. In matrix representation we thus have

$$\omega \begin{bmatrix} \tilde{h}_1 \\ \tilde{q}_1 \end{bmatrix} = e^{-iKx} \begin{bmatrix} 0 & \mathrm{L}_{12}(e^{-iKx}\tilde{q}_1) \\ \mathrm{L}_{21}(e^{-iKx}\tilde{h}_1) & \mathrm{L}_{22}(e^{-iKx}\tilde{q}_1) \end{bmatrix} \begin{bmatrix} \tilde{h}_1 \\ \tilde{q}_1 \end{bmatrix}, \tag{3.71}$$

or equivalently

$$\omega \begin{bmatrix} \tilde{h}_1 \\ \tilde{q}_1 \end{bmatrix} = \begin{bmatrix} 0 & \mathrm{L}_{12}^K \\ \mathrm{L}_{21}^K & \mathrm{L}_{22}^K \end{bmatrix} \begin{bmatrix} \tilde{h}_1 \\ \tilde{q}_1 \end{bmatrix}. \tag{3.72}$$

Making use of the fact that

$$\mathrm{L}_{12}^K \tilde{q}_1 = -e^{-iKx}(e^{iKx}\tilde{q}_1)_x = -(iK\tilde{q}_1 + \tilde{q}_{1x}), \tag{3.73}$$

$$\mathrm{L}_{22}^K \tilde{q}_1 = e^{-iKx}(c_0 e^{iKx}\tilde{q}_1 + (c_1 e^{iKx}\tilde{q}_1)_x) = c_0\tilde{q}_1 + c_1(iK\tilde{q}_1 + \tilde{q}_{1x}), \tag{3.74}$$

$$\begin{aligned} \mathrm{L}_{21}^K \tilde{q}_1 &= e^{-iKx}\Big(b_0 e^{iKx}\tilde{h}_1 + b_1(e^{iKx}\tilde{h}_1)_x + b_2(e^{iKx}\tilde{h}_1)_{xxx} + b_3\mathcal{H}\Big[(e^{iKx}\tilde{h}_1)_{xx}\Big]\Big) \\ &= b_0\tilde{h}_1 + b_1(iK\tilde{h}_1 + \tilde{h}_{1x}) + b_2((iK)^3\tilde{h}_1 + 3(iK)^2\tilde{h_{1x}} + 3iK\tilde{h}_{1xx} \\ &\quad + \tilde{h}_{1xxx}) + b_3 e^{-iKx}\mathcal{H}\Big[(e^{iKx}\tilde{h}_1)_{xx}\Big], \end{aligned} \tag{3.75}$$

we now consider our operators in Fourier space, as we seek to simplify our Hilbert transform term. Such consideration yields

$$\mathcal{F}(iK\tilde{h}_1 + \tilde{h}_{1x}) = i(K+k)\widehat{\tilde{h}}_1(k), \tag{3.76}$$

$$\mathcal{F}((iK)^3\tilde{h}_1 + 3(iK)^2\tilde{h}_{1x} + 3iK\tilde{h}_{1xx} + \tilde{h}_{1xxx}) = [i(K+k)]^3\widehat{\tilde{h}}_1(k), \tag{3.77}$$

$$\begin{aligned}\mathcal{F}\Big(e^{-iKx}\mathcal{H}\Big[(e^{iKx}\tilde{h}_1)_{xx}\Big]\Big) &= \mathcal{F}\Big(e^{-iKx}\mathcal{H}\Big[e^{iKx}((iK)^2\tilde{h}_1 + 2iK\tilde{h}_{1x} + \tilde{h}_{1xx})\Big]\Big),\\ &= -i\,\mathrm{sgn}(k+K)\mathcal{F}\Big((iK)^2\tilde{h}_1 + 2iK\tilde{h}_{1x} + \tilde{h}_{1xx}\Big),\\ &= -i\,\mathrm{sgn}(k+K)(i(k+K))^2\widehat{\tilde{h}}_1(k).\end{aligned} \tag{3.78}$$

We hence have a representation for our linearised system which can be analysed numerically in Fourier space, and the spectrum of the linearised operator can be obtained, providing the necessary information on the stability of the corresponding steady-state solution. We first produce diagrams showing the relationship between R_c and A_0 for the WIBL model in the sinusoidal case, and discuss the results.

In Figure 3.92 we see that the sinusoidal wall is very strongly stabilising at large amplitudes for $W_e = 0$, and significantly less stabilising at these amplitudes if we instead have $W_e = 50$ or $W_e = 100$. Although we note that increasing the electric field strength shifts the curves down at high amplitudes, we still observe that in all cases the critical Reynolds number increases monotonically with our sinusoidal wall amplitude, such that the effect of the topography and the electric field in tandem does not change depending on the electric field strength – the sinusoidal wall is always stabilising and the critical Reynolds number increases with A_0. In the $W_e = 0$ case we note a point at $A_0 \approx 18$ that signals a decrease in the rate of increase in the critical Reynolds number as a function of the wall amplitude. In the $W_e = 10$ case we see this point shifted to the right, and for higher electric field strengths it does not appear and presumably occurs instead at higher wall amplitudes than those included here, which in turn would approach the limit of minimum film thickness.

In comparing the WIBL and long-wave models in the case of a sinusoidal wall then, we may say the following. Firstly, we note the large discrepancy between predicted critical Reynolds numbers; in the long-wave case we observe the critical Reynolds number never increasing past $R_c = 1.35$ for any investigated value of amplitude of electric field strength, whereas in the WIBL model we see that for $W_e = 0$ we have $R_c = 27.16$, a surprisingly large value. Direct comparisons are shown in Figure 3.91 for the cases

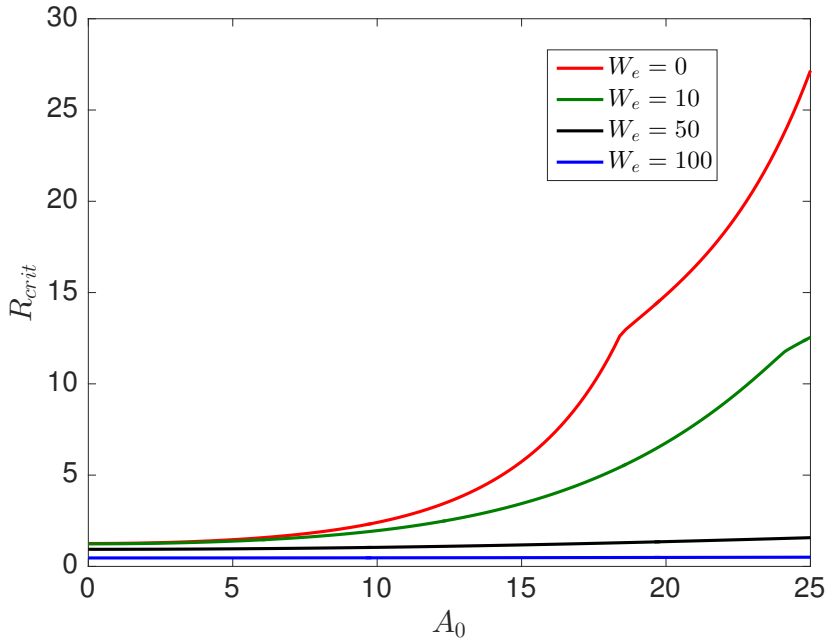

Figure 3.90: *Plot of the critical Reynolds number against the rescaled sinusoidal wall amplitude for $W_e = 0$ (red), $W_e = 10$ (green), $W_e = 50$ (black) and $W_e = 100$ (blue) for $L_0 = 150$ in the WIBL model.*

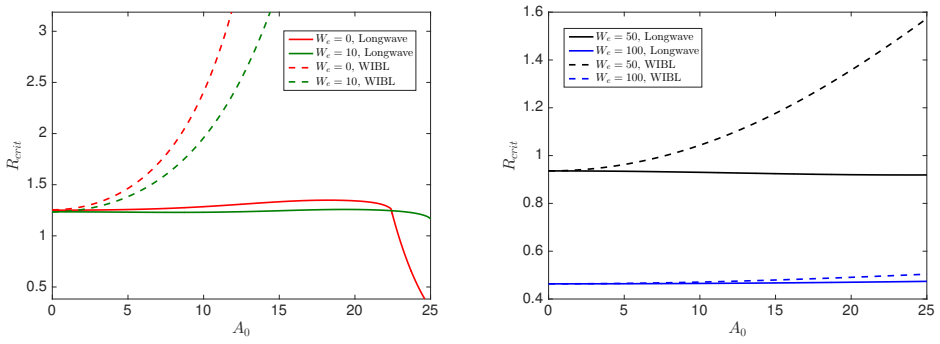

Figure 3.91: *Plot of the critical Reynolds number against the rescaled sinusoidal wall amplitude in the case of $W_e = 0, 10$ (left) and $W_e = 50, 100$ (right) for $L_0 = 150$ in the long-wave and WIBL models.*

of $W_e = 0, 10$ (left panel) and $W_e = 50, 100$ (right panel). In general we see that for larger electric Weber numbers there is less discrepancy between the two models, with the $W_e = 100$ case showing only small quantitative differences between the long-wave and WIBL models. Contrariwise in the case of $W_e = 0$ we not only see a large difference in the magnitudes of the critical Reynolds number, but also a fundamentally different relationship between R_c and W_e. In the WIBL model the sinusoidal wall is strongly stabilising for all amplitudes, whereas in the long-wave model the wall is weakly destabilising for small amplitudes, somewhat strongly destabilising for large amplitudes, and weakly stabilising for intermediate amplitudes.

This behaviour of the critical Reynolds number for the WIBL model is consistent with

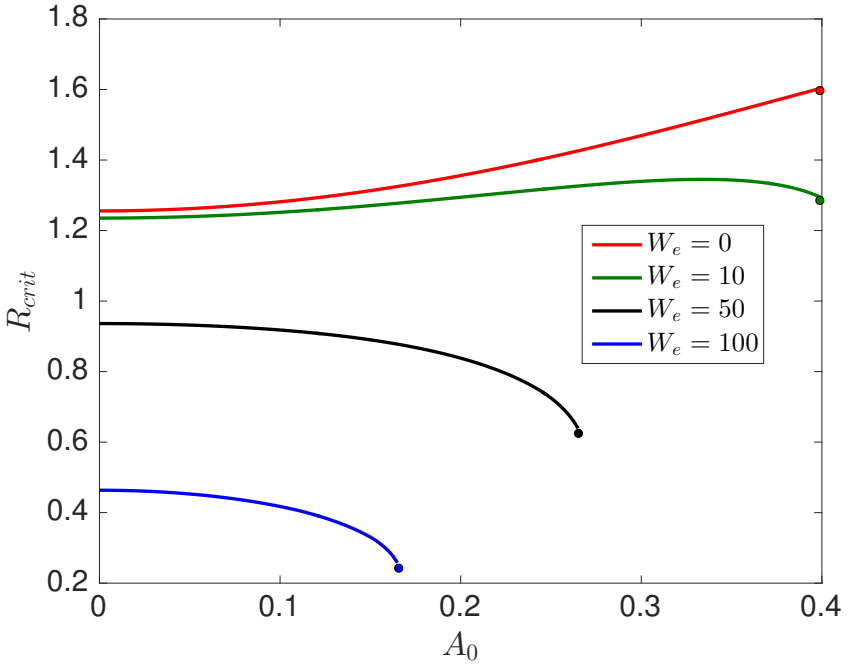

Figure 3.92: *Plot of the critical Reynolds number against the rescaled rectangular wall amplitude for $W_e = 0$ (red), $W_e = 10$ (green), $W_e = 50$ (black) and $W_e = 100$ (blue) for $L_0 = 57$ in the WIBL model.*

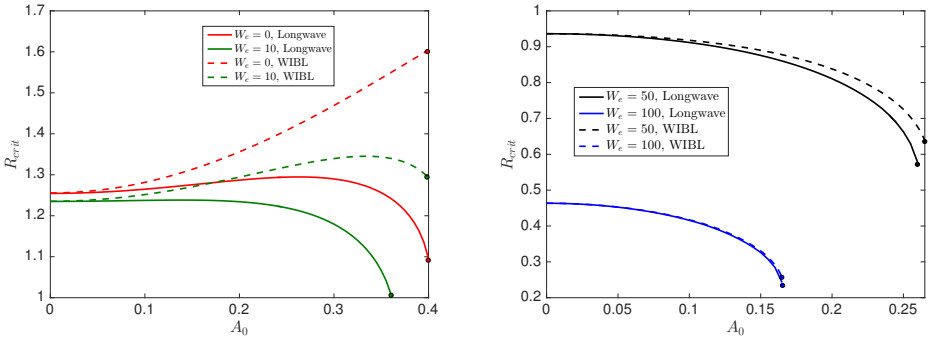

Figure 3.93: *Plot of the critical Reynolds number against the rescaled rectangular wall amplitude in the case of $W_e = 0, 10$ (left) and $W_e = 50, 100$ (right) for $L_0 = 150$ in the long-wave and WIBL models.*

the time-dependent simulations carried out earlier, where scaled sinusoidal wall amplitudes of $A_0 = 17$ and $A_0 = 24$ were stabilising for both $W_e = 0$ and $W_e = 45$, with only the $W_e = 200$ case causing convective instabilities for both scaled amplitudes. As the $W_e = 200$ case is unstable even for a flat wall at zero Reynolds number, the numerical approach outlined previously fails here, and if we wish to investigate $W_e \geq 200$ a new methodology is required.

In the case of a rectangular wall, the relationship between R_c and A_0 for the WIBL model is instead shown in Figure 3.92, where we observe the following. In the case of $W_e = 0$ we find that R_c increases proportionally with the rectangular wall amplitude

and is hence stabilising for all amplitudes. In the $W_e = 10$ case however, we instead observe that the wall is stabilising up until $A_0 \approx 0.34$ at which point the wall begins to become destabilising, although still remains more stabilising than the flat wall case. For $W_e = 50, 100$ we instead see that the wall is destabilising for all amplitudes, and the degree to which the wall is destabilising is proportional to the amplitude of the wall. We also, of course, see that as we increase our electric Weber number, it has the primary effect of lowering the critical Reynolds number, due to the known destabilising properties.

Figure 3.93 shows in the cases of $W_e = 0, 10$ and $W_e = 50, 100$ the comparison between the long-wave and WIBL models in terms of predictions for the critical Reynolds number as a function of scaled wall amplitude in the rectangular wall case. Generally we see much closer agreement between the two models whilst using rectangular topography instead of sinusoidal; for $W_e = 50, 100$ we see very little qualitative difference between the two models except that the WIBL model terminates at slightly greater scaled wall amplitudes and that the critical Reynolds numbers near these stopping points are slightly greater as well.

In the $W_e = 0, 10$ cases we observe larger discrepancies between the models; for $W_e = 0$ the long-wave model is destabilising at large amplitudes, as opposed to the WIBL model which is strongly stabilising at large amplitudes and indeed stabilising everywhere. For $W_e = 10$ the long-wave model predicts that the wall is always destabilising, whereas in the WIBL model for $W_e = 10$ we instead have that the wall is stabilising up until $A_0 \approx 0.34$, at which point it becomes less stabilising for greater amplitudes but still stabilising overall.

Chapter 4

Bifurcation diagrams of steady-state and time-periodic solutions

4.1 Methodology

Here we outline the methodology involved in solving our equation systems numerically using a pseudospectral Fourier representation. We first assume that the PDE may be approximated by an infinite-dimensional system of ODEs, and subsequently the corresponding time-periodic solutions and steady-states are then represented as periodic orbits and fixed points, respectively, of a finite-dimensional approximation of this infinite-dimensional system, following the methodology outlined by Lin et al. [50]. When solving the long-wave model, our solution is represented as a summation of time-dependent Fourier coefficients for h, whereas when solving the WIBL model we instead have our solution as a summation of time-dependent Fourier coefficients for both h and q, i.e. we have

$$h(x,t) = \sum_{k=-\infty}^{\infty} \widehat{h}_k(t) e^{ikx}, \tag{4.1}$$

$$q(x,t) = \sum_{k=-\infty}^{\infty} \widehat{q}_k(t) e^{ikx}. \tag{4.2}$$

In this way, we are able to represent our original PDE as a system of ODEs in Fourier space of the form

$$\frac{d\widehat{h}_k}{dt} = F_k(\widehat{\boldsymbol{h}}), \tag{4.3}$$

for the long-wave equation or of the form

$$\frac{d\widehat{h}_k}{dt} = G_k(\widehat{\boldsymbol{q}}), \tag{4.4}$$

$$\frac{d\widehat{q}_k}{dt} = H_k(\widehat{\boldsymbol{h}}, \widehat{\boldsymbol{q}}), \tag{4.5}$$

for the WIBL model, where $k \in \mathbb{Z}$ and $\widehat{\boldsymbol{h}}$ denotes the vector of the Fourier coefficient for h and $\widehat{\boldsymbol{q}}$ denotes the vector of the Fourier coefficient for q. The number of modes in Fourier space is truncated, and here we truncate it to $-N \leq k \leq N$, where we typically use $N = 450$ for both models. When solving the WIBL model, we have $4k + 2$ Fourier modes ($2k+1$ from both h and q), $4k+1$ of which are unknown Fourier modes ($2k$ from h and $2k+1$ from q) due to the integral constraint fixing the zeroth Fourier mode of h. In the long-wave model we instead have $2k+1$ Fourier modes for h, where $2k$ are unknown Fourier modes and similarly we use an integral constraint which is equivalent to fixing the average film thickness within the liquid and, therefore, to fixing the zeroth Fourier coefficient of h. Also included for both models is a de-aliasing procedure, whereby we extend the number of Fourier modes in computing Fourier transforms by M such that we are able to perform the nonlinear operations in real space and subsequently ignore the contributions of these modes in Fourier space. An FFTW [28] algorithm is employed and Auto-07p [24] software is used for the pseudo-arclength continuation (where we typically continue in the amplitude of the wall A) such that steady-states and the location and classification of bifurcations may then be determined. Allgower and Georg [2] provide a detailed overview of related numerical continuation methods, whereas Kuznetsov [48] gives a comprehensive summary of applied bifurcation theory relevant to the present work.

Recent work by Lin et al. [51] details a numerical method for continuation which is applicable for a long-wave model which is affected by a normal electric field, and allows for the finding of time-periodic solutions in the travelling frame of reference, although this is not considered here. Due to our a posteriori knowledge of the types of bifurcations which are found whilst performing amplitude continuation for our models, we shall only give an overview of the most relevant bifurcations and dynamical classifications, namely saddle-node bifurcations, pitchfork bifurcations and Hopf bifurcations, although a comprehensive review of bifurcations methods in the context of fluid dynamics is given by Djikstra et al. [23], who also discuss quasi-periodic behaviour and chaotic attractors. For more insight into Fourier spectral methods within fluid mechanics the reader is referred to the monograph by Boyd [8], in addition to the monograph

by Karniadakis and Sherwin [44] and the monograph by Canuto et al. [10]. For spectral approaches within fluid mechanics using specifically MATLAB [36] we further have the work by Pozrikidis [64] and the well-known monograph by Trefethen [94].

In a saddle-node bifurcation, a pair of equilibria (corresponding to two different steady-state solution in the context of our work) coalesce at the bifurcation point (a certain value of the bifurcation parameter, such as the wall amplitude in the context of our work) and annihilate each other as the bifurcation parameter is increased or decreased. One of the equilibria must be more unstable than the other one (which can be stable). To be more precise, it must have a real positive eigenvalue which approaches the imaginary axis and crosses it at the saddle-node bifurcation as the bifurcation parameter varies and the equilibrium follows the bifurcatin curve.

In the context of our work, a pitchfork bifurcation to a family of steady-state solutions corresponds to the appearance of two additional families of steady-state solutions at the bifurcation point. The stability properties of the solutions of the main family change at the bifurcation point. To be more precise, there is a real eigenvalue that crosses the imaginary axis at the bifurcation point as the bifurcation parameter is varied. If all the other eigenvalues remain negative, we say that the pitchfork bifurcation is supercritical if the steady-state solutions of the two new families of solutions are stable and subcritical if the steady-state solutions of the two new families of solutions are unstable.

We may intuitively think of a Hopf bifurcation in the following way, as a paraphrase of the elegant statement by Marsden and McCracken [55] discussing the Abraham [1] picture of bifurcation; let us assume that we have some point attractor on a three-dimensional landscape, with the basin of attraction taking parabolic form. We may think of the time evolution of the system to be represented by the flow of water on the landscape. A Hopf bifurcation is then represented by a small hill forming at the bottom of this point attractor basin, such that rather than having a single point attractor, we now have a circular formation at the bottom of the basin. This circle represents a time-periodic solution to our system, and the basin of attraction now excludes the original point attractor. The time-periodic solution following the Hopf bifurcation is stable if the bifurcation is supercritical, and hence the time-periodic steady-state remains within a neighbourhood of the original steady-state prior to the bifurcation. In the case of a subcritical Hopf bifurcation, we instead have the interesting case of an orbitally unstable solution. Unstable periodic solutions are not typically physically observable in practice however, as slight perturbations may disturb the periodic behaviour, and hence

novel techniques are required to prepare the system such that these time-periodic solutions appear, see, for example, the work of Hassard, Kazarinoff and Wan [31] for a detailed approach in such cases.

4.2 Bifurcation diagrams

4.2.1 $L = 50$

Continuation is performed using Auto07p software [24] and the film thickness solutions are characterised by the norm

$$\|h_0\|^2 = \frac{1}{2L_c}\int_0^{2L_c} h_0^2(x)dx. \tag{4.6}$$

We start from the Nusselt flat film solution, and continue in the wall amplitude, stopping once the film thickness becomes zero. The wall period is $2L$ and the computational domain is chosen to be $4L$.

In Figure 4.1 we see steady-state branches in the case of no electric field, and with electric field of various strengths for $L = 50$ in the long-wave model for a sinusoidal wall. In the case of $W_e = 0$ corresponding to no electric field, we find a stable main branch of solution of period $2L$ which undergoes a subcritical pitchfork bifurcation, at which point the main branch becomes unstable, and a secondary subharmonic branch(es) of period $4L$ emerge, see the red dashed line. Note that each point of the red dashed line actually corresponds to a pair of solutions which can be obtained from each other by a shift in x by $2L$. The subharmonic branch is found to have a turning point (a saddle-node bifurcation), and the branch is unstable for all amplitudes. In this $W_e = 0$ case we fully recover the main branch and subharmonic branch found by Tseluiko, Blyth and Papageorgiou [98] for non-electrified film flow for the same parameter values. As the electric field strength increases, we find the main and subharmonic branches shift to the right and downwards. Both of these behaviours are explained in terms of the phase-shift between the free surface and the wall. For a non-electrified film flow it is known that the phase shift between the free surface and the topography is inherently negative, such that the liquid lags behind the wall to the left, see, for example, Tseluiko and Papageorgiou [99]. As the electric field increases, the phase shift increases (but decreases in absolute value) and the free surface moves to the right, such that the local

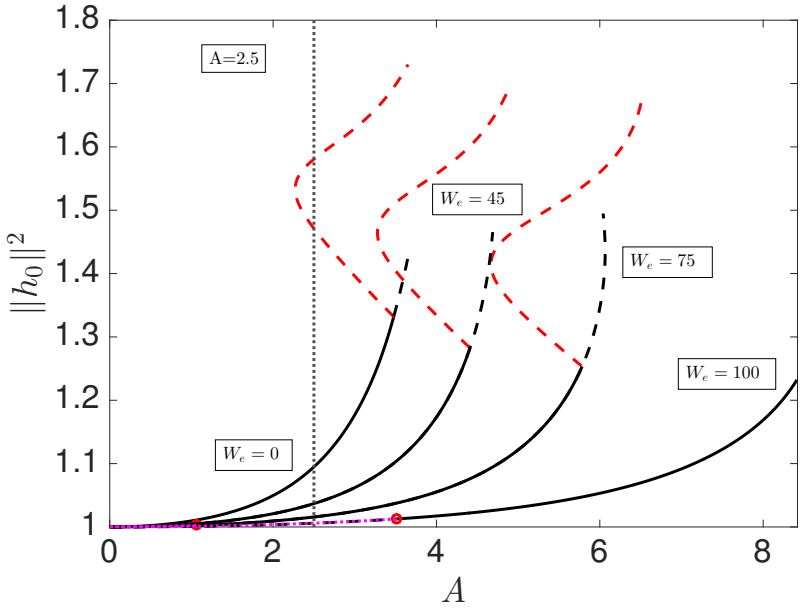

Figure 4.1: *Branches of steady-state solutions with $L = 50$, $K = 3364.5$, $R = 1.25$ and various electric Weber numbers for the long-wave model with a sinusoidal wall. The main, black branches denote 2L-periodic solutions, whereas the red branches denote subharmonic 4L-periodic solutions. Red circles correspond to Hopf bifurcations, solid lines correspond to stable solutions, and dashed lines correspond to unstable solutions. Pink dotted lines correspond to time-periodic solutions.*

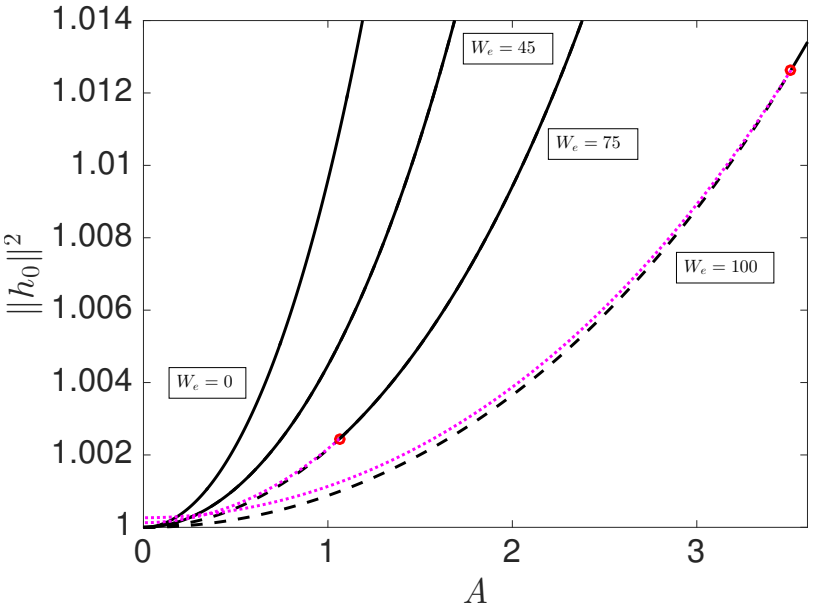

Figure 4.2: *Close-up of Figure 4.1 showing the time-periodic branches (pink dotted lines) following Hopf bifurcations. Both branches of time-periodic solutions are stable everywhere.*

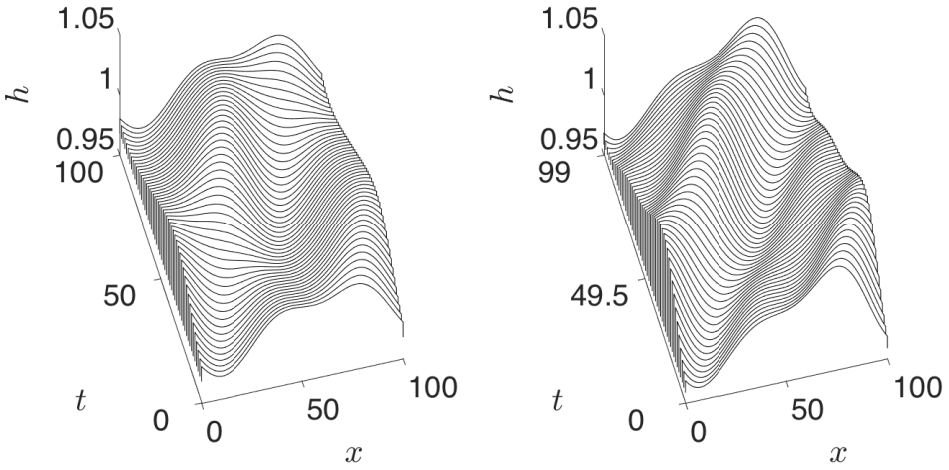

Figure 4.3: *Surface profiles of time-periodic solutions with* $A = 0.1$, $L = 50$, $K = 3364.5$, $R = 1.25$, *with* $W_e = 75$ *(left) and* $W_e = 100$ *(right) for the longwave model with a sinusoidal wall.*

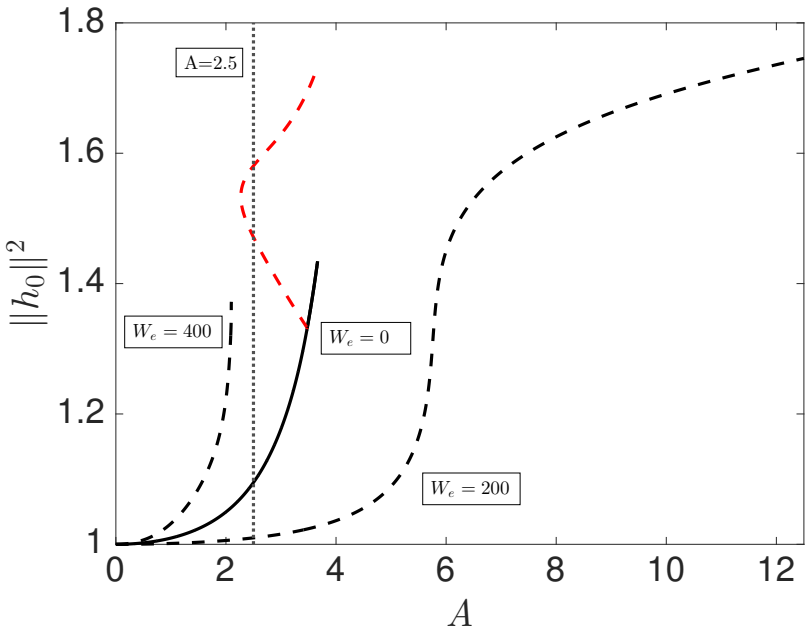

Figure 4.4: *Branches of steady-state solutions with* $L = 50$, $K = 3364.5$, $R = 1.25$, *and various electric Weber numbers for the long-wave model with a sinusoidal wall. The main, black branches denote 2L-periodic solutions, whereas the red branches denote subharmonic 4L-periodic solutions. Solid lines correspond to stable solutions, and dashed lines correspond to unstable solutions.*

film thickness becomes more uniform, corresponding to a decrease in the film thickness norm. As a consequence of the film thickness becoming more uniform, greater amplitudes of the wall can be accommodated before the film thickness becomes minimum and the stopping criterion is reached.

For $W_e = 75$ we see that a Hopf bifurcation occurs at $A = 1.062$, and that prior to this bifurcation the main branch is unstable. For $W_e = 100$ we also see the disappearance of the subharmonic secondary branch, and the main branch following the Hopf bifurcation is now stable until the film thickness becomes minimal, which occurs at larger wall amplitudes than noted previously. As discussed previously, the presence of a Hopf bifurcation indicates the presence of a family of time-periodic solutions [48], which are included in Figure 4.1 but difficult to distinguish as the time-periodic branch closely follows the main branch, although a close-up of this time-periodic branch is given in Figure 4.2. Both branches of time-periodic solutions were found to be stable everywhere following analysis of the diagnostic Auto-07p file and examination of the first Lyapunov coefficient which is negative for all periodic solutions. It can be seen that the time-periodic branches closely follow the shape of the main branch, although terminate slightly above the initial Nusselt flat film solution starting point. Surface profiles of time-periodic solutions chosen at $A = 0.1$ are given in Figure 4.3 for both branches. The periodicity of the solution for $W_e = 75$ was determined to be 100.029 dimensionless time-steps, whereas the periodicity in the $W_e = 100$ case was found to be 99.9461 dimensionless time-steps. As can be seen by comparing the initial profiles of the time-periodic solutions, we again see the characteristic increase in the deflection of the free surface as the strength of the electric field increases.

In Figure 4.4 we see the same $W_e = 0$ case, in addition to the two branches computed for higher electric Weber numbers of $W_e = 200$ and $W_e = 400$. In both cases, we see that the branches are unstable everywhere. In the $W_e = 200$ case, we note that the branch reaches its maximum value of the wall amplitude before terminating, suggesting that this Weber number is close to the number required to completely eliminate the phase shift. This is corroborated by examining the main $W_e = 400$ branch, which we would then expect to correspond approximately to a positive phase shift which is equal in magnitude to the non-electrified case, albeit with an opposite sign corresponding to the liquid now leading the topography, and indeed the $W_e = 400$ branch is seen to be qualitatively similar to the $W_e = 0$ case.

We now recompute the steady-state branches using the WIBL model for the same parameter values, the results of which are shown in Figure 4.5. The first most notable distinction is observed for $W_e = 0$ and $W_e = 45$, where we see that the branches are stable everywhere, with no subcritical pitchfork bifurcations or subharmonic 4L-periodic solutions. In the $W_e = 75$ case we still recover the Hopf bifurcation found in the long-wave case, although there is a discrepancy for the amplitude corresponding to

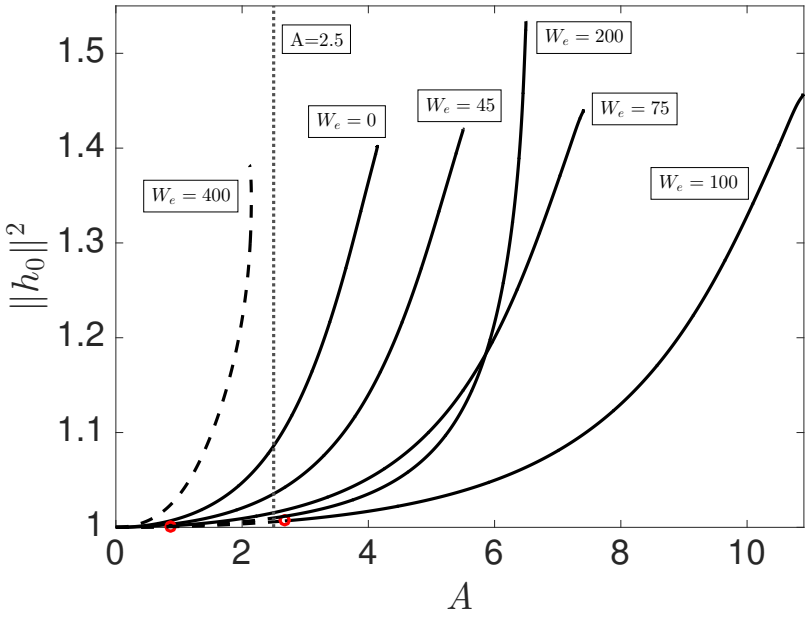

Figure 4.5: *Branches of steady-state solutions with $L = 50$, $K = 3364.5$, $R = 1.25$, and various electric Weber numbers for the WIBL model with a sinusoidal wall. The main, black branches denote $2L$-periodic solutions. Red circles correspond to Hopf bifurcations, solid lines correspond to stable solutions, and dashed lines correspond to unstable solutions. Pink dotted lines correspond to time-periodic solutions.*

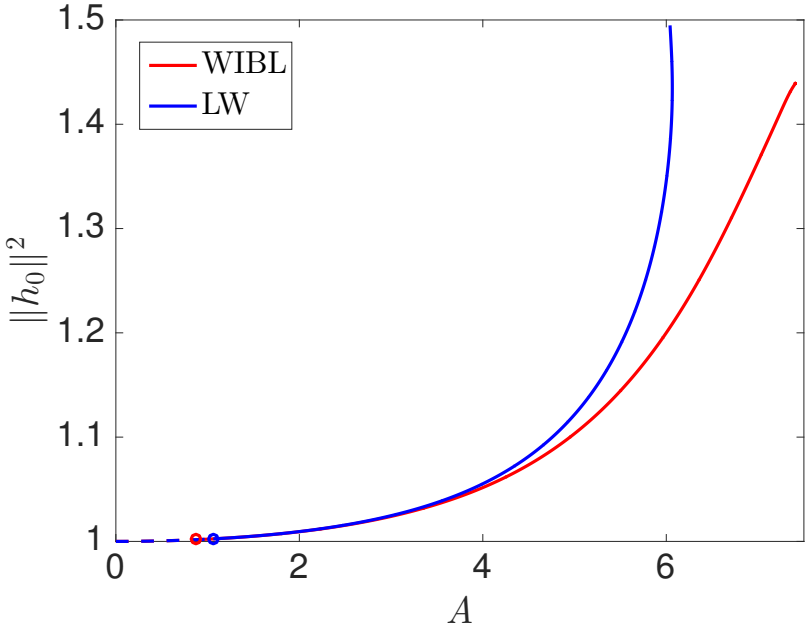

Figure 4.6: *Branches of steady-state solutions with $L = 50$, $K = 3364.5$, $R = 1.25$, and $W_e = 75$ for the long-wave (blue) and WIBL (red) models with a sinusoidal wall. Circles correspond to Hopf bifurcations, solid lines correspond to stable solutions, and dashed lines correspond to unstable solutions.*

this Hopf bifurcation, as we shall discuss shortly. This discrepancy is also noted in the $W_e = 100$ case, although it is otherwise qualitatively similar to the long-wave model except that the branch terminates for slightly higher wall amplitudes (at $A \approx 11$ rather than $A \approx 8.4$) and reaches higher film thickness norms, although the latter is at least partially a consequence of the former.

For $W_e = 200$ we begin to see greater discrepancies between the two models. In the long-wave case, the branch was unstable everywhere, whereas in the WIBL model we find the branch to be primarily stable, although with a Hopf bifurcation at $A = 2.52$, very similar to the Hopf bifurcation found at $A = 2.67$ in the $W_e = 100$ case, below which the branches are unstable. We also note that the branch itself is shifted further to the left in relation to the $W_e = 100$ case and reaches the maximum of the film thickness norm, which is consistent with the results observed for the long-wave model, however we also note that the branch terminates at a much lower wall amplitude ($A \approx 6$ rather than $A \approx 12.6$). For $W_e = 400$ the branch is qualitatively very similar to the equivalent branch for the long-wave model, and is unstable everywhere.

Figure 4.6 shows the difference in behaviours of the branches for the $W_e = 75$ cases computed previously for the long-wave (blue) and WIBL (red) models. The most obvious discrepancy occurs between the two models for larger wall amplitudes, where the film thickness norm for the long-wave model can be seen to turn back on itself, as opposed to the WIBL model, the film thickness norm of which increases with amplitude at a relatively constant rate. The Hopf bifurcation was found to occur at $A = 1.06$ in the long-wave model and $A = 0.87$ in the WIBL model, such that we notice an approximate 20% discrepancy between the amplitudes corresponding to the Hopf bifurcation for both models.

In general the two models disagree in their predictions for the wall amplitude corresponding to a Hopf bifurcation in the case of a prescribed electric Weber number, although the degree to which the predictions diverge appears to depend heavily on domain size, wall amplitude and electric Weber number, such that to make any conclusory statement a more thorough investigation would be required. Nevertheless, we make clear that the long-wave model does not typically underestimate the linear stability threshold in electrified films over no topography, nor for non-electrified flow over topography, and this discrepancy may be a result of interplay between the two features.

In Figure 4.7 we see the surface profile for various electric Weber numbers in the case of $A = 2.5$ for the parameters mentioned previously for sinusoidal topography for the

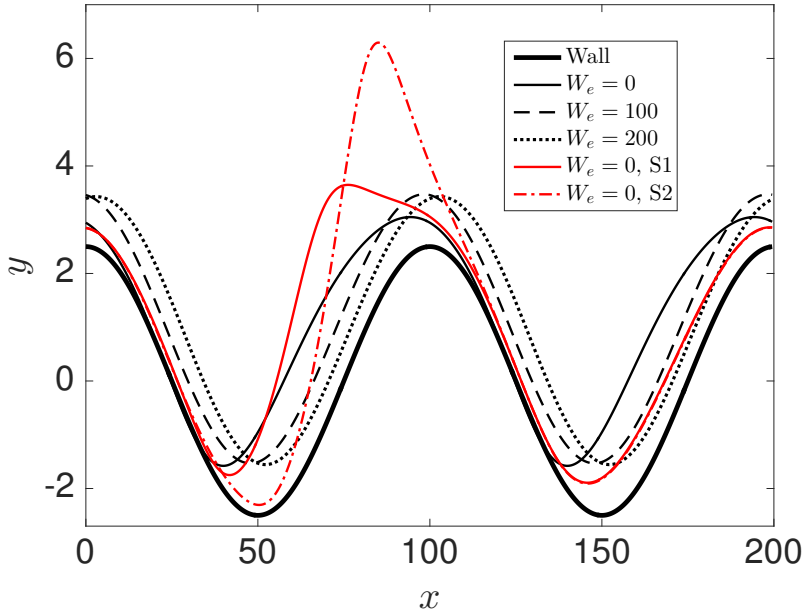

Figure 4.7: *Surface profiles with $A = 2.5$, $L = 50$, $K = 3364.5$, $R = 1.25$, and various electric Weber numbers for the long-wave model with a sinusoidal wall. S1 and S2 refer to the first and second steady-state solutions on the subharmonic branch respectively.*

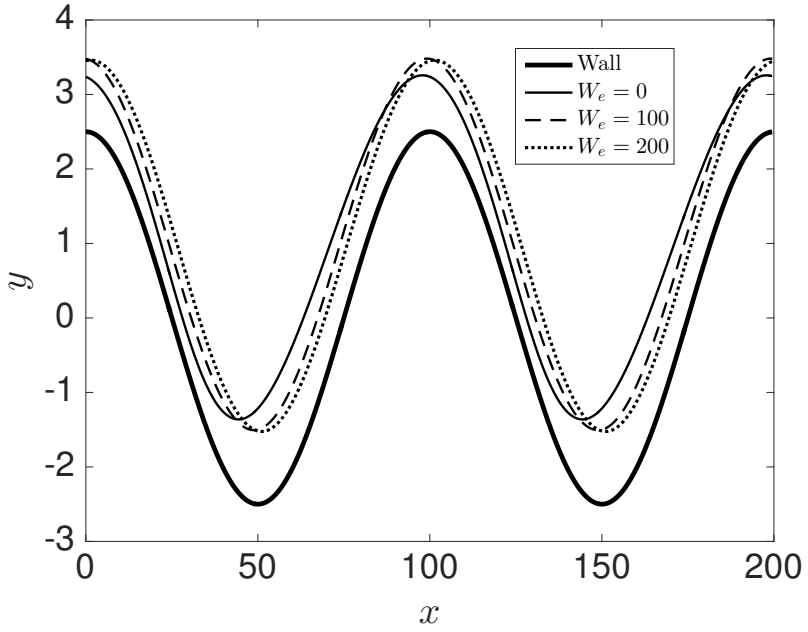

Figure 4.8: *Surface profiles with $A = 2.5$, $L = 50$, $K = 3364.5$, $R = 1.25$, and various electric Weber numbers for the WIBL model with a sinusoidal wall.*

long-wave model. In the $W_e = 0$ stable main branch case we see a large negative phase shift between the wall and the free surface, and the film is almost touching the wall on the downwards slopes. For both the first and second subharmonic solution we see behaviour somewhat akin to a capillary ridge which is commonly observed over rectangular topography, with a small downward deflection prior to a steep topographical change, followed by a thick region of the liquid. We remind the reader that both of these subharmonic solutions are unstable, as are all solutions on the subharmonic branch. For the unstable $W_e = 100$ solution, we see that the phase shift has increased and the free surface is now almost uniform. In the unstable $W_e = 200$ case, the free surface is now leading the wall, and the phase shift is positive. Re-examination of Figure 4.4 and Figure 4.5 makes clear that in the case of $W_e = 400$, the branch terminates before the $A = 2.5$ wall amplitude is reached in both models, and we do not find a steady-state solution for either model.

Figure 4.8 shows the surface profiles for the same parameter values, albeit for the WIBL model. Here we again find that the $W_e = 0$ case is stable and the $W_e = 100$ and $W_e = 200$ cases are unstable. We also note the lack of subharmonic solutions, due to the nonexistence of the subharmonic branch in the WIBL model. The most noticeable feature of the WIBL model in comparison to the long-wave model is that the effect of the electric field on the phase shift is less pronounced, and the initial phase shift for non-electrified flow is smaller, although we still observe an initial negative phase shift for $W_e = 0$ which becomes positive for $W_e = 200$.

4.2.2 $L_0 = 150$

The next steady-state branches and time-periodic solutions we wish to examine correspond to the parameter values discussed in Chapter 3 for $L_0 = 150$ with a sinusoidal wall and $L_0 = 57$ for a rectangular wall. We remind the reader that L_0 is defined as

$$L_0 = L\left(\frac{\sin\beta}{R}\right)^{1/3}. \tag{4.7}$$

Figure 4.9 shows the long-wave steady-state branches for $L_0 = 150$ and the sinusoidal wall case for various electric Weber numbers. In the $W_e = 0$ and $W_e = 10$ cases we

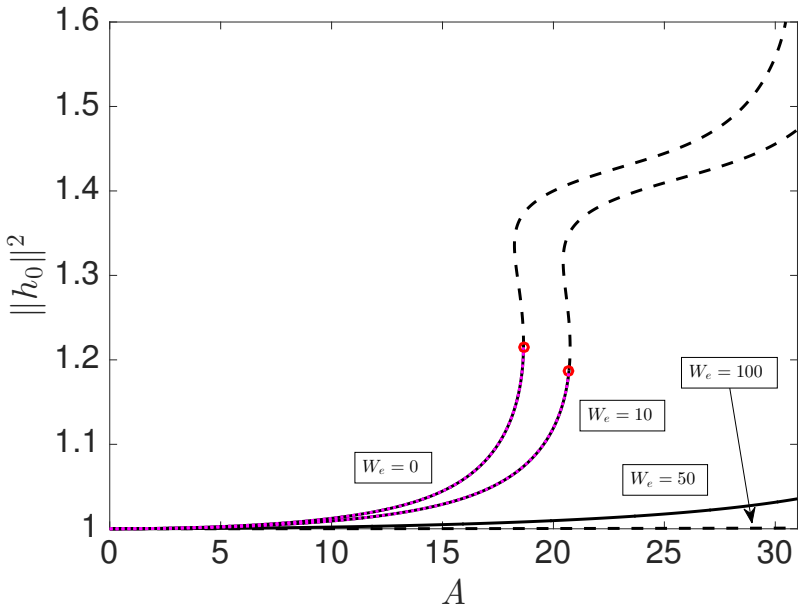

Figure 4.9: *Branches of steady-state solutions with $L_0 = 150$, $K = 3364.5$, $R = 1.25$, and various electric Weber numbers for the long-wave model and a sinusoidal wall. The main, black branches denote $2L$-periodic solutions. Red circles correspond to Hopf bifurcations, solid lines correspond to stable solutions, and dashed lines correspond to unstable solutions. Pink dotted lines correspond to time-periodic solutions.*

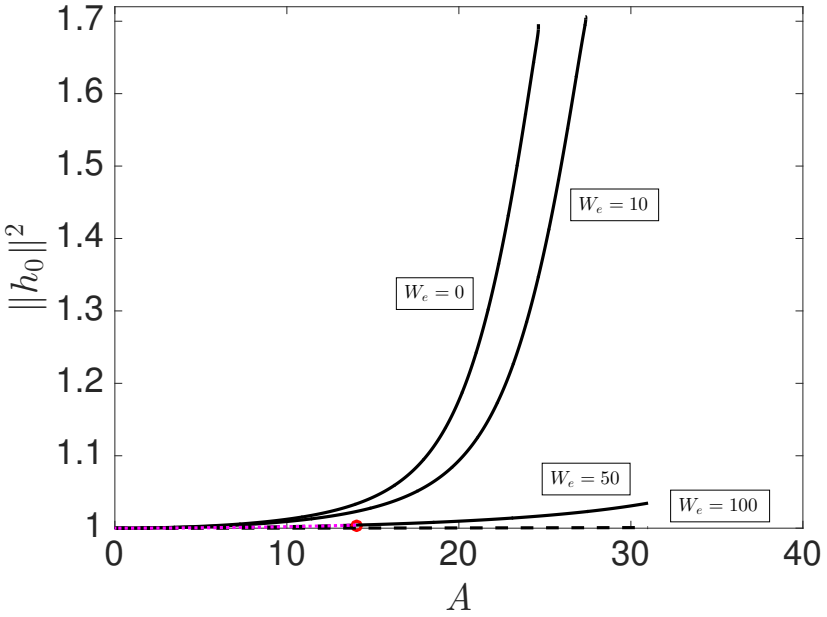

Figure 4.10: *Branches of steady-state solutions with $L_0 = 150$, $K = 3364.5$, $R = 1.25$, and various electric Weber numbers for the WIBL model and a sinusoidal wall. The main, black branches denote $2L$-periodic solutions. Red circles correspond to Hopf bifurcations, solid lines correspond to stable solutions, and dashed lines correspond to unstable solutions. Pink dotted lines correspond to time-periodic solutions.*

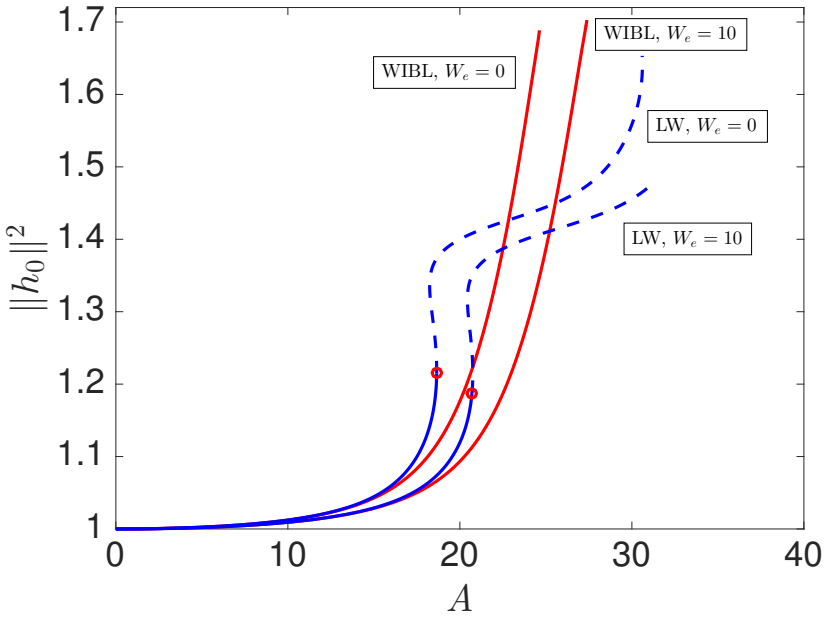

Figure 4.11: *Comparison between the long-wave (blue) and WIBL (red) models for the branches of steady-state solutions in the case of* $L_0 = 150$*,* $K = 3364.5$*,* $R = 1.25$*, and* $W_e = 0, 10$ *for a sinusoidal wall.*

observe qualitatively similar behaviour; for $W_e = 0$ and $W_e = 10$ we observe Hopf bifurcations at $A \approx 16.5$ and $A \approx 20.5$ respectively, and consequently time-periodic branches originating from these points, after which the main branches become unstable. The time-periodic branches were found to be unstable everywhere, and terminate when the wall amplitude reaches zero slightly above the main branch.

For $W_e = 50$ we find that the branch is stable for all wall amplitudes, and we also note the large overall decrease in the film thickness norm, corresponding to a decrease in the phase shift between the free surface and the wall. We thus find that for large-amplitude topography, the typically-destabilising normal electric field can be used to stabilise solutions which would otherwise be unstable without the effect of the electric field. In the $W_e = 100$ case, we find that the steady states are unstable everywhere, and the phase shift between the free surface and the wall is almost completely eliminated, resulting in a nearly constant film thickness norm.

Steady branches for the same parameter values albeit using the WIBL model are also produced, and may be seen in Figure 4.10. For $W_e = 0$ and $W_e = 10$ we now find that the main branch is stable everywhere, and we note that the branch termination corresponding to the film thickness becoming minimum occurs at a lower wall amplitude than observed for the long-wave model. In the $W_e = 50$ case, the branch is no longer completely stable for all amplitudes, and we now have a Hopf bifurcation at $A \approx 14$

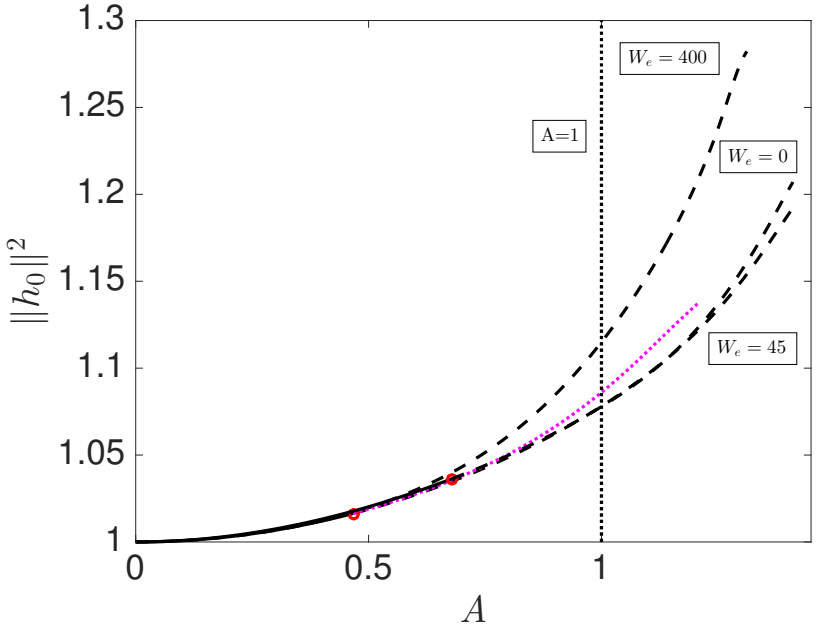

Figure 4.12: *Branches of steady-state solutions with $L_0 = 57$, $K = 3364.5$, $R = 1.25$, and various electric Weber numbers for the long-wave model and a rectangular wall. The main, black branches denote $2L$-periodic solutions. Red circles correspond to Hopf bifurcations, solid lines correspond to stable solutions, and dashed and dot-dashed lines correspond to unstable solutions. Pink dotted lines correspond to time-periodic solutions.*

which marks the transition from unstable at lower wall amplitudes, to stable at higher wall amplitudes. The time-periodic branches shown were found to be stable everywhere and closely follow the main branch, terminating slightly above it, consistent with previous computations. For $W_e = 100$ we observe a qualitatively very similar branch as in the long-wave case, with the branch being unstable everywhere and the film thickness norm remaining approximately constant for all amplitudes.

Figure 4.11 shows a direct comparison between the two models for $W_e = 0$ and $W_e = 10$. It can be seen that up until $A \approx 14$ for $W_e = 0$ and $A \approx 16$ for $W_e = 10$, the two models show excellent agreement, but after these points the predicted behaviours diverge significantly, with the long-wave model predicting instability and the WIBL model predicting stability.

4.2.3 $L_0 = 57$

We now return to the case of a rectangular wall with $L_0 = 57$ for the long-wave model, as shown in Figure 4.12. For $W_e = 0$, we see that the branch is primarily unstable, although for amplitudes lower than $A \approx 0.68$ which corresponds to a Hopf bifurcation,

the branch is stable. As the film thickness becomes minimal, the branch terminates. For $W_e = 45$ the Hopf bifurcation occurs at a lower wall amplitude of $A \approx 0.47$. In the $W_e = 400$ case, the branch is unstable everywhere, and we observe that the film thickness norm is greater than the corresponding norm in the $W_e = 0, 45$ cases for a given wall amplitude.

For Figure 4.13 corresponding to the same parameter values but for the WIBL model, we observe qualitatively different behaviour to the long-wave case. We find that the $W_e = 0$ branch is initially stable, and becomes unstable at $A \approx 0.70$ after a Hopf bifurcation, with all the other branches for $W_e = 0,\ 200$ and 400 being unstable everywhere. For $W_e = 100$ and 200 we observe that the continuation curve is shifted to the right relative to the non-electrified branch, whereas the $W_e = 400$ branch is shifted to the left relative to the non-electrified branch. Comparison between the film thickness norms computed using the long-wave model and WIBL model for $L_0 = 57$ and $W_e = 400$ is shown in Figure 4.14. Up until $A \approx 0.6$ the two models show good agreement, with the main divergence occurring after this point. Despite the divergence, the behaviour of the norms appears qualitatively somewhat similar until the film thickness becomes minimal and the branches terminate.

Figures 4.15 and 4.16 show the surface profiles for $W_e = 0,\ 200$ and 400 at $A = 1$ with $L_0 = 57$ for the long-wave and WIBL models, respectively. Describing the overall behaviour of both models to begin with, we note that in the $W_e = 0$ case, we have a reasonably smooth and uniform profile which has a negative phase shift relative to the rectangular topography. When the electric Weber number is increased to $W_e = 200$, we observe the capillary ridge becoming more pronounced and localised, and we also note the depression which occurs shortly after the upwards steps of the rectangular trough. For $W_e = 400$, the capillary ridge and depression at the top of the rectangular steps become even more pronounced and localised, although the most distinct and obvious change is inside the troughs themselves. As opposed to the parabolic behaviour which occurs for $W_e = 0$ and $W_e = 200$, for $W_e = 400$ we see the same oscillations which were noted by Tseluiko et al. [100] and Kalliadasis et al. [39] inside narrow trenches, where we observe a steep upward deflection and sharp depressions. Comparing the long-wave and WIBL models for $W_e = 0$ and $W_e = 200$, the surface profiles appear qualitatively very similar, however, differences may be observed for the $W_e = 400$ case, and these shall be closely examined in Figure 4.17. Here we see that the main

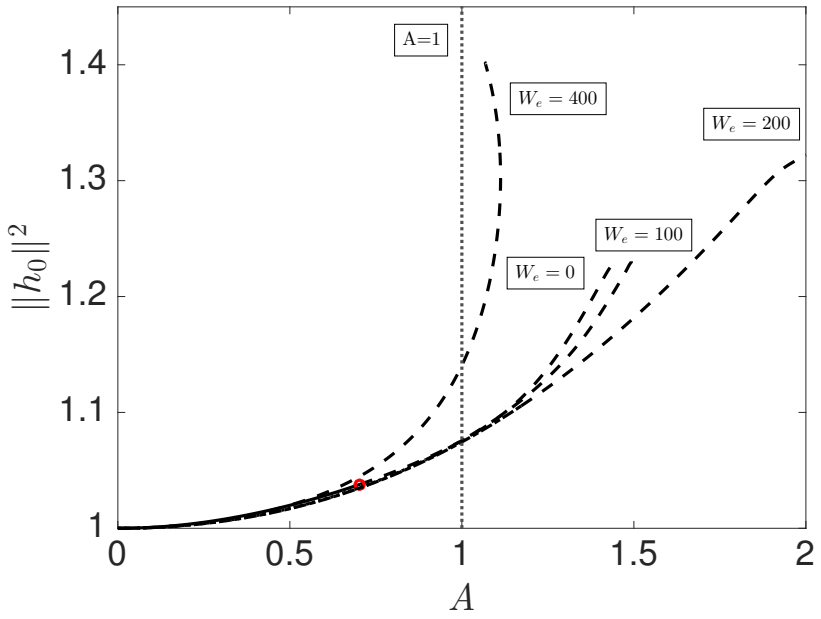

Figure 4.13: *Branches of steady-state solutions with $L_0 = 57$, $K = 3364.5$, $R = 1.25$, and various electric Weber numbers for the WIBL model and a rectangular wall. The main, black branches denote $2L$-periodic solutions. Red circles correspond to Hopf bifurcations, solid lines correspond to stable solutions, and dashed lines correspond to unstable solutions. Pink dotted lines correspond to time-periodic solutions.*

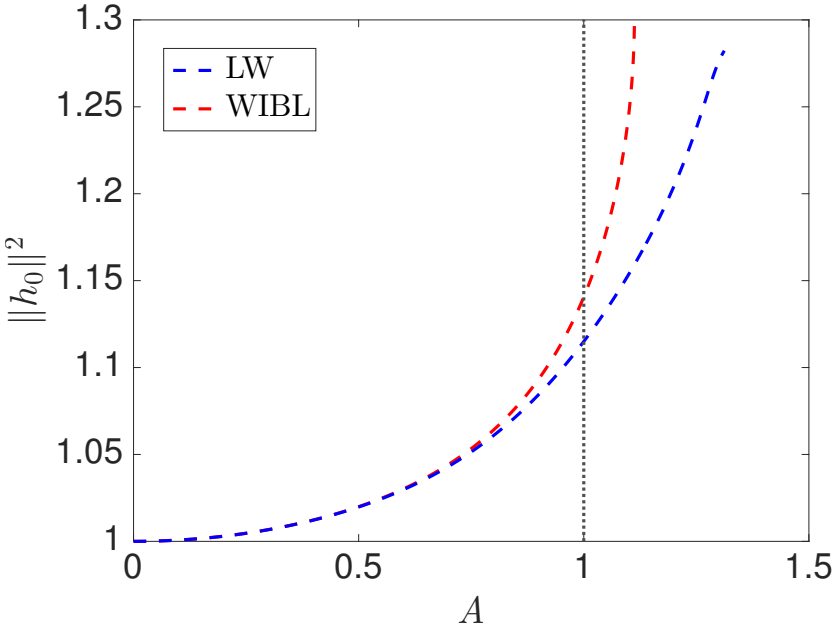

Figure 4.14: *Comparison between the long-wave (blue) and WIBL (red) models for the branches of steady-state solutions in the case of $L_0 = 57$, $K = 3364.5$, $R = 1.25$, and $W_e = 400$ for a rectangular wall.*

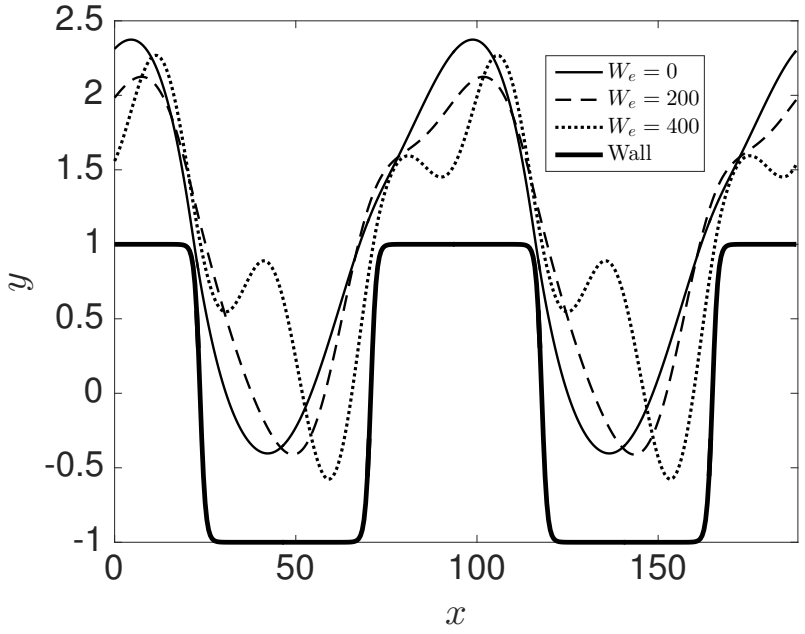

Figure 4.15: *Surface profiles with $A = 1$, $L_0 = 57$, $K = 3364.5$, $R = 1.25$, and various electric Weber numbers for the long-wave model with a rectangular wall.*

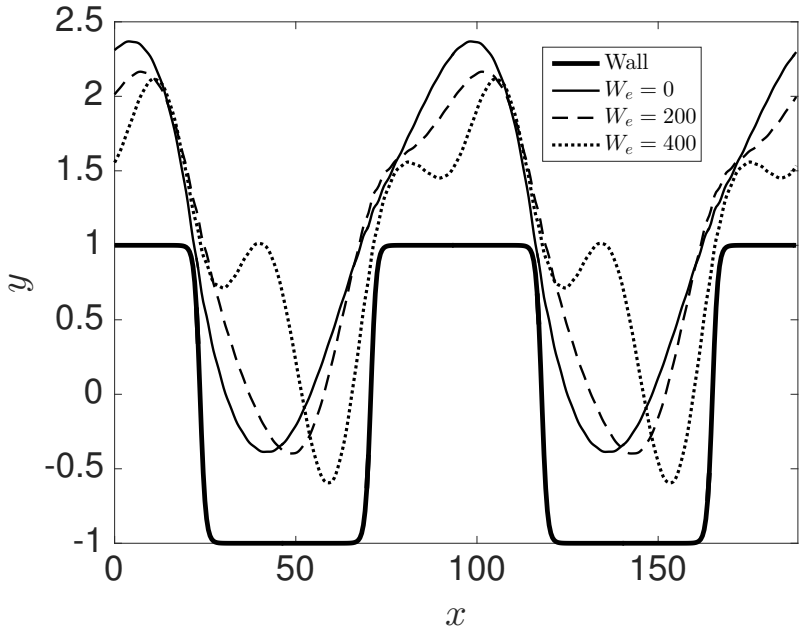

Figure 4.16: *Surface profiles with $A = 1$, $L_0 = 57$, $K = 3364.5$, $R = 1.25$, and various electric Weber numbers for the WIBL model with a rectangular wall.*

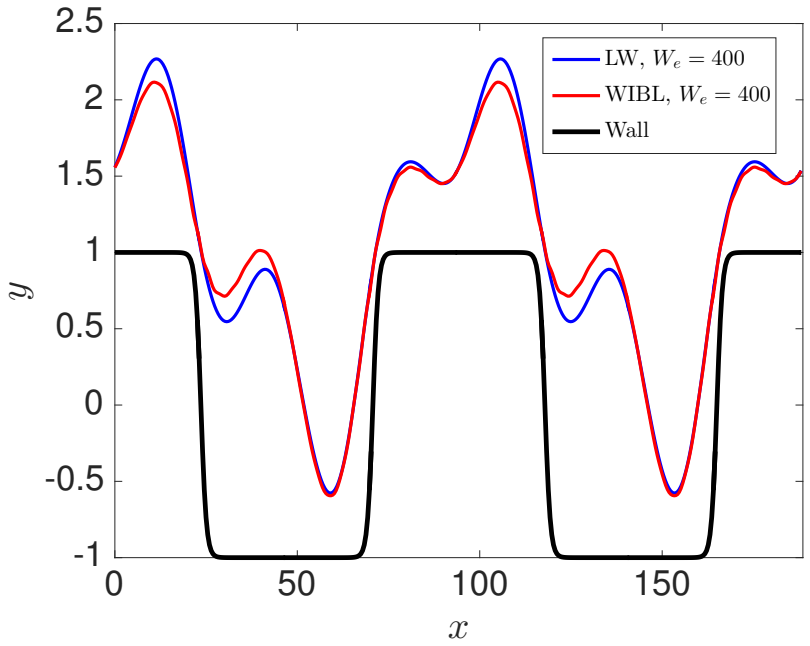

Figure 4.17: *Comparison between the long-wave (blue) and WIBL (red) models for the branches of steady-state solutions in the case of* $L_0 = 57$, $K = 3364.5$, $R = 1.25$, *and* $W_e = 400$ *for a rectangular wall.*

discrepancy is in the height of the capillary ridges and the upwards deflections within the rectangular trough., with the long-wave model predicting capillary ridges of greater amplitude, and upwards deflections within the trough of lower amplitude.

Chapter 5

Conclusion

5.1 Discussion

We have studied the effect of a normal electric field on liquid film flow down an inclined topographically structured wall. First, in Chapter 1 we outlined recent breakthroughs in electrohydrodynamics and thin film flow over topography, and gave a brief review of the pertinent literature.

In Chapter 2 we fully derived two models for thin film flow over inclined topography under the effect of a normal electric field – the long-wave model and the first-order weighted-residual integral boundary layer (WIBL) model. A hierarchy of models was provided, and the various modelling assumptions and boundary conditions were examined.

In Chapter 3 we derived analytical expressions for the critical value of the Reynolds number, R, as a function of the inclination angle, β, the capillary number, C, and the electric Weber number, W_e, for both models in the case of a flat wall. Dispersion relations were also provided for both models, and we discussed their inflection points. The transition from convective to absolute instability was determined numerically for both models as a function of the electric Weber number and the Reynolds number. We found that the long-wave model predicts absolute instability for $R > 15.02$ even in cases of non-electrified flow, and from the work of Brevdo et al. [9] we know that this is non-physical behaviour and is a failing of the model. Contrariwise, for the WIBL model we found that absolute instability is only obtained in cases where we have $W_e > 65.07$, and

for any electric Weber number lower than this threshold we find that the flow is convectively unstable regardless of the Reynolds number, at least within the $0 < R < 30$ range investigated. We may generally say that the main variable controlling the transition from convective to absolute instability for the long-wave model is the Reynolds number, whereas in the WIBL model it is the electric Weber number. The real parts of the most unstable wavenumbers were also determined numerically for both models as a function of the Reynolds number for various electric field strengths, and although we found close agreement for $R \lesssim 5$, for $R \gtrsim 5$ we instead found that the two models diverge in their predictions. The long-wave model appears to overestimate the real part of the most unstable wavenumber relative to the WIBL model by up to 40% for $R = 25$. Time-dependent simulations were produced in the case of a flat wall, and for sinusoidal topography with $L = 50$ and $L_0 = 150$, where we remind the reader that L_0 is a rescaled domain of the form

$$L_0 = L\left(\frac{\sin\beta}{R}\right)^{1/3}, \tag{5.1}$$

such that the domain (and indeed similarly for the amplitude in the case of amplitude rescaling) no longer depend on the Reynolds number. Time-dependent simulations were also produced for rectangular topography for $L_0 = 57$. For a flat wall the simulations are consistent with the convective to absolute instability transitions determined previously, and in the $L = 50$ case with no electric term, which corresponds to the work of Tseluiko, Blyth and Papageorgiou [98], we found excellent agreement. In the longwave model for $W_e = 45$, $L_0 = 150$ and $A_0 = 24$ we found that the electric field and the sinusoidal topography in conjunction are stabilising, whereas the same amplitude of the topography in the absence of the electric field is destabilising. In the rectangular wall case we found few qualitative differences between the long-wave and WIBL models, although the W_e = 200 case with $A_0 = 1.462$ appears to be transiently unstable for both models, yet was convectively unstable at this amplitude for $W_e = 0$ and $W_e = 45$, again indicative that the normal electric field may have some stabilising properties for certain domain sizes and topography amplitudes.

We also determined the critical Reynolds number as a function of the scaled wall amplitude for both models at various electric Weber numbers with $L_0 = 150$ in the sinusoidal case and $L_0 = 57$ in the rectangular case. The most obvious effect of increasing the electric Weber number is the lowering of the critical Reynolds number for a given amplitude, and this phenomena is observed for both models and for both topographies. Rectangular topography for non-electrified flow is stabilising at low to intermediate wall

amplitudes, and destabilising at high wall amplitudes, and for the long-wave model we find excellent agreement with the work by Tseluiko, Blyth and Papageorgiou [98]. For electrified flow, the critical Reynolds number monotonically decreases for increasing wall amplitude in both models. For sinusoidal topography in the long-wave model with non-electrified flow the wall is stabilising at low to intermediate wall amplitudes, and destabilising at high wall amplitudes. As the electric Weber number increases, the wall becomes stabilising for small and large amplitudes and destabilising for intermediate amplitudes. For sufficiently large electric Weber number, the critical Reynolds number increases monotonically with the wall amplitude. In the WIBL model the critical Reynolds number increases monotonically with wall amplitude for all electric Weber numbers. The predictions of the critical Reynolds number for a given amplitude, domain and Weber number are consistent with the time-dependent simulations in all cases.

In Chapter 4 we discussed the procedure for producing steady solutions to the long-wave and WIBL models. In the $L = 50$ sinusoidal case for non-electrified flow we recover the $2L$-periodic main branch with unstable $4L$-periodic subharmonic branch found by Tseluiko, Blyth and Papageorgiou [98] for the long-wave model. As the electric Weber number increases we find steady solutions at higher wall amplitudes due to the phase shift phenomena discussed previously. For sufficiently large electric Weber numbers we found Hopf bifurcations and time-periodic solutions which were found to be unstable everywhere. In the WIBL these subharmonic branches were not found, and the main branches were found to be stable for a wider range of amplitudes, generally speaking. Main branches and time-periodic branches were also produced for both models in the $L_0 = 150$ sinusoidal case and the $L_0 = 57$ rectangular case. In the former case for $W_e = 0$ and $W_e = 10$ we find close agreement between the two models until $A \approx 15$, at which point they begin to rapidly diverge, with the long-wave model predicting instability and the WIBL model predicting stability. In the latter case we find qualitatively very similar results in the long-wave and WIBL models. The bifurcation diagrams produced are consistent with the time-dependent simulations, the work on the critical Reynolds number as a function of scaled wall amplitude and the aforementioned work by Tseluiko, Blyth and Papageorgiou [98].

5.2 Further research

Due to the nature of the system under consideration there are multiple avenues for further research, and a myriad of possible directions in which a continuation of this

thesis may be taken. For minor extensions, for example, we could examine the case where both the liquid and the gas are perfect dielectrics and compare these results to the current work. It would also be of interest to consider leaky-dielectric liquids. We could also vary δ corresponding to the steepness of the rectangular troughs which in the current work has been taken to be $d = 0.1$ everywhere. With regards to the critical Reynolds number as a function of wall amplitude, we could determine numerically the transition at which the wall changes from monotonically destabilising with increasing amplitude to monotonically stabilising with increasing amplitude. Continuation could also be performed with respect to the electric Weber number for a given domain size, scaled amplitude and topography, such that we might determine the most stabilising or destabilising electric field strength. We could also further investigate the time-periodic branches, perhaps giving special attention to the effect of the normal electric field on the periodicity of solutions and free surface profiles. The topography could also be altered more significantly, and extended to more general rough topographies which are more closely related to those used in industry. The liquid in this work was taken to be water everywhere, and could also trivially be extended to other liquids such as silicon oils, for example.

As mentioned previously, it would also be possible to model the hydrodynamically inert gas as a hydrodynamically active one shearing the liquid, such that we might investigate the so-called 'flooding' phenomenon. The gas could also be taken taken to be an additional liquid instead separated by an interface, similar to the work by Mandal et al. [54] for a confined channel. Further extensions could include moving or heated walls, or we might consider the case of destabilising gravity for a hanging film. In the case of a heated wall we might consider either a uniformly heated wall or a heat profile which varies spatiotemporally.

For more thorough extensions, we might include the simplified second-order or full four-equation second-order WIBL models such that viscous diffusion terms are present, and examine the effects on the linear stability analysis. We could also compare the results obtained here to those obtained via DNS methods, or perhaps experimental approaches, although in the latter case we would have to employ a fixed flux constraint rather than a fixed volume constraint. The fluid could also be modelled as three-dimensional, perhaps taking into consideration the effect of cross-stream walls at the edges of the domain. It is thus clear that the problems discussed in this thesis have the potential for various interesting developments.

Bibliography

[1] R. Abraham. Introduction to morphology. Publications of the Department of Mathematics, University of Lyon, 9:38–174, 1972.

[2] E. L. Allgower and K. Georg. Numerical continuation methods: an introduction, volume 13 of Springer Series in Computational Mathematics. Springer Science & Business Media, 2012.

[3] K. Argyriadi, M. Vlachogiannis, and V. Bontozoglou. Experimental study of inclined film flow along periodic corrugations: The effect of wall steepness. Physics of Fluids, 18:012102, 2006.

[4] G. K. Batchelor. An introduction to fluid dynamics. Cambridge University Press, 2000.

[5] T. B. Benjamin. Wave formation in laminar flow down an inclined plane. Journal of Fluid Mechanics, 2:554–573, 1957.

[6] D. J. Benney. Long waves on liquid films. Journal of Mathematics and Physics, 45:150–155, 1966.

[7] M. G. Blyth, D. Tseluiko, T.-S. Lin, and S. Kalliadasis. Two-dimensional pulse dynamics and the formation of bound states on electrified falling films. Journal of Fluid Mechanics, 855:210–235, 2018.

[8] J. P. Boyd. Chebyshev and Fourier spectral methods. Courier Corporation, 2001.

[9] L. Brevdo, P. Laure, F. Dias, and T. J. Bridges. Linear pulse structure and signalling in a film flow on an inclined plane. Journal of Fluid Mechanics, 396:37–71, 1999.

[10] C. Canuto, M. Y. Hussaini, A. Quarteroni, and T. A. Zang Jr. Spectral methods in fluid dynamics. Springer Science & Business Media, 2012.

[11] Z. Cao, M. Vlachogiannis, and V. Bontozoglou. Experimental evidence for a short-wave global mode in film flow along periodic corrugations. Journal of Fluid Mechanics, 718:304–320, 2013.

[12] A. Castellanos. Electrohydrodynamics, volume 380 of CISM Courses and Lectures. Springer Science & Business Media, 2014.

[13] A. Castellanos and A. Gonzalez. Nonlinear electrohydrodynamics of free surfaces. Institute of Electrical and Electronics Engineers: Transactions on Dielectrics and Electrical Insulation, 5:334–343, 1998.

[14] H.-C. Chang. Traveling waves on fluid interfaces: normal form analysis of the Kuramoto–Sivashinsky equation. Physics of Fluids, 29:3142–3147, 1986.

[15] H.-C. Chang, E. A. Demekhin, and D. I. Kopelevich. Local stability theory of solitary pulses in an active medium. Physica D: Nonlinear Phenomena, 97:353–375, 1996.

[16] A. Charogiannis, M. Pradas, F. Denner, B. G. M. van Wachem, S. Kalliadasis, and C. N. Markides. Detailed hydrodynamic characterization of harmonically excited falling-film flows: A combined experimental and computational study. Physical Review Fluids, 2:014002, 2017.

[17] R. V. Craster and O. K. Matar. Dynamics and stability of thin liquid films. Reviews of Modern Physics, 81:1131–1198, 2009.

[18] S. J. D. D'Alessio, J. P. Pascal, and H. A. Jasmine. Instability in gravity-driven flow over uneven surfaces. Physics of Fluids, 21:062105, 2009.

[19] M. M. J. Decré and J.-C. Baret. Gravity-driven flows of viscous liquids over two-dimensional topographies. Journal of Fluid Mechanics, 487:147–166, 2003.

[20] I. Delbende, J.-M. Chomaz, and P. Huerre. Absolute/convective instabilities in the Batchelor vortex: a numerical study of the linear impulse response. Journal of Fluid Mechanics, 355:229–254, 1998.

[21] F. Denner, A. Charogiannis, M. Pradas, C. N. Markides, B. G. M. van Wachem, and S. Kalliadasis. Solitary waves on falling liquid films in the inertia-dominated regime. Journal of Fluid Mechanics, 837:491–519, 2018.

[22] D. M. Dewar and A. F. Anderson. Electro-hydrodynamic heat exchanger, Dec 2003. US Patent 6,659,172.

[23] H. A. Dijkstra, F. W. Wubs, A. K. Cliffe, E. Doedel, I. F. Dragomirescu, B. Eckhardt, A. Y. Gelfgat, A. L. Hazel, V. Lucarini, A. G. Salinger, et al. Numerical bifurcation methods and their application to fluid dynamics: analysis beyond simulation. Communications in Computational Physics, 15:1–45, 2014.

[24] E. J. Doedel, B. E. Oldeman, F. Dercole, R. Paffenroth, T. F. Fairgrieve, B. Sandstede, A. R. Champneys, Y. A. Kuznetsov, and X. Wang. AUTO-07P: Continuation and bifurcation software for ordinary differential equations. Available at http://www.dam.brown.edu/people/sandsted/auto/auto07p.pdf, 2012. Accessed: 5 November, 2015.

[25] J. A. Fay. Introduction to fluid mechanics. Massachusetts Institute of Technology Press, 1994.

[26] J. M. Floryan, S. H. Davis, and R. E. Kelly. Instabilities of a liquid film flowing down a slightly inclined plane. Physics of Fluids, 30:983–989, 1987.

[27] A. S. Fokas and D. T. Papageorgiou. Absolute and Convective Instability for Evolution PDEs on the Half-Line. Studies in Applied Mathematics, 114:95–114, 2005.

[28] M. Frigo and S. G. Johnson. The design and implementation of FFTW3. Proceedings of the Institute of Electrical and Electronics Engineers, 93:216–231, 2005. Available at http://www.fftw.org. Accessed: 5 November, 2015.

[29] A. Gonzalez and A. Castellanos. Nonlinear electrohydrodynamic waves on films falling down an inclined plane. Physical Review E, 53:3573–3578, 1996.

[30] J. B. Grotberg. Pulmonary flow and transport phenomena. Annual Review of Fluid Mechanics, 26:529–571, 1994.

[31] B. D. Hassard, N. D. Kazarinoff, and Y.-H. Wan. Theory and applications of Hopf bifurcation, volume 41 of London Mathematical Society: Lecture Note Series. Cambridge University Press, 1981.

[32] M. Hayes, S. B. G. O'Brien, and J. H. Lammers. Green's function for steady flow over a small two-dimensional topography. Physics of Fluids, 12:2845–2858, 2000.

[33] C. Heining and N. Aksel. Bottom reconstruction in thin-film flow over topography: Steady solution and linear stability. Physics of Fluids, 21:083605, 2009.

[34] J. A. Heras. The Galilean limits of Maxwell's equations. American Journal of Physics, 78:1048–1055, 2010.

[35] P. Huerre and P. A. Monkewitz. Absolute and convective instabilities in free shear layers. Journal of Fluid Mechanics, 159:151–168, 1985.

[36] MathWorks Inc. MATLAB, high-performance numeric computation and visualization software: reference guide. MathWorks, 1992. Available at https://uk.mathworks.com. Accessed: 5 November, 2015.

[37] S. W. Joo, S. H. Davis, and S. G. Bankoff. On falling-film instabilities and wave breaking. Physics of Fluids A: Fluid Dynamics, 3:231–232, 1991.

[38] S. Kakac, Y. Yener, and A. Pramuanjaroenkij. Convective heat transfer. CRC Press, 2013.

[39] S. Kalliadasis, C. Bielarz, and G. M. Homsy. Steady free-surface thin film flows over topography. Physics of Fluids, 12:1889–1898, 2000.

[40] S. Kalliadasis and G. M. Homsy. Stability of free-surface thin-film flows over topography. Journal of Fluid Mechanics, 448:387–410, 2001.

[41] S. Kalliadasis, C. Ruyer-Quil, B. Scheid, and M. G. Velarde. Falling liquid films, volume 176 of Applied Mathematical Sciences. Springer Science & Business Media, 2011.

[42] P. L. Kapitza. Viscosity of liquid helium below the λ-point. Nature, 141:74, 1938.

[43] P. L. Kapitza and S. P. Kapitza. Wave flow of thin viscous liquid films. Zhurnal Eksperimental'noj i Teoreticheskoj Fiziki, 19:105–120, 1949.

[44] G. Karniadakis and S. Sherwin. Spectral/hp element methods for computational fluid dynamics. Oxford University Press, 2013.

[45] H. Kim, S. G. Bankoff, and M. J. Miksis. The effect of an electrostatic field on film flow down an inclined plane. Physics of Fluids A: Fluid Dynamics, 4:2117–2130, 1992.

[46] H. Kim, S. G. Bankoff, and M. J. Miksis. The cylindrical electrostatic liquid film radiator for heat rejection in space. Journal of Heat Transfer, 116:986–992, 1994.

[47] P. A Kuchment. Floquet theory for partial differential equations, volume 60 of Operator Theory: Advances and Applications. Birkhäuser, 2012.

[48] Y. A. Kuznetsov. Elements of applied bifurcation theory, volume 112 of Applied Mathematical Sciences. Springer Science & Business Media, 2013.

[49] T.-S. Lin, M. Pradas, S. Kalliadasis, D. T. Papageorgiou, and D. Tseluiko. Coherent structures in nonlocal dispersive active-dissipative systems. SIAM Journal on Applied Mathematics, 75:538–563, 2015.

[50] T.-S. Lin, S. Rogers, D. Tseluiko, and U. Thiele. Bifurcation analysis of the behavior of partially wetting liquids on a rotating cylinder. Physics of Fluids, 28:082102, 2016.

[51] T.-S. Lin, D. Tseluiko, M. G. Blyth, and S. Kalliadasis. Continuation methods for time-periodic travelling-wave solutions to evolution equations. Applied Mathematics Letters, 86:291–297, 2018.

[52] J. Liu, J. D. Paul, and J. P. Gollub. Measurements of the primary instabilities of film flows. Journal of Fluid Mechanics, 250:69–101, 1993.

[53] N. A. Malamataris and V. Bontozoglou. Computer aided analysis of viscous film flow along an inclined wavy wall. Journal of Computational Physics, 154:372–392, 1999.

[54] S. Mandal, U. Ghosh, A. Bandopadhyay, and S. Chakraborty. Electro-osmosis of superimposed fluids in the presence of modulated charged surfaces in narrow confinements. Journal of Fluid Mechanics, 776:390–429, 2015.

[55] J. E. Marsden and M. McCracken. The Hopf bifurcation and its applications, volume 19 of Applied Mathematical Sciences. Springer Science & Business Media, 2012.

[56] J. R. Melcher and W. J. Schwarz Jr. Interfacial relaxation overstability in a tangential electric field. Physics of Fluids, 11:2604–2616, 1968.

[57] J. R. Melcher and G. I. Taylor. Electrohydrodynamics: a review of the role of interfacial shear stresses. Annual Review of Fluid Mechanics, 1:111–146, 1969.

[58] P. A. Monkewitz. The absolute and convective nature of instability in two-dimensional wakes at low Reynolds numbers. Physics of Fluids, 31:999–1006, 1988.

[59] A. Mukhopadhyay and B. S. Dandapat. Nonlinear stability of conducting viscous film flowing down an inclined plane at moderate Reynolds number in the presence of a uniform normal electric field. Journal of Physics D: Applied Physics, 38:138–143, 2004.

[60] T. Ooshida. Surface equation of falling film flows which is valid even far beyond the criticality. Physics of Fluids, 11:3247–3269, 1999.

[61] A. Oron, S. H. Davis, and S. G. Bankoff. Long-scale evolution of thin liquid films. SIAM Journal on Applied Mathematics, 69:931–980, 1997.

[62] A. Oron and C. Heining. Weighted-residual integral boundary-layer model for the nonlinear dynamics of thin liquid films falling on an undulating vertical wall. Physics of Fluids, 20:082102, 2008.

[63] L. F. Pease III and W. B. Russel. Linear stability analysis of thin leaky dielectric films subjected to electric fields. Journal of Non-Newtonian Fluid Mechanics, 102:233–250, 2002.

[64] C. Pozrikidis. Introduction to finite and spectral element methods using MATLAB. CRC Press, 2005.

[65] C. Pozrikidis. Introduction to theoretical and computational fluid dynamics. Oxford University Press, 2011.

[66] M. Pradas, S. Kalliadasis, and D. Tseluiko. Binary interactions of solitary pulses in falling liquid films. Institute of Mathematics: Journal of Applied Mathematics, 77:408–419, 2012.

[67] M. Pradas, D. Tseluiko, and S. Kalliadasis. Rigorous coherent-structure theory for falling liquid films: Viscous dispersion effects on bound-state formation and self-organization. Physics of Fluids, 23:044104, 2011.

[68] A. Pumir, P. Manneville, and Y. Pomeau. On solitary waves running down an inclined plane. Journal of Fluid Mechanics, 135:27–50, 1983.

[69] A. Ramos. Electrokinetics and electrohydrodynamics in microsystems, volume 530 of CISM Courses and Lectures. Springer Science & Business Media, 2011.

[70] R. S. Rao. Microwave engineering. PHI Learning, 2015.

[71] O. Reynolds. IV. On the theory of lubrication and its application to Mr. Beauchamp Tower's experiments, including an experimental determination of the viscosity of olive oil. Philosophical Transactions of the Royal Society of London, 177:157–234, 1886.

[72] W. Rohlfs, P. Pischke, and B. Scheid. Hydrodynamic waves in films flowing under an inclined plane. Physical Review Fluids, 2:044003, 2017.

[73] W. Rohlfs and B. Scheid. Phase diagram for the onset of circulating waves and flow reversal in inclined falling films. Journal of Fluid Mechanics, 763:322–351, 2015.

[74] C. Ruyer-Quil. Dynamique d'un film mince s'écoulant le long d'un plan incliné. PhD thesis, Laboratoire d'Hydrodynamique de l'École polytechnique, 1999.

[75] C. Ruyer-Quil and P. Manneville. Improved modeling of flows down inclined planes. The European Physical Journal B: Condensed Matter and Complex Systems, 15:357–369, 2000.

[76] C. Ruyer-Quil and P. Manneville. Further accuracy and convergence results on the modeling of flows down inclined planes by weighted-residual approximations. Physics of Fluids, 14:170–183, 2002.

[77] T. R. Salamon, R. C. Armstrong, and R. A. Brown. Traveling waves on vertical films: Numerical analysis using the finite element method. Physics of Fluids, 6:2202–2220, 1994.

[78] B. Sandstede and A. Scheel. Absolute and convective instabilities of waves on unbounded and large bounded domains. Physica D: Nonlinear Phenomena, 145:233–277, 2000.

[79] D. A. Saville. Electrohydrodynamics: the Taylor-Melcher leaky dielectric model. Annual Review of Fluid Mechanics, 29:27–64, 1997.

[80] B. Scheid, C. Ruyer-Quil, and P. Manneville. Wave patterns in film flows: modelling and three-dimensional waves. Journal of Fluid Mechanics, 562:183–222, 2006.

[81] H. Schlichting and K. Gersten. Boundary-layer theory. Springer, 2016.

[82] K. Serifi, N. A. Malamataris, and V. Bontozoglou. Transient flow and heat transfer phenomena in inclined wavy films. International Journal of Thermal Sciences, 43:761–767, 2004.

[83] V. Y. Shkadov. Wave flow regimes of a thin layer of viscous fluid subject to gravity. Fluid Dynamics, 2:29–34, 1967.

[84] T. M. Squires and S. R. Quake. Microfluidics: Fluid physics at the nanoliter scale. Reviews of Modern Physics, 77:977–1026, 2005.

[85] L. E. Stillwagon and R. G. Larson. Fundamentals of topographic substrate leveling. Journal of Applied Physics, 63:5251–5258, 1988.

[86] L. E. Stillwagon and R. G. Larson. Leveling of thin films over uneven substrates during spin coating. Physics of Fluids A: Fluid Dynamics, 2:1937–1944, 1990.

[87] H. A. Stone, A. D. Stroock, and A. Ajdari. Engineering flows in small devices: microfluidics toward a lab-on-a-chip. Annual Review of Fluid Mechanics, 36:381–411, 2004.

[88] G. I. Taylor. Disintegration of water drops in an electric field. Proceedings of the Royal Society of London A, 280:383–397, 1964.

[89] G. I. Taylor and A. D. McEwan. The stability of a horizontal fluid interface in a vertical electric field. Journal of Fluid Mechanics, 22:1–15, 1965.

[90] B. S. Tilley, P. G. Petropoulos, and D. T. Papageorgiou. Dynamics and rupture of planar electrified liquid sheets. Physics of Fluids, 13:3547–3563, 2001.

[91] R. J. Tomlin, D. T. Papageorgiou, and G. A. Pavliotis. Three-dimensional wave evolution on electrified falling films. Journal of Fluid Mechanics, 822:54–79, 2017.

[92] H. Tougou. Long waves on a film flow of a viscous fluid down an inclined uneven wall. Journal of the Physical Society of Japan, 44:1014–1019, 1978.

[93] B. Tower. First report on friction experiments. Proceedings of the Institution of Mechanical Engineers, 34:632–659, 1883.

[94] L. N. Trefethen. Spectral methods in MATLAB. Society for Industrial and Applied Mathematics, 2000.

[95] Y. Y. Trifonov. Viscous film flow down corrugated surfaces. Journal of Applied Mechanics and Technical Physics, 45:389–400, 2004.

[96] D. Tseluiko and M. G. Blyth. Effect of inertia on electrified film flow over a wavy wall. Journal of Engineering Mathematics, 65:229–242, 2009.

[97] D. Tseluiko, M. G. Blyth, and D. Papageorgiou. Absolute and convective instabilities in non-local active-dissipative equations arising in the modelling of thin liquid films. 4th Micro and Nano Flows Conference, 2014.

[98] D. Tseluiko, M. G. Blyth, and D. T. Papageorgiou. Stability of film flow over inclined topography based on a long-wave nonlinear model. Journal of Fluid Mechanics, 729:638–671, 2013.

[99] D. Tseluiko, M. G. Blyth, D. T. Papageorgiou, and J.-M. Vanden-Broeck. Effect of an electric field on film flow down a corrugated wall at zero Reynolds number. Physics of Fluids, 20:042103, 2008.

[100] D. Tseluiko, M. G. Blyth, D. T. Papageorgiou, and J.-M. Vanden-Broeck. Electrified viscous thin film flow over topography. Journal of Fluid Mechanics, 597:449–475, 2008.

[101] D. Tseluiko, M. G. Blyth, D. T. Papageorgiou, and J.-M. Vanden-Broeck. Viscous electrified film flow over step topography. SIAM Journal on Applied Mathematics, 70:845–865, 2009.

[102] D. Tseluiko, M. G. Blyth, D. T. Papageorgiou, and J.-M. Vanden-Broeck. Electrified falling-film flow over topography in the presence of a finite electrode. Journal of Engineering Mathematics, 68:339–353, 2010.

[103] D. Tseluiko, M. G. Blyth, D. T. Papageorgiou, and J.-M. Vanden-Broeck. Electrified film flow over step topography at zero Reynolds number: an analytical and computational study. Journal of Engineering Mathematics, 69:169–183, 2011.

[104] D. Tseluiko and D. T. Papageorgiou. Wave evolution on electrified falling films. Journal of Fluid Mechanics, 556:361–386, 2006.

[105] D. Tseluiko and D. T. Papageorgiou. Nonlinear dynamics of electrified thin liquid films. SIAM Journal on Applied Mathematics, 67:1310–1329, 2007.

[106] D. Tseluiko and D. T. Papageorgiou. Dynamics of an electrostatically modified Kuramoto–Sivashinsky–Korteweg–de Vries equation arising in falling film flows. Physical Review E, 82:016322, 2010.

[107] J.-M. Vanden-Broeck. Free-surface flow over an obstruction in a channel. Physics of Fluids, 30:2315–2317, 1987.

[108] J.-M. Vanden-Broeck. Gravity-capillary free-surface flows. Cambridge University Press, 2010.

[109] R. Vellingiri, D. Tseluiko, and S. Kalliadasis. Absolute and convective instabilities in counter-current gas–liquid film flows. Journal of Fluid Mechanics, 763:166–201, 2015.

[110] S. Veremieiev, H. M. Thompson, M. Scholle, Y. C. Lee, and P. H. Gaskell. Electrified thin film flow at finite Reynolds number on planar substrates featuring topography. International Journal of Multiphase Flow, 44:48–69, 2012.

[111] C.-Y. Wang. Liquid film flowing slowly down a wavy incline. American Institute of Chemical Engineers Journal, 27:207–212, 1981.

[112] C.-Y. Wang. Thin film flowing down a curved surface. Zeitschrift für angewandte Mathematik und Physik ZAMP, 35:532–544, 1984.

[113] A. Wierschem, V. Bontozoglou, C. Heining, H. Uecker, and N. Aksel. Linear resonance in viscous films on inclined wavy planes. International Journal of Multiphase Flow, 34:580–589, 2008.

[114] A. Wierschem, M. Scholle, and N. Aksel. Vortices in film flow over strongly undulated bottom profiles at low Reynolds numbers. Physics of Fluids, 15:426–435, 2003.

[115] Y. Xie. Solving the generalized benney equation by a combination method. International Journal of Nonlinear Science, 15:350–354, 2013.

[116] C.-S. Yih. Stability of liquid flow down an inclined plane. Physics of Fluids, 6:321–334, 1963.